MEASUREMENT OF THE PRODUCTION RATE OF THE CHARM JET RECOILING AGAINST THE W BOSON USING THE DØ DETECTOR AT THE FERMILAB TEVATRON COLLIDER.

by

MAHSANA AHSAN

M.S., Punjab University, Pakistan, 2001

AN ABSTRACT OF A DISSERTATION

submitted in partial fulfillment of the
requirements for the degree

DOCTOR OF PHILOSOPHY

Department of Physics
College of Arts and Sciences

KANSAS STATE UNIVERSITY
Manhattan, Kansas
2008

Abstract

This dissertation describes a measurement of the rate of associated production of the W boson with the charm jet in the proton and anti-proton collisions at the center-of-mass energy of 1.96 TeV at the Fermilab Tevatron Collider. The measurement has direct sensitivity to the strange quark content inside the proton. A direct measurement of the momentum distribution of the strange quark inside the proton is essential for a reliable calculation of new physics signal as well as the background processes at the collider experiments. The identification of events containing a W boson and a charm jet is based on the leptonic decays of the W boson together with a tagging technique for the charm jet identification based on the semileptonic decay of the charm quark into the muon. The charm jet recoiling against the W boson must have a minimum transverse momentum of 20 GeV and an absolute value of pseudorapidity less than 2.5. This measurement utilizes the data collected by the DØ detector at the Fermilab Collider. The measured rate of the charm jet production in association with the W boson in the inclusive jet production with the W boson is 0.074 ± 0.023, which is in agreement with the theoretical predictions at the leading order in Quantum Chromodynamics.

MEASUREMENT OF THE PRODUCTION RATE OF THE CHARM JET RECOILING AGAINST THE W BOSON USING THE DØ DETECTOR AT THE FERMILAB TEVATRON COLLIDER.

by

MAHSANA AHSAN

M.S., Punjab University, Pakistan, 2001

A DISSERTATION

submitted in partial fulfillment of the
requirements for the degree

DOCTOR OF PHILOSOPHY

Department of Physics
College of Arts and Sciences

KANSAS STATE UNIVERSITY
Manhattan, Kansas
2008

Approved by:

Major Professor
Tim Bolton

Abstract

This dissertation describes a measurement of the rate of associated production of the W boson with the charm jet in the proton and anti-proton collisions at the center-of-mass energy of 1.96 TeV at the Fermilab Tevatron Collider. The measurement has direct sensitivity to the strange quark content inside the proton. A direct measurement of the momentum distribution of the strange quark inside the proton is essential for a reliable calculation of new physics signal as well as the background processes at the collider experiments. The identification of events containing a W boson and a charm jet is based on the leptonic decays of the W boson together with a tagging technique for the charm jet identification based on the semileptonic decay of the charm quark into the muon. The charm jet recoiling against the W boson must have a minimum transverse momentum of 20 GeV and an absolute value of pseudorapidity less than 2.5. This measurement utilizes the data collected by the DØ detector at the Fermilab Collider. The measured rate of the charm jet production in association with the W boson in the inclusive jet production with the W boson is 0.074 ± 0.023, which is in agreement with the theoretical predictions at the leading order in Quantum Chromodynamics.

Table of Contents

Table of Contents v

List of Figures viii

List of Tables xii

Acknowledgements xv

Dedication xvi

Preface xxi

1 Theoretical Background 1
- 1.1 Standard Model Introduction . . . 1
  - 1.1.1 Spontaneous symmetry breaking . . . 4
- 1.2 Electroweak Interaction . . . 7
- 1.3 Aspects of Quantum Chromodynamics . . . 8
  - 1.3.1 Renormalization group equation . . . 10
  - 1.3.2 Asymptotic freedom . . . 11
  - 1.3.3 Color confinement . . . 12
  - 1.3.4 Perturbative QCD dynamics . . . 12
  - 1.3.5 Non-perturbative QCD dynamics . . . 12
- 1.4 Standard Model Limitations and New Physics Models . . . 13
  - 1.4.1 Grand unification . . . 15
  - 1.4.2 Supersymmetry . . . 16

2 $p\bar{p} \rightarrow W$+jets Production Mechanism 19
- 2.1 Proton Structure . . . 19
  - 2.1.1 Parton distribution functions of proton . . . 21
- 2.2 $p\bar{p} \rightarrow Wg$ and $p\bar{p} \rightarrow Wq'$ Processes . . . 21
- 2.3 Jet Fragmentation . . . 26
- 2.4 Leading Order in α_s W+jets Cross Sections . . . 27
- 2.5 $W+c$ Process . . . 28
  - 2.5.1 Constraining s quark parton distribution function at $p\bar{p}$ collider . . . 29
  - 2.5.2 s quark contribution in W + c-jet production . . . 32
  - 2.5.3 Signature of new physics . . . 33

3 The Tevatron Accelerator and the DØ Experiment **35**
3.1 The Accelerator Complex . . . 35
3.1.1 Cockroft-Walton accelerator . . . 36
3.1.2 LINAC . . . 37
3.1.3 Booster . . . 38
3.1.4 Main injector . . . 38
3.1.5 Tevatron ring . . . 39
3.2 The DØ Detector . . . 39
3.2.1 $p\bar{p}$ collisions and luminosity . . . 40
3.2.2 Central tracking system . . . 43
3.2.3 Solenoid magnet . . . 47
3.2.4 Preshower detectors . . . 48
3.2.5 Calorimetry . . . 49
3.2.6 Muon spectrometer . . . 52
3.2.7 Data acquisition system and triggers . . . 55

4 Objects Identification and Event Reconstructions **58**
4.1 Track . . . 58
4.1.1 Alternative algorithm . . . 59
4.1.2 Histogramming track finding . . . 59
4.2 Primary Vertex . . . 60
4.3 Calorimeter Objects . . . 62
4.3.1 Electron . . . 62
4.3.2 Jets . . . 64
4.4 Muon . . . 66
4.5 Missing Transverse Energy . . . 67

5 Monte Carlo Simulation **68**
5.1 Monte Carlo Generators . . . 68
5.1.1 ALPGEN . . . 69
5.1.2 PYTHIA . . . 70
5.2 Detector Simulation . . . 70
5.3 Signal and Background Samples Generations . . . 71

6 Data Analysis and W+jets Selection **75**
6.1 W Boson Selection . . . 76
6.1.1 Corrections for the detector inefficiencies . . . 85
6.1.2 Data/MC comparison of W boson kinematics . . . 87
6.2 Jet Selections . . . 88
6.3 Background Sources to W+jets . . . 91
6.3.1 Multijet background . . . 92
6.3.2 Z+jets background . . . 100
6.3.3 Estimation of the background size . . . 100

7 W+c Selection **107**
7.1 Heavy Flavor Jets . . . 107
7.2 Muon Tagging of Heavy Flavor Jets . . . 108
7.3 Discrimination of W+c-jet Process . . . 109
7.3.1 Physics background sources to W+c-jet . . . 112
7.3.2 Multijet background to W+c-jet . . . 127
7.4 Efficiency of W+c-jet Selection . . . 130
7.4.1 Muon tagging efficiency . . . 132
7.4.2 Data-to-MC scale factor for the muon tagging efficiency . . . 133
7.4.3 Correction for the muon trigger biases . . . 134
7.5 Consistency for $W + c$-jet . . . 135

8 Measurement of Cross section Ratio of $p\bar{p} \rightarrow W$+c-jet to $p\bar{p} \rightarrow W$+jets Processes **142**
8.1 Cross Section Ratio $\frac{\sigma(p\bar{p}\rightarrow W+c\text{-jet})}{\sigma(p\bar{p}\rightarrow W+\text{jets})}$ . . . 142
8.2 Systematic Uncertainties . . . 145
8.2.1 Jet energy scale uncertainty . . . 148
8.2.2 Relative p_T resolution of jet in data and MC . . . 148
8.2.3 ϵ_c^ℓ systematic uncertainty . . . 148
8.2.4 f_c^ℓ systematic uncertainty . . . 149
8.2.5 PDF uncertainty . . . 149
8.3 Results . . . 150
8.4 Statistical Significance of the $\frac{\sigma(p\bar{p}\rightarrow W+c\text{-jet})}{\sigma(p\bar{p}\rightarrow W+\text{jets})}$ Measurement . . . 153

9 Conclusion **157**
9.1 Future Prospects . . . 157

Bibliography **164**

A Probabolity of muons from π and K decays in jets **165**

List of Figures

1.1 Higgs mass constraints in electroweak precision measurement 13
1.2 Tevatron's upper limit on the Higgs production 15
1.3 Corrections to Higgs mass 16

2.1 Partonic level $qg \to Wq'$ Feynman diagrams 22
2.2 $q\bar{q}' \to Wg$ Feynman diagram 22
2.3 Leading order (LO) diagrams 27
2.4 $sg \to Wc$ Feynman diagrams 28
2.5 $dg \to Wc$ Feynman diagrams 29
2.6 $bg \to Wc$ Feynman diagrams 29
2.7 A distribution of the s-quark and $\bar{s}$-quark momentum fraction contributing to the $W+c$ final state. The parton density function of the s-quark is obtained from the CTEQ6.1M sets. 33
2.8 A comparison of the strange quark parameterizations from the CTEQ6.5M and MRSTNLO2004 PDF sets. 34

3.1 Fermilab accelerators chain 36
3.2 Cockroft-Walton machine 37
3.3 Linear accelerator (LINAC) at Fermilab 38
3.4 Schematic view of the DØ detector at Fermilab 40
3.5 Coordinate system choice at DØ 41
3.6 Delivered and recorded luminosity at DØ 42
3.7 Luminosity monitor at DØ for measurement of luminosity 43
3.8 Central tracking system at DØ 44
3.9 Schematic view of the Silicon detector at DØ 45
3.10 Schematic view of an SMT ladder 46
3.11 Schematic view of an CFT 47
3.12 Schematic view of Solenoid magnet at DØ 48
3.13 Schematic view of a unit preshower detector at DØ 49
3.14 Schematic view of DØ calorimeter 50
3.15 Schematic view of Uranium layers in two unit cells filled with Liquid Argon . 51
3.16 Schematic view of segmentation of calorimeter sections 52
3.17 Schematic view of layers of drift chambers in DØ muon system 53
3.18 Schematic view of layers of scintillating counters in DØ muon system 54
3.19 Schematic view of mini drift tube comb in the muon system 55
3.20 Schematic view of data flow at DØ 57
3.21 Schematic view of data flow at DØ 57

4.1 An illustration of Histogramming track finding (HTF) algorithm. 60
4.2 An illustration of hit pattern in an event. 61

5.1 Distributions of the u, d, s partons and gluon momentum fractions of the proton obtained from the CTEQ6L PDF sets. 74

6.1 Drell-Yan dilepton event. 85
6.2 The W transverse mass M_T^W reconstructed from the data and MC simulation at DØ in W+jets events. 88
6.3 The W transverse momentum p_T reconstructed from the data and MC simulation at DØ in W+jets events. 89
6.4 The $\Delta\phi(\mu, \not\!\!E_T)$ distribution in inclusive $W(\rightarrow \mu\nu)$+jets sample before $\Delta\phi(\mu, \not\!\!E_T) > 0.4$ cut. 90
6.5 The jet transverse momentum p_T distribution in the data and MC simulation at DØ in W+jets events. 92
6.6 The jet multiplicity distribution in the data and MC simulation at DØ in W+jets events. 93
6.7 The electron mis-identification rate estimated from Jet-EM data sample as a function of $\not\!\!E_T$. 102
6.8 The electron mis-identification rate estimated from Jet-EM data sample as a function of p_T^e. 103
6.9 The electron selection efficiency estimated from $Z \rightarrow e^+e^-$ data sample as a function of p_T^e. 104
6.10 The muon misidentification rate estimated from "Jet-MU" data sample. . . . 105
6.11 The muon isolation efficiency estimated from "Jet-MU" data sample. 106

7.1 The distribution of invariant mass, $M_{\mu\mu}$, of two final state muons in the $W(\rightarrow \mu\nu)$+μ-tagged jet sample before the cut $M_{\mu\mu} < 70$ GeV cut. 111
7.2 The $\Delta\phi(\mu, \not\!\!E_T)$ distribution in the $W(\rightarrow \mu\nu)$+μ-tagged jet sample before $\Delta\phi(\mu, \not\!\!E_T) > 0.4$ cut. 112
7.3 $q\bar{q}' \rightarrow WQ\bar{Q}'$ Feynman diagrams 113
7.4 A few possible Feynam diagrams contributing to the Z + jets final state. . . 113
7.5 Possible Feynman diagrams at LO for W^+W^- production. The intermiate propagator is a boson on the left hand side and a quark fermion on the right hand side. 114
7.6 $t\bar{t}$ pair production and single top production subprocesses. 114
7.7 Possible diagrams for $W + b$ and $W + b\bar{c}$ processes. Contribution to these background processes is suppressed by small cross sections. 116
7.8 The jet p_T distribution of the μ-tagged jet in the $W(\rightarrow e\nu)$+μ-tagged jet sample after the final selection. 117
7.9 The jet p_T distribution of the μ-tagged jet in the $W(\rightarrow \mu\nu)$+μ-tagged jet sample after the final selection. 118

7.10 The correction factor for the background contributed from the light quark-jet in the W + jets sample is shown as a function of fully corrected jet p_T at the particle level. 120
7.11 Energy loss (dE/dx) distribution of the pions, kaons and proton as a function of the tracks p_T. At high p_T the discrimination between proton, kaon and pion goes to zero. 121
7.12 A comparison of data for the ratio of the OS weighted tracks to SS weighted present in the leading jet with the ratio of the OS pions to SS pions present in the jet is shown as a function of track transverse momentum p_T. 122
7.13 A comparison of data for the ratio of the OS weighted tracks to SS weighted present in the leading jet with the ratio of the OS pions to SS pions present in the jet is shown as a function of track transverse momentum p_T. 123
7.14 A comparison of the ratio of the OS pions to SS pions present in the jet with the ratio of the OS pions to SS pions present in the jet is shown as a function of their transverse momenta. 124
7.15 Distribution of the invariant mass of K^o_S reconstructed from two oppositely charged tracks present in the jet in the data and MC samples of W + jets. Low statistics is due to high p_T restriction on the reconstructed K^o_S. 125
7.16 A comparison of the rate of reconstructed K^o_S with $p_T > 4$ GeV in jet in data and simulation is shown here as a function of proper decay length, PDL, as defined in the text. 126
7.17 $q\bar{q} \to c\bar{c}$ and $q\bar{q} \to b\bar{b}$ subprocesses. 128
7.18 The dependence of asymmetry variable, A^μ_c, on the c-jet p_T estimated from the simulation of $W + c$-jet sample. 132
7.19 The efficiency of the μ-tagged jet convoluted with the correction factor needed to apply to selected events to adjust the shift in the jet p_T spectrum caused by the missing energy due to the semileptonic decays, which is estimated from the W + jets sample for c-jet, b-jet and light-jet. 133
7.20 The invariant mass distribution reconstructed from a muon and a track with opposite charges present in the jet cone. The distribution peaks around the J/ψ mass of 3.1 GeV, and fitted with the Gaussian for the J/ψ signal and an exponential for the background. 134
7.21 The invariant mass distribution reconstructed from two oppositely charged muons present in the jet cone. The distribution peaks around the J/ψ mass of 3.1 GeV, and fitted with the Gaussian for the J/ψ signal and a straight line for the background. 135
7.22 The figure provides the efficiencies of the muon reconstruction estimated using the $J/\psi \to \mu^+\mu^-$ data and MC sample corresponding to three jet p_T bins. Blue points show the data-to-MC scale factor in the muon reconstruction efficiency. 136

7.23 (a) The relative transverse momenta of the muon with the axis formed by the jet momentum direction and the muon momentum direction, $p_T^{\rm rel}$, (b) Schematic diagram for the distance of closest approach (also called impact parameter) of the displaced track with respect to the primary vertex. 138
7.24 (a) Comparison of the shape of the muon $p_T^{\rm rel}$ for the b, c and light jet with the background subtracted data, $(N_{OS}^{\ell} - f_c^{\ell} N_{SS}^{\ell})$, distribution in the combined channels, the MC distributions are normalized to the data entries, (b) Comparison of $p_T^{\rm rel}$ distribution for the background-subtracted $(N_{OS}^{\ell} - f_c^{\ell} N_{SS}^{\ell})$ data in the combined electron and muon channels with the expectations from the MC simulation. 139
7.25 (a) Comparison of the shapes of the muon $\frac{a}{\sigma_a}$ for the b, c and light jet with the background subtracted data, $(N_{OS}^{\ell} - f_c^{\ell} N_{SS}^{\ell})$, distribution in the combined channels, the MC distributions are normalized to the data entries, (b) Comparison of $\frac{a}{\sigma_a}$ distribution for the background-subtracted $(N_{OS}^{\ell} - f_c^{\ell} N_{SS}^{\ell})$ data in the combined electron and muon channels with the expectations from the MC simulation. 140
7.26 (a) Comparison of the shapes of the jet mass of μ-tagged jet for the b, c and light jet with the background subtracted data, $(N_{OS}^{\ell} - f_c^{\ell} N_{SS}^{\ell})$, distribution in the combined channels, the MC distributions are normalized to the data entries, (b) Comparison of the shapes of the ratio of the jet mass to the jet p_T of μ-tagged jet for the b, c and light jet with the background subtracted data, $(N_{OS}^{\ell} - f_c^{\ell} N_{SS}^{\ell})$, distribution in the combined channels, the MC distributions are normalized to the data entries. 141

8.1 Measured ratio $\frac{\sigma(p\bar{p}\to W+c\text{-jet})}{\sigma(p\bar{p}\to W+\text{jets})}$ as a function of jet p_T. (a) $W \to e\nu$ mode, (b) $W \to \mu\nu$ mode. 151
8.2 Combined measurement of the ratio $\frac{\sigma(p\bar{p}\to W+c\text{-jet})}{\sigma(p\bar{p}\to W+\text{jets})}$ in the electron channel and the muon channel. 152
8.3 The probability distribution of the expectations of the cross section ratio R_{bkd} in the null hypothesis. In the ensemble test all possible configurations of the OS and SS events and the inclusive W + jets events are obtained by allowing variations according to the systematics uncertainties associated with the parameters. 156

List of Tables

1.1 Leptons and quarks 4
1.2 Supersymmetric extension of SM 18

2.1 The measured parameters of the strange quark distributions obtained from the QCD (LO or NLO) fit to the data in the ν-nucleon deep inelastic scattering experiments are given here. Each of these measured parameter specifically corresponds to the non-strange quark and anti-quark density function (listed in last column) used in the fitting procedure. In the fifth column $\Delta a_\nu = a_{\bar{\nu}} - a_\nu$. 31

5.1 ALPGEN+PYTHIA MC sample cross sections times branching ratio. 72

6.1 Trigger used for the data selection in the electron channel. The f^{EMF} is the fraction of electromagnetic energy deposited in the EM section of the calorimeter, and the definition of f^{iso} is given in Eq. 4.1. 77
6.2 Continued table for the trigger lists used for the data selection in the electron channel. The f^{EMF} is the fraction of electromagnetic energy deposited in the EM section of the calorimeter, and the definition of f^{iso} is given in Eq. 4.1. 78
6.3 Continued table for the trigger lists used for the data selection in the electron channel. The f^{EMF} is the fraction of electromagnetic energy deposited in the EM section of the calorimeter, and the definition of f^{iso} is given in Eq. 4.1. 79
6.4 Trigger used for the data selection in the muon channel. Some triggers requires an isolated muon requirements with respect to the tracks and the calorimeter energy cells, the thresholds are $p_T^{trkHalo} < 3$ and $E_T^{halo} < 3$, the variables are defined in Sec. 6.1. 80
6.5 Continued list of triggers used for the data selection in the muon channel. Some triggers requires an isolated muon requirements with respect to the tracks and the calorimeter energy cells, the thresholds are $p_T^{trkHalo} < 3$ and $E_T^{halo} < 3$, the variables are defined in Sec. 6.1. 81
6.6 Event yields in MC and data sample after the selection criteria described in Secs. 6.1 and 6.2. 91
6.7 Electron mis-identification rate, $\epsilon^e_{\rm MJ}$, electron efficiency, ϵ^e_W, for passing the cuts $P_{trk}(\chi^2) > 0.01$ and $LH_e > 0.85$. Event yields N^e_L and N^e_T in the W+jets data sample corresponds to the selection before and after the stricter cuts are imposed. The first column is for the run ranges corresponding to the periods when no substantial changes in the electron trigger requirements were made. 97

6.8 Estimated size of the multijet background, N^e_{MJ} and $\epsilon^e_{MJ} \times N^e_{MJ}$, before and after the tight cuts ($P_{trk}(\chi^2) > 0.01$ and $LH_e > 0.85$) are applied to the inclusive W + jets samples. The number of real W + jets events determined from the matrix method are given in the third and fifth columns for electron with and without tight criteria respectively. The first column is for the run ranges corresponding to the periods when no substantial changes in the electron trigger requirements were made. 98
6.9 Multijet fraction f^e_{MJ} in the final W + jets sample that is estimated from the data sample. All errors quoted here are statistical. The multijet background decreases with increasing p_T of electron. In the very high p_T region [60-200], a relatively small increment in the estimated f^e_{MJ} indicates the contamination of the $Z \to e^+e^-$. 98

7.1 Event yields in MC and data sample after the muon-tagged jet requirement in the $W(\to e\nu)$ + jets sample. 115
7.2 Event yields in MC and data sample after the muon-tagged jet requirement in the $W(\to \mu\nu)$ + jets sample. 115
7.3 Absolute systematic uncertainties associated with the background correction factor $f^\ell_{c^-}$. To evaluate these uncertainties, $\sigma(W + c\text{-jet})$ is varied by 100%, $\sigma(W + b\bar{b})$ and $\sigma(W + c\bar{c})$ by 50%, pion multiplicity by 6%, $K^\pm/\pi^\pm$ by 20%. 128
7.4 Efficiencies for muon identification and reconstruction determined from the data and MC using the "tag and probe" method applied to the reconstructed $J/\psi \to \mu^+\mu^-$. 136

8.1 Summary of quantities used in W+c-jet cross section ratio; the first uncertainties quoted are statistical and the second systematic. 146
8.2 Summary of quantities used in W+c-jet cross section ratio for the jet $p_T > 20$ and $|\eta| < 2.5$; the first uncertainties quoted are statistical and the second systematic. 147
8.3 Cross section ratio measurement combined in the electron and muon decay channels; the first uncertainties quoted are statistical and the second systematic. The systematic uncertainties are considered to be fully correlated between the electron and muon channels. 147
8.4 Average uncertainties associated with ϵ^ℓ_c. The uncertainty due to $K^{\mu\text{JES}}_{c\text{-jet}}$ varies with the jet p_T bin, larger for low p_T bin and smaller for high p_T bin. . 149
8.5 Fractional systematic uncertainties on the measurement in the $W \to e\nu$ and the $W \to \mu\nu$ channels. 150
8.6 Combined fractional systematic uncertainties on the measurement in the $W \to e\nu$ and the $W \to \mu\nu$ channels. 150

Acknowledgments

There have been many people who supported me during various phases of this work. Running the DØ experiment itself is a huge effort by the collaboration of more than 600 talented people. I do not have enough words to thank them all for running and managing the experiment so successfully. Without their involvements this dissertation would not have been possible.

I like to express my special gratitude to my Ph.D supervisor Prof. Tim Bolton for giving me an opportunity to work on this thesis, for advising me on physics analysis, and for his generosity in taking care of me throughout my Ph.D career. I was not only blessed with his valuable guidance on the physics analysis, but also received special care from him on various problems that a non-native resident can usually face in the US. In fact, I was able to pass my test for drivers license due to his training.

I feel very lucky in working in an environment where I found very supportive, coordinating and friendly faculty members, Larry Weaver, Noel Stanton, Yurii Maravin, Glen Horton-Smith; and all postdocs in the high energy physics group at Kansas State University.

My first supervisor Prof. Dr. Mujahid Kamran, who is currently Vice Chancellor at the University of Punjab, Pakistan, initially inspired me to go for the higher studies in the field of particle physics. I used to seek his advice continuously on various aspects including learning physics. My career towards Ph.D was promoted by his kind guidance and his reference letters to the Kansas State University.

I like to thank Kristian Harder for his kind help at very initial stage of learning the DØ software tools while working on the development of a cluster monitoring tool for the silicon tracking detector. With my limited experience with the C++ programming language, he was very patient in answering my naive questions related to the code debugging. His wife is also very thoughtful and his cute daughter very entertaining.

I feel very pleasure in thanking Don Lincoln who as an active member of the QCD

physics group guided me in utilizing the data analysis tools. His continuous encouragement and inspirations in fixing the problems helped me a lot in learning how to do physics analysis. I really appreciate his promptness in answering my questions and his kindness in creating a very comfortable environment for physics discussions. All QCD group conveners Drew Alton, Markus Wobisch and Duncan Brown have been very supportive in providing everything I needed. They did a wonderful job in improving the quality of this work, and bringing it to the platform of the HEP conferences. I am very thankful to Micheal Begel for helping me understand the ALPGEN Monte Carlo samples and for his feedback towards the physics analysis as well.

I would not miss thanking all members of my editorial board at DØ for playing their major role in reviewing the physics analysis and for providing lots of feedback for the improvement of the analysis.

I like to thank my colleagues at Kansas State University, Mansoora Shamim, Jasmine Foster, Mark Smith, Alexey Ferapontov and Ketino Kaadze for sharing a nice time. I am deeply indebted to my kind hearted friend Mansoora for helping and guiding me in all difficulties I faced since I first met her in Pakistan. We spent six years living together in the US, and I have learned much from her.

The supporting staff members at Physics department, Pamela Anderson, Peggy Metthews, Jane Peterson, Deanna Selby and Lisa McNeil have been very kind and helpful in arranging for everything I needed.

I am most grateful to my parents for loving and taking care of me, and for encouraging me to achieve my goal. Without their support, I could not be able to withstand with this painstaking task.

I am very thankful to my Uncle Masood and his late wife Auntie Ghazala for taking special care of me. My acknowledgement list is still incomplete, I do not have enough words to sufficiently thank all those people who have been very kind and supportive to me throughout my career.

Dedication

To my loving parents M. Ahsan and J. Ahsan.

Preface

The subject of particle physics has played major role in the development of our revolutionary ideas for a better understanding of the universe. The scope of particle physics is very broad. Particle physicists try to address the questions such as why the universe is the way it is by studying the nature of the fundamental building blocks of the matter and the underlying principles of the interactions involving them. There are four types of forces known to exist in nature; gravitational, electromagnetic, weak and strong force. Since past century, particle physicists have made significant progress in developing the concepts of elementary particles while looking for the internal structure of particles deep down to the smaller and smaller sizes using increasingly high energy probes. Earlier in the twentieth century, atoms are found to have substructure consisting of electrons and nucleus, where the nucleus contains the protons and neutrons. While electron is known to be an elementary, the protons and neutrons are composite particles containing quarks. The standard model (SM) of particle physics predicts the quarks to be structureless particles.

Presently existing high energy experiments prove that the SM of particle physics is a successful theory, although not a complete theory. In past decades, it has become very important to perform stringent tests for the validity of the SM as much as possible, and to explore the existence of new physics phenomena that is not yet described by the SM. According to the SM, the elementary particles are classified into the leptons and quarks, which come in three generations. The second and third generations are carbon copy of the first generation except the mass differences. Each particle has its anti-particle with exactly the same mass but opposite quantum properties.

The proton is the most stable composite particle used in the high energy scattering experiments to study its constituents as well as to analyze the particles emerging out of the collisions. A dynamic proton consists of three valence quarks belonging to the first family of quarks interspersed in a sea of pairs of quark and anti-quark and the gluons produced

from the continuously interacting valence quarks via the strong force. The quark anti-quark pairs produced in the proton belong to mostly the first generation of quarks, with relatively decreasing probability from the higher and heavier generations. All these quarks and gluons present in the proton are collectively known as partons. The particles produced in the final state as a result of the proton and anti-proton collisions are analyzed to get an insight into the internal structure of the proton. The quarks do not exist in isolation, as they are produced in the final state they immediately fragment into shower of collinear particles by emitting the gluons. This shower of collinear particle is known as jet.

This dissertation presents a measurement of the production rate of the jet initiated by the charm quark recoiling against the W boson, W+c-jet, in an inclusive sample of events containing jets in conjunction with the W boson, W + jets, in $p\bar{p}$ collisions. Precise measurements of processes involving a jet initiated by a heavy flavor (bottom or charm) quark recoiling against the vector bosons (W or Z) are very important at the collider experiments to increase the discovery potential of the new phenomena in high energy physics. Such processes form background to several interesting standard model processes as well as new physics processes. Though, a large number of theoretical calculations of the production cross sections of W/Z+b or c-quark final states are available, these processes have not been studied extensively at collider experiments. The few available measurements are described elsewhere [1–3]. The W+c-quark process contributes significantly as a background to the rare processes predicted by the standard model such as Higgs boson production, the heaviest quark known as top quark production, and new physics processes such as those predicted by supersymmetry models (e.g $\tilde{t} \rightarrow \tilde{\chi}_0 c$ process, when the small mass of the supersymmetric top quark, $\tilde{t}$, allows it to decay dominantly into a charm quark and a neutral supersymmteric particle, $\tilde{\chi}_0$, called neutralino).

The measurement presented in this dissertation is sensitive to the size of one of the second generation quark, known as strange quark, content inside the proton. The momentum distribution of the strange quark in the proton is so far determined only at the fixed-target

inelastic experiments where the high energy neutrinos beam is made incident to the nucleon. At fixed-target experiments, the scale Q of the momentum transferred to the proton is about two orders of magnitude below that is obtained at the Tevatron. It is therefore important to test the universality of the evolution of strange quark distribution at high momentum scale. Measurement of the production rate of W+c-jet is the only golden SM process that is directly sensitive to the strange quark distribution function in the proton. Current global fits of the parton distribution functions poorly estimate the uncertainty on the magnitude and shape of the strange quark momentum distribution function of the proton [4]. The strange quark also contributes to the production of supersymmetric charged Higgs doublet via $s\bar{c} \rightarrow H^+$ or $\bar{s}c \rightarrow H^-$. Currently there is about 30% uncertainty associated with the strange quark momentum distribution, which motivates the necessity to precisely measure the W+c-jet cross section. The implications of the electroweak parameters such as $\sin^2\theta_W$ and CKM mixing matrix element $|V_{cs}|^2$ also induce sensitivity into the calculation of W+c-jet production cross section.

For the analysis of W + c-jet final state, the ALPGEN cross section package interfaced with PYTHIA simulation package is used to study the kinematic properties of the process and for the comparison with the data. ALPGEN calculates the tree level matrix elements which corresponds to the calculations for the strong interactions at the short distances, and PYTHIA takes the short distance physics process from ALPGEN and simulates the effects for long distance strong interactions such as fragmentation and hadronization of the quarks produced in the final state.

The measurement is performed for the ratio of the production cross section of $p\bar{p} \rightarrow W$+c-jet process to $p\bar{p} \rightarrow W$+jets process using the data collected at the DØ detector at the Fermilab Tevatron Collider. The ratio benefits from large cancellation of the uncertainties in the theoretical models as well as the experimental uncertainties. The charm jets in W+c-jet sample are identified from the semileptonic decay of the charmed meson into a muon. The charge correlation between the muon from the charmed meson decay in the

charm jet and the lepton from the associated W boson decay is a key feature to discriminate signal from the background. The dominant background processes involving light-flavored quarks recoiling against the W boson (W+u, W+d, W+s) have only a small ($\sim 15\%$) correlation between the final state leptons. This weak correlation is due to so called leading particle effect. Under this effect a muon being produced by the decays of higher transverse momentum pions ($\pi^{\pm}$) and kaons ($K^{\pm}$) is more probable than that from soft $\pi^{\pm}/K^{\pm}$. On the other hand, the processes (W+g, W+$c\bar{c}$, W+$b\bar{b}$) contributing significantly to the signal events do not produce charge correlation in the final state. Other background processes are suppressed by small cross sections or by small coupling between the quarks via weak interactions allowed by nature. Therefore, the background to W+c-jets is extracted from the data sample by using the events comprising uncorrelated final state leptons and by applying only weakly model dependent small residual correction.

The measurement of the ratio of the W+c-jet cross section to the inclusive W+jets cross section for the jet transverse momentum, p_T, above 20 GeV and the absolute value of pseudorapidity, $|\eta|$, below 2.5 is $0.074 \pm 0.019 \pm^{0.012}_{0.014}$ in agreement with the predictions of the standard model as implemented in ALPGEN and PYTHIA. The measurement of the fraction of $W + c$-jet final state as a function of the jet p_T is also performed by distributing the statistics limited dataset into three bins where jets have pseudorapidity $|\eta| < 2.5$.

The thesis is organized as follows: Chapter 1 gives an overview of the standard model along with its limitations. Chapter 2 explains the production mechanism of W+jets and W+c-jet final states. A brief description of the apparatus used for this measurement is given in Chapter 3, while Chapter 4 briefly describes how events are reconstructed at the DØ experiment. Chapter 5 explains the Monte Carlo models used for the analysis. Chapter 6 describes the data analysis and events selection criteria of the W + jets sample. The strategy to identify the W+c-jet final state in the data sample is explained in Chapter 7, and the measurements of the fraction of the W+c-jet sample in an inclusive W+jets sample for the jet $p_T > 20$ GeV and the pseudorapidity $|\eta| < 2.5$ is explained in Chapter 8. The

final Chapter 9 summarizes the result and sheds some light on the future prospects of this measurements.

Throughout the thesis, the natural system of units defined in high energy physics is used. In this system of units the constants of relativistic quantum mechanics, the speed of light, c, and the Plank's constant, $\hbar$, are defined as dimensionless constants with values equal to unity. Based on the dimensional analysis, energy, mass and momentum get same units of GeV, and the time and position get units of GeV^{-1}.

Chapter 1

Theoretical Background

1.1 Standard Model Introduction

The standard model (SM) is a successful theory of the elementary particles and the interaction governing them, which provides our current understanding of the universe. The elementary matter particles are categorized into quarks and leptons according to the SM. These are spin-1/2 particles that satisfy the Fermi-Dirac statistics and are known as fermions. The elementary matter particles undergo four types of fundamental interactions in nature by exchanging gauge particles. These interactions are gravitational, electromagnetic, weak and strong. The gauge particles are graviton for the gravitational force, photon (γ) for the electromagnetic force, $W^{\pm}$ and Z bosons for the weak force, and gluon for the strong force. They carry spin-1 quantum numbers (except the graviton which carry spin-2) and satisfy Bose-Einstein statistics. Since the spin-1 field transforms as a vector under the Lorentz transformation, these are known as the vector bosons. The gravitational interaction is well understood only classically, and is described as a result of the geometrical curvature of space and time according to the theory of General Relativity. Currently, there is no experimentally manifested theory that encompasses the gravitational force. The SM has ability to describe the properties of only three of the four known forces of nature: electromagnetic, weak and strong. The electromagnetic force that is well known for more than a century binds the atoms together. It is responsible for the phenomena such as photoelectric effect

and Compton effect. The weak force is responsible for the radioactive β decay of nuclei, and the strong force keeps nucleons bound together in the nucleus. The weak force is the only interaction in which the two physical systems that are mirror images of each other do not behave equally; this phenomenon is called parity violation. The fact that W boson of weak interaction couples only to the left-handed fermions enforces the parity violation [5]. The handedness is determined from the particle's spin direction compared to its momentum direction. If the spin direction is parallel to the momentum direction, the particle is said to be right-handed. If the spin direction is anti-parallel to the momentum direction, the particle is said to be left-handed.

Based upon the symmetry found in nature, some mathematical symmetry principles, termed as "symmetry groups", are associated with these forces describing their properties [5]. The symmetry groups providing the mathematical description of electromagnetic, weak and strong interactions in the SM are $U_Y(1)$, $SU_L(2)$ and $SU_c(3)$, where one hypercharge (Y) generator B^μ is associated with $U_Y(1)$ group, three gauge generators, W_a^μ; (a =1,2,3), belong to $SU_L(2)$ symmetry group and eight color gauge operators, G_α^μ; (α =1,2,...,8), belong to $SU_c(3)$. The $U(n)$ denotes an $n \times n$ unitary matrix ($U(1)^\dagger U(1) = 1$) of a mathematical group describing the space-time dependent rotations, and $SU(n)$ denotes an n-dimensional square matrix of a special unitary group where the determinant of the matrix is unity. The invariance of physical quantities under the symmetry group transformation leads to conservation laws, such as charge conservation and isospin conservation. A charge is a measure of the coupling strength between the fundamental particles experiencing a particular force. An "electric" charge determines the strength of the electromagnetic force, "weak" charge determines the strength of the weak force and the "color" charge represents the strength of the strong force. The electric charge is the most familiar in nature as we experience it in everyday life. The weak and color charges are not as familiar because the weak and strong forces are involved only at very small (invisible) scale. An isospin is the generator of $SU(2)$ transformation; it is mathematically similar to spin.

Like the Mendeleev's periodic table of chemical elements, the quarks and leptons participating in the fundamental interaction are arranged into three generations of leptons and quarks. Each generation of these particles comes in a doublet.

$\begin{pmatrix} \nu_e \\ e^- \end{pmatrix}$, $\begin{pmatrix} \nu_\mu \\ \mu^- \end{pmatrix}$, and $\begin{pmatrix} \nu_\tau \\ \tau^- \end{pmatrix}$ are lepton doublets.

$\begin{pmatrix} u \\ d \end{pmatrix}$, $\begin{pmatrix} c \\ s \end{pmatrix}$, and $\begin{pmatrix} t \\ b \end{pmatrix}$ are quark doublets.

The first particle of each lepton doublet known as neutrino is electric charge neutral, while the second particle have charge -1 e. For each quark doublet, the upper element has fractional charge $\frac{2}{3}$ e, while the lower element has fractional charge $-\frac{1}{3}$ e. All particles have their anti-particles with the same mass and energy but opposite quantum numbers, and therefore each doublet has its conjugate. All charged leptons (electron, muon and tau) experience the weak and electromagnetic force, but do not take part in the strong interaction. Neutrinos being the charged neutral particles interact only via the weak force. Quarks experience all forces of nature, because they carry the color charge as well as the electromagnetic charge. Second and third generations are carbon copy of first generation of the leptons and quarks in terms of all quantum numbers, but carry different masses and energies. The matter we see in everyday life is made up of only the quarks and leptons belonging to the first family. The second and third families of leptons and quarks are seen in excited states of the matter that exist shortly, e.g in cosmic rays or in the high energy collisions of matter.

Masses of quarks and leptons increase with the generation. The top quark, discovered in 1995, has the highest mass known in the world of elementary particle physics. However, the $SU_c(3) \times SU_L(2) \times U_Y(1)$ symmetry of the SM Lagrangian implies that all spin-$\frac{1}{2}$ fermions

leptons					quarks				
	electric charge (e)	spin	lifetime sec	mass GeV		electric charge (e)	spin	lifetime sec	mass GeV
e	-1	1/2	1.4×10^{34}	0.000511	up u	2/3	1/2	-	0.0015 to 0.0030
ν_e	0	1/2	-	-	down d	-1/3	1/2	-	0.0030 to 0.0070
μ	-1	1/2	2.2×10^{-6}	0.105	charm c	2/3	1/2	4×10^{-13}	1.3
ν_μ	0	1/2	-	-	strange s	-1/3	1/2	-	0.1
τ	-1	1/2	2.9×10^{-13}	1.77	top t	2/3	1/2	$< 10^{-23}$	170
ν_τ	0	1/2	-	-	bottom b	-1/3	1/2	1.5×10^{-12}	4.5

Table 1.1: Leptons and quarks [6].

and spin-1 gauge bosons are massless. Particles gain masses by introducing a hypothetical neutral scalar field, known as Higgs, that interacts with the fermions and bosons in such a way that the mass terms become gauge invariant. The vacuum state of this scalar field is not local gauge invariant, and we say that symmetry is not exact but it is spontaneously broken. The Higgs mechanism is a result of the spontaneous breaking of local gauge symmetry, as described in Sec. 1.1.1, in the particle physics world. It accounts for the fact that the particles with highest Yukawa coupling with Higgs gain higher mass [5, 7]. To complete verification of the standard model of particles, the Higgs must be discovered.

1.1.1 Spontaneous symmetry breaking

It is important for a physical theory to be renormalizable (that means physical quantities are calculable and finite) and locally gauge invariant. Consider a physical complex scalar field $\Phi(x) = \frac{1}{\sqrt{2}}(\phi_1 + i\phi_2)$ transforming into a $\Phi'(x)$ field under global gauge transformation such that $\Phi'(x) = e^{i\theta}\Phi(x)$ where θ is constant parameter in space-time. The Lagrangian of

the scalar spinless field $\Phi(x)$ is [5]

$$\mathcal{L} = \underbrace{(\partial^\mu \Phi)^\dagger (\partial_\mu \Phi)}_{\text{K.E}} - \underbrace{V(\Phi^\dagger \Phi)}_{\text{P.E}}, \tag{1.1}$$

where the first term is the kinetic energy density and the second term is the effective potential energy density. Consider the potential energy density of the form

$$V(\Phi^\dagger \Phi) = \mu^2 \Phi^\dagger \Phi + \lambda (\Phi^\dagger \Phi)^2. \tag{1.2}$$

The Lagrangian is invariant under the global gauge transformation. For a bounded potential $\mu^2 > 0$, and the minima of the potential occurs where $\phi_1 = 0$ and $\phi_2 = 0$. For $\mu^2 < 0$ case this ground state becomes unstable, and new minima occurs at $v = \pm\sqrt{-\mu^2/\lambda}$. The potential energy density no longer remains symmetric around the minima $\pm v$. By picking up one of the two possibilities of the ground states (either v or $-v$) in this case we break the global symmetry of the Lagrangian. Expanding the potential around one of the ground state, say v as $\Phi = \frac{1}{\sqrt{2}}(v + \xi + i\zeta)$ the Lagrangian becomes [5]

$$\mathcal{L}' = \underbrace{\frac{1}{2}(\partial^\mu \xi)^2 + \frac{1}{2}(\partial^\mu \zeta)^2 + \underbrace{\mu^2 \xi^2}_{\xi \text{ mass term}}}_{\text{K.E}} + \underbrace{\frac{\mu^2}{2} v^2 + \frac{\lambda}{4} v^4}_{\text{const.}} + \underbrace{\lambda v \xi \zeta^2 + \frac{\lambda}{2}\xi^2 \zeta^2 + \frac{\lambda}{4}\xi^4 + \frac{\lambda}{4}\zeta^4}_{\text{higher order terms}}. \tag{1.3}$$

The real field ξ in the $\mathcal{L}'$ expression appears to have mass $\sqrt{2}\mu$, while there is no mass term for the field ζ. Such massless field that appears after breaking the global symmetry of the ground state is known as the Goldstone boson.

Under the local gauge transformation of U(1), the field $\Phi(x)$ transforms as $\Phi'(x) = e^{i\theta(x)}\Phi(x)$, here $\theta(x)$ is space-time dependent gauge parameter. For a Lagrangian to be local gauge invariant, ∂_μ is replaced by $D_\mu = \partial_\mu + iqA_\mu$, where the gauge field transforms as $A_\mu \to A'_\mu = A_\mu - \frac{1}{q}\partial_\mu \theta$. The Lagrangian then becomes

$$\mathcal{L} = \underbrace{(D^\mu \Phi)^\dagger (D_\mu \Phi) - \frac{1}{4} F^{\mu\nu} F_{\mu\nu}}_{\text{K.E}} - V(\Phi^\dagger \Phi), \tag{1.4}$$

where the kinetic energy term for the gauge field A_μ is $-\frac{1}{4}F^{\mu\nu}F_{\mu\nu}$, where $F_{\mu\nu} = \partial_\mu A_\nu - \partial_\nu A_\mu$. The local gauge invariance of the Lagrangian requires the gauge boson field A_μ to

be massless, therefore no mass term for A^μ can be added by hand. The local symmetry breaking of the ground state is introduced by expanding the Φ around one of the new ground state $v = \sqrt{-\mu^2/\lambda}$ and inserting it into the Lagrangian in Eq. 1.4 as [5]

$$\begin{aligned}\mathcal{L}' &= \underbrace{\frac{1}{2}(\partial^\mu\xi)^2 + \frac{1}{2}(\partial^\mu\zeta)^2 - \frac{1}{4}F^{\mu\nu}F_{\mu\nu} + \underbrace{\mu^2\xi^2 + q^2v^2A^2}_{\text{mass terms}}}_{\text{K.E}} + 2qvA_\mu(\partial^\mu\zeta) \\ &+ \underbrace{\frac{\mu^2}{2}v^2 + \frac{\lambda}{4}v^4}_{\text{const.}} \\ &+ \underbrace{2qA_\mu(\xi(\partial^\mu\zeta) - \zeta(\partial^\mu\xi)) + 2q^2v\xi A^2 + q^2A^2(\xi^2+\zeta^2) + \lambda v\xi\zeta^2 + \frac{\lambda}{2}\xi^2\zeta^2 + \frac{\lambda}{4}(\xi^4+\zeta^4)}_{\text{higher order terms}}.\end{aligned} \tag{1.5}$$

One finds the real scalar ξ field and the gauge field A_μ to be massive in the local gauge invariant Lagrangian while the scalar field ζ is massless. The unphysical terms like $2qvA_\mu(\partial^\mu\zeta)$ can be made to disappear by redefining the real scalar fields such that [5]

$$\Phi(x) = \frac{1}{\sqrt{2}}(v + h(x))e^{\Theta(x)/v},$$

and by making a new choice of the gauge field $A_\mu \to A_\mu - \frac{1}{qv}(\partial_\mu\Theta(x))$. Substituting the expression for $\Phi(x)$ and the new choice of gauge field A_μ in the Eq. 1.4, one would get

$$\mathcal{L}'' = \underbrace{\frac{1}{2}(\partial_\mu h)^2 - \lambda^2v^2h^2 + \frac{1}{2}q^2v^2A^2 - \frac{1}{4}F_{\mu\nu}F^{\mu\nu}}_{\text{K.E}} - \underbrace{\frac{1}{4}\lambda h^4 + \frac{1}{2}q^2A^2h^2 + q^2vA^2h}_{\text{interaction terms}}. \tag{1.6}$$

This Lagrangian is free of the Goldstone bosons, but it does contain a massive scalar field $h(x)$ and a massive gauge boson A_μ. The Goldstone boson is said to be absorbed by the massless gauge boson. As a consequence of the interaction of gauge field with the real massive scalar field, the gauge boson acquires mass. By breaking the local gauge symmetry of the ground state the gauge invariance of the Lagrangian is preserved for a massive gauge field by introducing a massive scalar field known as Higgs. It can also been shown that the fermions couple with Higgs and gain masses depending on their Yukawa coupling with

Higgs [5].

The $U(1)$ spontaneous symmetry mechanism can be generalized to the $SU_L(2) \times U_Y(1)$ by requiring that the vacuum expectation value of the scalar field is not invariant under $SU_L(2) \times U_Y(1)$ transformation. In this case Higgs gives masses to three out of four vector gauge bosons of the unified electromagnetic and weak interactions, while the photon remains massless. The method to give mass to the vector bosons ($W^{\pm}$, Z) of weak interaction is known as "electroweak symmetry breaking".

1.2 Electroweak Interaction

Electromagnetic and weak interactions are described by the principles of quantum mechanics and special theory of relativity collectively known as quantum field theory (QFT). The field theory describing the electromagnetic interactions is known as quantum electrodynamics (QED). The vector gauge boson (photon) of electromagnetic interaction does not carry any charge or mass and hence does not conduct any self-coupling, in contrast to the vector gauge bosons of weak interaction that carry the flavor charge as well as the mass (at the energy scale $\mathcal{O}(100)$ GeV) under the Higgs mechanism. For the weak interaction such a field theory is often referred as non-Abelian QFT, or Yang-Mills QFT, which involves the self-coupling of the boson fields that in terms of group theory are expressed as the non-commuting generators. In the SM the electromagnetic and weak interaction are explained by a single unified QFT, and are associated with the unified symmetry group $SU(2)_L \times U(1)_Y$. Glashow, Salam and Weinberg (won Nobel prize in 1979) proposed a model in which the electromagnetic and weak forces can be interpreted as a single force where electromagnetic and weak coupling strengths are related and become equal after a particular energy scale (of the order of 10^{15} GeV). The coupling constant g and g' of $SU(2)$ and $U(1)$ gauge theories, respectively, are related by $\frac{g'}{g} = \tan\theta_W$, where $g \sin\theta_W = e$ and $g' \cos\theta_W = e$, where θ_W is the Weinberg mixing angle which cannot be predicted by SM, and measured experimentally with value close to unity.

According to the unification theory of the electroweak interactions, the mass eigen states (W_μ^1, W_μ^2, W_μ^3, and B_μ) can be expressed in terms of the physical states (W_μ^+, W_μ^-, Z_μ, A_μ). The physical states (W_μ^+, W_μ^-, Z_μ) are massive, while A_μ that represents the photon remains massless after the spontaneous symmetry breaking.

$$W_\mu^\pm = \frac{1}{\sqrt{2}}(W_\mu^1 \pm iW_\mu^2), \tag{1.7}$$

$$Z_\mu = (-\sin\theta_W B_\mu + \cos\theta_W W_\mu^3), \tag{1.8}$$

$$A_\mu = (\cos\theta_W B_\mu + \sin\theta_W W_\mu^3). \tag{1.9}$$

The introduction of Higgs as a consequence of spontaneous symmetry breaking not only solves the problem of local gauge invariance of electroweak Lagrangian, but also resolves the renormalizibity of the electroweak interaction cross sections. The cross sections of $W^\pm$ bosons scattering processes and self-interactions are proportional to the center-of-mass energy, $E_{\rm cm}$, and hence diverges as $E_{\rm cm} \to \infty$. In that case electroweak theory become unrenormalizable. Such divergences are exactly cancelled by the Feynman diagrams with Higgs as a propagator of W^+W^- scattering process.

1.3 Aspects of Quantum Chromodynamics

Quantum Chromodynamics (QCD) is a quantum field theory that describes the color interaction between the fundamental particles such as quarks and gluons. Quarks come in three "colors" [1], red, green or blue, and anti-quark can have anti-red (cyan), anti-green (magenta), or anti-blue (yellow). Gluons are bi-colored objects, they carry a color and anti-color such that net color is not white. The term "color" does not have the same meaning as an optical color, but it does have very similar convention.

The strong force is held responsible for keeping the quarks and gluons together in the bound states known as hadrons (further subgrouped into baryons and mesons depending on

[1] Color is just a label in QCD.

their spins). There are two distinctive mechanisms in QCD called *asymptotic freedom* and *confinement* (to be discussed shortly) that explain why quarks appear to be free particles when hadrons are struck by highly energetic particles and why quarks and gluons can not exist in free states at low energies or at higher than fermi distances. Only color singlet bound states of quarks exist in nature, implying that the hadrons are colorless composite particles. As mentioned in the previous section, the color transformation of quarks follow the algebra of the fundamental $SU(3)_c$ group representation that has eight generators corresponding to eight bi-colored gluon states. Like the SM of weak interactions, QCD is a non-Abelian gauge theory, and the matrices T in the representation of $SU(3)_c$ satisfy the following relation [8],

$$[T^a, T^b] = if^{abc}T^c, \tag{1.10}$$

where $a, b, c = 1, 2, 3, \ldots, 8$, and f^{abc} are the structure constants of the $SU(3)_c$ group. The non-Abelian nature of QCD theory corresponds to the self interaction of the gluons via the color exchanges. This distinguishes QCD from quantum electrodynamics (QED), where photons do not couple each other. The Feynman rules describing the dynamics of massive quarks and massless gluons can be derived from a local gauge invariant QCD Lagrangian density given as

$$\mathcal{L} = \sum_{\text{flavors}} \bar{q}(x)(i\not{D} - m)q(x) - \frac{1}{4}F^a_{\mu\nu}F^{\mu\nu}_a, \tag{1.11}$$

where $\not{D} = \gamma^\mu D_\mu$ and $D_\mu = \partial_\mu + i\alpha_s T_a A^a_\mu$ is a covariant derivative, where α_s is the strong coupling constant. The γ_μ are the covariant gamma matrices that satisfy the commutation relation $\{\gamma_\mu, \gamma_\nu\} = 2g^{\mu\nu}$, where $g^{\mu\nu}$ is the metric tensor. The field strength tensor $F^a_{\mu\nu}$ expressed in terms of the gluon field A^a_μ is

$$F^a_{\mu\nu} = \partial_\mu A^a_\nu - \partial_\nu A^a_\mu - \alpha_s f_{abc} A^b_\mu A^c_\nu. \tag{1.12}$$

The third term on the right hand side of Equation 1.12 represents the self-interaction of gluons. The kinetic energy term of the QCD Lagrangian is not purely kinetic, but instead

include the self-interaction between gluons. For a renormalizable theory, each term in Lagrangian should have a mass dimension four so that the action S which is the integral of the Lagrangian over all space-time is a dimensionless quantity, i.e $S = \int \mathcal{L} dx^4$. Therefore the quark field $q(x)$ has mass dimension $\frac{3}{2}$ and the gluon (gauge) field has mass dimension 1. Local gauge invariance of the Lagrangian is held responsible for the renormalizability of the theory. Under local gauge transformation of $q(x) \rightarrow e^{i\theta_a(x)T^a} q(x)$, the non-Abelian field A^a_μ must transform as

$$A^a_\mu \rightarrow A^a_\mu - \frac{1}{\alpha_s}\partial_\mu \theta^a(x) - f^{abc}\theta^b(x)A^c_\mu, \tag{1.13}$$

so that the Lagrangian given by Eq. 1.11 remains invariant.

1.3.1 Renormalization group equation

The running of the strong force coupling strength α_s at various energy scales is developed from the concept of renormalization which is required for any quantity to be physical. The renormalized quantum field theory removes the ultra-violent divergences after introducing an arbitrary cutoff scale μ. A physical quantity, for example invariant amplitude of strong interaction process, $\mathcal{M}(Q^2, \mu^2, \alpha_s)$, that depends on the energy scale Q and that is expressed in perturbation series of coupling α_s must not depend on the choice of the renormalization scale μ. This can be validated if $\mathcal{M}$ depends on the ratio Q^2/μ^2, i.e $\mathcal{M}(Q^2, \mu^2, \alpha_s)$=$\mathcal{M}(Q^2/\mu^2, \alpha_s)$. Mathematically, the μ^2 independence of $\mathcal{M}(Q^2/\mu^2, \alpha_s)$ can be expressed as

$$\begin{aligned} \mu^2 \frac{d}{d\mu^2}\mathcal{M}(Q^2/\mu^2, \alpha_s) = 0, \\ \left[\mu^2\frac{\partial}{\partial\mu^2} + \mu^2\frac{\partial\alpha_s}{\partial\mu^2}\frac{\partial}{\partial\alpha_s}\right]\mathcal{M}(Q^2/\mu^2, \alpha_s) = 0. \end{aligned} \tag{1.14}$$

This is known as the renormalization group equation [8]. After introducing new variables $t = \ln(Q^2/\mu^2)$ and $\beta(\alpha_s) = \mu^2\frac{\partial\alpha_s}{\partial\mu^2}$, Eq. 1.14 becomes

$$\left[-\frac{\partial}{\partial t} + \beta(\alpha_s)\right]\mathcal{M}(e^t, \alpha_s) = 0. \tag{1.15}$$

At $Q^2 = \mu^2$, $\mathcal{M}(1, \alpha_s)$ is a solution of this equation indicating that energy scale dependence of $\mathcal{M}(1, \alpha_s)$ comes through the coupling strength $\alpha_s(Q^2)$ in a renormalized theory. From Eq. 1.15, there are two sets of useful equations.

$$\frac{\partial \alpha_s(Q^2)}{\partial t} = \beta(\alpha_s(Q^2)), \tag{1.16}$$

$$\frac{\partial \alpha_s(Q^2)}{\partial \alpha_s} = \frac{\beta(\alpha_s(Q^2))}{\beta(\alpha_s)}, \tag{1.17}$$

where $\alpha_s = \alpha_s(\mu^2)$. Once $\mathcal{M}$ is determined at the fixed scale, it can be predicted for any energy scale from Eq. 1.15.

1.3.2 Asymptotic freedom

In QED, the electric charge is screened via the vacuum polarization at large distances. Therefore the magnitude of the charge is small at large distances or low energies, while it is large at small distances or high energies. Due to non-Abelian nature of QCD, the gluons involve self-coupling and the color charge becomes larger at higher distances or low energies. From renormalization group equation, the expression for $\beta(\alpha_s)$ in terms of the coupling α_s at a given energy scale Q is

$$\beta(\alpha_s) = Q^2 \frac{\partial \alpha_s}{\partial Q^2}. \tag{1.18}$$

The parameter $\beta(\alpha_s)$ is expanded perturbatively [9, 10] as

$$\beta(\alpha_s) = -b\alpha_s^2(Q^2)\left[1 + b'\alpha_s(Q^2) + \mathcal{O}(\alpha_s^2(Q^2))\right], \tag{1.19}$$

where $b = (33 - 2n_f)/12\pi$, n_f denotes the number of light flavors with $m_f^2 << Q^2$. Keeping only the terms of order $\alpha_s^2(Q^2)$, and substituting the expression 1.19 into the expression 1.18 and integrating over the interval $[Q^2, \mu^2]$ we get

$$\begin{aligned} \alpha_s(Q^2) &= \frac{\alpha_s(\mu^2)}{1 + \alpha_s(\mu^2) b \ln(Q^2/\mu^2)}, \\ &= \frac{\alpha_s(\mu^2)}{1 + \frac{\alpha_s(\mu^2)}{2\pi}(33 - 2n_f)\ln(Q^2/\mu^2)}. \end{aligned} \tag{1.20}$$

From this expression, as $Q^2 \to \infty$, the coupling constant $\alpha_s(Q^2) \to 0$, and the coupling is said to be "running" at high Q^2. At very high momentum scale, the quarks are free particles, therefore in deep inelastic scatterings they interact as point-like particles.

1.3.3 Color confinement

From the running of the coupling constant $\alpha_s(Q^2)$, the interaction between the quarks and gluons become stronger at low energy scales or large distances ($\mathcal{O}(10^{-15}$ m)). Therefore quarks and gluons cannot exist in free state. The bound state of quarks and gluons is known as hadron, which is a colorless object. The momentum scale at which $\alpha_s(Q^2)$ diverges is usually known as Λ_{QCD} parameter. In terms of Λ_{QCD} the strong coupling becomes

$$\alpha_s(Q^2) = \frac{12\pi}{(33 - 2n_f)\ln(Q^2/\Lambda^2_{QCD})}. \tag{1.21}$$

Experimentally known fact is that Λ_{QCD} is around 200 MeV.

1.3.4 Perturbative QCD dynamics

If the momentum scale $Q^2 >> \Lambda^2_{QCD}$, the coupling constant α_s is small (less than 1), therefore the higher order terms in α_s will be small compared to the first order in α_s. The perturbative calculation of an observable upto a few orders will be valid in such case. In high energy collisions the cross sections of the quark-quark, quark-gluon, or gluon-gluon interactions would be finite and can be evaluated perturbatively. The deep inelastic lepton-nucleon scattering and hadron-hadron scattering experiments are therefore used to test the validity of the perturbation theory of QCD.

1.3.5 Non-perturbative QCD dynamics

If the momentum scale $Q^2 < \Lambda^2_{QCD}$, the α_s becomes greater than 1, and the terms involving higher order in α_s becomes more important. In such case the perturbative calculations will no longer be valid. Examples of such dynamics are the emission of soft (low p_T) gluon by a quark or gluon. Another example would be the splitting of a gluon into two collinear

quarks or gluons. The QCD dynamic of the partons (quarks and gluons) present in a proton cannot be evaluated using the perturbative theory, because of the presence of soft and collinear quark/gluon radiations, as is discussed in Sec. 2.1.1. Similarly hadronization, the formation of color confined objects from the quarks and gluons, mechanism of the hadrons that occurs after a hard scatter is an example of non-perturbative QCD dynamics. The parton distribution functions of proton and hadronization process are treated via non-perturbative models.

1.4 Standard Model Limitations and New Physics Models

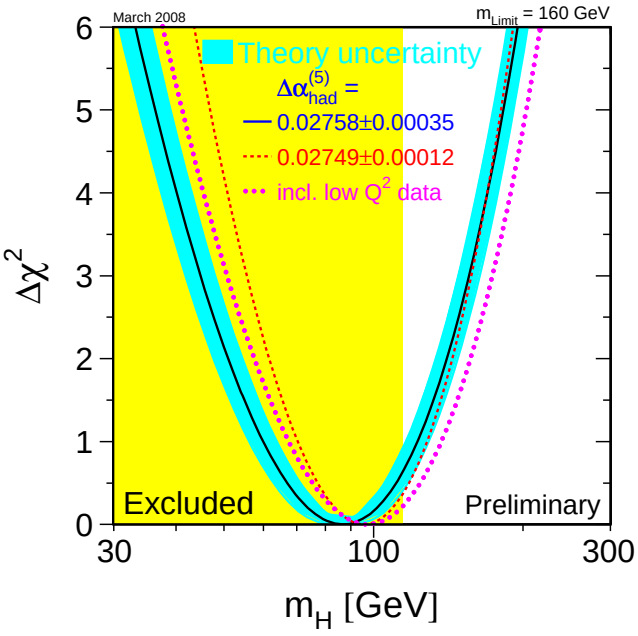

Figure 1.1: Higgs mass constraints by the precision electroweak measurements at LEP and Tevatron experiments [11].

While SM does very good job in describing the properties and principles of currently known fundamental particles and the interactions among them, there are some questions

unexplained in the realm of SM. The most profound ones are why there are exactly three generations of leptons and quarks; why higher generations are heavier than the lower ones; why the Higgs field that is held responsible for the masses of quarks, lepton and gauge particles as postulated by the SM is failed to discover so far; why our universe is left out with only the matter particles while matter-anti-matter are equally produced in pair creation processes; what makes the proton a stable particle (lifetime $\approx 10^{30}$ years), while proton decay into a neutral pion (π^o) and a positron, e^+, is predicted as a consequence of the unification of QCD and electroweak interactions at 10^{16} GeV energy scale; the existence of the cosmological dark matter undescribed by the SM, that is responsible for about 25% density of the universe as the cosmological data suggests.

The vacuum expectation value v of the Higgs can be estimated from the measurements of the SM parameters at low energy experiments. In the standard electroweak model the mass of W boson is $M_W = \frac{1}{2} g_W v$, which can be related to the Fermi coupling constant ($G_F = 1.166 \times 10^{-5}$ GeV^{-2}) of four-point fermion interaction via $\frac{G_F}{\sqrt{2}} = g_W^2/8M_W^2$. This implies that $v = \frac{1}{\sqrt{2}G_F} \approx 246$ GeV. The Higgs mass is related to v as $M_H = \sqrt{2\lambda}v$, where λ is an arbitrary dimensionless coupling that is not predicted by the SM. Therefore the mass of Higgs has to be measured experimentally. Vacuum stability requirement sets a lower theoretical bound [12] on the Higgs mass of the order of 10 GeV, and the validity of perturbative calculations of physical quantities such as Higgs decay width set the upper theoretical bound [13] of up to 1 TeV. Current experiments set constraints on the mass of the Higgs boson, and low mass ($\approx$ 100 GeV) Higgs are more favored, as Fig. (1.1) shows that the upper limit on the Higgs mass is 160 GeV at the 95% confidence level. Figure 1.2 shows a recent result from the experiments at the Tevatron Collider that set the limits on the production cross section of the Higgs boson after searching for it in various accessible decay modes allowed by the Higgs mass.

It might be true that the SM is just a low energy interpretation of a more comprehensive new (undiscovered) physics model whose discovery is presently beyond the energy reach of

the existing particle physics experiments such as Fermilab, where proton (p) and anti-proton ($\bar{p}$) collides at the center-of-mass energy of 1.96 TeV. The newly built highest energy p-p collider experiment at 14 TeV located at Eurpeon particle physics laboratory (CERN) in Geneva, Switzerland will be looking for new physics in summer 2008.

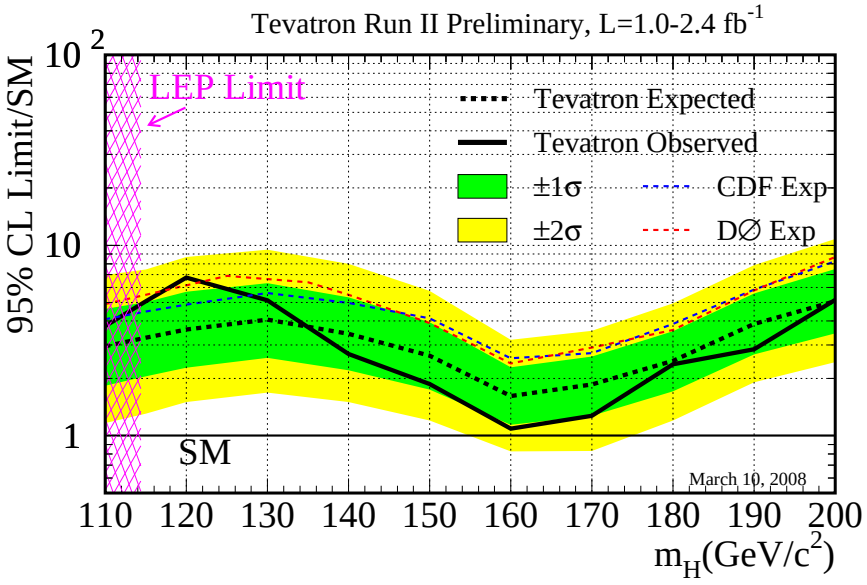

Figure 1.2: The combined upper limit of Higgs boson production by two experiments CDF and DØ at the Tevatron collider [14].

1.4.1 Grand unification

Grand unification theory (GUT) is a generalization of electroweak $SU(2) \times U(1)$ unification to the unification of $SU(3)$, $SU(2)$ and $U(1)$ gauge theories. In this unification the strong, weak and electromagnetic coupling constants become equal at an energy scale of order 10^{15} GeV. In contrast to the SM, the value of the parameter $\sin^2 \theta_W$ can be predicted by GUT at a particular energy scale, and the predicted value at 10 GeV scale is ≈ 0.2, which is very close to the measured value at low Q^2 electroweak precision experiments [15, 16]. If

one choose $SU(5)$ as a grand group of $SU(3) \times SU(2) \times U(1)$ then the unified force is associated with 24 gauge bosons, of which there are 8 gluons, 4 electroweak gauge bosons ($W^{\pm}$, Z^o, γ) and 12 new heavy bosons ($\approx 10^{15}$ GeV) known as technicolors denoted as X, Y that carry both color and electroweak charges. The presence of such heavy particles will allow an extremely slow ($\approx 10^{30}$ years) proton decay into a neutral π meson and a positron ($p \rightarrow \pi^o + e^+$) at the cost of baryon and lepton number violations. Further consideration is that at the very early stages of the universe the charge (C) or charge-parity (CP) was violated and the technicolor and anti-technicolor particles decayed with different rates into the quarks and anti-quark that led to excess of the matter over the anti-matter. However, there is not yet any experimental evidence for the existence of technicolor.

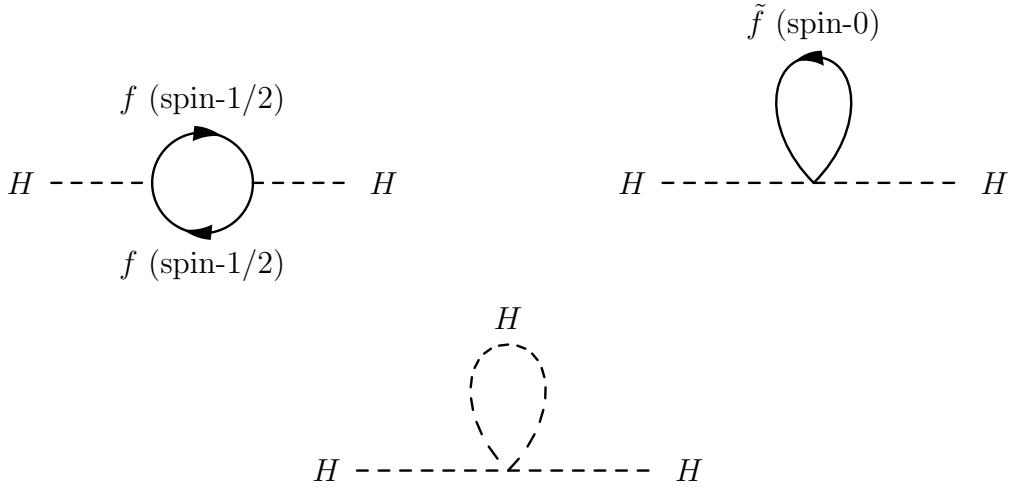

Figure 1.3: Corrections to Higgs mass.

1.4.2 Supersymmetry

A symmetry transformation relating the fermions with the bosons is known as supersymmetry (SUSY). It is the principle developed in various models that describe physics at arbitrarily high energies as large as the Plank mass scale ($\approx 10^{19}$ GeV). A supersymmetry

model is an extension to the SM, according to which every fermion in SM such as quark or lepton has its supersymmeric scalar partner known as supersymmetric quark or lepton or simply "squark" or "slepton", respectively. Similary every vector gauge boson in SM has its supersymmetric gauge boson partner known as gaugino. Conventionally, to name a SUSY partner an "s" is placed before the SM fermions names and an "ino " is added after the SM boson names. The spin difference between the SM particles and their supersymmetric partners is 1/2 unit [17]. For illustration purpose, Table 1.2 lists the particles with spin-0, spin-1 and spin-2 in the supersymmetric extension to the SM.

Due to the Higgs coupling with fermions and boson as shown in Fig. 1.3, there are quantum correction terms contributing to the Higgs mass that are proportional to the momentum scale, the masses of the fermions and bosons and the Yukawa coupling constant. Given the fact that the top quark mass is high (recent combined result at Tevatron, $m_t = 172.6 \pm 0.8(\text{stat}) \pm 1.1(\text{syst})$ GeV [18]) the higher order correction terms becomes dominant over the lowest order term and the Higgs mass diverges at very high momentum scale. Even at low momentum scale (of the order of M_W) the Higgs mass becomes very large dominated by the top quark mass that arises because of the Higgs coupling with the fermions. Due to its own mass, it exhibits self-coupling, as shown in Fig. 1.3, that also contributes to the Higgs mass. Hence the quantum corrections to the SM Higgs predict very massive Higgs. A minimal supersymmetry model (MSSM) proposes the solution to hierarchy of the Higgs mass by extending the SM particles to twice as large, so that all divergences are exactly cancelled. In SUSY models a single scalar Higgs is not enough for the local gauge invariant interactions between the fermions and Higgs. Additionally, according to the renormalization theory a triangle anomaly (where vector bosons appear in a triangular loop) proportional to the sum of the hypercharges of all fermions is not zero, if there is only one supersymmetric partner to the SM scalar Higgs known as Higgsino (a spin 1/2 particle). SUSY predicts a Higgs doublet of $SU(2)$ group, one element that couples to the up-type quarks have hypercharge ($Y = 2(Q - I_3) = 1$) and the other with the hypercharge $Y = -1$ that couples to the

particles	spin 0	spin 1/2	spin 1	$SU(3)_c$, $SU(2)_L$, $U(1)_Y$ $Y = 2(Q - I_3)$
squarks, quarks 3 generations (doublet)	$(\tilde{u}_L,\ \tilde{d}_L)$	$(u_L,\ d_L)$		$(\mathbf{3},\ \mathbf{2},\ \frac{1}{3})$
squark, quark 3 generations (singlet)	$\tilde{u}_R$	u_R		$(\mathbf{3},\ \mathbf{1},\ \frac{4}{3})$
squark, quark 3 generations (singlet)	$\tilde{d}_R$	d_R		$(\mathbf{3},\ \mathbf{1},\ -\frac{2}{3})$
sleptons, leptons 3 generations (doublet)	$(\tilde{\nu}_L,\ \tilde{e}_L)$	$(\nu_L,\ e_L)$		$(\mathbf{1},\ \mathbf{2},\ -1)$
slepton, lepton 3 generations (singlet)	$\tilde{e}_R$	e_R		$(\mathbf{1},\ \mathbf{1},\ -2)$
gluino, gluon		$\tilde{g}$	g	$(\mathbf{8},\ \mathbf{1},\ 0)$
winos, W boson		$\tilde{W}^{\pm},\ \tilde{W}^3$	$W^{\pm},\ W^3$	$(\mathbf{1},\ \mathbf{3},\ 0)$
bino, B boson		$\tilde{B}_o$	B_o	$(\mathbf{1},\ \mathbf{1},\ 0)$
Higgsinos, Higgs	$(\tilde{H}_u^+,\ \tilde{H}_u^o)$	$(H_u^+,\ H_u^o)$		$(\mathbf{1},\ \mathbf{2},\ 1)$
Higgsinos, Higgs	$(\tilde{H}_d^o,\ \tilde{H}_d^-)$	$(H_d^o,\ H_d^-)$		$(\mathbf{1},\ \mathbf{2},\ -1)$

Table 1.2: Supersymmetric extension of SM.

down-type quarks. The MSSM model predicts at least one light Higgs with mass less than 135 GeV [17].

Except the spin difference, the mass and quantum properties of the SUSY particles should be exactly equal to their SM partners. However, the fact that the SUSY particles are not observed so far implies that supersymmetry must be a broken symmetry, and these particles acquire very high masses. The upper limit on their masses is 1 TeV [17]. The lower limits are being placed by experiments where the sparticles are not observed in the kinematic regime predicted by SUSY models.

Chapter 2

$p\bar{p} \rightarrow W+$jets Production Mechanism

2.1 Proton Structure

The proton is the most stable composite particle that is used in hadron collider experiments to explore new physics and to carry out precision measurements of the SM parameters. High energy collider experiments provide excellent probe of the internal structure of the proton. It is crucial to precisely measure the proton structure, because the production probability of various interesting SM processes depends on the precise knowledge of the fraction of momentum carried by the quarks and gluons inside the proton. This is also important in particular for the theoretical cross section calculations of physics processes beyond the SM. The constituents of the proton are collectively known as partons. A proton consists of two u quarks and one d quark that are known as the "valence quarks" that define the quantum properties of the proton. The valence quarks constantly interact with each other via the exchange of gluons, and the radiated gluons in proton create additional $q\bar{q}$ pairs, which in turn produce more gluons from pair annihilation. The $q\bar{q}$ pairs produced in proton are known as "sea quarks". The momentum density functions of the valence and the sea quarks in the proton satisfy the following relations

$$\int_0^1 dx \left[u(x) - \bar{u}(x)\right] = 2, \tag{2.1}$$

$$\int_0^1 dx \left[d(x) - \bar{d}(x)\right] = 1, \tag{2.2}$$

$$\int_0^1 dx\,[s(x) - \bar{s}(x)] = 0, \tag{2.3}$$

$$\int_0^1 dx\,[c(x) - \bar{c}(x)] = 0, \tag{2.4}$$

$$\int_0^1 dx\,\left[b(x) - \bar{b}(x)\right] = 0, \tag{2.5}$$

where $q(x)$, $q = u, d, s, c, b$, represents a momentum distribution function of a q parton inside the proton, where x denotes the momentum fraction carried by the partons and lies between '0' and '1'. The valence quarks carry relatively larger momentum fraction than the sea quarks at high x, while at low x the sea quarks contribution dominates. Among the sea quarks the light quarks (u, d, s) contribution is dominant over the heavy quarks (c and b). Since the top quark is the heavy particle and decays within 10^{-23} sec, it does not contribute to the proton structure. It is the only color object that can exist in free state, but for an extremely short time. Gluons have been found experimentally to carry about 50% of the proton's momentum.

The structure of the proton can be measured experimentally using the principles of momentum conservation. Such principles are called momentum sum rules that are generally expressed in terms of the parton density in the proton. Examples are:

$$\int_0^1 \frac{1}{2x}\,[F_2^{\nu n} - F_2^{\nu p}]\,dx = 1, \tag{2.6}$$

which is known as Alder's sum rule [19], where $F_2^{\nu n}$ and $F_2^{\nu p}$ are the structure functions that are measured in neutrino experiments in ν-neutron and ν-proton deep inelastic scatterings. This is based on the fact that the neutron contains two d valence quarks, while the proton contains only one d valence quark. And, similarly the following expression

$$\int_0^1 \frac{1}{2x}\left[xF_3^{\nu p} + xF_3^{\bar{\nu} p}\right] dx = 3, \tag{2.7}$$

is known as Gross-Lwellyn-Smith's sum rule [20], where $F_3^{\nu p}$ and $F_3^{\bar{\nu} p}$ are the structure functions that are measured in neutrino experiments in ν-proton and $\bar{\nu}$-proton deep inelastic

scatterings. Such sum rules have been employed in low Q^2 experiments to measure the proton structure.

2.1.1 Parton distribution functions of proton

A parton distribution function (PDF) of the proton represents the momentum fraction of the proton carried by the parton. The PDFs cannot be calculated perturbatively, because they represent the low momentum behavior of quarks and gluons inside the proton. But they can be directly measured at the deep inelastic fixed target such as ν-N experiments or the proton collider experiments. They depend on the x and the momentum transfered Q^2 scale which is equal to the square of sum of four-momenta of all particles in the final state in the hadron collisions. The Q^2 dependence (scaling violation) of the PDF arises because of the presence of the gluon that are radiated by partons with high "x" within the proton. As Q^2 increases, more partons will be seen surrounding a quark, consequently changing the momentum distribution of that quark.

The parton distribution functions are measured at one particular energy scale Q^2, and evaluated for any higher energy scale using the Dokshitzer-Gribov-Lipatov-Alterilli-Parisi (DGLAP) [21–25] equations of QCD.

2.2 $p\bar{p} \to Wg$ and $p\bar{p} \to Wq'$ Processes

In the hard collisions of the proton-antiproton, one of the parton from the proton interacts with another parton from the anti-proton. The rate at which the partons interact with each another inside a proton is much smaller than the rate at which the cross-partons from the colliding proton and anti-proton interact at high momentum. Hence the interaction between partons from two different hadrons is point like, also referred to as elastic scattering. As mentioned earlier in Chapter 1, the W boson is a charged particle and participate only in the flavor changing interactions. In the production of W+g or W+quark final state at the leading order, both weak and strong interactions are involved at two different vertices of the

Feynman diagram, which is a pictorial representation of an interaction process suggested by Feynman. Such final states are possible through the interaction of a quark (q) with an anti-quark ($\bar{q}'$) of different flavor producing a W boson along with a gluon (g) that is radiated by one of the two initially interacting quarks, or via a quark-gluon interaction where quark in turn interacts with an anti-quark produced from the gluon splitting into $q\bar{q}$ pairs. Figures 2.1 and 2.2 show the possible Feynman diagrams of the partonic level processes $q\bar{q}' \to Wg$ and $qg \to Wq'$. A coupling constant is associated with each vertex in these diagrams. The α_W and α_s are the coupling constants of weak and strong interactions, respectively. The weak interaction coupling constant α_W is related to the fine structure constant of electromagnetic interactions, $\alpha = \frac{e^2}{4\pi}$, via the relation $\alpha_W = \frac{e^2}{8M_W^2 \sin^2\theta_W} = \frac{\pi\alpha}{2M_W^2 \sin^2\theta_W}$, as described in Sec. 1.2.

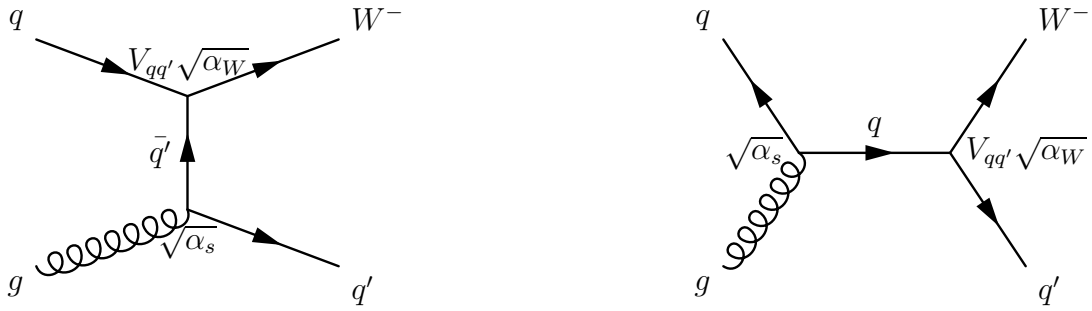

Figure 2.1: Partonic level $qg \to Wq'$ Feynman diagrams.

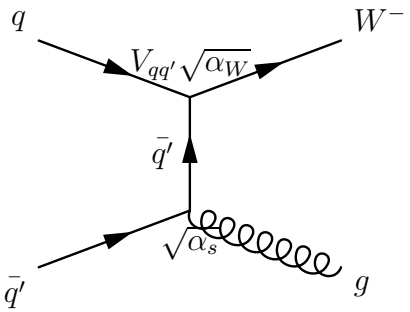

Figure 2.2: $q\bar{q}' \to Wg$ Feynman diagram.

The total cross section that represents the interaction probability of the $p\bar{p} \to Wg$ or

$p\bar{p} \to Wq'$ final state is given as [26]

$$\sigma[p\bar{p} \to Wg] = \sum_{i,k} \int_0^1 \int_0^1 dx_p dx_{\bar{p}} f_i(x_p, Q^2, \mu_F) f_k(x_{\bar{p}}, Q^2, \mu_F) \hat{\sigma}[q\bar{q'} \to Wg], \quad (2.8)$$

$$\sigma[p\bar{p} \to Wq'] = \sum_{i,k} \int_0^1 \int_0^1 dx_p dx_{\bar{p}} f_i(x_p, Q^2, \mu_F) f_k(x_{\bar{p}}, Q^2, \mu_F) \hat{\sigma}[q\bar{g} \to Wq'], \quad (2.9)$$

where p and $\bar{p}$, on the right hand side of these equation, label the proton and anti-proton, and the summation is over all initial state partons participating in this process. The partonic level cross section $\hat{\sigma}$ represents short distance QCD, while the PDFs $f_i(x_p, Q^2, \mu_F)$ represent the long distance QCD that cannot be calculated perturbatively, with μ_F a factorization scale that defines the boundary between two regimes. Factorization is performed to absorb all collinear singularities, due to the parallel emission of radiations, into an observable. The $\hat{\sigma}$ in expression 2.8 denotes the parton level cross section, which is defined as

$$\hat{\sigma} = \int \frac{\sum_{\text{spins}} |\mathcal{M}|^2 dQ}{F}, \quad (2.10)$$

where $\mathcal{M}$ is the invariant amplitude, and

$$dQ = (2\pi)^4 \delta(p_p + p_{\bar{p}} - p_W - p_j) \frac{d^3 p_W}{(2\pi)^3 2E_W} \frac{d^3 p_j}{(2\pi)^3 2E_j}, \quad (2.11)$$

is the phase space density of the final state particles, where j denotes the quark or the gluon in the final state, and $F = 2\hat{s}$ is the initial flux of interacting particles. The differential cross section may be written as

$$\hat{\sigma} = \int \frac{\sum_{\text{spins}} |\mathcal{M}|^2}{2\hat{s}} (2\pi)^4 \delta(p_p + p_{\bar{p}} - p_W - p_j) \frac{d^3 p_W}{(2\pi)^3 2E_W} \frac{d^3 p_j}{(2\pi)^3 2E_j}, \quad (2.12)$$

The invariant amplitudes of the $q\bar{q}' \to Wg$ and $qg \to Wq'$ are given as [26]

$$\sum_{\text{spins}} |\mathcal{M}|^2 (q\bar{q}' \to Wg) = (C_F \alpha_s) \left(\frac{\pi \alpha |V_{qq'}|^2}{2M_W^2 \sin^2 \theta_W} \right) \left(\frac{\hat{t}^2 + \hat{u}^2 + 2\hat{s} M_W^2}{\hat{t}\hat{u}} \right), \quad (2.13)$$

$$\sum_{\text{spins}} |\mathcal{M}|^2 (qg \to Wq') = (C_F \alpha_s) \left(\frac{\pi \alpha |V_{qq'}|^2}{2M_W^2 \sin^2 \theta_W} \right) \left(\frac{\hat{s}^2 + \hat{t}^2 + 2\hat{u} M_W^2}{\hat{s}\hat{t}} \right). \quad (2.14)$$

where C_F denotes the color factor of the strong interaction with coupling constant α_s. In expressions 2.13 and 2.14, s, t and u are called Mandelstam variables that are invariant under the Lorentz transformation. These are defined as

$$s = (p_1 + p_2)^2 \,,\ t = (p_1 - p_3)^2 \,,\ u = (p_1 - p_4)^2 = (p_2 - p_3)^2 \,, \tag{2.15}$$

where p_1, p_2, p_3 and p_4 represent the 4-momentum vectors of particles in the process 1 $2 \rightarrow 3$ 4, the indices represents the particle number, and $p_1 + p_2 = p_3 + p_4$ according to the conservation of the 4-momentum. In the high energy physics the $\sqrt{s}$ represents the center-of-mass energy. In the relativistic limit, $p_i \gg M_i$, where M_i denotes the mass of the ith particle, the variables may be given as

$$s = (p_p + p_{\bar{p}})^2 \sim 2p_p.p_{\bar{p}}, \tag{2.16}$$

$$t \sim M_W^2 - \sqrt{s}e^{-y}m_T, \tag{2.17}$$

$$u \sim M_W^2 - \sqrt{s}e^{y}m_T, \tag{2.18}$$

where $m_T = \sqrt{M_W^2 + p_{TW}^2}$ denotes the transverse mass, and y denotes the rapidity of the W boson which is defined as

$$y = \frac{1}{2}\ln\left(\frac{E_W + p_{zW}}{E_W - p_{zW}}\right), \tag{2.19}$$

E_W and p_{zW} are the energy and the component of W boson momentum in the z-direction (or longitudinal direction), respectively. In the relativistic limit ($\frac{m}{E} \rightarrow 0$) the rapidity can be approximated to pseudorapidity, η, defined as

$$\eta = -\ln\left[\tan\left(\frac{\theta}{2}\right)\right], \tag{2.20}$$

where θ is the angle with respect to the z-axis. The Mandelstam variables ($\hat{s}$, $\hat{t}$, $\hat{u}$) with "$\wedge$" over them represent the kinematic quantities at the parton level, and are related to the variables s, t and u. The parton carries a fraction "x_p" of the proton's momentum (p_p),

therefore its 4-momentum can be expressed as $x_p p_p$. Hence

$$\hat{s} = x_p x_{\bar{p}} s, \tag{2.21}$$

$$\hat{t} = M_W^2 - \sqrt{s} x_p e^{-y} m_T, \tag{2.22}$$

$$\hat{u} = M_W^2 - \sqrt{s} x_{\bar{p}} e^{y} m_T. \tag{2.23}$$

The presence of $V_{qq'}$ in the expressions for invariant amplitudes (2.13 and 2.14) is based on the fact that quarks undergo mixing via the exchange of the charged vector boson of weak interaction with a certain probability. The mixing strength are given by the elements of unitary matrix $V_{\rm CKM}$ [6] of Cabibbo, Koboyashi and Maskawa,

$$V_{\rm CKM} = \begin{pmatrix} V_{ud} & V_{us} & V_{ub} \\ V_{cd} & V_{cs} & V_{cb} \\ V_{td} & V_{ts} & V_{tb} \end{pmatrix},$$

that relates the flavor eigen states with the mass eigen state. In terms of the experimentally measured values [6] of matrix elements $V_{\rm CKM}$ is given by

$$V_{\rm CKM} = \begin{pmatrix} 0.97377 \pm 0.00027 & 0.2257 \pm 0.0021 & (4.31 \pm 0.30) \times 10^{-3} \\ 0.230 \pm 0.011 & 0.957 \pm 0.094 & (41.6 \pm 0.6) \times 10^{-3} \\ (7.4 \pm 0.8) \times 10^{-3} & (1.5 \pm 0.9) \times 10^{-3} & > 0.78 \end{pmatrix}.$$

The unitary condition on the CKM matrix implies that

$$|V_{ud}|^2 + |V_{us}|^2 + |V_{ub}|^2 = 1,$$

$$|V_{cd}|^2 + |V_{cs}|^2 + |V_{cb}|^2 = 1,$$

$$|V_{td}|^2 + |V_{ts}|^2 + |V_{tb}|^2 = 1.$$

In the presented analysis, W^- (W^+) is identified through its leptonic decays $W^- \to e^- \bar{\nu}_e$ ($W^+ \to e^+ \nu_e$) and $W^- \to \mu^- \bar{\nu}_\mu$ ($W^+ \to \mu^+ \nu_\mu$). The branching fraction (BF) of the W into a lepton-neutrino pair ($\ell \nu_\ell$) is

$$BF(W \to \ell \bar{\nu}_\ell) = \frac{\Gamma(W \to \ell \bar{\nu}_\ell)}{\sum \Gamma(W \to \ell \bar{\nu}_\ell) + \sum \Gamma(W \to q_i \bar{q}_j')}, \tag{2.24}$$

where [6]

$$\Gamma(W \to \ell\bar{\nu}_\ell) = \frac{e^2 M_W}{48\pi \sin^2\theta_W}, \tag{2.25}$$

$$\Gamma(W \to q\bar{q}') = 3|V_{qq'}|^2 \frac{e^2 M_W}{48\pi \sin^2\theta_W}, \tag{2.26}$$

where a factor of 3 difference in the Eq. 2.26 comes from the possibility for each quark to carry three different colors. Hence,

$$BF(W \to \ell\bar{\nu}_\ell) = \frac{1}{3 + 3(|V_{ud}|^2 + |V_{us}|^2 + |V_{ub}|^2 + |V_{cd}|^2 + |V_{cs}|^2 + |V_{cb}|^2)} \sim \frac{1}{9}. \tag{2.27}$$

2.3 Jet Fragmentation

A quark produced as a result of hard scattering fragments into several $q\bar{q}$ pairs and gluons such that total momentum of the initial quark is shared among all fragments. This process is known as parton shower, for which the calculations can be treated almost perturbatively above a certain cutoff scale of the order of 1 GeV. The fragments tend to move collinear to the direction of the initial quark. The shower of fragments following a particular direction is known as a jet. Because of the color confining nature of QCD, the fragments materialize into the color-singlet hadrons via soft interactions, a process known as hadronization. The hadronization is independent of the nature of the hard scattered process that creates a quark in the final state, meaning that the fragmentation function representing the probability of a hadron to carry a momentum fraction z of the initial quark are universal. Just as the parton density function describes the probability of a parton to carry a momentum fraction of a hadron, the transition of a hadron from a parton is described by the fragmentation function $D(z)$. This function can be measured at one momentum scale, which can be used to make predictions at the other momentum scales in different experiments. Three classes of non-perturbative hadronization models [27–32] (Independent fragmentation model, String model, and Cluster model) are available for the calculation of total production cross sections of various processes, and are tested at different momentum scales of the experiments.

The integral of the fragmentation function $D(z)$ with respect to z gives the average number of hadrons produced by a quark. An average number of hadrons in a jet increases logarithmically with the energy of the original quark [33]. Gluon emission by quark or anti-quark lead to Q^2 scaling violation of the fragmentation functions, and like PDFs the evolution equations are used to predict the functions at different momentum scales. A jet initiated by a gluon has different characteristics from that initiated by a quark. The gluon-initiatied jet is broader, while the quark-initiated jet is narrower at high energies. The fragmentation function of hadrons in gluon-jets is softer than that in the quark-jets, and therefore a gluon-jet contains hardons with higher multiplicity than that of a quark-jet.

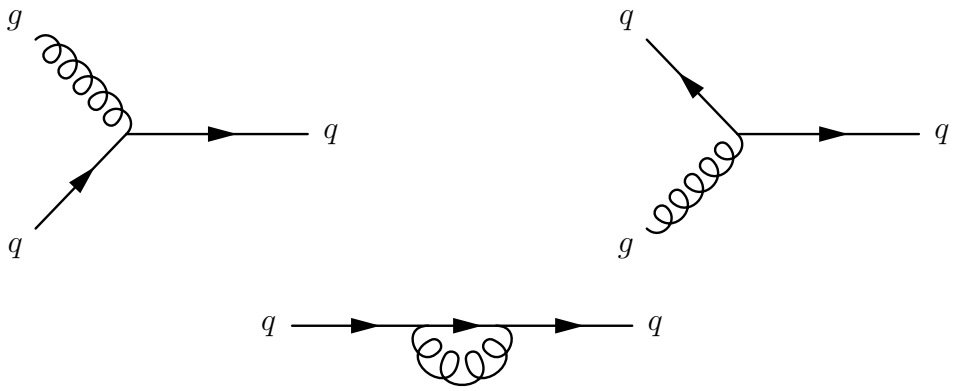

Figure 2.3: These LO diagrams include single (real or virtual) gluons, and LO diagrams in α_s. The diagrams with virtual gluon cancel the collinear singularities.

2.4 Leading Order in α_s W+jets Cross Sections

Generally, the order of α_s in the Feynman diagram determines the order of the cross section. The diagrams with first power in α_s is known as leading order. At high momentum scale of the order of M_W mass, α_s is small (~ 0.2); therefore, higher order terms in the total cross section will be smaller than the leading order (LO). Thus, a perturbative calculation of the production cross section of the parton level process upto two orders in α_s is enough to get

the total cross section.

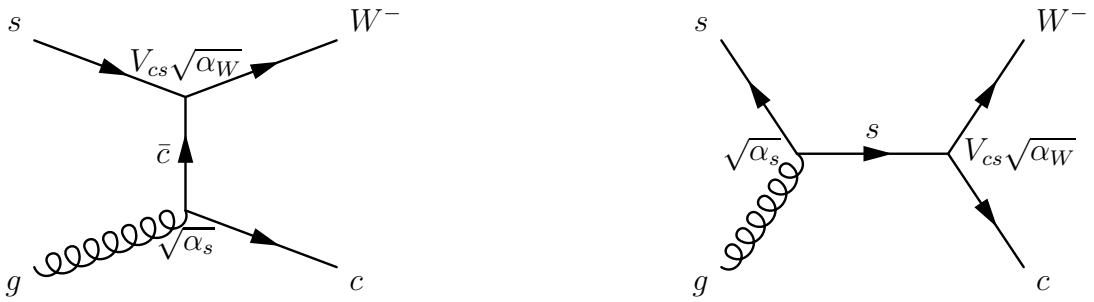

Figure 2.4: $sg \to Wc$ Feynman diagrams.

2.5 W+c Process

The W+c final state in $p\bar{p}$ collisions is one of the subprocesses of the $p\bar{p} \to Wq'$. At the parton level, W+c final state is initiated by the interaction of the gluon with an s quark or with a d quark in the proton. A leading order cross section of the W+c process can be expressed as.

$$\begin{aligned}\sigma(p\bar{p} \to Wc) &= \int_0^1 \int_0^1 dx_p dx_{\bar{p}} \, ([s(x_p,Q^2)g(x_{\bar{p}},Q^2) + s(x_{\bar{p}},Q^2)g(x_p,Q^2)]\hat{\sigma}_{sg} \\ &\quad +[d(x_p,Q^2)g(x_{\bar{p}},Q^2) + d(x_{\bar{p}},Q^2)g(x_p,Q^2)]\hat{\sigma}_{dg} \\ &\quad +[b(x_p,Q^2)g(x_{\bar{p}},Q^2) + b(x_{\bar{p}},Q^2)g(x_p,Q^2)]\hat{\sigma}_{bg}). \end{aligned} \tag{2.28}$$

Total production cross section depends on the d, s, b and g partons momentum densities inside the interacting protons. The d quark being a valence quark has larger contribution in the proton compared to the s or b quark contributions which only appear as sea quarks. However, the parton level cross sections $\hat{\sigma}_{dg}$, $\hat{\sigma}_{sg}$ and $\hat{\sigma}_{bg}$ depend on the CKM matrix elements V_{cd}, V_{cs} and V_{cb}, as can be seen in the expression (2.14). Nature allows s quark to couple with a c quark with the highest probability compared to a d quark or a b quark (i.e $V_{cs} \gg V_{cd} \gg V_{cb}$ as described in the previous section). The contribution from b parton to the W+c process is negligible due to very small $b(x_p, Q^2)$ and tiny V_{cb}. Consequently, the

production of W+c is dominated by the s-g interaction. By performing the calculations using cross section package COMPHEP [34], it turns out that about 85% contribution to the W+c production comes from the s-g interaction and the remaining 15% from the d-g interaction. Since the production cross section of W+c process depends on the electroweak parameters such as $\sin^2\theta_W$ and CKM mixing matrix element $|V_{cs}|^2$, the measurement has direct sensitivity to these parameters as well.

Figure 2.5: $dg \to Wc$ Feynman diagrams.

Figure 2.6: $bg \to Wc$ Feynman diagrams.

2.5.1 Constraining s quark parton distribution function at $p\bar{p}$ collider

The W+c final state is directly sensitive to the s quark PDF. Measurement of this final state in the p-$\bar{p}$ collision experiment gives an insight to the sea quarks inside the proton.

Previous measurements of s quark PDFs

The s quark has been measured so far only at the fixed target experiments in the ν-N interaction [35–41]. The momentum scale of these experiments were $\mathcal{O}(10)$ GeV^2, which is two to three orders of magnitudes below that of the production of $W+c$ process at the Tevatron collider. In most of these measurements the magnitude and shape of the s and $\bar{s}$ quark distribution was generally defined in terms of the non-strange sea quarks distribution functions $\bar{u}(x, Q^2)$ and $\bar{d}(x, Q^2)$ of the proton.

$$s(x) = \kappa_\nu \frac{\bar{u}(x, Q^2) + \bar{d}(x, Q^2)}{2}(1-x)^{a_\nu}, \tag{2.29}$$

$$\bar{s}(x) = \kappa_{\bar{\nu}} \frac{\bar{u}(x, Q^2) + \bar{d}(x, Q^2)}{2}(1-x)^{a_{\bar{\nu}}}, \tag{2.30}$$

where κ is a constant that refers to the magnitude of the strange sea. The neutrino scattering with the nucleus measures the s quark distribution and the anti-neutrino scattering with the nucleus measures the $\bar{s}$ quark distribution. As the parameters κ_ν and $\kappa_{\bar{\nu}}$ has been measured to be non-unity, measurements favor a non-symmetric $SU(3)$ flavor sea. Table 2.1 summarizes the parameters of the strange sea distributions measured in few ν-nucleon experiments for illustration purposes.

The latest analysis [35] of NuTeV determines the size of asymmetry in $s(x)$ and $\bar{s}(x)$ distributions. The asymmtery in $s(x)$ and $\bar{s}(x)$ distributions had been thought to explain the 3σ discrepancy in the NuTeV measurement of $\sin^2\theta_W$ from the world average. In this analysis [35] the shape and the size of the strange quark momentum distribution is expressed in a slightly different form using more parameters than those given in Eqs. 2.29 and 2.30. The $s(x)$ and $\bar{s}(x)$ are expressed as

$$s(x) = \frac{s^+(x) + s^-(x)}{2}, \tag{2.31}$$

$$\bar{s}(x) = \frac{s^+(x) - s^-(x)}{2}, \tag{2.32}$$

Exp.	κ_ν	$\kappa_{\bar{\nu}}$	a_ν	$a_{\bar{\nu}}$	$< Q^2 >$	PDFs
					GeV^2	
NuTeV [36]	0.44 ± 0.07	0.45 ± 0.11	1.17 ± 1.38	1.08 ± 0.60	21.1	CTEQ [42]
Charm II [37]	$0.39^{+0.10}_{-0.09}$	$\kappa_{\bar{\nu}} = \kappa_\nu$	$1.12^{+1.29}_{-1.26}$	$a_{\bar{\nu}} = a_\nu$	20	CTEQ [43]
CCFR [38]	$0.48^{+0.06}_{-0.05}$	$\kappa_{\bar{\nu}} = \kappa_\nu$	$-0.02^{+0.66}_{-0.63}$	$\Delta a_\nu = -0.46 \pm 0.87$	25.5	CCFR [44]
CCFR [39]	$0.37^{+0.05}_{-0.04}$	$\kappa_{\bar{\nu}} = \kappa_\nu$	0	0	22.2	CCFR [44]

Table 2.1: The measured parameters of the strange quark distributions obtained from the QCD (LO or NLO) fit to the data in the ν-nucleon deep inelastic scattering experiments are given here. Each of these measured parameter specifically corresponds to the non-strange quark and anti-quark density function (listed in last column) used in the fitting procedure. In the fifth column $\Delta a_\nu = a_{\bar{\nu}} - a_\nu$.

where $s^+(x)$ and $s^-(x)$ are defined as

$$s^+(x) = \kappa^+(1-x)^{\alpha^+} x^{\gamma^+} \left[\bar{u}(x) + \bar{d}(x)\right], \tag{2.33}$$

$$s^-(x) = s^+(x) \tanh\left[\kappa^-(1-x)^{\alpha^-} x^{\gamma^-} \left(1 - \frac{x}{x_o}\right)\right], \tag{2.34}$$

where the fit parameters [35] $\kappa^+ = 0.58$, $\alpha^+ = 1.40$, $\gamma^+ = 0.098$, $\kappa^- = -0.0094$, $\alpha^- = 6.59$ and $\gamma^- = 0.004$ are the NLO fit to the di-muon data of NuTeV. The size of the asymmetry $\int_0^1 [xs(x) - x\bar{s}(x)]\, dx$ needed to explain the 3σ discrepancy in the $\sin^2\theta_W$ by NuTeV measurement is of the order of $\sim +0.007$, while the measured asymmetry of $0.00196^{+0.00161}_{-0.00125}$ is insufficient.

It has become important to test the universality of the s quark parton distribution functions and to test the QCD itself by measuring these PDFs at the hadron colliders. The measurement of the production rate of W+c final state in an inclusive W+jets sample presented in this dissertation would be an excellent tool for constraining the s quark PDF.

2.5.2 s quark contribution in $W + c$-jet production

As the $W + c$ final state is dominantly (85%) initiated by the s quark with the gluon interaction, the measurement of $W + c$ provides an insight into the s quark content of the proton. Figure 2.7 shows the distribution of the proton's momentum fraction x carried by the s quark participating in the $W + c$ final state in the kinematic domain of final state particles accessible at the Tevatron. This shows that the x region of the s quark that can be constrained at the Tevatron is in the range 0.01-1. The minimum momentum transferred squared scale Q^2 at which s quark PDF can be constrained by the $W + c$ production rate measurement is $\mathcal{O}(M_W^2)$. The distributions shown in Fig. 2.7 considers the parton density function obtained from CTEQ6L [45] PDF for the theoretical calculations of $W + c$ predictions using the ALPGEN package [46] described briefly in Sec. 5.1.1. These PDFs are obtained from the DGLAP evolution of the distributions determined from the global fit analysis of the measurements performed at low momentum squared scale $\mathcal{O}(10)$ GeV. The uncertainties associated with s quark PDF in CTEQ6L set is about $5 - 10\%$ level. However, it still does not reflect a true uncertainty as the CTEQ6L PDF parametrization of the s quark is obtained from the non-strange sea quark as $r[\bar{u}(x) + \bar{d}(x)]/2$, where r is considered to be a constant factor for which no uncertainty is assigned. A comparison of the parametrization of the s quark PDF by the latest version of CTEQ6.5M [47] with the MRSTNLO2004 [48] parametrization shows that strange quark PDF has not been well constrained in the domain accessible to the Tevatron as shown in Fig. 2.8. A recent global analysis [4] for the s quark PDF fit from deep inelastic scattering measurements shows that there is about 20% uncertainty associated with the the size and shape of the s quark momentum distribution. Thus, a direct measurement of $W + c$ production rate is important to nail down the uncertainties associated with the s quark PDF. These measurements have recently been performed at the two experiments (CDF and D0) at the Tevatron [3, 49], one of these measurement are being described in this dissertation.

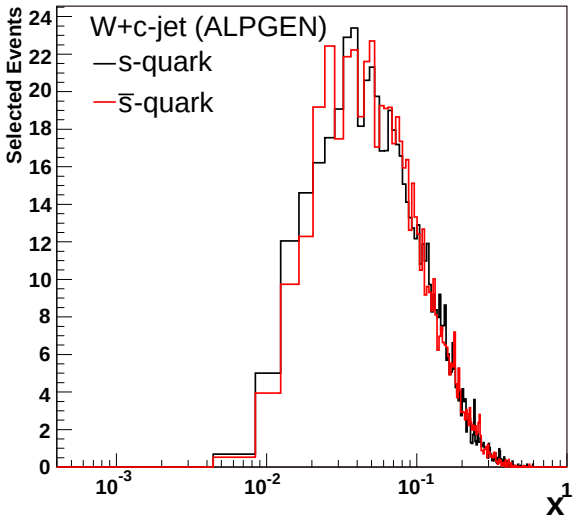

Figure 2.7: A distribution of the s-quark and $\bar{s}$-quark momentum fraction contributing to the $W + c$ final state. The parton density function of the s-quark is obtained from the CTEQ6L sets.

2.5.3 Signature of new physics

The s or $\bar{s}$ quark PDF is also sensitive to the production of the supersymmetric processes such as $s\bar{c} \rightarrow H^-$ or $c\bar{s} \rightarrow H^+$, where H^- (H^+) is a negatively (positively) charged Higgs as introduced in Sec. 1.4.2. Therefore constraining s quarks is of particular importance in searches of new physics, as well as in calculating the SM backgrounds. The $W+c$ final state mimics the signature of new physics processes such as $\tilde{t_1} \rightarrow c\tilde{\chi}^o_1$, where $\tilde{t_1}$ is the lighter partner of two supersymmetric top quark eigen-states. This decay is kinetically allowed in a SUSY model known as MSSM (Minimal supersymmetric model containing more than 100 free parameters) where $\tilde{\chi}^o_1$ known as neutralino is the lightest supersymmetric particle (LSP). The lightest supersymmetric particle is also considered as the candidate of the dark matter that is responsible of $\sim 25\%$ density of the universe.

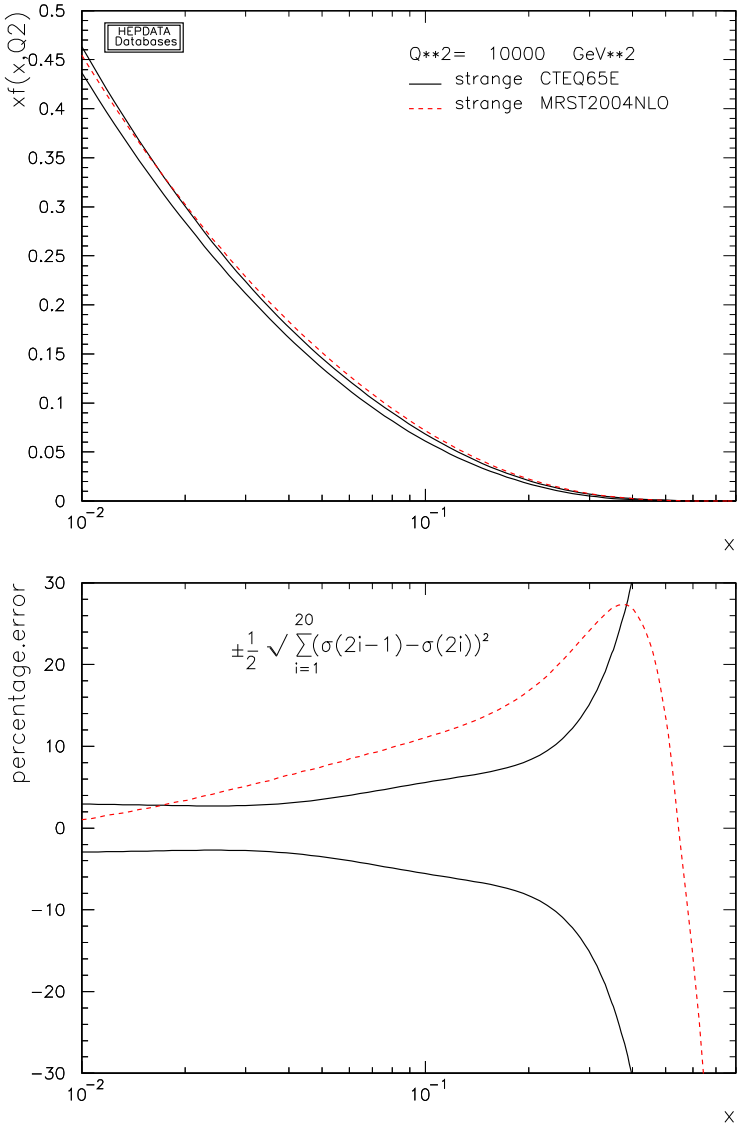

Figure 2.8: A comparison [50] of the strange quark parameterizations from the CTEQ6.5M and MRSTNLO2004 PDF sets. Black lines on the top plot represent the upward and downward distributions of the s quark according to CTEQ6.5M fit and the red dashed lines show the s quark momentum distribution according to the MRSTNLO2004. In the bottom plot the black line shows the percentage uncertainty on the s quark PDF due to CTEQ6.5M error analysis and the red dashed line show a percentage difference of the central fit CTEQ6.5M from the MRSTNLO2004. It is important to note that presented uncertainty do not reflect a true uncertainty on the s quark distribution as it is determined from the non strange sea. This figure also shows that the strange quark PDF is not well constrained.

Chapter 3

The Tevatron Accelerator and the DØ Experiment

The Fermilab Tevatron is currently the world's highest energy machine that accelerates the proton and anti-proton in circular orbits moving in the opposite directions, and collides them at the center-of-mass energy of $\sqrt{s} = 1.96$ TeV. The beam of protons or anti-protons is created as discrete bunches of particles. These bunches collide at two locations named CDF and DØ in the ring. The collision points are surrounded by arrays of detecting devices that identify the nature of the particles emerging from the collision. The measurement presented here is performed using the data collected by the DØ experiment during the period from April 2002–Feburary 2006, known as "Run IIa" period. This chapter describes the accelerator chain needed to boost up the energy of the proton upto 980 GeV and the DØ detecting devices measuring the energy, position and momentum of various particles at different levels.

3.1 The Accelerator Complex

Protons and anti-protons are produced and accelerated upto 980 GeV using a chain of accelerators as shown in Figure 3.1. Different stages of acceleration employed for smooth acceleration are described below.

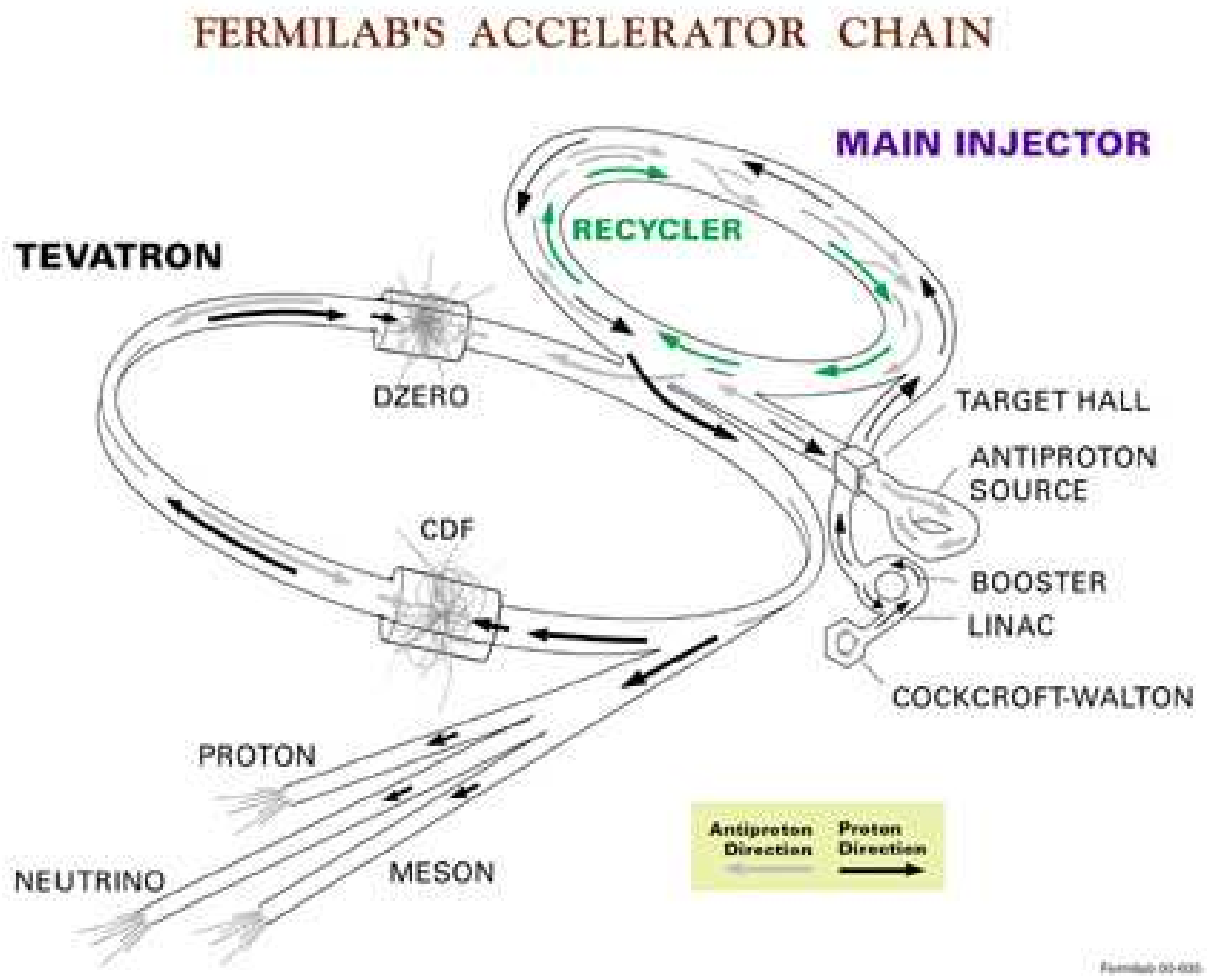

Figure 3.1: Schematic diagram of Fermilab accelerators complex. Courtesy Fermilab visual media services.

3.1.1 Cockroft-Walton accelerator

The acceleration of protons begins with Cockroft-Walton machine where the protons in the form of negatively charged hydrogen H^- atoms are created from an electron bonding with a hydrogen atom. The H^- ions are then passed through a DC voltage ladder as shown in Fig. 3.2 producing a voltage difference of 750 keV.

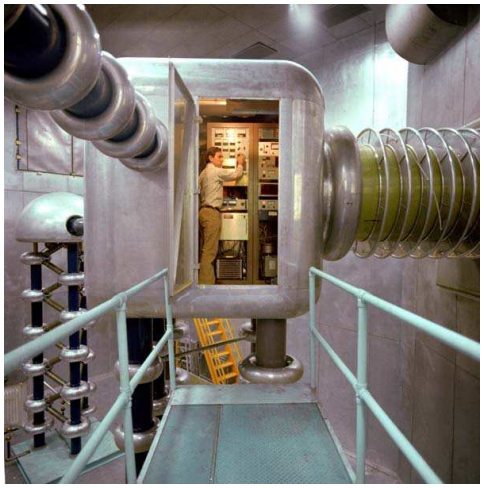

Figure 3.2: Cockroft-Walton pre-accelerator. Courtesy Fermilab visual media services.

3.1.2 LINAC

The H^- ions with 750 keV of kinetic energy further accelerate in a 130 m long linear accerelerator (LINAC) consisting of a series of drift tubes separated by vacuum gaps. Ions pass through the drift tubes where they are accelerated by the Radio Frequency (RF) cavities across the gap. The RF source produces alternative electric field (with the frequency of 200 MHz in the beginning and 805 MHz towards the end) that lets the ions accelerate toward the next drift tube as long as the direction of the electric field is along the direction of motion of the ions. The phase velocity of the electromagnetic wave and the ion's velocity is kept matched at all locations where accelerations occur so that ions continue to energize. As the ion's energy increases, the length of drift tubes and vacuum gaps increases to keep the velocity of the ion matching with the phase velocity of the electromagnetic wave. The alternating electric field concentrates the continuous ion beam into bunches, with a pulse length of about 80 μs. After the ions are accelerated to 400 MeV, they are further passed through the carbon foil to strip the electrons off and leaving only the positively charged protons.

Figure 3.3: Linear accelerator (LINAC) at Fermilab. Courtesy Fermilab visual media services.

3.1.3 Booster

At this stage of acceleration, 400 MeV protons are injected into a synchrotron, called booster, which is 472 m in circumference. The protons are accelerated using RF cavities to 8 GeV after circulating in the "booster" within 33 ms. Each proton bunch consists of the order of 10^{12} protons.

3.1.4 Main injector

The Main Injector (MI) is a circular synchrotron with 3319 m in circumference that accepts 8 GeV of protons from the booster. It raises the protons energy to 120 GeV, whence they impinge upon the nickel target to produce the anti-protons and other short-lived particles. About one million of 120 GeV protons are needed to produce 20 anti-protons with energy upto 8 GeV. The particles from the target are collimated using lithium lensing, and the magnets are used to transfer only the negatively charged anti-protons to the debuncher and eventually to the accumulator (the triangular shaped ring with flattened edges as shown in Fig. 3.1). The antiprotons from the target comes off with various energies, and the debuncher consisting of RF is used to equalize the energy of anti-protons before sending

them to the accumulator. Anti-protons are stored in the accumulator ring until needed. A technique known as stochastic cooling is used to intensify the anti-proton beam both in debuncher and accumulator. From the accumulator, anti-protons are transferred back to the MI which is ramped to 150 GeV to accelerate both the protons and anti-protons circulating in the opposite directions in the same tunnel.

3.1.5 Tevatron ring

The final stage of accelerator is the Tevatron with a radius of 1 km to which 36 bunches of proton and anti-proton having energy of 150 GeV are injected. Each bunch of proton or anti-proton consists of the order of 10^{10} particles. The Tevatron has RF cavities in the sector "F" to accelerate the beams of proton and anti-proton to 980 GeV. There are about 1000 Niobium-Titanium superconducting magnets producing 4.2 T magnetic field to guide and focus the proton and anti-proton beams in closed paths. It takes about 30 seconds to turn magnets to 4.2 T, by that time beam takes about more than one million revolutions in the ring of 6.28 km in circumference, and due to RFs the particles energy increases by 650 keV in each revolution. After the energy reaches to 980 GeV, the beams are focused using low beta magnets and made to collide with the center-of-mass energy of 1.96 TeV, at two interaction points at "B0" (also called "Collider Detector at Fermilab" or "CDF" for short) and DØ. Protons and antiprotons cross one another every 396 ns. Detectors are built around the collision points to analyze the particles emerging out of the interactions.

3.2 The DØ Detector

The DØ detector [51] is about 18 m long, 10 m high and 12 m wide hermetic device that surrounds the beam pipe, and detects the particle after the collision occurs at the center of the detector. It employs tracking and energy measuring devices in layers and covers an enormous kinematic phase space to detect the undiscovered particles. Major components of the detectors are central tracking system, magnets, calorimeter and the muon detectors.

The DØ has also employed a trigger and data acquisition system to record only interesting events for analyses. A schematic view of the DØ detector is shown in Fig. 3.4.

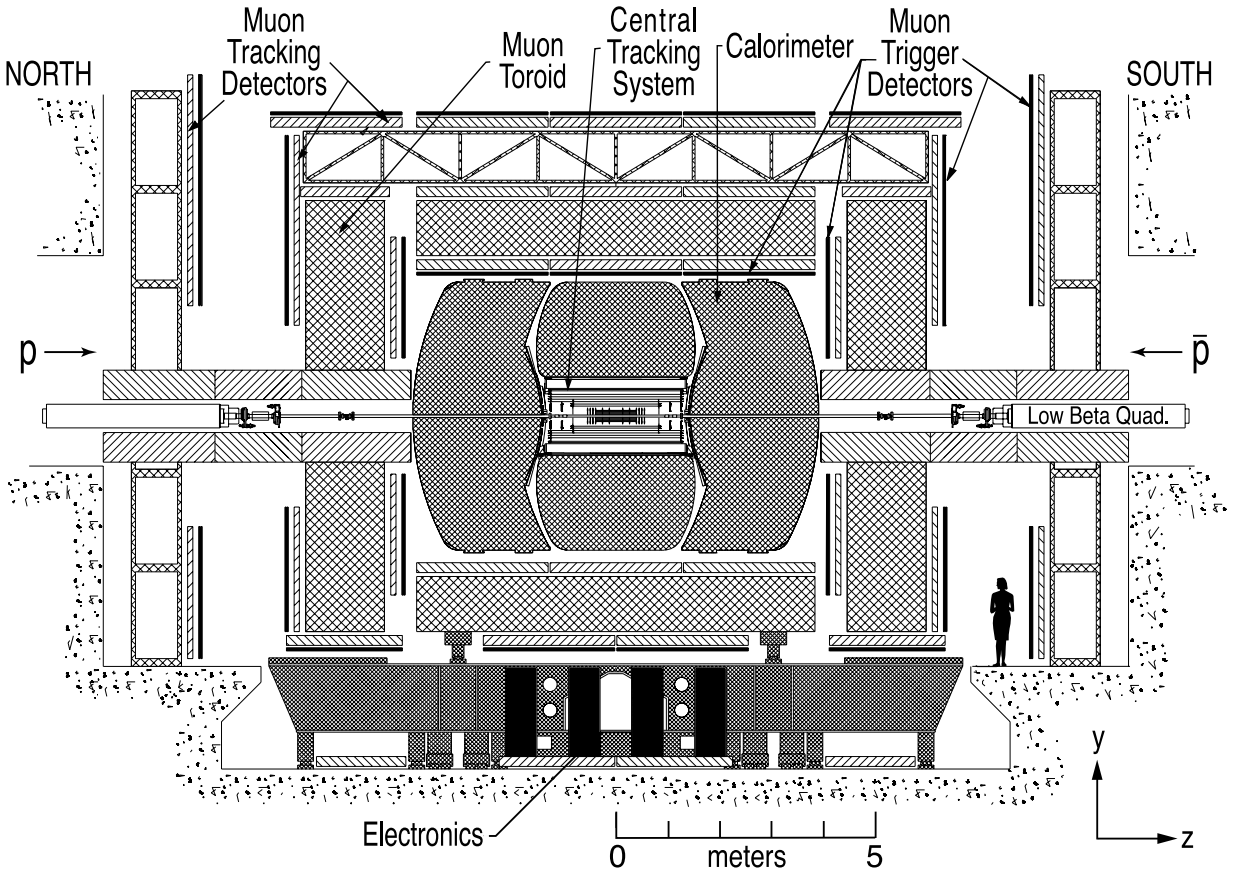

Figure 3.4: Schematic view of the DØ detector at Fermilab.

3.2.1 $p\bar{p}$ collisions and luminosity

The co-ordinate system of the DØ is defined such that the proton's direction of motion is along the z-axis and anti-proton is in the opposite direction. According to the Fig. 3.4, y-axis is upward perpendicular to the z-axis in the paper plane, and x-axis is out of the paper. The pseudorapidity η defined in Eq. 2.20 has larger values closer to the z-axis which is called the "forward region", and is 0 perpendicular to the z-axis. The domain near $|\eta| \approx 0$ is known as the "central region". After the collisions, particles come out transverse to the beam pipe and their transverse momentum is defined as $p_T = \sqrt{p_x^2 + p_y^2} = |\vec{p}| \sin\theta$

and longitudinal momentum is expressed as $p_z = |\vec{p}| \cos\theta$. Similarly the transverse energy is $E_T = E \sin\theta$, where $\vec{p}$ and E represents three-dimensional momentum and total energy of the particles and θ is the polar angle with respect to the z-axis. The momentum co-ordinates can also be expressed as $p_x = p_T \cos\phi$, $p_y = p_T \sin\phi$, $p_z = p_T \sinh\eta$ and $|\vec{p}| = p_T \cosh\eta$, where ϕ defined as $\phi = \tan^{-1}\left(\frac{p_y}{p_x}\right)$ is the azimuthal angle.

After the discovery of the top quark in 1995, the Tevatron and its two detectors underwent major upgrades, and started re-operation in 2001. After the commissioning of the various detector components, data taking began in spring 2002, that is the start of "Run II" period.

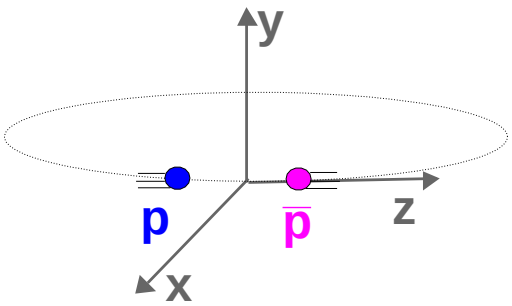

Figure 3.5: Coordinate system choice at DØ. Circle represents the circular path of the proton and anti-proton in the ring, and the origin of xyz-coordinate system represents the interaction point of $p\bar{p}$ beam at DØ.

The instantaneous luminosity is a measure of beam interactions per unit area per unit time. It is directly proportional to the number of particles, n_p, in the proton beam, the number of particles, $n_{\bar{p}}$ in the antiproton beam, the rate, f, at which they interact and inversely proportional to the cross-sectional area of the beams.

$$\mathcal{L} = f\frac{n_p n_{\bar{p}}}{4\pi\sigma_x\sigma_y}, \tag{3.1}$$

where σ_x and σ_y represent the transverse and longitudinal profiles of the beams, respectively. Tevatron was designed to deliver about 10^{32} cm^{-2} sec^{-1} of instantaneous luminosity, which was achieved in 2005. The luminosity integrated over time is called integrated luminosity, which is expressed in units of inverse barns, b^{-1}, where 1 b = 10^{-24} cm^2. The measurement presented in this dissertation utilized about 1 fb^{-1} of integrated luminosity, where "fb" stands for femtobarn.

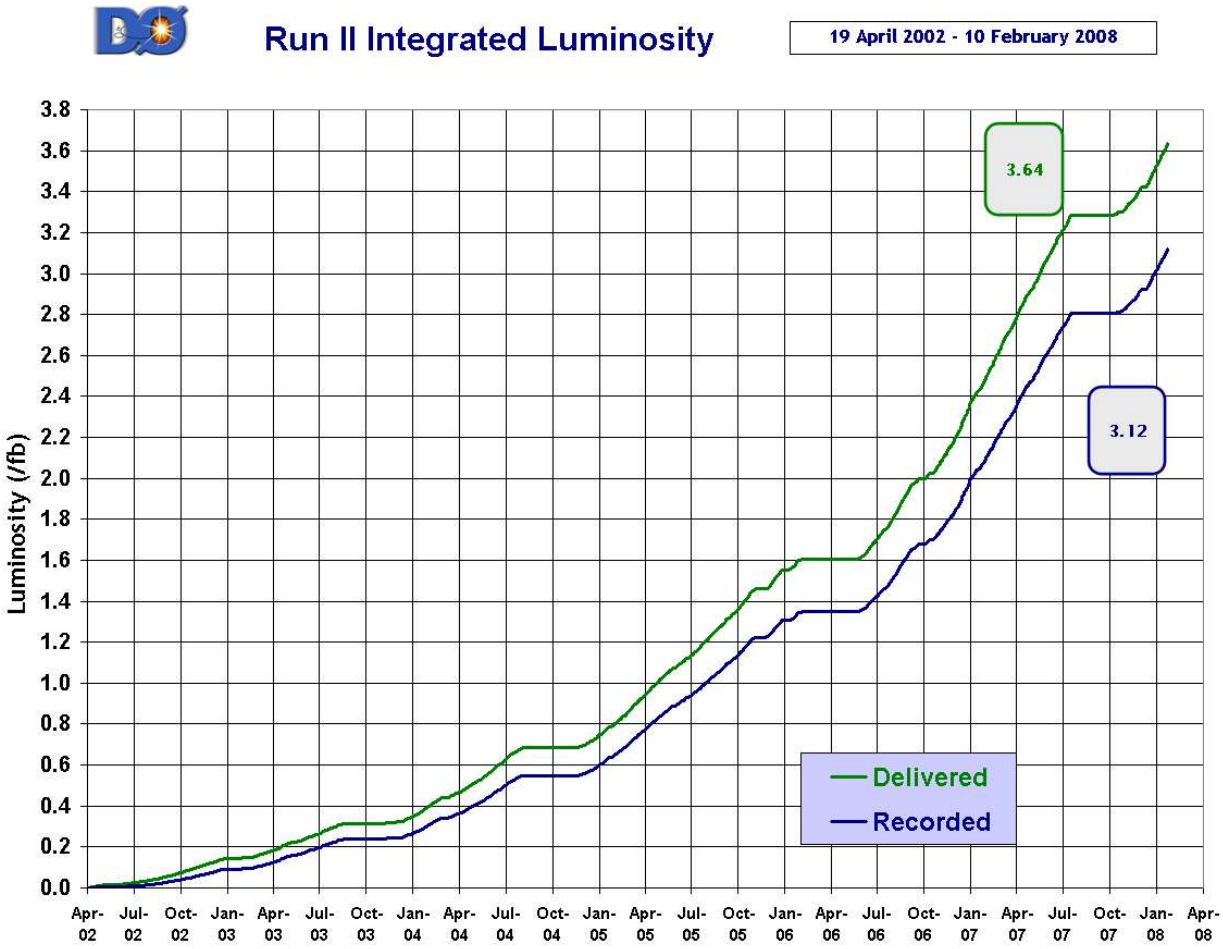

Figure 3.6: Delivered and recorded luminosity at DØ.

Luminosity is also measured at DØ using the luminosity monitors located at $z = \pm 140$ cm and covers the region $2.7 < |\eta| < 4.4$ as shown in Fig. 3.7. The measurement is derived

from the Poisson probability of no interactions that is given as [52]

$$P(0) = e^{\frac{-\bar{\mathcal{L}}_{LM}\sigma_{LM}^{eff}}{f}}\left(2e^{\frac{-\bar{\mathcal{L}}_{LM}\sigma_{LM}^{SS;eff}}{2f}} - e^{\frac{-\bar{\mathcal{L}}_{LM}\sigma_{LM}^{SS;eff}}{f}}\right), \tag{3.2}$$

where σ_{LM}^{eff} represents the effective cross section measured from particles hits in photomultiplier tubes in the luminosity monitor at both the north and south ends of the DØ detector, $\sigma_{LM}^{\mathrm{SS};eff}$ represents the effective cross section only at one of the two ends (here "SS" is acronym for single sided), and f is the beam frequency. Using this probability information the luminosity is measured as

$$\mathcal{L}_{LM} = \frac{f}{\sigma_{LM}^{eff}} \ln\left(2P(0)^{\left(\frac{\sigma_{LM}^{SS;eff}}{\sigma_{LM}^{eff}}-1\right)} - P(0)^{\left(\frac{2\sigma_{LM}^{SS;eff}}{\sigma_{LM}^{eff}}-1\right)}\right). \tag{3.3}$$

The analysis presented is not sensitive to the uncertainty in the measurements of the integrated luminosity.

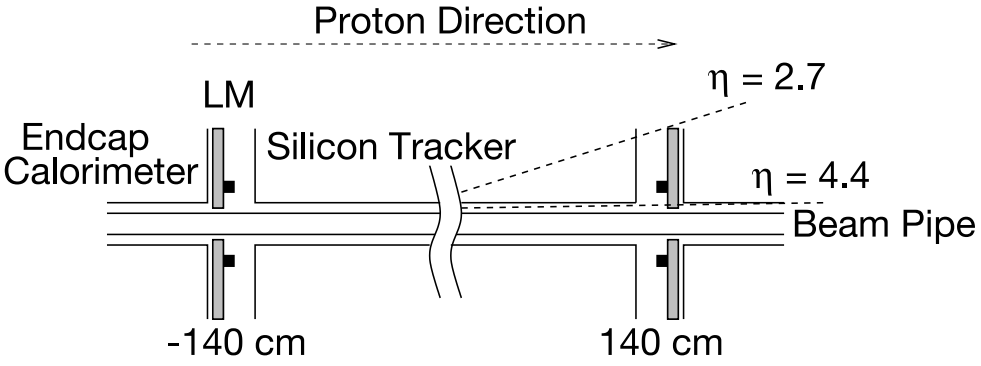

Figure 3.7: Luminosity monitor at DØ for measurement of luminosity.

3.2.2 Central tracking system

The tracking system is the first set of layers of detector surrounding the beryllium beam pipe with outer diameter 3.8 cm and length 2.37 m that measures the paths of the charged particles. A solenoid magnet producing 2 T of magnetic field is employed around the tracking system for charge and momentum measurements of the tracks. The tracker consists

of silicon microstrip tracker (SMT) and a central fiber tracker (CFT). Combining the information from SMT and CFT, a primary interaction vertex can be constructed with a resolution of 35 μm along the z-axis. Accurate construction of primary vertex improves the accuracy of the measurement of leptons and jets transverse momentum, and the missing transverse energy. The tracker can also locate the displaced vertices with good resolution that are required for the identifications of a jet initiated from a b- or c- quarks. Components of the tracking systems are described below.

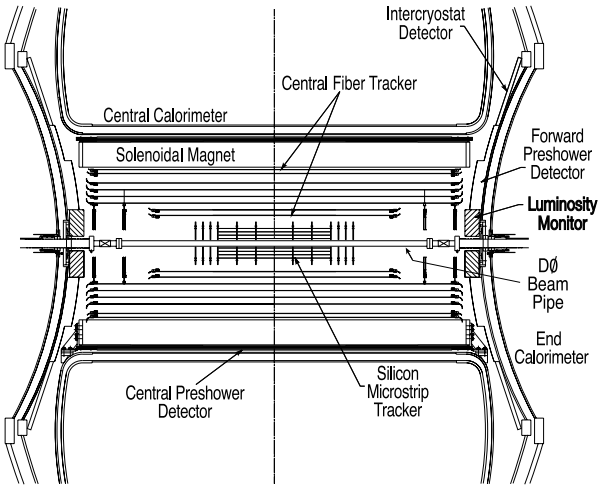

Figure 3.8: Central tracking system at DØ.

Silicon microstrip tracking detector

The silicon detector, as shown in Fig. 3.9, is the innermost detector of DØ consisting of fabricated layers of thin silicon wafers oriented parallel or perpendicular to the beam pipe. A charge particle passes through the depeleted region of the silicon, and produces electron-hole pairs that are separated by electric fields and collected by the capacitors and later read-out in the form of the electronic signals. Assemblies of detector modules, as shown in Fig. 3.9, are divided into three types called barrels, F-disks and H-disks. There are six barrels consisting of axially oriented silicon wafers arranged concentrically called ladders, a schematic structure of ladder is shown in Fig. 3.10. There are twelve F-disks and four

H-disks consisting of vertically oriented wafers that are called wedges. In the central region (close to $z = 0$ and small η) each barrel is capped by an F-disk, consisting of 12 wedges, on the either side of the z-axis. The remaining three F-disks are located in a unit outside the barrel-F-disk system on both side of the z-axis. H-disks consisting of 24 wedges are located at high z-positions to cover the larger η regions. The barrels are located at $z = 6.2, 19.0, 31.8$ cm, F-disk are located at $|z| = 12.5, 25.3, 38.2, 43.1$, and 53.1 cm, and H-disks are located at $|z| = 100.1, 121.0$ cm. Combining all ladders and wedges, there are 912 readout modules in total. Each silicon ladder or wedge consists of readout strips, 384 strips for single-sided and 640 strips for the double-sided ladders and 1024 strips for wedges, parallel to one of the longer edge of the wafer. Silicon system consists of $792,576$ individual channels.

SMT provides an excellent measurement of the positions of charge particles trajectories. In each readout module the distance between two strips is 50 μm which gives a resolution of less than 10 μm in the track position measurement. In the central region the radial distance covered by the silicon tracker is upto 10 cm with respect to the beam pipe center. In the forward region the silicon tracker occupies from 9 cm to 26 cm providing total $|\eta|$ coverage upto 3.0.

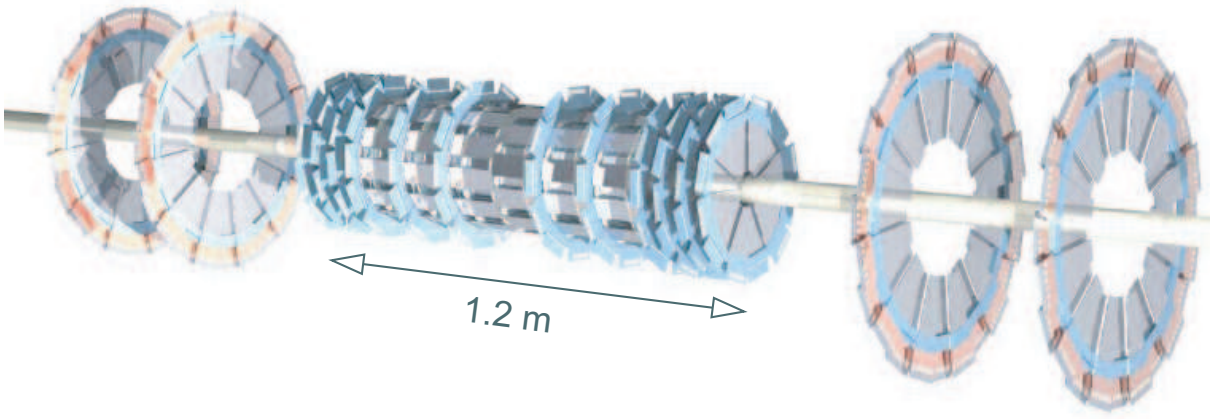

Figure 3.9: Schematic view of the Silicon detector at DØ.

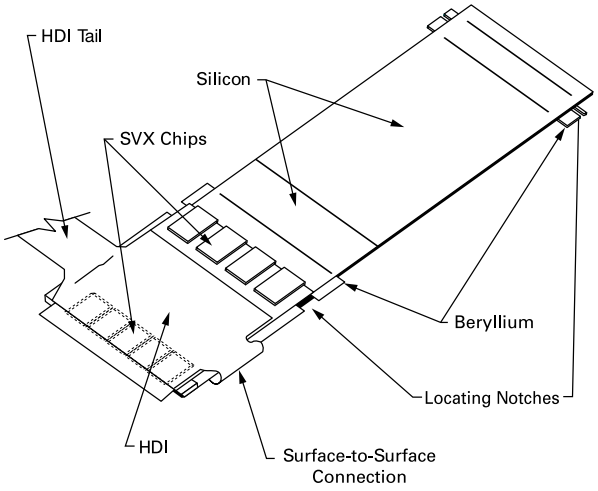

Figure 3.10: Schematic view of an SMT ladder.

Central fiber tracking detector (CFT)

After SMT comes the fiber tracking system covering the radial distance from 20 cm to 52 cm with respect to the beam pipe and the η upto 2. The tracker consists of scintillating fibers, having 835 μm diameter, mounted in two layers around each of eight concentric support cylinders, first layer is along the beam line called axial layer and second one has $\pm 3^o$ stereo angle with respect to the axial layer. A scintillating fiber is composed of organic compound surrounded by claddings to provide total internal reflection inside the fiber. To carefully position, the scintillator fibers are assembled into ribbons consisting of 256 fibers arranged in two layers of 128 fibers each. Length of the innermost cylinder is 1.66 m and the outer cylinder is 2.52 m. Charged particles pass through the scintillating fibers that emit photons which are carried by the clear waveguides connected to one end of the scintillator fibers. The other end of the fiber is coated with aluminum for a reflectivity of about 90%. The photons with the wavelength in the range of the yellow-green light ($\approx$ 540 nm) are sent to silicon avalanche photodetectors, known as visible light photon counters (VLPC), to convert them into electronic signals for readout. To minimize the noise to the electronic signals, VLPCs operate at 9 K and provide a quantum efficiency of 75%. A spatial resolution of

100 μm is achieved using the fiber tracker.

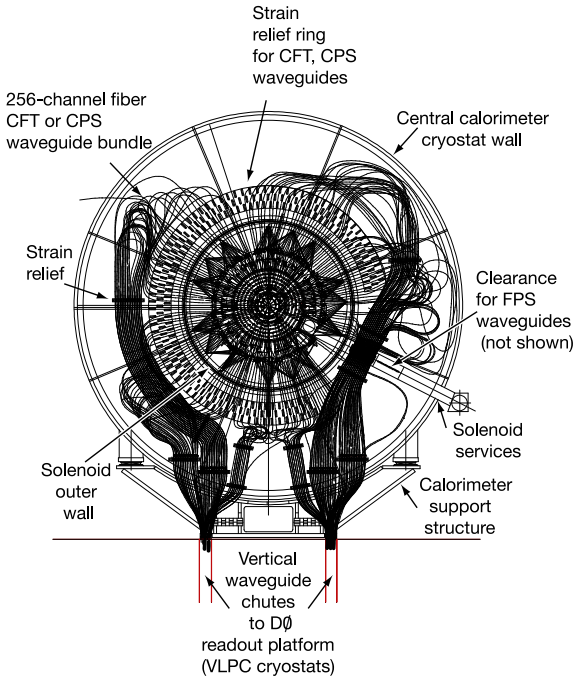

Figure 3.11: Schematic view of CFT.

3.2.3 Solenoid magnet

The central tracking system is surrounded by a superconducting solenoid magnet operating at 2 T. The inner radius of the magnet is $\sim$ 54 cm, the outer radius is $\sim$ 71 cm, and the length of the cylinder is 2.73 m. Overall thickness of the solenoid is 0.87 radiation length (X_o). Magnetic field strength is strong inside the cylindrical volume of the solenoid and field lines are parallel to the beam pipe. Outside the solenoid the strength is negligible. Charged particle emerging out of the collision are bent around due to the magnetic field, which allows good measurement of charge to the transverse momentum ratio of the tracks. The magnet is designed to operate at both forward and reverse polarities. Outside the first layer of the muon system is a toroid that provides tracking for the muon.

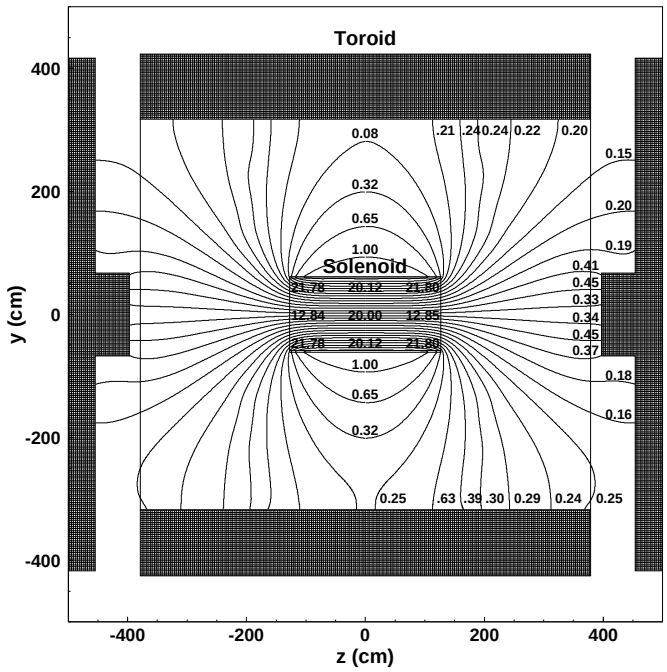

Figure 3.12: Schematic view of Solenoid magnet at DØ.

3.2.4 Preshower detectors

Preshower detectors improve the identification of the photons and electrons. Due to their fast response, these detectors can be used for first level of triggering. These are made of triangular strips of scintillator. There is a wavelength shifting fiber in the center of the strips. The fiber has a diameter of 835 μm, with one end coated with silver and the other end connected to the clear waveguide fiber that transmit the light to the VLPCs for readout. The central preshower detector (CPS) located in the 5 cm gap between the solenoid and the central calorimeter covers the region $|\eta| < 1.3$. There are two forward preshower detectors attached to the end calorimeter faces and covers the region $1.5 < |\eta| < 2.5$. The CPS and FPS detectors are capable of measuring both the position and energy of the particles.

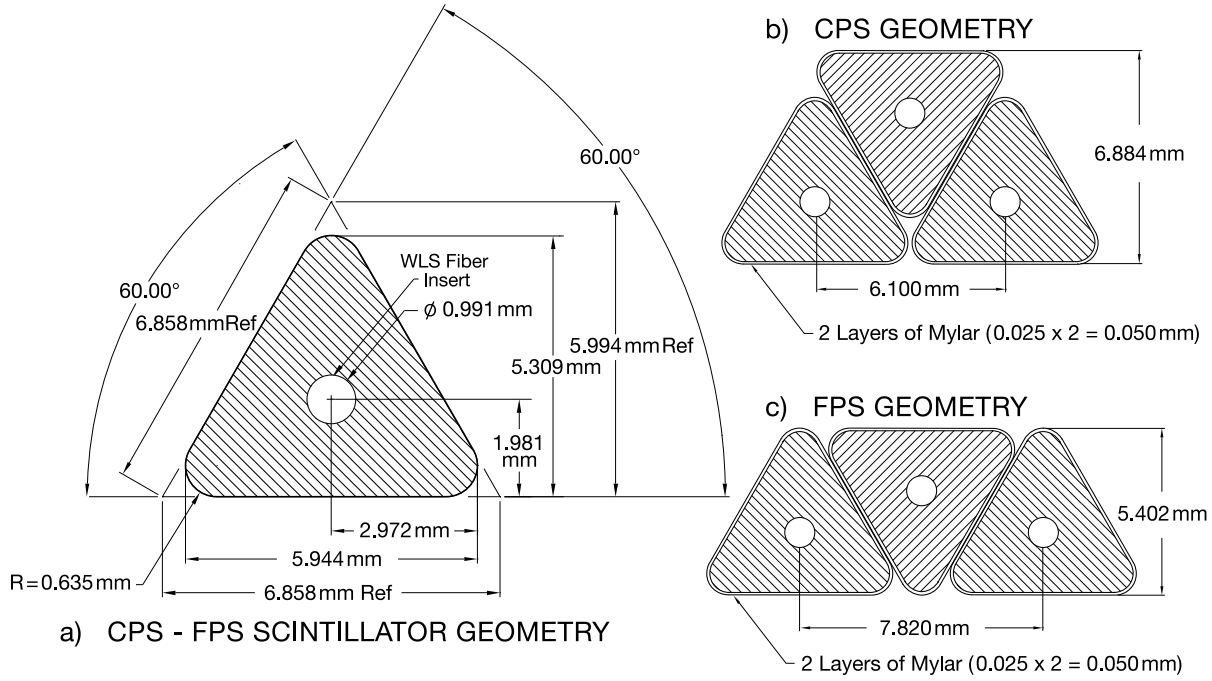

Figure 3.13: Schematic view of a unit preshower detector at DØ.

3.2.5 Calorimetry

The calorimeters are used to measure the energy of electromagnetically interacting particles such as electrons and photons and the strongly interacting particles such as stable hadrons (pions, kaons, protons, neutrons). Measurement of total energy balance in events in the transverse plane allows identification of neutrino that leaves the detector without interaction. The DØ calorimeter is divided into three subsystems: one central calorimeter (CC) covering $|\eta| \leq 0.8$ and two end calorimeters (EC) on either side of the CC extending the coverage to $|\eta| \leq 4$. The calorimeter in the CC region begins with the inner radius of 75 cm and the outer radius of 86 cm from the beam line. The EC calorimeters are in a cylindrical shape, as shown in Fig. 3.14, that has inner radius of about 4 cm and outer radius of 86 cm from the beam line. Each calorimeter comprises an electromagnetic section (EM), that is closer to the beam interaction region, followed by fine and coarse hadronic sections. Liquid-argon is used as the active medium in all three calorimeters and each one is located in its own

cryostat to maintain the temperature to 90 K. Further, different absorber or shower plates are used in different sections. In the EM section, depleted uranium plates with thickness of 3 mm or 4 mm are used in the CC or EC. In the fine hadronic section, absorber plates have thickness of 6 mm which are made of uranium-niobium alloys. The coarse hadronic section contains 46.5 mm thick plates of copper in the CC and stainless steel in the EC.

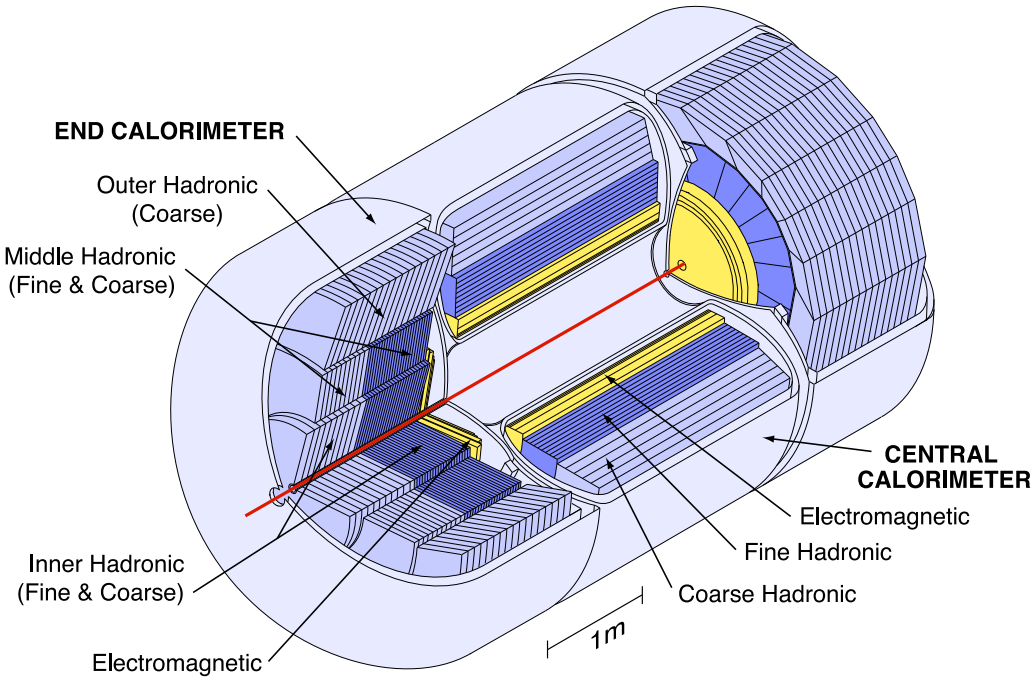

Figure 3.14: Schematic view of DØ calorimeter.

An electron or photon entering the calorimeter experiences the electric field of the atoms in the absorber layers and produce further photons and electron-positron pairs. The energy of the initial electron or photon is shared among the shower particle that enter the liquid argon gap of thickness 2.3 mm and ionize the atoms. It takes 450 ns for the ions to drift towards the cells connected to the positive high voltages (2 kV) that are further digitized and read out. A unit cell of absorber and liquid argon is shown in Fig. 3.15. The process continues until whole energy of initial particle is absorbed, and energy deposited is measured by the length of the shower. Hadrons being heavier than electrons are not affected by the atomic electric fields in the absorber material, but they interact with the

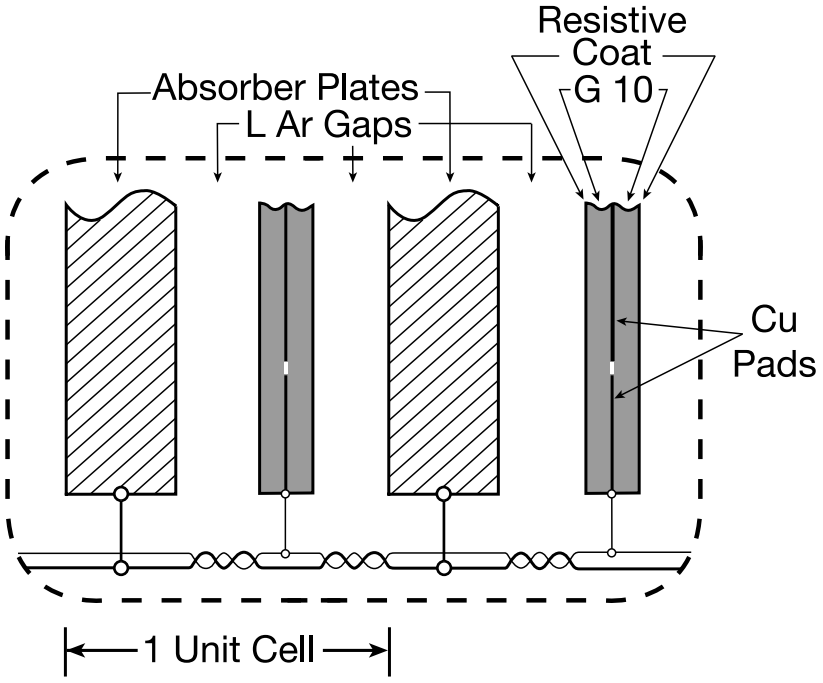

Figure 3.15: Schematic view of Uranium layers in two unit cells filled with Liquid Argon.

nuclei of dense material and due to residual strong interaction produce more hadrons. They travel longer distance than electrons before they shower. The thickness of the absorbers is designed so that all electrons, photons and hadronic jet are absorbed inside the calorimeter. Electromagnetic showers have typical transverse sizes of 1-2 cm, and hadronic showers have typical shower sizes of 10 cm. The EM section has 4 layers with the total electromagnetic thickness in all layers is 20 X_o (21.4 X_o) in the CC (EC) region, where X_o is the typical distance traveled by a photon before producing an electron/positron pairs, or by an electron before experiencing a Coulomb interaction with the atoms of the absorber. The thickness in the hadronic section is 7 λ, where λ is the distance traveled by the pion or kaon before producing shower, or before interacting with the nuclei of the absorber.

For a better measurement of the position and the amount of energy deposited by the particles, the calorimeter has finely segmented cells that varies in η-ϕ dimensions. Figure 3.16 gives a schematic view of an octant of the calorimeter. In all layers of EM modules, except the third one, cell sizes are $\Delta\eta \times \Delta\phi = 0.1 \times 0.1$. The third layer having maximum shower

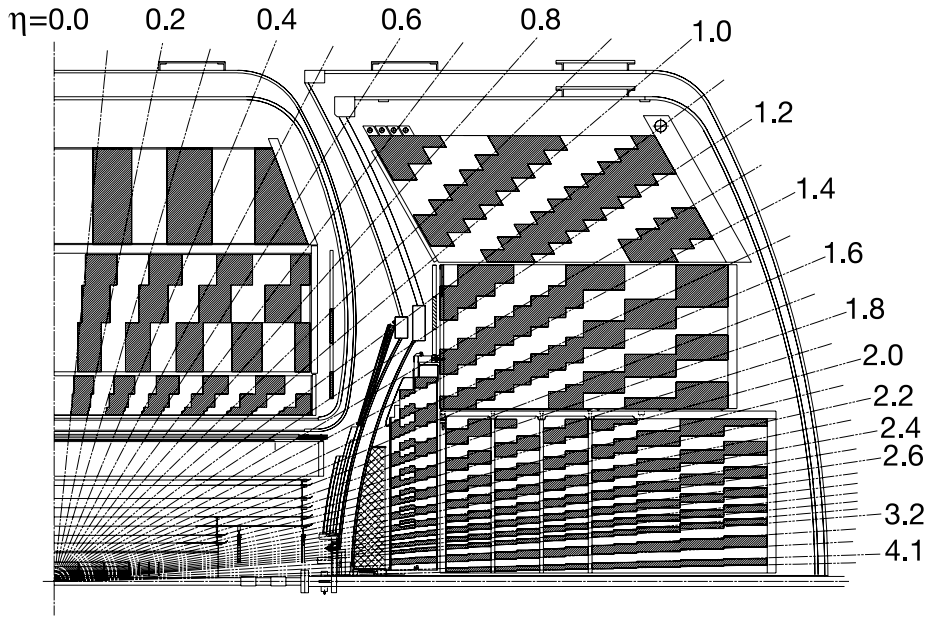

Figure 3.16: Schematic view of segmentation of calorimeter sections.

has twice more granularity, i.e, $\Delta\eta \times \Delta\phi = 0.05 \times 0.05$. Fine hadronic modules have cell sizes $\Delta\eta \times \Delta\phi = 0.1 \times 0.1$ in all four layers, while the single coarse hadronic layer have the granularity of $\Delta\eta \times \Delta\phi = 0.2 \times 0.2$. Deposited energy is measured in units of tower which represents the layers of cells within $\Delta\eta \times \Delta\phi = 0.2 \times 0.2$ space.

The region $0.8 < |\eta| < 1.4$ between the CC and EC is called Inter-Cryostat Region (ICR), which is covered by a subsystem called Inter-Cryostat Detector (ICD). There are single cell calorimeter structures within the CC and EC cryostats called the massless gaps. Attached to the exterior of each EC cryostat is a circular structure consisting of 1.25 cm thick scintillating materials divided into 16 tiles of size $\Delta\eta \times \Delta\phi \approx 0.3 \times 0.4$. Each tile is further subdivided into 12 small tiles of sizes $\Delta\eta \times \Delta\phi = 0.1 \times 0.1$.

3.2.6 Muon spectrometer

The outermost subsystem of the DØ is the muon system. Among all particles produced after the collision, muons travel the largest distance, which set the design of the muon

detecting devices to be placed in the last. Due to higher mass relative to the electrons, muons are very unlikely to radiate a photon and lose very small energy (about 2.5 GeV) into the calorimeter before leaving it. Any signal that is recorded by the outermost layers of DØ outside the calorimeter is identified as muon. Though all subdetectors of DØ presented in this dissertation are quite important to the measurement performed, the muon system has the key importance in identifying the $W+c$ final state.

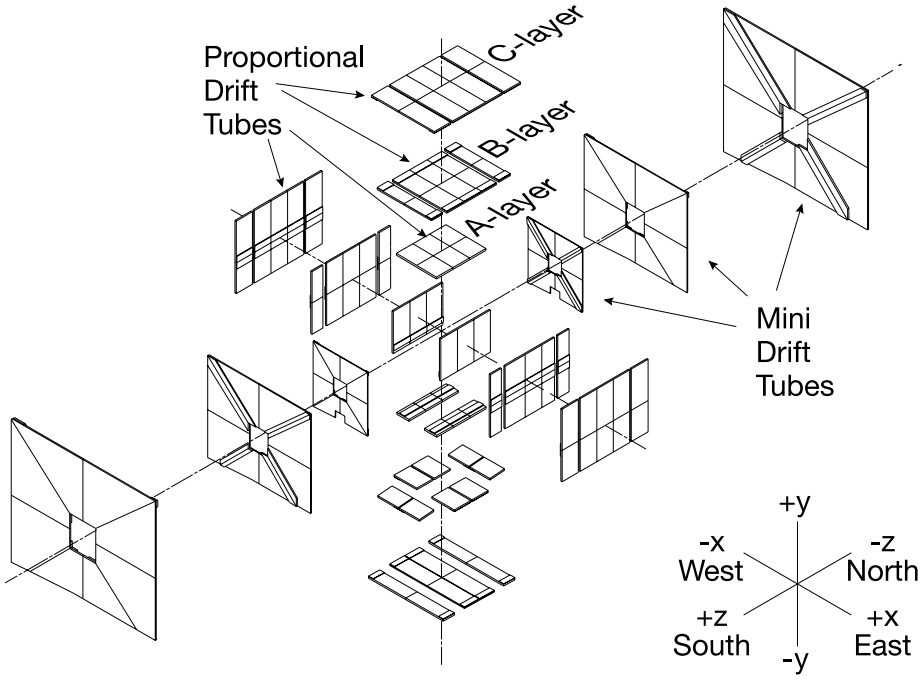

Figure 3.17: Schematic view of layers of drift chambers in DØ muon system.

The muon system consists of three layers: first layer (A-layer) is situated just after the calorimeter, followed by a toroidal magnet and two other layers (B-layer and C-layer). Toroidal magnet provides ≈ 1.8 T magnetic field for tracking in the central region ($|\eta| < 1$), and ≈ 1.9 T in the forward region ($1 < |\eta| < 2$). Muon system is designed to remove the cosmic background using the backward timing counters, such that particles traveling from outside the detector towards the beam pipe are rejected.

Central muon system consists of three layers of proportional drift tube (PDT) chambers, a toroidal magnet, $A\phi$ scintillation counters, and cosmic cap and bottom scintillation

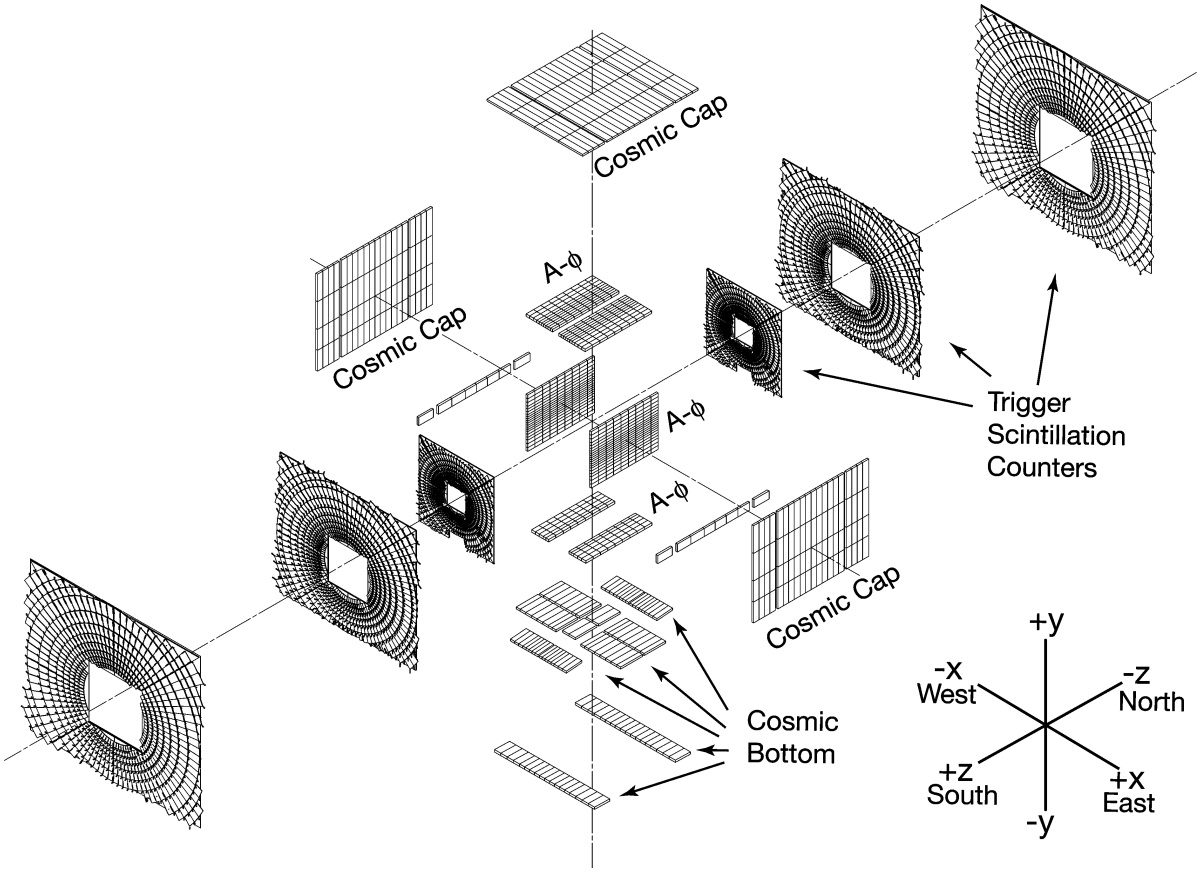

Figure 3.18: Schematic view of layers of scintillating counters in DØ muon system.

counters. PDTs with typical sizes of 2.8×5.6 m^2 are located in three layers in the central region. These are designed to determine the position of hits made by muon track with a resolution of about 1 mm. These are made of aluminum tubes consisting of about 72 or 96 drift cells with an anode wire at the center of each cell and cathode pads above and below the wire. Tubes are filled with a mixture of Ar, CH_4 and CF_4 gases. Muon passes through the drift tube ionizing the gas mixture, and the charges drift towards the anode and are sent to the readout electronics. Drift time of an electron in the PDT to reach the anode is 500 ns compared to the 396 ns of beam crossing time. Scintillator counters play role in the muon identification. Based on the timings of the muon arrival at each layer, one can tell a muon produced after $p\bar{p}$ collision from a cosmic ray muon. Light is produced upon a muon

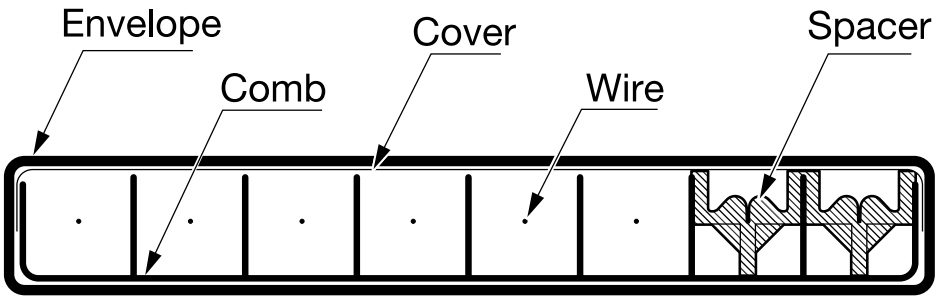

Figure 3.19: Schematic view of mini drift tube comb in the muon system.

passage through the scintillator, which is collected by the photomultiplier tube.

The forward muon system consists of three layers of mini drift tubes (MDT), a toroidal magnet, three layers of trigger scintillating counters and shielding from the beam pipe. In the forward region trigger scintillators have full coverage in three layers, while trigger scintillators are available for only A and C-layers in the central muon system, schematic view of the muon scintillators is given in Fig. 3.18. MDTs consisting of eight cells as illustrated in Fig. 3.19, with 9.4×9.4 mm^2 size each, which is smaller than PDTs. MDTs filled with an organic gas mixture of CH_4 and CF_4 have faster drift time (132 ns) compared to PDTs.

3.2.7 Data acquisition system and triggers

For the physics analysis the events after $p\bar{p}$ collisions are recorded using sophisticated electronics and algorithms, and are stored in tape. In the inelastic collisions occurring after every 396 ns (or at the rate of 2.5 MHz) most of the times particles come out with small angles with respect to the beam. Particles from the violent collisions are more interesting at DØ for new physics that emerge with larger angles with respect to the beam axis. The DØ detector collects the event informations and try to make quick decisions (within a few micro seconds) about retaining or discarding the events using three levels of trigger system. During most of the Run IIa period, each level of trigger was so designed that out of 1.7 million events per second only 50 most interesting events should be recorded on tape due to limited CPUs resources available.

The first level of trigger have to make extremely fast decisions about events with interesting features, as it has to consider all events coming out of the collisions. These triggers take an input at the rate of 1.7 MHz and select only about 2 k events every second. It comprises the hardware trigger elements from central fiber tracker (L1CTT), calorimeter (L1CAL), and the muon system (L1Muon). These trigger elements check for the thresholds for the calorimeter energy tower, transverse momentum in the central tracking system and the muon system.

The second level of triggers take informations from the L1 triggers and use specific preprocessor boards and global trigger boards to make trigger decisions. These triggers take an input at the rate of about 2 kHz and accept events at the rate of about 1 kHz. Preprocessor boards collect informations from the readout of individual sub-detectors as well as from the L1 trigger hardware elements. This information is used to construct the physics objects from each subdetector.

The third level of trigger look at the event information in more detail and uses online reconstruction algorithm to construct physics objects and select ones that pass specific threshold. L3 triggers accept events at the rate of 50 Hz for recording on tape for offline reconstruction and physics analysis. With the increase in the luminosity, this bandwidth recently increased to 100 Hz for "Run IIb" data taking period.

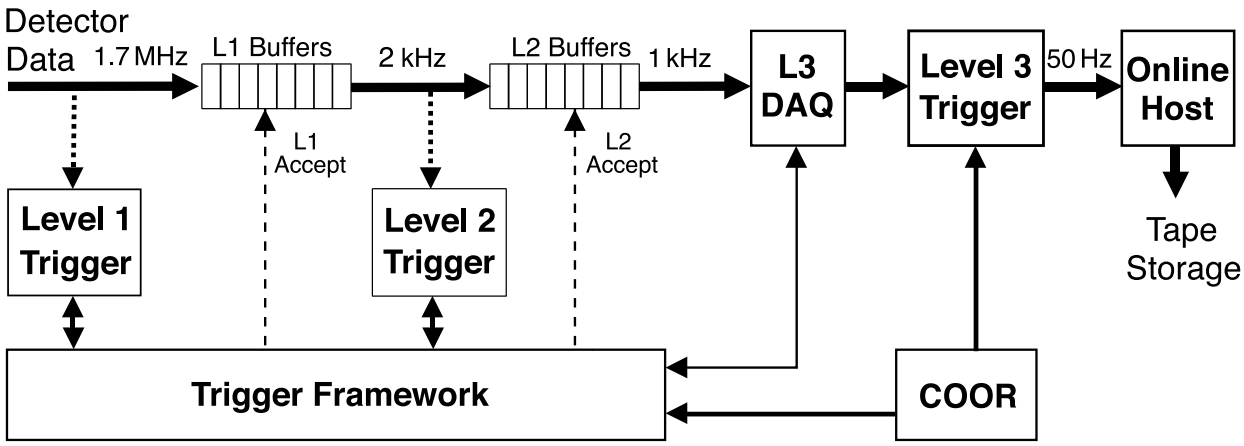

Figure 3.20: Schematic view of data flow at DØ.

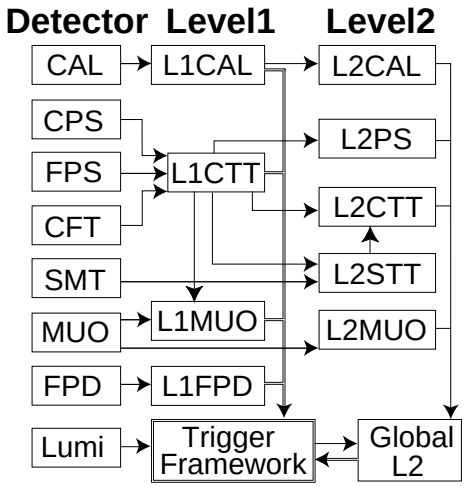

Figure 3.21: Schematic view of data flow from detector elements to the L1 trigger components to the L2 trigger components at DØ.

Chapter 4

Objects Identification and Event Reconstructions

This chapter describes how an event reconstruction takes place using the information obtained from all sub-detectors. The primary physics objects reconstructed in events are tracks; vertices; calorimeter objects such as electrons, photons and jets; muons; and missing energy. The digitized readout from sub-detectors is sent to the computing farms for offline reconstruction for detailed analysis. Calibration and alignment algorithms are employed to perform events reconstruction. Analyzers access fully reconstructed data and carry out the physics object selections following a certain criteria based on the signal signatures.

4.1 Track

Tracks representing the three dimensional trajectories of the charged particles are reconstructed using the hits information in the tracking detectors. Hits are measurements of points through which the charged particle has passed through. A hit is formed at the location where an electron-hole pair is created in the silicon strip upon the passage of the charge particle through the SMT. In the CFT detector, it is formed in the fiber where a photon emits when a charge particle passes through it. To construct a track, the hits locations are first constructed using an algorithm "track hit clustering" (THC) that considers the geometry of the tracking detector. Then a combination of two methods are employed to

reconstruct and filter good tracks in events, these are "alternative algorithm" (AA) method and "histogramming track finding" (HTF) method.

4.1.1 Alternative algorithm

The AA method [53] initially picks any combination of three 2-dimensional hits in the silicon barrels or disks then hypothesize the track extrapolation to subsequent layers from these hits. The advantage of starting from SMT is in having less hits per unit area compared to that in CFT. Track extrapolation starts from the inner tracking layers moving outwards covering all layers of the CFT. An expected window is formed in every layer to search for the hits associated with the track hypothesis. If a hit is found in the search window, it is associated with the track if the χ^2 of the track fit is less than a certain value. If no hit is found, it is counted as "missed hit". The process of track extrapolation continues until all layers are finished or until three hits are missed. Tracks are also expected with fewer than three hits in the SMT region due to the powered off or dead HDIs, that could reduce the track reconstruction efficiency. Such tracks are recovered from the tracks extrapolation that starts from the CFT region, combined with the information of primary interaction point in each event for backward extrapolation.

4.1.2 Histogramming track finding

The histogramming track finding algorithm (HTF) [54] preselects the hits with their position (x-y) information in the transverse plane. The histogramming procedure is based on the fact that set of all hits produced by each track is characterized by its curvature ρ and the azimuthal angle ϕ representing the direction of the track at (0,0) as shown in Fig. 4.1(a). Therefore set of all hits in (x-y) space are represented by a point in the (ρ-ϕ) track parameter space. Similarly, each hit in the coordinate space is represented by a set of lines in the (ρ-ϕ) space intersecting at one point as illustrated in Fig. 4.1(b). A procedure known as "Hough transformation" [55] is used to transform the set of hits of a particle in the x-y plane into a single point (ρ,ϕ) in ρ-ϕ space. The track parameter space is divided into cells of ρ-ϕ that

are incremented for every hit. A peak finder is employed to determine the maxima in the 2D histogram corresponding to the hits of a single particle trajectory, which consequently determines the parameters of the track. After the track parameters are constructed, the noisy or fake tracks are discarded using the Kalman filter [56] procedure.

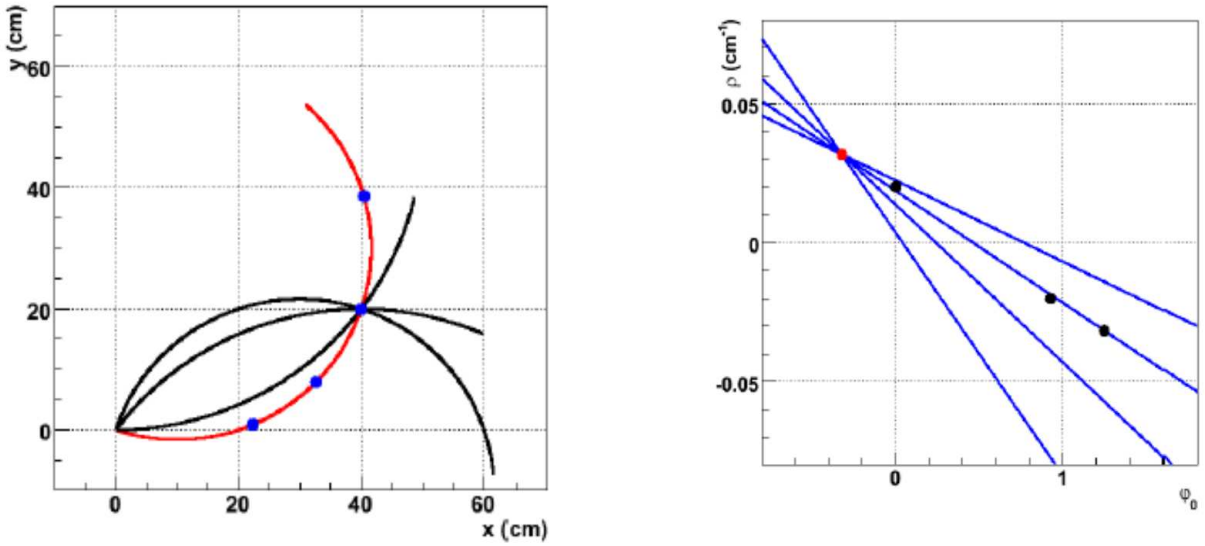

(a) **(b)**

Figure 4.1: An illustration of Histogramming track finding (HTF) algorithm [54]. (a) The hits produced by a track in the x-y plane. This shows that hits lie in the trajectory of the particles. (b) In the (ρ, ϕ) space the hits are represented by a single point whose coordinates are the curvature ρ and the direction ϕ of the track.

4.2 Primary Vertex

The primary vertex (PV) refers to the location of the hard scatter interaction in a $p\bar{p}$ collision. The PV is constructed from the extrapolation of reconstructed tracks in events

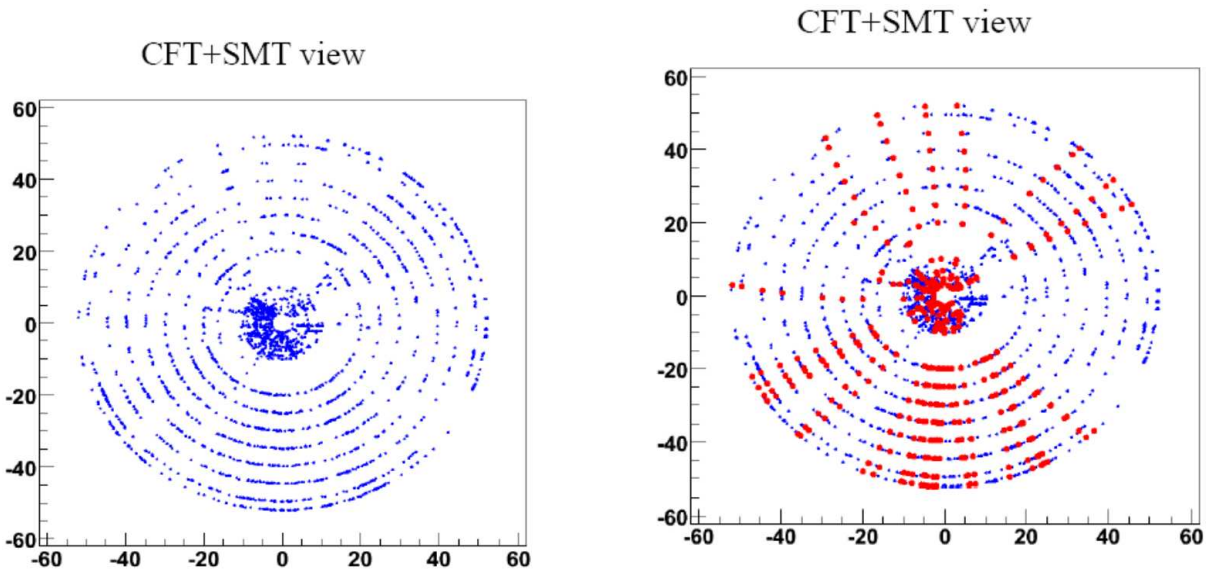

(a) **(b)**

Figure 4.2: An illustration of hit pattern in an event after $p\bar{p}$ collision. (a) Cluster of hits in the SMT and CFT detectors, total number of hits can range from 10^3–10^6 per events. (b) In this figure the red points represents the hits that are associated with a track using the HTF method.

to a vertex where they intersect in three-dimensional space. A vertex associated with maximum number of tracks having high transverse momentum is generally referred to as a candidate of PV. Due to the presence of the low energy interactions and underlying events along with the hard scatterings in the $p\bar{p}$ interactions, it is important to discriminate the PV from other possible vertices located close to the beam pipe. In the events containing b and c quarks decaying close to the beam have secondary vertices produced within a few millimeter from the hard scatter vertices. Tracks from the secondary vertices generally have relatively higher χ^2 distribution to the PV. Identification of the right PV is crucial

for reducing the fake objects such as fake electrons, muons and missing transverse energy, that is the signature of neutrino in the event.

In this analysis the "adaptive primary vertex" (APV) algorithm [57] is used to construct the primary vertices of the events. The APV primary vertex selection falls in three steps. Firstly, a cluster of tracks having minimum $p_T > 0.5$ GeV and at least 2 hits found in the SMT detector are selected. Secondly, a vertex is fitted after selecting the tracks in two passes. In the first pass the tracks giving highest contribution to the track-PV χ^2 are removed, and the Kalman vertex fitting algorithm [58] determines the location and width of the beam. In the second pass the tracks must have small distance of closest approach (dca) with respect to the beam position determined in the first pass. Thirdly, the selected tracks are fitted to a common vertex using the APV fitting algorithm. After all possible vertex candidates are obtained, the one with the smallest probability of being associated to the underlying or minimum bias (inelastic $p\bar{p}$ scattering) event is considered as the hard scatter vertex [59].

4.3 Calorimeter Objects

Energy deposited in the calorimeter is used as a primary tool to construct the electrons and jets. Electrons are identified in the electromagnetic region of the calorimeter, and the jets are identified in the hadronic regions of the calorimeter, as well as the EM calorimeter.

4.3.1 Electron

A cluster of energy towers in the electromagnetic part of the calorimeter is considered as an electron candidate. The cluster must have a large (90%) amount of its energy contained in the EM part of the calorimeter. The towers clustering is based on the "simple-cone" (scone) algorithm [60]. According to this algorithm, a seed calorimeter cell with transverse energy $E_T > 1.5$ GeV is considered, and the total energy in a narrow cone around the seed in the $\eta - \phi$ space is defined such that $\Delta\mathcal{R} = \sqrt{\Delta\eta^2 + \Delta\phi^2}$ is less than 0.2. An electromagnetic

cluster of an electron tends to deposit energy in a narrow cone in the EM layers. Therefore, for an isolation of this cluster from the nearby deposited energy, the fraction f^{iso} of the energy deposited in a halo cone ($0.2 < \Delta\mathcal{R} < 0.4$) with respect to that in the 0.2 cone is required to be less than 15%.

$$f^{iso} = \frac{E_{tot}(0.4) - E_{EM}(0.2)}{E_{EM}(0.2)}, \tag{4.1}$$

where $E_{tot}(0.4)$ represents the total energy deposited in the electromagnetic, preshower detector and the fine hadronic regions of the calorimeter, and $E_{EM}(0.2)$ represents the energy deposited only in the electromagnetic region of the calorimeter.

A variable constructed out of seven or eight variables examines the shower shape of the electron and compares it to that of a hadronic shower shape [61]. The variables used to construct the H-matrix include the energy fractions in each of the four layers of the EM calorimeter, the shower width in r-ϕ in the third layer, the shower width in z in the third layer, the total shower energy, and location of the primary vertex. In the case of H-matrix with seven variables the shower width in z is excluded. The H-matrix H is defined as an inverse of the covariance matrix M whose elements are

$$M_{ij} = \frac{1}{N}\sum_{n=1}^{N}(x_i^n - < x_i^n >)(x_j^n - < x_j^n >), \tag{4.2}$$

where x_i^n represents ith variable of the nth cluster and $< x_i^n >$ represents the expectation value of that variable for an electron. The H-matrix χ^2_{HM} variable defined as

$$\chi^2_{HM} = \sum_{ij}(x_i^k - < x_i^k >)H_{ij}(x_j^k - < x_j^k >), \tag{4.3}$$

determines the consistency of the longitudinal and transverse energy profile with that expected for an electron.

To discriminate an electron from the photon, which is a neutral particle, a reconstructed track in the central tracking system should be spatially matched to the EM calorimeter cluster. The spatial matching requirement is imposed using a χ^2 probability of the track to

be consistent with that of the EM cluster. For an electron, the $P_{trk}(\chi^2)$ probability should be greater than 0.01 [62]. The χ^2 is defined as

$$\chi^2 = \left(\frac{\delta\phi}{\sigma_\phi}\right)^2 + \left(\frac{\delta z}{\sigma_z}\right)^2 + \left(\frac{(E_T/p_T) - 1}{\sigma_{E_T/p_T}}\right)^2, \tag{4.4}$$

where the first two terms correspond to the spatial matching in ϕ and z, of the cluster and track, and the third term represents the E_T of the cluster matching to the p_T of the track. Here σ_ϕ, σ_z and σ_{E_T/p_T} represent the estimate of the uncertainties in ϕ, z and E_T/p_T.

Further identification of the electron is based on another variable that is likelihood discriminant (LH_e) constructed from eight variables [62]. This variable combines the tracker and calorimeter informations with the expected distributions for electrons and jet background. These variables are the spatial χ^2 track matching probability, H-matrix with eight variables, E_T/p_T matching, electromagnetic fraction, distance of closest approach to the primary vertex, number of tracks in 0.05 cone, p_T of all tracks in 0.4 cone around the matched track of electron, average number of hits in the central preshower strips in cluster. The number of track restriction further discriminates the electron from the photon conversions ($\gamma \to e^+e^-$) or from neutral pion ($\pi^o \to \gamma\gamma$), as more tracks are expected from the e^+e^- pairs.

In this analysis, the electron candidate track should have high transverse momentum $p_T > 10$ GeV and it must originate within 3 cm of the PV.

4.3.2 Jets

Jets are formed from the quarks and gluons fragmenting into further quarks and gluon in the calorimeter shower. Due to the color confinement, these quarks/gluons immediately (10^{-23} sec) materialize into colorless hadrons. Therefore one observes a stream of particles in the calorimeter nearly collinear with the direction of the original quark produced at the hard scatter. Identification and reconstruction of a jet is based on the information of the energy flow of the collimated particles in the calorimeter along the direction of the parent quark. Jets are reconstructed using iterative seed-based mid-point cone algorithm [63] with

cone radius $\mathcal{R}_{\text{cone}} = 0.5$ in η-ϕ space. This algorithm uses the four-momentum information of all particles in a defined cone. According to this algorithm, preclusters are first selected that are formed in a 0.3 cone radius from the items around an energy cell with $p_T > 0.5$ GeV. These pre-clusters are called seeds that are used to form a proto-jet candidate defined within cone size 0.5. The proto-jet selection is an iterative process until the axis of the cone defined around the seed coincides with the proto-jet axis. For an infrared and collinear safety of the algorithm, mid-points between two nearby proto-jets such that $\Delta\mathcal{R} < 2R_{\text{cone}}$ is chosen as a seed. The proto-jets candidates are redetermined using the four-momentum information of the items in the 0.5 cone until the cone stability reaches. These proto-jets are selected with the minimum $p_T > 8$ GeV. After the preselection, the proto-jets which are close to each other are merged or split depending on the fraction of the total shared energy.

To remove the fake jets from the calorimeter noise or other physics sources a set of restrictions are imposed on the reconstructed jets for physics analysis [64]. These cuts are described below:

- The fraction of energy deposited in the EM layers should be more than $0.03 - 0.05$ depending on the detector η region, but less than 0.95.
- The ratio of the energy in the hottest (highest energy) cell to that in the second hottest cell should be less than 10.
- At least one calorimeter tower containing 90% of the jet's energy.
- The minimum restriction on the fraction of energy deposited in the coarse hadronic region varies from 0.40 to 0.60, depending on the detector η region. The reason of the η-dependent cut is the different amount of absorber materials in the calorimeter in different η regions.
- In the central region ($|\eta| < 2.0$), jets are required to have a matched track with $p_T > 2$ GeV and the $\chi^2 < 3$ within ΔR between the track and the jet axis less than 0.5.

- The fraction of total energy from L1 trigger towers in the event with respect to the total transverse momentum, excluding the energy deposited in coarse hadronic region, of the jet into jets should be more than 0.5 for the hard jets with $p_T > 15$ GeV in the central region [65]. This threshold varies from 0.1 to 0.35 for the jet in the end cap or forward regions, depending on the jet p_T.

The four-momentum of the reconstructed jet is calibrated so that it corresponds to the truth four-momentum of the jet [66]. The calibration factors depend on the measured jet's energy E_{jet}^{meas}, jet's η, cone size R_{cone} and the luminosity $\mathcal{L}$. The jet energy scale (JES) corrected energy of the jet is defined as

$$E_{jet}^{\text{ptcl}} = \frac{E_{\text{jet}}^{\text{meas}} - E^{\text{offset}}(R_{\text{cone}}, \eta, \mathcal{L})}{R_{\text{response}}(E_{\text{jet}}^{\text{meas}}, \eta) \times R_{\text{shower}}(E_{\text{jet}}^{\text{meas}}, R_{\text{cone}}, \eta)}, \tag{4.5}$$

where $E^{\text{offset}}(R_{\text{cone}}, \eta, \mathcal{L})$ denotes the offset in the measured energy of jets that is not associated with the hard scatter but is contributed from multiple particle interactions, underlying events, calorimeter and electronic noise, or pile-up from previous bunch crossings. The factor $R_{\text{response}}(E_{\text{jet}}^{\text{meas}}, \eta)$ is the response of the calorimeter to the hadrons that corrects for the inefficiencies due to the dead material in the detector, and $R_{\text{shower}}(E_{\text{jet}}^{\text{meas}}, R_{\text{cone}}, \eta)$ is the fraction of the particle energy contained inside the jet cone.

4.4 Muon

Muons identification and reconstruction is based on the detector informations from the outer muon systems as well as the central tracking system. A local muon (muon in the A, B or C-layers) track is reconstructed from the scintillator and the wire chamber hits. After the reconstruction, qualities and types of the muons are defined that depend on the number of hits in the A, B or C-layers of the muon system and the possibility of finding a matched track reconstructed in the central tracking system [67]. The momentum resolution of the central tracker track is better than the local muon momentum resolution.

Muon entering into the detector from the cosmic rays are rejected based on the timing

information in the A and B or C-layers. A non-cosmic muon should produce hits in each layer within 10 ns. Further, the central tracker track should have a small distance of closest approach to the PV in the transverse plane, and should be originated within a few centimeters of PV position along the beam direction.

4.5 Missing Transverse Energy

The missing transverse energy $\not\!\!E_T$ is the last quantity that is constructed after the reconstruction of all physics objects. It is a measure of an imbalance of the transverse momentum in the event that is an indication of the presence of neutrinos or other unknown particles that leave the detector without interaction. For W+jets events, it is generally defined as

$$\vec{\not\!\!E}_T = -\left(\sum_{i=1}^{N} \vec{p}_T^{\,i} + \vec{p}_T^{\,\ell}\right), \tag{4.6}$$

where the sum is over all calibrated jet's p_T in the events, and p_T^{ℓ} represents the transverse momentum of the lepton from the W boson decay.

In practice as described elsewhere [68], it is first constructed as the vector sum of energy deposited in the calorimeter cells excluding the coarse hadronic region. An energy correction is applied to the electromagnetic objects, followed by the jet energy scale (JES) corrections to the hadronic parts. The energy fraction contributed to the transverse momentum of jets from the coarse hadronic calorimeter is later added to the resulting $\not\!\!E_T$. Muons do not deposit much energy into the calorimeter, therefore their contribution should be included by vectorially adding the muon momentum measured from the global fit.

Chapter 5

Monte Carlo Simulation

This chapter describes the Monte Carlo (MC) simulations that is used to study the $W+c$ and $W+$jets processes theoretically. The Monte Carlo is a technique using pseudo-random numbers to statistically build observables. This technique is adopted in several packages for event generation. Events simulation begins with the production of events using Monte Carlo generators that employ theoretical models and perform the numerical calculations of the cross sections. The generated events are then processed through another set of software that folds those events into real data-like events based on the detector geometry and response. In the final stage these events are reconstructed by constructing the objects such as electrons, jets, muons and $\not\!\!E_T$ as described in the previous chapter.

5.1 Monte Carlo Generators

Events are generated using the Monte Carlo techniques that are based on a random number generator using Poisson statistics. The evaluation and generation of the matrix elements and decay widths of the hard scattering process is performed using the programs such as ALPGEN [46] and PYTHIA [69]. The interacting parton's momentum information is incorporated in the full cross section calculation using the PDFs extracted by the CTEQ collaboration.

5.1.1 ALPGEN

ALPGEN is a MC generator that is specifically developed to perform the matrix element calculations at the tree level of the hard scatter process involving multiple partons in the final states at the hadron colliders [46]. This package allows up to six partons generated in association with the W/Z production at high center-of-mass energy. These calculations are performed at the leading order in α_s at the parton-level. For the factorizations the $\overline{\text{MS}}$ scheme is used in which only the leading order in α_s terms are absorbed in the PDFs. The calculations for V+jets processes can be made for various choices of factorization and normalization scales, μ_F and μ_R respectively. Common choices are $\sqrt{m_V^2 + \sum_{\text{j}} p_{Tj}^2}$, $\sqrt{\sum_{\text{j}} p_{Tj}^2}$ or m_V, where m_V represents the mass of the vector boson (W/Z bosons) and p_{Tj} is the transverse momentum of a parton in the final state.

The higher order contribution of the order of $\alpha_s^n \log^{2n}(Q)$, in the leading logarithmic approximation, due to the parton evolutions into n soft partons are incorporated using the MC programs performing the parton emission and the formation of hadrons from the partons. An event with n+1 jets can be obtained either from n+1 parton final state that evolve with soft and collinear radiations or from n parton final state where one of the n partons produce a hard and large angle radiation to form an extra jet. For the parton evolutions, the ALPGEN is interfaced with the parton shower generators such as PYTHIA package described in Sec. 5.1.2. At the same time a factorization scheme is employed that determines which of the two paths for an n+1 jet final state to follow [70]. The multiple matrix elements are merged with the parton evolutions by reweighting the matrix element weights with the Sudakov form factors described elsewhere [71]. These factors provide the probability of gluon or parton emissions at a reasonable transverse momentum p_T, and treat the divergences from soft radiations. Further, a veto of the parton showers is required in the phase space that is already covered by the parton-level configuration to minimize an over-counting of the final state partons [46]. The samples with different parton multiplicities are combined together with appropriate weights to make an inclusive sample. This factorization scheme

of combining the first order tree level matrix element generators with the parton shower generators is known as MLM prescription described in detail elsewhere [70].

For the analysis presented in this dissertation, the ALPGEN version v2.05 is used. The generators continue to develop for the improvement based on tuning of the theoretical parameters according to the measurements.

5.1.2 PYTHIA

PYTHIA is a MC program widely used to generate the events in the high energy interaction of two partons producing two particles in the final state. PYTHIA provides both the standard model and beyond the SM (such as SUSY) theoretical frameworks to generate a wide variety of processes for high energy physics analyses. It has an ability to produce the complete event properties starting from the hard parton-level ($2 \rightarrow 2$) scattering to the fragmentation and hadronization. It utilizes probabilistic calculations of the emissions of the initial state and final state radiations from the interacting and outgoing particles. These calculations can be merged with the first order matrix element calculations.

While ALPGEN handles the multiple parton final state at tree level, PYTHIA is interfaced with ALPGEN to incorporate the parton evolution. The matrix element generation process is merged with the fragmentation and hadronization process. The merging schemes have been studied by the theorists. These are proved to work reasonably well in incorporating the next-to-leading order effects from the parton emission with the multiple parton matrix elements [46].

The PYTHIA version used for the presented analysis is v6.323.

5.2 Detector Simulation

Full detector simulation of the MC events is performed by employing two DØ packages [72] named d0gstar and d0sim in the MC production chain. The d0gstar package is based on the GEANT package [73]. It determines how much energy is deposited in the active areas

of the detector and models the passages of the particles through the detector. It utilizes the detector geometry and response to allow events flow through the efficient regions of the subdetectors. The d0gstar is interfaced with EVTGEN [74] package that produces the particle decays, such as from the heavy mesons or baryons (more common ones are $D^{\pm}$, D^{o}, $B^{\pm}$, Λ etc) or from the light hadrons ($\pi^{\pm}$, π^{o}, $K^{\pm}$ and K^{o} etc) occurring in various parts of the detectors depending on their lifetimes. The informations of the decay products are stored in the event if the decay occurred in the tracking regions (such as SMT or CFT).

The use of d0sim package is to perform the electronics simulations, by adding the noise and inefficiencies from the SMT, CFT, calorimeter, and the muon systems. The pile-ups in the calorimeter expected from previous events are added to each event. An over-lapping of the hard scattered events with the zero-bias events is performed to simulate them as real data events. The zero-bias events are real data events that are random samplings of all beam crossings, regardless of whether anything was seen in the detector. Full event information is saved as "RawDataChunk", and is directed to another package in the chain called "d0reco".

The d0reco package is used to reconstruct the event objects from the "RawDataChunk" as described in the previous chapter. At this level, the data and MC can be analysed on similar grounds.

5.3 Signal and Background Samples Generations

For the theoretical studies of the signal and background processes, vector boson+jet and $t\bar{t}+nlp$ final events are generated with the ALPGEN interfaced with PYTHIA employing MLM scheme for parton-to-jet matching. The "nlp" stands for n number of light partons produced at the tree level. Some ($2 \rightarrow 2$) background processes, such as $W^{+}W^{-}$, WZ and ZZ, are generated using PYTHIA only. Events with single top quark in the final state contributing as background are generated using the COMPHEP package [34]. The CTEQ6L [45] PDF set is used for the momentum distributions of the interacting partons in the proton. A

ALPGEN samples and the cross sections					
Sample	N_{gen}	$\sigma \times BR$ (pb)	Sample	N_{gen}	$\sigma \times BR$ (pb)
$W(\rightarrow \ell\nu) + 2c + 0lp$	481572	24.01 ± 0.03	$W(\rightarrow \ell\nu) + 0lp$	14439016	4623.34 ± 4.87
$W(\rightarrow \ell\nu) + 2c + 1lp$	336400	13.26 ± 0.02	$W(\rightarrow \ell\nu) + 1lp$	8119705	1279.37 ± 2.11
$W(\rightarrow \ell\nu) + 2c + 2lp$	332547	5.39 ± 0.02	$W(\rightarrow \ell\nu) + 2lp$	4493703	303.83 ± 0.84
$W(\rightarrow \ell\nu) + 2c + 3lp$	372248	2.51± 0.01	$W(\rightarrow \ell\nu) + 3lp$	2330583	72.18 ± 0.24
$W(\rightarrow \ell\nu) + 2b + 0lp$	738761	9.35 ± 0.01	$W(\rightarrow \ell\nu) + 4lp$	1567682	16.34 ± 0.10
$W(\rightarrow \ell\nu) + 2b + 1lp$	261300	4.27± 0.01	$W(\rightarrow \ell\nu) + 5lp$	721952	5.94 ± 0.04
$W(\rightarrow \ell\nu) + 2b + 2lp$	171411	1.54 ± 0.01	$Z(\rightarrow ee) + 0lp$	860517	139
$W(\rightarrow \ell\nu) + 2b + 3lp$	163674	0.75 ± 0.01	$Z(\rightarrow ee) + 1lp$	187031	41.8
$t\bar{t} + 0lp$	283463	1.3	$Z(\rightarrow ee) + 2lp$	88689	10.2
$t\bar{t} + 1lp$	98425	0.6	$Z(\rightarrow ee) + 3lp$	93479	3.5
$t\bar{t} + 2lp$	92517	0.3	$Z(\rightarrow \mu\mu) + 0lp$	482243	140.3
$W(\rightarrow \ell\nu) + c + 0lp$	307471	46.0 ± 2.3	$Z(\rightarrow \mu\mu) + 1lp$	209276	41.6
$W(\rightarrow \ell\nu) + c + 1lp$	279947	16.8 ± 1.1	$Z(\rightarrow \mu\mu) + 2lp$	103886	10.3
$W(\rightarrow \ell\nu) + c + 2lp$	168046	4.5 ± 0.6	$Z(\rightarrow \mu\mu) + 3lp$	104292	3.5
$W(\rightarrow \ell\nu) + c + 3lp$	112149	1.0 ± 0.2	$Z(\rightarrow \tau\tau) + 0lp$	461797	140.3
$W(\rightarrow \ell\nu) + c + 4lp$	44817	0.4 ± 0.1	$Z(\rightarrow \tau\tau) + 1lp$	204433	42.1
WW	478006	11.5	$Z(\rightarrow \tau\tau) + 2lp$	96557	10.3
ZZ	95949	1.6	$Z(\rightarrow \tau\tau) + 3lp$	93722	3.5
WZ	87504	3.7	tbq	626875	0.777
			tb	628530	0.345

Table 5.1: ALPGEN+PYTHIA MC sample cross sections times branching ratio is given in this table. For the W + jets final state generation, the W boson is allowed to decay leptonically. For the $t\bar{t}$ final state generation, one of the W boson from the top quark decay is allowed to decay leptonically and the other is allowed to decay hadronically to mimic the signature of W + jets final state. The WW, WZ and ZZ process generation is inclusive. For the single top quark final state production, tbq and tb, the W boson from the top quark decay is allowed to subsequently decay into leptons.

comparison of u, d, s and g momentum distributions is shown in Fig. 5.1. The minimum p_T of the matched final state partons is required to be 8 GeV and the angular separation between the two partons is restricted to be less than 0.5. The dynamic normalization and factorization scale, $Q = \sqrt{m_V^2 + \sum_{\mathrm{j}} p_{Tj}^2}$, is chosen at which these samples are generated, where m_V is the mass of the vector boson and p_{Tj} is the transverse momenta of the final state partons. The ALPGEN cross sections times branching fractions for all processes at this scale are given in Table 5.1. These cross sections and the number of generated events are used to normalize the selected events to the data integrated luminosity, $\mathcal{L}$, for comparison with the data sample. The normalization weight associated with each sample is $\frac{\mathcal{L}\sigma_i}{N_i}$, where σ_i denotes the cross section and N_i represents the number of selected events in the ith sample.

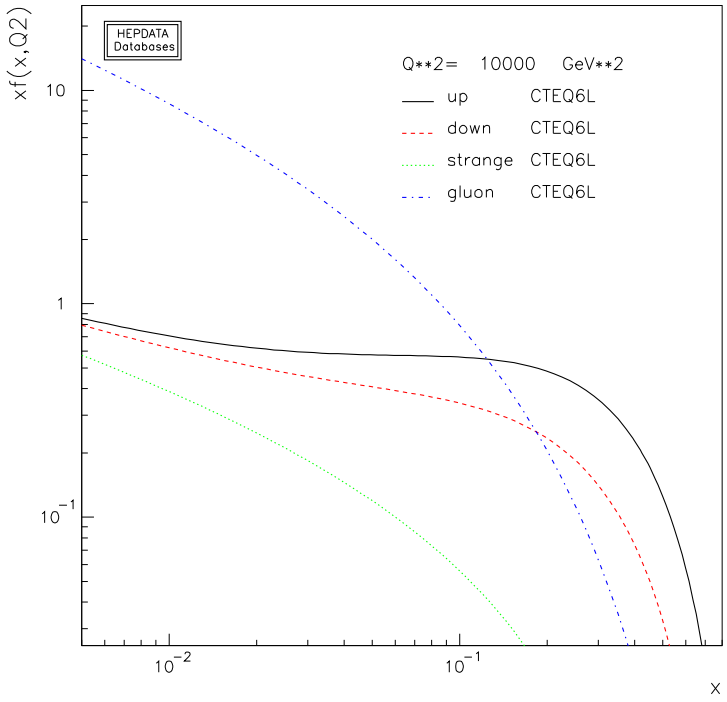

Figure 5.1: Distributions of the u, d, s partons and gluon momentum fractions of proton obtained from the CTEQ6L sets. At high x, the valence quark contribution dominates and at low x the sea quarks and gluon dominate.

Chapter 6

Data Analysis and W+jets Selection

This chapter describes how the data is analyzed after proceeding with a selection criteria based on the signal event topology. Event selection of the data for an offline analysis is performed using ROOT [75] based analysis tool "Common Analysis Format Environment" (cafe) [76] developed at DØ. The data and background event files are saved in the thumbnail format, which are converted into easily analyzable ROOT formatted files via the package "tmb_analyze".

This measurement utilizes about 1 fb^{-1} luminosity of data collected at DØ during the period April 2002–February 2006. The data samples are centrally skimmed into different major datasets by the Common Samples Group (CSG) [77] for use by the DØ analyzers depending on their signal kinematics. The "EMinclusive" and "MUinclusive" skims are used for the W+jets candidate selection. The data samples initially contained 335 M events in EMinclusive skim and 330 M events in MUinclusive skim. The definition of these skims are given below:

EMinclusive:

- At least one EM object reconstructed with Simple cone (scone) algorithm, described elsewhere [60].
- The transverse momentum of the EM object must be greater than 20 GeV.

MUinclusive:

- At least one muon passing loose requirements should be present in the skim. This muon must have produced a scintillator hit and at least two wire hits in the A-layer of the muon system. Or, it has produced at least one scintillator hit and two wire hits in the B or C-layers of the muon system.

- The transverse momentum of the muon measured by the central tracking system should be 8 GeV.

Events must pass the trigger requirements at L1, L2 and L3 as described in Tables 6.1-6.3 and 6.4- 6.5. The trigger names change with the data taking period depending on the modification in the selection criteria. The single EM triggers require one electron candidate to pass a selection criteria as listed in Tables 6.1- 6.3. The single muon triggers restrict that at least one muon in the local muon system fired the trigger, and at least one track reconstructed in the central tracker with high transverse momentum ($p_T > 10$ GeV) be found. Most of the single muon triggers are unrestricted at L2.

6.1 W Boson Selection

The production cross section of the W+jets at the center-of-mass energy of $\sqrt{s} = 1.96$ TeV is of the order of 10^3 pb. The W boson decays leptonically into lepton ℓ and neutrino ν_ℓ pairs or hadronically into quark-antiquark pairs. The selection of W boson by identifying the leptonic decay products is rather cleaner than the selection based on the identification of the jets initiated by quarks. The jet selection is dominated by the multijet background which makes it difficult to isolate the signal. Because of the large W mass (~ 80 GeV), the leptonic decay product from the W boson tends to have high p_T, (typically $20 - 40$ GeV). The presence of an associated jet with the W boson boosts its momentum along the x-y directions, and therefore the W boson itself gains small transverse momentum changing the p_T of the lepton as well. For the event selection for $W^- \to e^-\bar{\nu}_e$ or $W^+ \to e^+\nu_e$ modes (electron channel), each event must contain at least one electron. For $W^- \to \mu^-\bar{\nu}_\mu$ or

Trigger name	L1 calorimeter tower	L2 EM cluster threshold	L3 electron shower shape and E_T requirements
EM_MX	1 calorimeter trigger tower $E_T > 15$ GeV	unrestricted	no shower shape cut, $E_T > 30$ GeV
EM_MX_SH	1 calorimeter trigger tower $E_T > 15$ GeV	unrestricted	Loose, $E_T > 20$ GeV
EM_MX_EMFR8	1 calorimeter trigger tower $E_T > 15$ GeV	unrestricted	$f^{EMF} > 0.8$, $E_T > 30$ GeV
EM_HI trigger tower $E_T > 10$ GeV	1 calorimeter	>= 12 GeV unrestricted for runs below 171829	no shower shape cut, $E_T > 30$ GeV
EM_HI_SH	1 calorimeter trigger tower $E_T > 10$ GeV	>= 12 GeV unrestricted for runs below 171829	Loose, $E_T > 20$ GeV
EM_HI_EMFR8	1 calorimeter trigger tower $E_T > 10$ GeV	>= 12 GeV unrestricted for runs below 171829	$f^{EMF} > 0.8$, $E_T > 40$ GeV
E1_SHT20	1 calorimeter trigger tower $E_T > 11$ GeV	unrestricted	Tight, $E_T > 20$ GeV
E2_SHT20	2 calorimeter trigger towers $E_T > 6$ GeV	unrestricted	Tight, $E_T > 20$ GeV
E3_SHT20	1 calorimeter trigger tower $E_T > 9$ GeV 2 calorimeter trigger towers $E_T > 3$ GeV	unrestricted	Tight, $E_T > 20$ GeV
E4_SHT20	1 calorimeter trigger tower $E_T > 9$ GeV, one track $p_T > 10$ GeV	unrestricted	Tight, $E_T > 20$ GeV

Table 6.1: Trigger used for the data selection in the electron channel. The f^{EMF} is the fraction of electromagnetic energy deposited in the EM section of the calorimeter, and the definition of f^{iso} is given in Eq. 4.1.

Trigger name	L1 calorimeter tower	L2 EM cluster threshold	L3 electron shower shape and E_T requirements
E1_SH30	1 calorimeter trigger tower $E_T > 11$ GeV	>= 15 GeV	Loose, $E_T > 30$ GeV
E2_SH30	2 calorimeter trigger towers $E_T > 6$ GeV	>= 15 GeV	Loose, $E_T > 30$ GeV
E3_SH30	1 calorimeter trigger tower $E_T > 9$ GeV 2 calorimeter trigger towers $E_T > 3$ GeV	>= 15 GeV	Loose, $E_T > 30$ GeV
E4_SH30	1 calorimeter trigger tower $E_T > 11$ GeV	Single tower object $E_T > 11$ GeV $f^{iso} < 0.2$	Loose, $E_T > 30$ GeV
E1_L50	1 calorimeter trigger tower $E_T > 11$ GeV	unrestricted	Loose, $E_T > 50$ GeV
E1_VL70	1 calorimeter trigger tower $E_T > 11$ GeV	unrestricted	Very loose, $E_T > 50$ GeV
E1_NC90	1 calorimeter trigger tower $E_T > 11$ GeV	>= 15 GeV	No, $E_T > 90$
E1_SHT22	1 calorimeter trigger tower $E_T > 11$ GeV	>= 15 GeV	Tight, $E_T > 22$ GeV
E2_SHT22	2 calorimeter trigger towers $E_T > 6$ GeV	>= 15 GeV	Tight, $E_T > 22$ GeV
E3_SHT22	1 calorimeter trigger tower $E_T > 9$ GeV 2 calorimeter trigger towers $E_T > 3$ GeV	>= 15 GeV	Tight, $E_T > 22$ GeV

Table 6.2: Continued table for the trigger lists used for the data selection in the electron channel. The f^{EMF} is the fraction of electromagnetic energy deposited in the EM section of the calorimeter, and the definition of f^{iso} is given in Eq. 4.1.

Trigger name (continued)	L1 calorimeter tower	L2 EM cluster threshold	L3 electron shower shape and E_T requirements
E4_SHT22	1 calorimeter trigger tower $E_T > 11$ GeV	Single tower object $E_T > 11$ GeV $f^{iso} < 0.2$	Tight, $E_T > 22$ GeV
E1_L70	1 calorimeter trigger tower $E_T > 11$ GeV	>= 15 GeV	Loose, $E_T > 70$ GeV
E1_SHT25	EM cluster $E_T > 12$ GeV	2 trigger towers E_T sum >= 15	Tight, $E_T > 25$ GeV
E3_SHT25	EM cluster $E_T > 12$ GeV	1 trigger tower $E_T > 11$ GeV $f^{iso} < 0.20$	Tight, $E_T > 25$ GeV
E4_SHT25	2 EM objects $E_T > 6$ GeV	EM cluster $E_T > 6$ GeV	Tight, $E_T > 25$ GeV
E1_SH35	EM cluster $E_T > 12$ GeV	2 trigger towers E_T sum >= 15	Loose, $E_T > 35$ GeV
E3_SH35	EM cluster $E_T > 12$ GeV	1 trigger tower $E_T > 11$ GeV $f^{iso} < 0.20$	Loose, $E_T > 35$ GeV
E4_SH35	2 EM objects $E_T > 6$ GeV	EM cluster $E_T > 6$ GeV	Loose, $E_T > 35$ GeV

Table 6.3: Continued table for the trigger lists used for the data selection in the electron channel. The f^{EMF} is the fraction of electromagnetic energy deposited in the EM section of the calorimeter, and the definition of f^{iso} is given in Eq. 4.1.

Trigger name	L1 muon, region, scintillator hit requirements, track p_T	L2	L3 local Muon or central track
MU_W_L2M5_TRK10	CFT wide region, scintillator trigger min-bias condition	Medium muon, $p_T > 5$ GeV	central track $p_T > 10$ GeV
MUW_A_L2M3_TRK10	CFT wide region, tight scintillator, loose wire hits	Medium muon, $p_T > 3$ GeV	central track $p_T > 10$ GeV
MUW_W_L2M3_TRK10	CFT wide region, tight scintillator, loose wire hits	Medium muon, $p_T > 3$ GeV	central track $p_T > 10$ GeV
MUH1_TK12	CFT wide region, tight scintillator track $p_T > 10$ GeV	unrestricted	central track $p_T > 12$ GeV
MUH1_LM15	CFT wide region, tight scintillator track $p_T > 10$ GeV	unrestricted	muon $p_T > 15$ GeV
MUH1_TK12_TLM12	CFT wide region, tight scintillator a track $p_T > 10$ GeV	unrestricted	central track $p_T > 12$ GeV, loosely central track matched local muon $p_T > 12$ GeV
MUH1_ITLM10	CFT wide region, tight scintillator a track $p_T > 10$ GeV	unrestricted	central track $p_T > 10$ GeV, central track matched local muon $p_T > 10$ GeV

Table 6.4: Trigger used for the data selection in the muon channel. Some triggers requires an isolated muon requirements with respect to the tracks and the calorimeter energy cells, the thresholds are $p_T^{trkHalo} < 3$ and $E_T^{halo} < 3$, the variables are defined in Sec. 6.1.

Trigger name (continued)	L1 muon, region, scintillator hit requirements, track p_T	L2	L3 local Muon or central track
MUH1_ILM15	CFT wide region, tight scintillator a track $p_T > 10$ GeV	unrestricted	isolated muon $p_T > 15$ GeV
MUH8_TK12_TLM12	wide muon region tight scintillator loose wire hits muon $p_T > 10$ GeV track $p_T > 10$ GeV	unrestricted	central track $p_T > 12$ GeV, loosely central track matched local muon $p_T > 12$ GeV
MUH8_ILM15	wide muon region tight scintillator loose wire hits muon $p_T > 10$ GeV track $p_T > 10$ GeV	unrestricted	central track $p_T > 10$ GeV, central track matched isolated local muon $p_T > 10$ GeV
MUH8_ITLM10	wide muon region tight scintillator loose wire hits muon $p_T > 10$ GeV track $p_T > 10$ GeV	unrestricted	central track $p_T > 10$ GeV, central track matched isolated local muon $p_T > 10$ GeV

Table 6.5: Continued list of triggers used for the data selection in the muon channel. Some triggers requires an isolated muon requirements with respect to the tracks and the calorimeter energy cells, the thresholds are $p_T^{trkHalo} < 3$ and $E_T^{halo} < 3$, the variables are defined in Sec. 6.1.

$W^+ \to \mu^+\nu_\mu$ modes (muon channel), event selection is based on the requirement of at least one muon. The decay mode $W \to \tau\nu$ is considered only via the leptonic decay of τ with branching fraction of 17%. The taus from the W bosons that decay into the electrons contribute to the electron channel and those decaying into the muons contibute to the muon channel. Thus the signature of W+jets final state is a lepton+$\not\!\!E_T$+jets. The electron or muon must pass the following set of cuts:

Electron identification: The criteria to identify an electron is well studied by the EMID group at DØ as illustrated elsewhere [78].

1. The EM cluster reconstructed using the simple-cone algorithm must deposit 90% of its energy in the EM part of the calorimeter, as described in Sec. 4.3.1.

2. The isolation of the cluster, f^{iso}, as defined in Sec. 4.3.1, must satisfy $f^{iso} < 0.15$.

3. The χ^2_{HM} variable constructed from the H-matrix of seven variables as described in Sec. 4.3.1 must satisfy $\chi^2_{HM} < 12$ for an electron that lies in the central calorimeter (CC) ($|\eta| < 1.1$). For an electron that is located in the end-calorimeter (EC) ($1.5 < |\eta| < 2.5$), the χ^2_{HM} constructed from an H-matrix of eight variables must satisfy $\chi^2_{HM} < 20$.

4. The electron measured by the calorimeter is matched to a track reconstructed in the central tracking system. The track match χ^2 probability $P_{trk}(\chi^2)$ as defined in Sec. 4.3.1 must be greater than 0.01. The p_T of the track matched to the electron is required to have high transverse momentum ($p_T > 10$ GeV).

5. The log likelihood discriminant LH_e of electron that combines the tracker and the calorimeter information using the expected distributions of the electron and the jet background must be greater than 0.85.

6. Electron track has the distance of closest approach in the longitudinal direction with respect to the primary vertex to be less than 3 cm. The primary vertex is located

within $|z| < 60$ cm, i.e within the longitudinal region covered by the CFT.

7. The transverse momentum of the electron is required to satisfy $p_T^e > 20$ GeV.

Muon identification:

The muon satisfies following set of selection criteria:

1. The muon must have track segments both in the A-layer and the BC-layer.

2. It must have produced two wire hits and one scintillator hit in the A-layer.

3. It must have at least two wire hits in the B or C-layer and at least one scintillator hit in the B or C-layer, except in the region not covered by these layers at the bottom ($4.25 < |\phi| < 5.15$) of the detector due to the support structure.

4. Muon has a cosmic veto requirement based on the timing requirements on the A, B or C-layers.

5. The transverse momentum of the muon is required to satisfy $p_T > 20$ GeV.

6. The muon is required to be isolated. It is separated from the axis formed by any jet found in event by $\Delta\mathcal{R}(\mu, \text{jet}) > 0.5$. The total transverse energy deposited in the Halo cone ($0.1 < \Delta\mathcal{R} < 0.4$) around the muon direction, $E_T^{halo} = \sum_{i=1}^{N_{cells}} E_T^i$, is less than 2.5 GeV. Similarly the total transverse momentum of the track that lies within $\Delta\mathcal{R} < 0.5$, except the muon matched track, with respect to the muon axis, $p_T^{trkHalo} = \sum_i^{trks} p_T^i$, should be less than 2.5 GeV. Further, the ratios E_T^{halo}/p_T^μ and $p_T^{trkHalo}/p_T^\mu$ are required to be less than 0.15, where p_T^μ is the transverse momentum of the muon determined from the global fit.

7. A track reconstructed in the central tracking system is matched with the muon track reconstructed in the local muon system. The $\chi^2/ndof$ of the track fit should be less than 4. The distance of closest approach (dca) of the track should be less than 0.2 cm, if track has no hits produced in the SMT system. The dca is less than 0.02 cm

if track is reconstructed with hits produced in the SMT system. This selection cut suppresses the muon track from the b or c quark decay into muon in the $b\bar{b}$ or $c\bar{c}$ sample that would otherwise produce the signature of W+jets via muon+$\not\!\!E_T$+jets final state.

8. The central track matched to the local muon must have a distance of closest approach in the longitudinal direction with respect to the primary vertex to be less than 3 cm. The primary vertex is located within $|z| < 60$ cm, i.e within the longitudinal region covered by the CFT.

Missing transverse energy selection:

1. The imbalance of the transverse momentum in an event is an indicator of neutrino that escapes detection. The missing transverse energy is considered as the magnitude of the vector sum of the transverse momenta of all objects reconstructed in event after the energy scale correction, as described in Sec. 4.5.

2. To reduce the missing energy $\not\!\!E_T$ reconstructed from the underlying events and the multijet background, the missing transverse energy is required to be at least 20 GeV.

3. The $\Delta\phi$ between the lepton and $\not\!\!E_T$ should be at least 0.4 to suppress the Drell-Yan di-lepton background process as shown in Fig. 6.1, where one of the leptons produces the bremsstrahlung radiations that would deposit energy in the calorimeter and would be reconstructed as jet. Vectorially adding the transverse momenta of all objects (jet and muon) in the event would give an imbalance in the direction closer to the second lepton p_T direction, resulting in a small value of $\Delta\phi(\mu, \not\!\!E_T)$. The importance of imposition of a $\Delta\phi$ cut is more evident in the muon channel with di-muon events that contribute to the signal W+c-jet events after the final selection, as will be described in Chapter 7. Figure 6.4 shows the $\Delta\phi(\mu, \not\!\!E_T)$ distribution in an inclusive $W(\rightarrow \mu\nu)$+jets sample after applying all selection cuts except the $\Delta\phi(\mu, \not\!\!E_T)$ requirement. This figure also shows that the largest contribution in the low $\Delta\phi(\mu, \not\!\!E_T)$ comes from Z+jets events

included in the MC samples. The Z+jets are those events in which the invariant mass of two final state leptons from the boson decay is in the mass window $[60, 130]$ GeV.

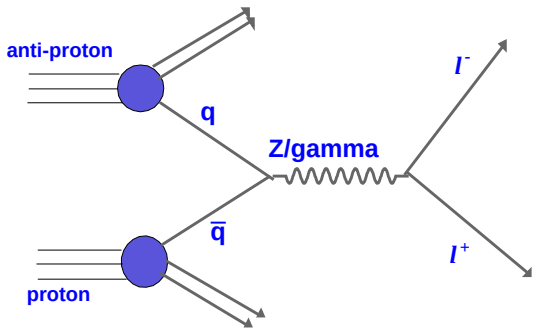

Figure 6.1: Drell-Yan dilepton event.

6.1.1 Corrections for the detector inefficiencies

The MC simulation in general incorporates all detector effects and inefficiencies in the various parts of subdetectors. But with the aging of the detector and the increase in the luminosity, a small fraction of the detector components become inefficient, malfunctioning or dead during the data taking. Such kinds of effects that slightly change over the period of time are not well modeled in the MC. For a direct comparison of kinematics of W+jets events in the MC simulation with the folded data, the MC events need to be corrected for remaining inefficiencies in the objects reconstructions compared to that in the data. The data that is corrected for the detector effects and objects reconstruction inefficiencies is called folded data. The inefficiencies, with sizes around 10% or less, of the electron and

muon identifications and reconstructions are determined using a technique known as tag-and-probe method [67, 79]. According to this method, $Z \to \ell^+\ell^-$ events are reconstructed from two oppositely charged leptons satisfying basic loose selections by fitting the invariant mass of two leptons to the Z boson mass peak [67, 79]. One of the lepton is considered as a "tag" lepton that must satisfy the tight selection criteria. The lepton on the other side is known as "probe" which is required to pass the specific requirement for which the efficiency is desired to be measured. The fraction of the number of events where both the "tag" and "probe" pass the criteria is considered as the efficiency for a particular selection cut.

$$\epsilon^{\text{reco}}_{\text{lepton}} = \frac{N^{\text{tag+probe}}}{N^{\text{tag}}}, \tag{6.1}$$

where N^{tag} denotes the number of events when the "tag" lepton passes the cuts and the "probe" lepton may or may not pass these cuts, and $N^{\text{tag+probe}}$ denotes the number of events when both "tag" and "probe" leptons pass the selection cut.

The relative difference in the data and MC efficiencies of the lepton reconstruction is considered as the scale factor (SF) by which the MC is reweighted to correct to the data. Muon identification efficiency varies over the detector $\eta - \phi$ regions and has dependence on the p_T of muons. It is relatively higher in the region around $|\eta| = 1$ and increases with muon p_T, and on average it is 75% in data sample. The average scale factor for the muon identification efficiencies is 0.97. The tracking efficiency is measured to be 91% on average from $Z \to \mu^+\mu^-$ data sample, and the scale factor to correct the MC is 0.93. Electron reconstruction and identification efficiencies also have small dependence on the $\eta-\phi$ location of electron in the detector due to ϕ dependent inefficiencies in the CFT tracking system which is not well modelled in MC simulation. Average electron identification efficiency is 80% in data and 85% in the MC. The average scale factor for the combined efficiency of electron identification and track reconstruction is $0.94 \times 0.93 = 0.87$.

6.1.2 Data/MC comparison of W boson kinematics

After selecting a good lepton (electron or muon) and the missing transverse $\not\!\!E_T$, an event with W boson candidate is selected by requiring that the transverse mass, $M_T^W = [2\not\!\!E_T p_T^\ell (1 - \cos\phi(\not\!\!E_T, p_T^\ell))]^{\frac{1}{2}}$, constructed from the lepton p_T^ℓ and $\not\!\!E_T$ should lie in the region $40 < M_T < 120$ GeV. Figure 6.2 shows the distribution of the W boson transverse mass in the data and MC samples after imposing the above mentioned cuts. The presence of at least one jet with the transverse momentum $p_T > 20$ GeV in each event is imposed in both the data and MC samples. The jet selection criteria is described in detail in Sec. 6.2. After this selection the $W(\rightarrow e\nu)$+jets data sample has $82,747$ events and the $W(\rightarrow \mu\nu)$+jets data sample has $57,944$ events, while the theoretical predictions are given in Table 6.6. A reasonable agreement between data and MC implies that the selection cut applied to the data sample indeed remove the instrumental background (or the background from the underlying events) contributed to W boson reconstruction. The MC prediction includes the contribution from the processes W+light-jets, $Wb\bar{b}$, $Wc\bar{c}$, Z+light-jets, $t\bar{t}$, WW and the data driven multi-jet (MJ) background. The MC samples are combined by applying cross section weights as given in Table 5.1, and are reweighted by the scale factors discussed in Sec. 6.1.1.

Due to the cut imposed on the minimum number of jets with a certain p_T threshold, the reconstructed W boson have relatively harder p_T compared to that of an inclusive W boson sample (without any jet restriction). Figure 6.3 shows the p_T distribution of the W boson in the selected sample. Data exhibit relatively softer distribution than the MC simulation, which suggests that the ALPGEN+PYTHIA sample needs to be tuned up specifically in the low p_T region. The soft gluons emission process contributes dominantly to the low p_T^W region, and the radiations emission from the high p_T recoiling parton contribute dominantly in the high p_T region. The corrections to the p_T spectrum in low p_T region can be made by the soft gluon resummation techniques [80, 81], while in the high p_T region the pQCD calculations are adequate. On the other hand, the ratio measurement itself is insensitive to

the small discrepancies in the shapes of the W boson p_T^W distributions in the data and MC.

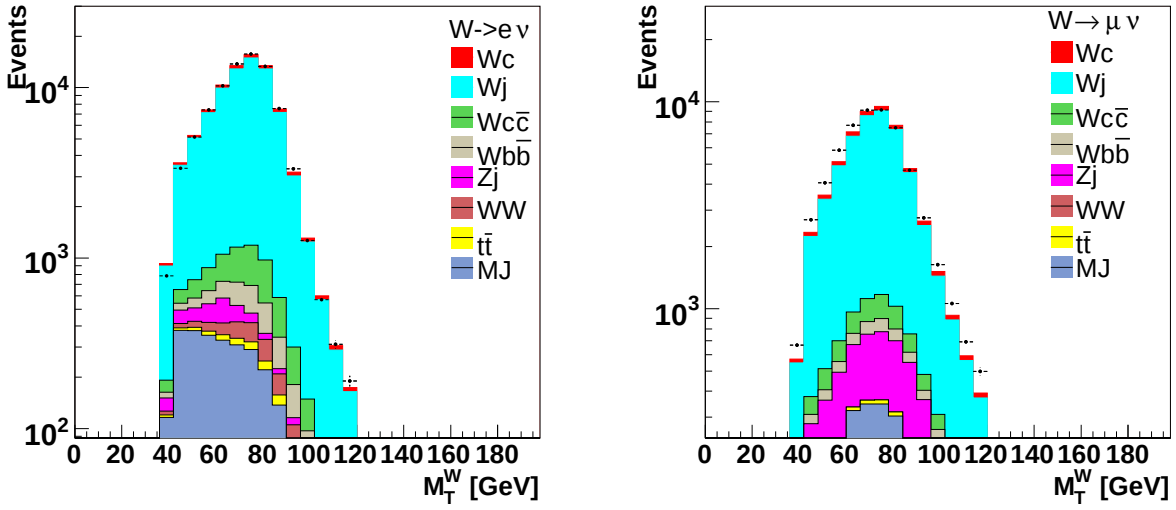

(a) (b)

Figure 6.2: The W transverse mass M_T^W reconstructed from the data and MC simulation at DØ in W+jets events. (a) $W(\rightarrow e\nu)$+jets sample, (b) $W(\rightarrow \mu\nu)$+jets sample.

6.2 Jet Selections

For the selection of W+jets candidates at least one jet must be present in association with the reconstructed W boson. Each jet p_T is calibrated for the jet energy scale as defined by Eq. 4.5. The leading jet, the highest p_T jet in event, must have a minimum p_T above 20 GeV and $|\eta| < 2.5$. Jets with p_T below 20 GeV are not well calibrated, and are accompanied by the large JES uncertainties. Non-leading jets are defined if they have minimum $p_T > 15$ GeV. The jets initiated by the c or b quarks may contain a reconstructed muon due to the semileptonic decays of b/c quarks. A muon can also be present due to the π and K decays within the detector volume. It could as well be a fake muon that is reconstructed due to the punch-through energy entering into the muon system. Further, due to the lepton conservation, a real muon must be accompanied by a neutrino that leaves

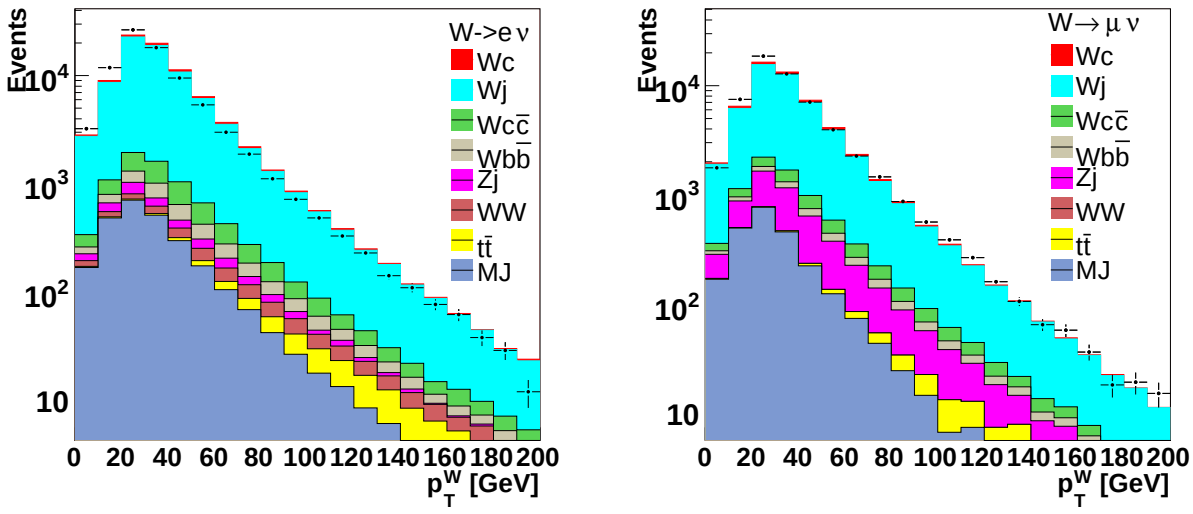

(a) (b)

Figure 6.3: The W transverse momentum p_T reconstructed from the data and MC simulation at DØ in W+jets events. (a) $W(\rightarrow e\nu)$+jets sample, (b) $W(\rightarrow \mu\nu)$+jets sample.

the detector without interaction. The muon itself deposits very little (less than 2.5 GeV) in the calorimeter system. For such jets containing a reconstructed muon, their JES calibrated transverse momenta do not take into account the missing energy due to the semileptonic decay products. This would imply that for a 20 GeV jet containing a muon with 4 GeV could have the true p_T in the ballpark of 28 GeV. For an inclusive W+jets sample, the fraction of such events is very small (less than 5%), and the effect can simply be ignored. However, this significantly impact the W+c-jet sample selection which is remedied by applying validated correction. This correction is discussed in detail in Chapter 7.

The jet p_T spectrum also have uncertainty due to jet momentum resolution defined in general terms as the average difference in the well calibrated jet p_T^{reco} from its true p_T^{true} value. The resolution is determined from the Gaussian width of the $p_T^{reco} - p_T^{true}$ distribution [82–84]. In this context, the hadronic jet are considered, i.e, the jet without containing the semileptonic decay products. The true p_T of the jet is not known in practice in the data, therefore some assumptions are made to find a true p_T reference. A Z/γ+jet event has the

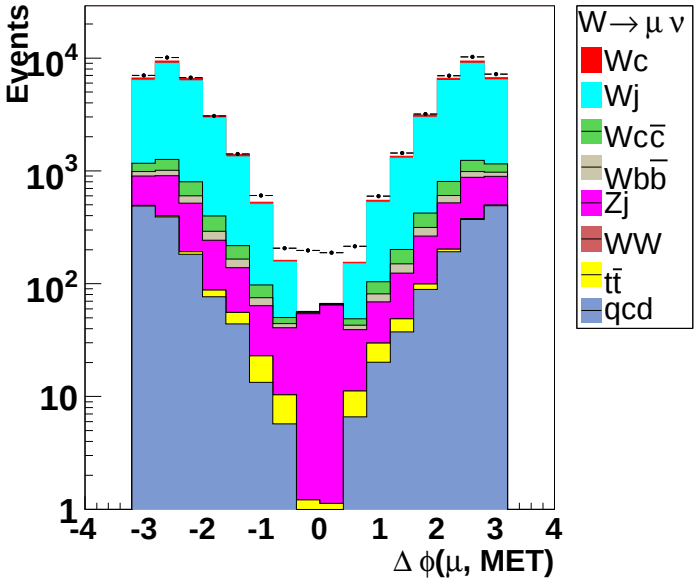

Figure 6.4: The $\Delta\phi(\mu, \not\!\!E_T)$ distribution in inclusive $W(\rightarrow \mu\nu)$+jets sample before $\Delta\phi(\mu, \not\!\!E_T) > 0.4$ cut. The restriction on $\Delta\phi(\mu, \not\!\!E_T) > 0.4$ suppresses the experimental background and the physics Drell-Yan background.

Z boson or photon and the jet produced back-to-back, thus using the momentum balancing the Z boson or photon p_T can be considered as a true reference for the jet p_T after Z boson or photon p_T is well calibrated. Therefore the average asymmetry in the jet and photon p_T with respect to the photon p_T in such events is considered to determine the relative jet p_T resolution [82–84].

$$\frac{\sigma_{p_T}}{p_T} = \sigma_{\Delta S}, \tag{6.2}$$

$$\Delta S = \frac{|p_{T\text{jet}} - p_{T\gamma}|}{p_{T\gamma}}. \tag{6.3}$$

The relative resolution is parametrized in terms of jet p_T as

$$\frac{\sigma_{p_T}}{p_T} = \sqrt{\frac{N^2}{p_T^2} + \frac{S^2}{p_T} + C^2}. \tag{6.4}$$

The parameters are N, S and C as abbreviated from "Noise", "Stochastic" and "Constant" are determined from fit to ΔS in various p_T bins [82–84]. The jet p_T resolution

Selected W+jets events in data and MC		
Process	$W(\to e\nu)$+jets	$W(\to \mu\nu)$+jets
$W + c$-jet	4301.4 ± 27.3	2576.1 ± 18.9
$W + c\bar{c}$	2683.6 ± 13.4	1623.4 ± 9.3
$W + b\bar{b}$	1229.5 ± 5.7	728.2 ± 3.9
$W +$ light-jet	71561.6 ± 112.2	45204.7 ± 79.8
$Z +$ jets	711.7 ± 12.1	2649.1 ± 21.1
WW	539.0 ± 3.7	417.7 ± 3.3
$t\bar{t}$	213.5 ± 1.0	119.7 ± 0.7
single-top	111.9 ± 0.3	75.7 ± 0.27
MJ	2650 ± 64	2360 ± 178
Total prediction	83890.3 ± 124.7	55678.9 ± 197.4
Data	82747	57944

Table 6.6: Event yields in MC and data sample after the selection criteria described in Secs. 6.1 and 6.2.

in data differs by about $10 - 20\%$ compared to that in MC. Therefore jets are smeared to reproduce the jet p_T resolution observed in data by following a procedure developed at DØ known as "JSSR", an acronym for Jet Smearing Shifting and Removing, is applied [82]. According to this procedure the jet p_T in the MC is smeared by the r.m.s of the quadratic difference in the jet p_T resolutions in data and MC, i.e. by $\sqrt{(\sigma_{p_T}^{\rm data})^2 - (\sigma_{p_T}^{\rm MC})^2}$, where $\sigma_{p_T}^{\rm data}$ denotes the jet p_T resolution in data and $\sigma_{p_T}^{\rm MC}$ denotes the jet p_T resolution in MC. The jet p_T in MC is further shifted by a factor obtained from the difference in the mean value of ΔS distribution in data and MC. The calibrated jets below the p_T threshold of 15 GeV are removed in both the data and MC. This threshold is obtained from the turn-on curve of the jet reconstruction efficiency at the plateau. Figure 6.5 shows a comparison of the jet p_T distribution between data and MC in the $W +$ jets sample.

6.3 Background Sources to W+jets

There are background sources that pass the signal selection cuts and hence produce a fake reconstructed W boson associated with jets. Such background originate mainly due to the mis-identification of isolated lepton which are candidate of the decay product of W boson.

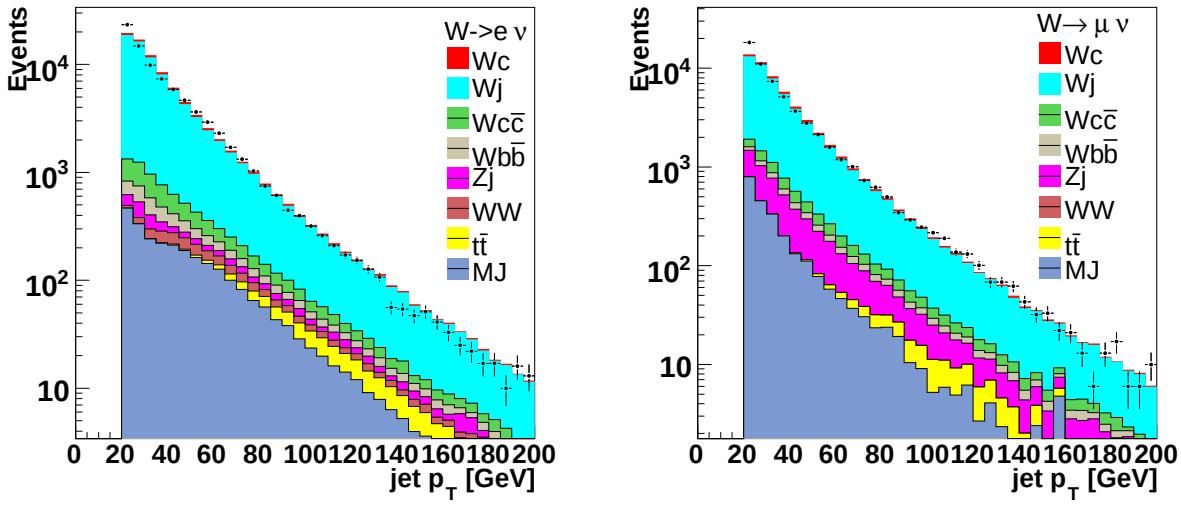

(a) **(b)**

Figure 6.5: The jet transverse momentum p_T distribution in the data and MC simulation at DØ in W+jets events. (a) $W(\rightarrow e\nu)$+jets sample, (b) $W(\rightarrow \mu\nu)$+jets sample.

The processes contributing to the fake W+jets events are multijet, γ+jets and Z+jets events. In the electron channel the multijet and γ+jets background contribute dominantly, while in the muon channel multijet and Z+jets background processes participate. The amount of multijet background is determined from the data sample, while the fraction of Z+jets contributing to W+jets is estimated from the simulation as described below.

6.3.1 Multijet background

To estimate the size of the multijet background, a procedure known as the "matrix method" is followed. The procedure consists of solving a set of two simultaneous equations expressing event yields in terms of the real W+jets and the multijet background in two correlated data sets. The first equation corresponds to the events yields after the application of all cuts except that the lepton discrimination or isolation cuts are relaxed, and the second equation represents the number of events in the dataset after all cuts are imposed. The second

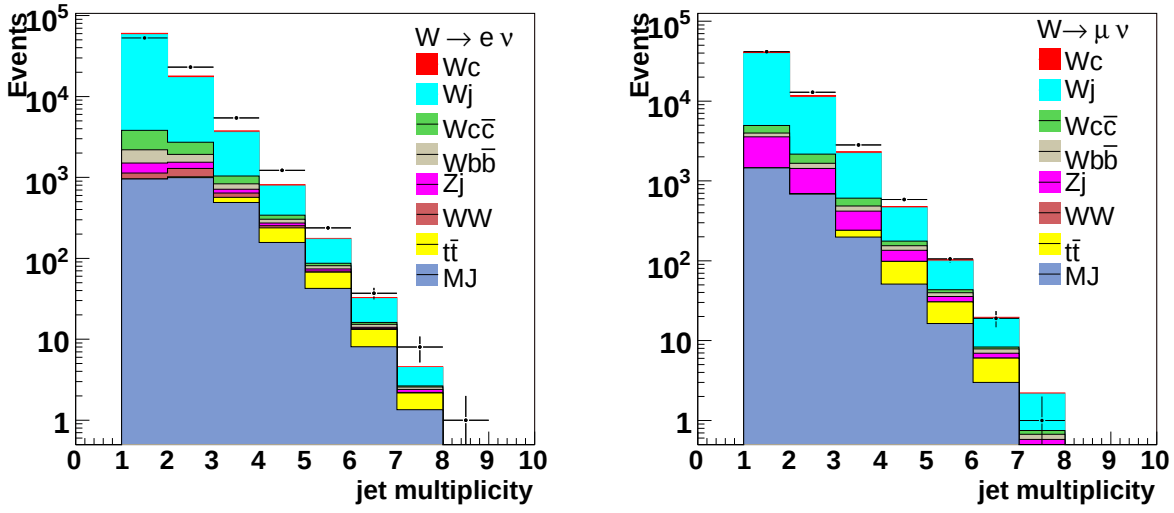

(a) **(b)**

Figure 6.6: The jet multiplicity distribution in the data and MC simulation at DØ in W+jets events. (a) $W(\rightarrow e\nu)$+jets sample, (b) $W(\rightarrow \mu\nu)$+jets sample.

dataset is a subset of the first one with loose lepton selection.

$$N_L^\ell = N_W^\ell + N_{MJ}^\ell, \tag{6.5}$$

$$N_T^\ell = \epsilon_W^\ell N_W^\ell + \epsilon_{MJ}^\ell N_{MJ}^\ell, \tag{6.6}$$

where N_L^ℓ (N_T^ℓ) denotes the event yield in the dataset where the lepton reconstructing a W boson passes as loose (tight) selection, and N_W^ℓ represents a true number of W+jets events in the loose selection and N_{MJ}^ℓ represents the amount of multijet background contributing to the W+jets after the application of loose lepton selection cuts. The ϵ_W^ℓ is relative efficiency of a loose lepton to pass a tight selection cut, and ϵ_{MJ}^ℓ represents the relative probability of producing a fake lepton reconstructing a W boson after imposing stricter cuts in the multijet sample. Solving the simultaneous Eqs. 6.5 and 6.6 for N_W^ℓ and N_{MJ}^ℓ gives

$$N_W^\ell = \frac{N_T^\ell - \epsilon_{MJ}^\ell N_L^\ell}{\epsilon_W^\ell - \epsilon_{MJ}^\ell}, \tag{6.7}$$

$$N_{MJ}^\ell = \frac{N_T^\ell - \epsilon_W^\ell N_L^\ell}{\epsilon_{MJ}^\ell - \epsilon_W^\ell}. \tag{6.8}$$

The ϵ^{ℓ}_{W} and ϵ^{ℓ}_{MJ} are measured in the data samples in both lepton channels, as described below. The contribution of multijet background events in the final W+jets candidates is evaluated as $\epsilon^{\ell}_{MJ} \times N^{\ell}_{MJ}$. Similarly the actual number of the W+jets events is $\epsilon^{\ell}_{W} \times N^{\ell}_{W}$. This technique is well developed at DØ and has been used in several analyses involving the studies of W + jets [85, 86].

Multijet background in electron channel:

A jet or photon passing the electron selection criteria can fake as an isolated electron. The probability of the jet faking as an electron is estimated from the data sample, denoted as "Jet-EM" sample, consisting of back-to-back jet and electron events. The electron in this sample presumably is a fake electron, but otherwise such events are characteristics of QCD di-jet or γ + jet processes. Events in this dataset pass all selection cuts as listed in Sec. 6.1, except that the cuts on the track match probability $P_{trk}(\chi^2)$ variable and the log likelihood discriminant LH_e variable are removed. In addition, each event must contain only one jet that satisfy the condition of azimuthal separation between the fake electron and jet of $\Delta\phi > 2.84$ and that $\not\!\!E_T < 10$ GeV to remove the signal contamination into the background region. Events passing this criteria are an indicator of γ + jet or di-jet event, where the photon or jet is mis-identified as an electron. The probability of the mis-identified electron in this dataset to satisfy the $P_{trk}(\chi^2) > 0.01$ and $LH_e > 0.85$ conditions is extracted from the fraction of those events that pass these cuts.

$$\epsilon^{e}_{MJ} = \frac{N^{T}_{\text{Jet-EM}}}{N^{L}_{\text{Jet-EM}}}, \tag{6.9}$$

where $N^{L}_{\text{Jet-EM}}$ denotes the number of events with the application of loose requirements to the mis-identified electron in the "Jet-EM" sample, and $N^{L}_{\text{Jet-EM}}$ is the number of events in the subset of "Jet-EM" data sample where the mis-identified electron satisfies $P_{trk}(\chi^2) > 0.01$ and $LH_e > 0.85$ requirements. Since the two yields are correlated as numerator is a subset of the denominator, the binomial statistics is considered to evaluate the error on ϵ_{MJ} as

given by,

$$\delta\epsilon^{e}_{MJ} = \sqrt{\frac{\epsilon_{MJ}(1-\epsilon_{MJ})}{N^{L}_{\text{Jet-EM}}}}. \tag{6.10}$$

Due to variations in the electron shower shape requirements in the single electron trigger selections during different data taking periods, there are biases in the mis-identified rate of electron. To counteract the effect of biases, the electron mis-identification rate measurement is performed for each period when trigger conditions were not preserved in the global trigger upgrade, as listed in Table 6.7. Figures 6.7 and 6.8 show ϵ^{e}_{MJ} as a function of $\not\!\!E_T$ and mis-identified electron p_T, respectively. The ϵ^{e}_{MJ} has only small dependence on the $\not\!\!E_T$ reflecting the fact that the dataset used to estimate the electron mis-identification rate has very small signal $W+$jets contribution. The $\not\!\!E_T$ in the di-jet or $\gamma+$jet process does not arise from the physical kinematics of the process, but is instead due to the uncorrelated underlying events associated with each process.

In order to estimate the relative efficiency of loose electron to pass the tighter restriction, the $Z \to e^+e^-$ dataset is used. The $Z \to e^+e^-$ data set is constructed from the events containing the invariant mass, $m_Z = \sqrt{(p_{e^+} + p_{e^-})^2}$, of two oppositely charged electrons in the Z boson mass peak region [70-110] GeV, where p_{e^+} and p_{e^-} are the four-momenta of two electrons. Both electrons in this data sample satisfy all criteria as listed for the electron identification in Sec. 6.1, except that the $P_{trk}(\chi^2) > 0.01$ and $LH_e > 0.85$ cuts are relaxed. To evaluate the efficiency of the stricter cuts, one of the electron is considered as "tag" that must pass tight cuts, and the number of events containing a "tag" electron is denoted $N^{\text{tag+probe}}_{Z\to e^+e^-}$. While the other electron is considered as "probe" for which the efficiency is determined. Hence, the efficiency is defined as the fraction of events where "probe" electron also satisfy the tight requirements.

$$\epsilon^{\ell}_{W} = \frac{N^{\text{tag+probe}}_{Z\to e^+e^-}}{N^{\text{tag}}_{Z\to e^+e^-}}, \tag{6.11}$$

where $N_{Z\to e^+e^-}^{\text{tag+probe}}$ are number of events containing both "tag" and "probe" electrons passing the tight cuts. To avoid the trigger biases in the efficiency ϵ_W^ℓ estimation caused by the changes in trigger definitions, it is measured separately for various data collecting periods as listed in Table 6.7. Possible background contribution to the reconstructed $Z \to e^+e^-$ events from the QCD interactions is negligibly small and ignored. Figure 6.9 shows the electron selection efficiency as a function of the electron p_T. There is drop in the efficiency with the increasing p_T of electron measured by the calorimeter which is caused by the E_T/p_T matching requirement along with the spatial matching in the electron track measured by the central tracking system and the EM cluster. Here E_T refers to the transverse energy measured by the calorimeter and p_T refers to the transverse momentum of the matched track measured by the central tracking system. An electron producing bremsstrahlung radiations loses energy. The minimum p_T required for the matched track in the central system is 10 GeV, which is relatively small compared to the minimum electron E_T measured by the calorimeter. This difference in the thresholds makes E_T/p_T matching worse as electron gets higher E_T.

The size of multijet background in the inclusive W + jets data sample, N_{MJ}^ℓ, before imposing the tight selection for electron, is computed from Eq. 6.7. The numbers of inclusive W + jets candidates before and after imposing the tight restrictions are given in Table 6.7 for the respective data taking periods. The multijet background size extracted from the data sample before the tight cuts are applied, a mixture of real W + jets and multijet background, is given in Table 6.8. Estimated multijet background, $\epsilon_{MJ}^e \times N_{MJ}^\ell$, in the final W + jets sample is given in this table for different run periods which sums up to 2651.6 ± 64.1. The fraction, f_{MJ}^e, of multijet events that contribute to the signal is given by

$$f_{MJ}^e = \frac{\epsilon_{MJ}^e \times N_{MJ}^e}{N_T^e}, \tag{6.12}$$

where $N_T^e = 82747$. Thus, the estimated mean of the multijet background fraction is $f_{MJ}^e = 0.032 \pm 0.001(\text{stat})$.

Electron mis-identification rate, efficiency and W + jets candidates				
Periods	ϵ^e_{MJ}	ϵ^e_W	N^e_L	N^e_T
< 173101	0.126 ± 0.002	0.847 ± 0.007	3642 ± 60	2513 ± 50
$173516 - 178721$	0.125 ± 0.002	0.825 ± 0.005	9086 ± 95	6047 ± 78
$178722 - 194568$	0.154 ± 0.001	0.819 ± 0.003	26194 ± 161	19182 ± 139
$194569 - 208122$	0.151 ± 0.001	0.817 ± 0.002	40492 ± 201	29312 ± 171
$208204 - 210711$	0.149 ± 0.001	0.805 ± 0.004	15956 ± 126	11203 ± 106
> 210835	0.100 ± 0.001	0.797 ± 0.004	23036 ± 152	14626 ± 120

Table 6.7: Electron mis-identification rate, $\epsilon^e_{\rm MJ}$, electron efficiency, ϵ^e_W, for passing the cuts $P_{trk}(\chi^2) > 0.01$ and $LH_e > 0.85$. Event yields N^e_L and N^e_T in the W+jets data sample corresponds to the selection before and after the stricter cuts are imposed. The first column is for the run ranges corresponding to the periods when no substantial changes in the electron trigger requirements were made.

Due to small dependence of the electron selection efficiency on the electron p_T, the extracted fraction f^e_{MJ} of the multijet background contributed to the final W + jets sample has small dependence on the electron p_T. Table 6.9 shows the estimated f^e_{MJ} for various p_T regions of electron. To account for the effect of the electron p_T dependency, the deviation from the average value of the estimated multijet background fraction is assigned as a 16% systematic uncertainty on the estimation. Additionally, a conservative uncertainty of 20% is assigned covering the systematics effects due to the presence of signal events in the Jet-EM sample. After incorporating the systematic uncertainties, the estimated f^e_{MJ} becomes $0.032 \pm 0.001 \pm 0.008$.

Multijet background in muon channel:

The multijet background contributed to the inclusive $W(\rightarrow \mu\nu)$+jets sample is mainly from the misidentified isolated muon. In the $c\bar{c}$ or $b\bar{b}$ production the b or c quarks can decay semileptonically into muon that could possibly leave the reconstructed jet cone and could pass the muon isolation restrictions with a small probability. Such events can also fulfill the requirements of presence of $\not\!\!E_T$ in the events above a minimum threshold. The requirement of the distance of closest approach of the muon track with respect to the primary vertex suppresses large fraction of such background. The remaining contribution is measured using

Computed N^e_{MJ}, N^e_W, $\epsilon^e_{MJ} \times N^e_{MJ}$ and $\epsilon^e_W \times N^e_W$				
Periods	N^e_{MJ}	N^e_W	$\epsilon^e_{MJ} \times N^e_{MJ}$	$\epsilon^e_W \times N^e_W$
< 173101	792.8 ± 77.1	2849.1 ± 58.2	100.0 ± 9.9	2413.0 ± 53.4
$173516 - 178721$	2071.9 ± 121.8	7014.1 ± 93.8	258.7 ± 15.5	5788.3 ± 85.2
$178722 - 194568$	3432.9 ± 215.8	22761.1 ± 172.0	528.5 ± 33.4	18653.5 ± 155.6
$194569 - 208122$	5677.6 ± 265.2	34814.4 ± 210.2	855.2 ± 40.2	28456.8 ± 189.0
$208204 - 210711$	2499.0 ± 166.3	13457.0 ± 132.9	372.5 ± 25.0	10830.5 ± 118.6
> 210835	5350.5 ± 195.7	17685.5 ± 154.6	536.7 ± 20.1	104089.3 ± 139.7

Table 6.8: Estimated size of the multijet background, N^e_{MJ} and $\epsilon^e_{MJ} \times N^e_{MJ}$, before and after the tight cuts ($P_{trk}(\chi^2) > 0.01$ and $LH_e > 0.85$) are applied to the inclusive $W +$ jets samples. The number of real $W +$ jets events determined from the matrix method are given in the third and fifth columns for electron with and without tight criteria respectively. The first column is for the run ranges corresponding to the periods when no substantial changes in the electron trigger requirements were made.

Dependence of the multijet background fraction, f^e_{MJ}, on electron p^e_T			
p^e_T GeV	N^e_T	$\epsilon^e_{MJ} \times N^\ell_{MJ}$	f^e_{MJ}
20–30	17085 ± 130.71	884.3 ± 37.4	0.052 ± 0.002
30–40	32662 ± 180.726	966.4 ± 38.8	0.030 ± 0.001
40–50	24761 ± 157.356	512.7 ± 30.4	0.021 ± 0.001
50–60	14421 ± 120.087	259.3 ± 23.1	0.018 ± 0.002
60–200	9294 ± 96.4054	359.3 ± 34.0	0.039 ± 0.004

Table 6.9: Multijet fraction f^e_{MJ} in the final $W +$ jets sample that is estimated from the data sample. All errors quoted here are statistical. The multijet background decreases with increasing p_T of electron. In the very high p_T region [60-200], a relatively small increment in the estimated f^e_{MJ} indicates the contamination of the $Z \to e^+e^-$.

the similar matrix method as applied for the electron channel.

The probability to fake a muon from a jet is determined using a data sample, denoted as "Jet-MU" sample that comprises events containing a muon and jet separated by an azimuthal angle $\Delta\phi(\mu, \text{jet}) > 2.84$. The $\not\!\!E_T$ in these events is restricted to be less than 10 GeV to ensure a di-jet sample where the muon coming from decay of heavy flavor quarks or in-flight $\pi^{\pm}$ and $K^{\pm}$ satisfies the isolation requirements. The selection cuts described in Secs. 6.1 and 6.2 are applied to the muon and jets except that the restriction on the muon isolation is loosened. The muon is required to be separated from the jet axis formed by the closest jet by $\Delta R(\mu, \text{jet}) > 0.5$, while the E_T^{halo} and $p_T^{trkHalo}$ variables remain unrestricted. Fraction of these selected events satisfying the additional isolation restrictions determines the muon fake rate defined as

$$\epsilon_{MJ}^{\mu} = \frac{N_{\text{Jet-MU}}^{T}}{N_{\text{Jet-MU}}^{L}}, \tag{6.13}$$

where $N_{\text{Jet-MU}}^{L}$ denotes the number of events with the application of loose requirements to the muon in the "Jet-MU" sample, and $N_{\text{Jet-MU}}^{L}$ is the number of events in the subset of "Jet-MU" data sample where the muon also satisfies the restrictions on E_T^{halo} and $p_T^{trkHalo}$ as described in Sec. 6.1. Due to approximate uniformity of the restriction imposed by the single muon triggers over the various data taking periods, the ϵ_{MJ}^{μ} has negligibly small dependence on the run numbers. However this has large dependence on the muon p_T, as shown in Figure 6.10. The average value of ϵ_{MJ}^{μ} is 0.485 ± 0.004(stat.). There are $N_L^{\mu} = 63932$ events in the $W(\rightarrow \mu\nu) + \text{jets}$ candidates sample passing all requirements before imposing the muon isolation restriction. After imposing the isolation requirement, $N_T^{\mu} = 59100$ events survive in this sample.

The efficiency of the muon passing the isolation criteria is determined from the $Z \rightarrow \mu^+\mu^-$ sample using the "tag and probe" method. The average estimated efficiency is $\epsilon_W^{\mu} = 0.961 \pm 0.001$(stat.). Figure 6.11 shows dependency of this efficiency on the muon p_T, detector η and ϕ. Using the Eq. 6.8, the estimated multijet background contributed to the final sample of $W + \text{jets}$ is $\epsilon_{MJ}^{\mu} \times N_{MJ}^{\mu} = 2401 \pm 178$ events. This implies that the

fraction of background from the misidentified muon events in the final $W+$jets sample is $f^{\mu}_{MJ} = 0.041 \pm 0.003$(stat.). A conservative uncertainty of 50% associated with the muon p_T systematics is assigned to the factor f^{μ}_{MJ}. Due to the presence of the signal events in the Jet-MU sample used to estimate the misidentified muon, a variation of 20% is possible in the estimated f^{μ}_{MJ} which is assigned as an additional systematic uncertainty. Because of small multijet background size, these seemingly large uncertainties do not contribute drastically into the total uncertainties of inclusive $W+$jets events extracted from data. After incorporting all systematic uncertainties, the estimated multijet fraction amounts to $f^{\mu}_{MJ} = 0.041 \pm 0.003(\text{stat.}) \pm 0.029(\text{syst.})$.

6.3.2 Z+jets background

The Z boson production associated with jets can form a background to the inclusive $W+$jets production, if one of the lepton from Z boson decay is not reconstructed or missed by the detector. This missing lepton is reconstructed as the missing transverse momentum and produces the topology of $W+$jets events.

It is not uncommon for one of the muon from Z boson to be missed by the detector in the region where $4.25 < \phi < 5.15$ and $|\eta| \lesssim 1.1$, and contribute as the $\not\!\!E_T$ of the event. Due to relatively smaller detector acceptance for the muon compared to that of the electron, the contribution of $Z(\rightarrow \mu^+\mu^-)+$jets background production is expected to be relatively larger than the $Z(\rightarrow e^+e^-)+$jets background in the electron channel.

6.3.3 Estimation of the background size

An estimate of the size of the $Z+$jets background follows from ALPGEN and PYTHIA simulations of $Z+$jets production. The fraction, f^{ℓ}_{Z} where $\ell = e, \mu$, of $Z+$jets events that pass the requirements imposed for $W+$jets selection is defined as

$$f^{\ell}_{Z} = \frac{N_{Zj}}{N_{Wj} + N_{Wc\bar{c}} + N_{Wb\bar{b}} + N_{Wc} + N_{Zj}}, \tag{6.14}$$

where N_{Zj} represents the number of selected inclusive Z + jets events including the contributions from $Z + c\bar{c}$ and $Z + b\bar{b}$ processes. The N_{Wj}, $N_{Wc\bar{c}}$, $N_{Wb\bar{b}}$ and N_{Wc} denote MC predictions of W + light-jet, $W + c\bar{c}$, $W + b\bar{b}$ and $W + c$-jet productions, respectively, that satisfy the selection cuts. The contributions from the $t\bar{t}$ and WW are negligibly small and ignored. Events yields from ALPGEN and PYTHIA simulations for individual processes are given in Table 6.6. In the electron channel this fraction is estimated to be $f_Z^e = 0.009 \pm 0.001$(stat) and in the muon channel it is $f_Z^\mu = 0.050 \pm 0.001$(stat). The systematic uncertainties are dominated by the relative cross section uncertainties for each process. The production cross section uncertainties relative to the Z + jets production is assigned to be 15% for W + light-jet, 50% for the $W + c\bar{c}$, $W + b\bar{b}$ and $W + c$ relative to W + light-jet. Varying the cross section of individual processes by their uncertainties gives an estimate of 13% uncertainty on the fraction f_Z^ℓ. Adding the statistical and systematic uncertainties in quadrature gives the estimate of $f^e = 0.009 \pm 0.001$ for the $Z(\rightarrow e^+e^-)$+jets fraction and $f^\mu = 0.050 \pm 0.007$ for the $Z(\rightarrow \mu^+\mu^-)$ + jets fraction in the final W + jets candidates.

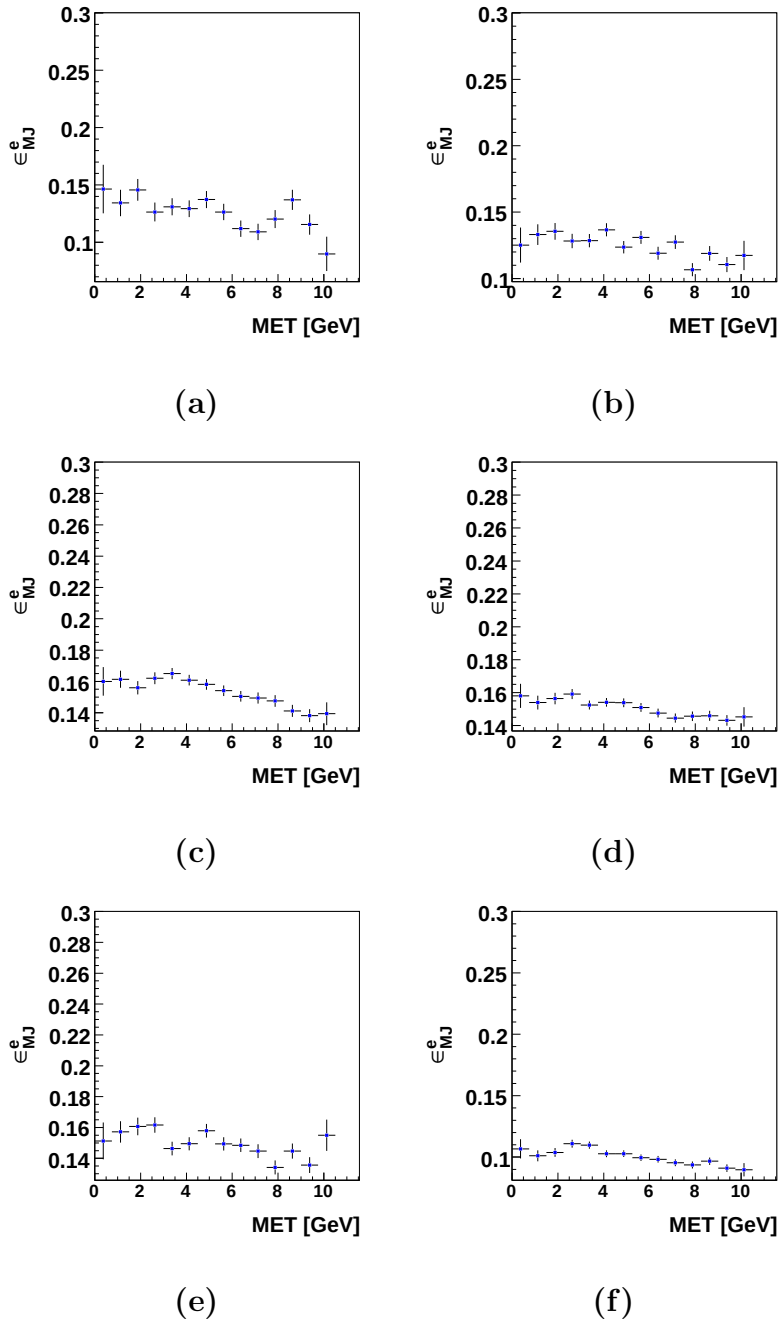

Figure 6.7: The electron mis-identification rate estimated from Jet-EM data sample as a function of $\not\!\!E_T$, (a) run range [< 173101], (b) run range [173516-178721], (c) run range [178722-194568], (d) run range [194569-208122], (e) run range [208204-210711], (f) run range [> 210835].

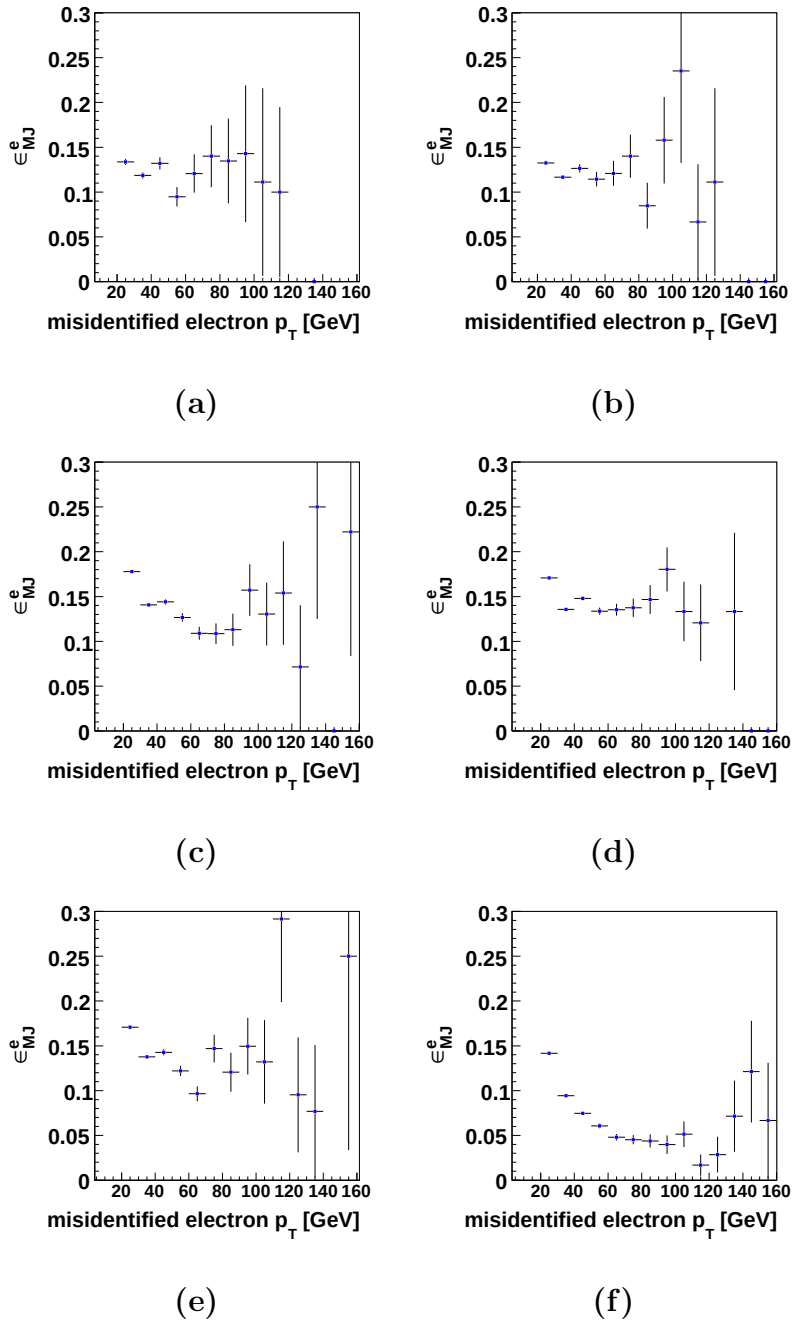

Figure 6.8: The electron mis-identification rate estimated from Jet-EM data sample as a function of p_T^e, (a) run range [$<$ 173101], (b) run range [173516-178721], (c) run range [178722-194568], (d) run range [194569-208122], (e) run range [208204-210711], (f) run range [$>$ 210835].

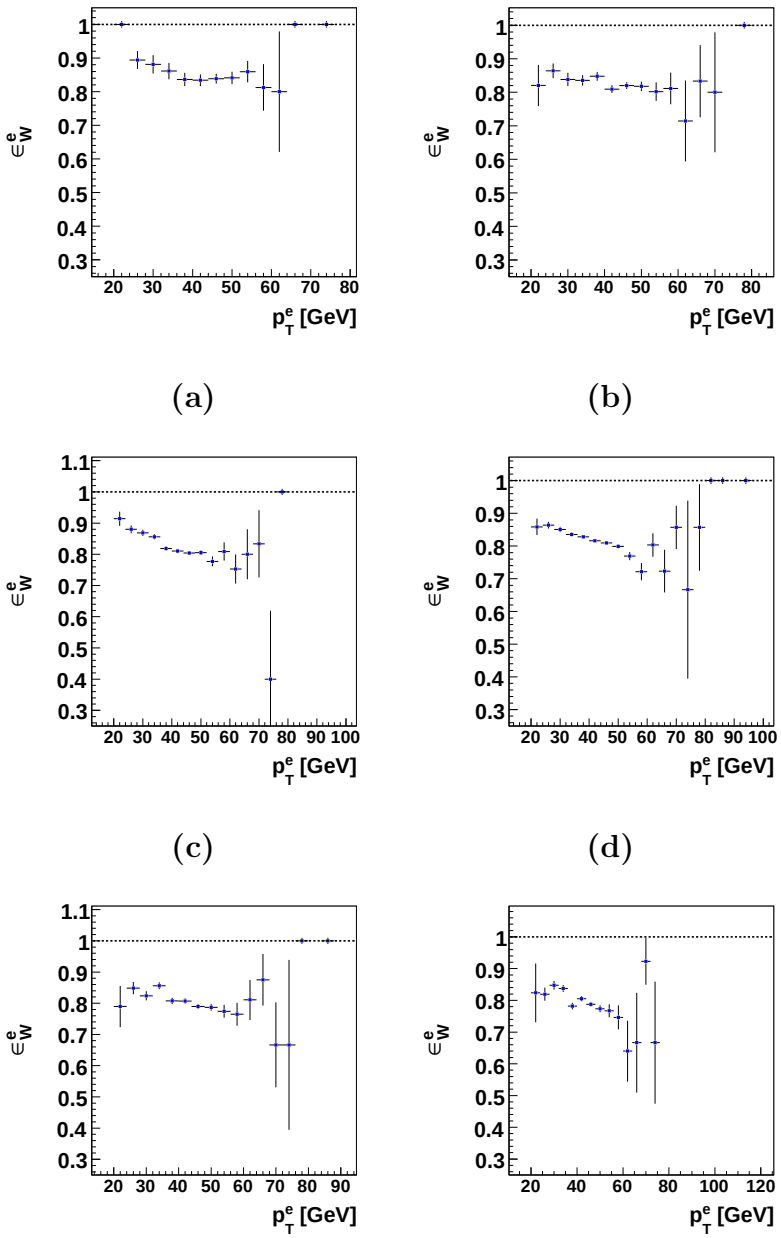

Figure 6.9: The electron selection efficiency estimated from $Z \rightarrow e^+e^-$ data sample as a function of p_T^e, (a) run range [< 173101], (b) run range [173516-178721], (c) run range [178722-194568], (d) run range [194569-208122], (e) run range [208204-210711], (f) run range [> 210835].

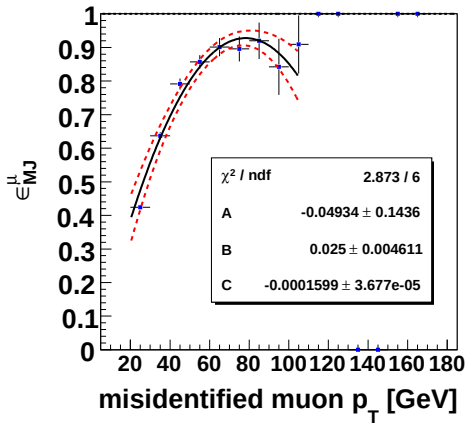

(a)

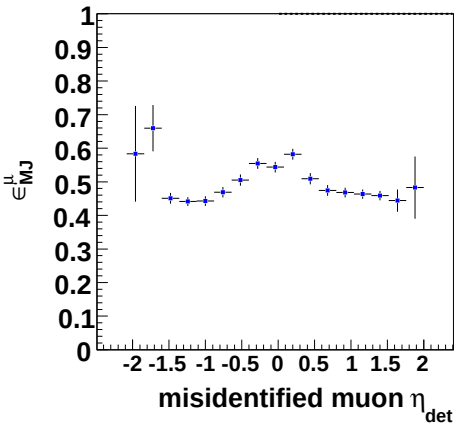

(b)

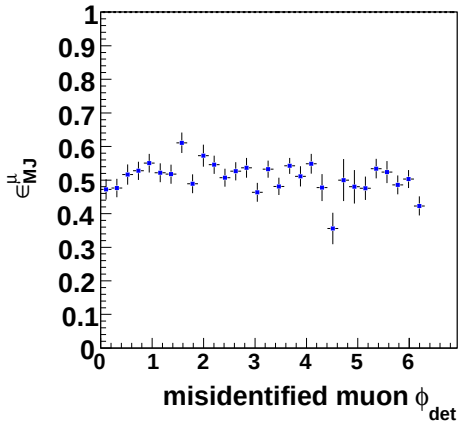

(c)

Figure 6.10: The muon misidentification rate estimated from "Jet-MU" data sample, (a) function of muon p_T, (b) function of detector η, (c) function of detector ϕ.

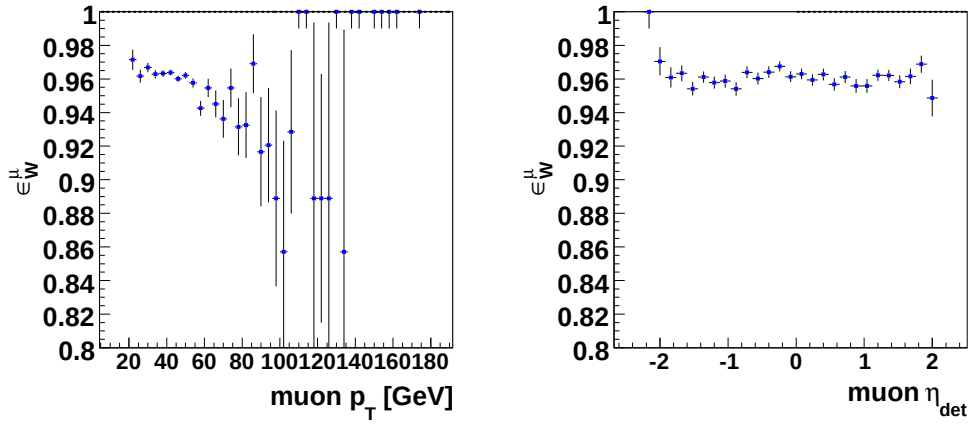

(a) (b)

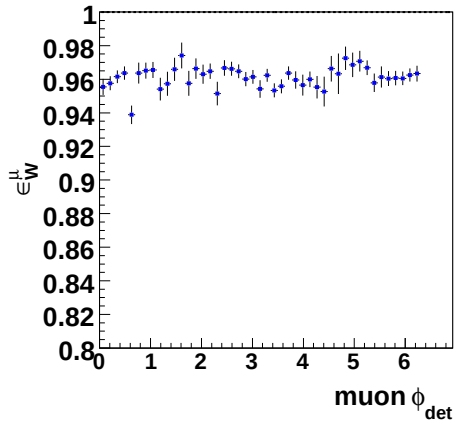

(c)

Figure 6.11: The muon isolation efficiency estimated from "Jet-MU" data sample, (a) function of muon p_T, (b) function of detector η, (c) function of detector ϕ.

Chapter 7

$W+c$ Selection

This chapter describes the strategy to select the $W+c$ final state out of an inclusive W+jets data sample. The selection begins with the data sample that enrich in jets initiated by the heavy flavor quarks.

7.1 Heavy Flavor Jets

A jet originated from b or c quark is known as heavy flavor jet, because b and c flavored quarks carry higher masses compared to the u, d, s quarks. A quark is said to be heavy if its Compton wavelength, $\frac{1}{m_Q}$, is much greater than the inverse of hadronic radius ($\approx \frac{1}{200}$ MeV^{-1}). It is however difficult in practice to tell whether b or c quark initiated the jet. The heavy flavor (HF) jets are identified based on the characteristics of b and c quarks, such as high mass and longer lifetime. Particle with relatively longer lifetime travels relatively larger distance within the detector before it decays. Secondary vertices can be constructed with good resolutions from the tracks of the daughter particles. The small pitch (about 0.05 mm) of the silicon detectors allows the identifications of jets initiated by the relativistic b or c quarks, if the distance between the reconstructed secondary decay vertex and the primary interaction vertex is over 2 mm.

In the MC simulation, a jet is labeled as b-jet, c-jet or light-jet depending on whether it contains b, c or light($udsg$) partons or hadron collinear with the jet axis. The efficiencies of reconstruction and identification of a HF or light jet are studied in the simulation and

applied to the data. A jet satisfying the specific requirements based on the heavy flavor quark properties is tagged. The tagging efficiency of b- (c-, light-) jet is defined as the ratio of the number of tagged b- (c-, light-) jet to the total number of b- (c-, light-) jet.

$$\epsilon^{tag} = \frac{N_{jet}^{tag}}{N_{jet}}. \tag{7.1}$$

7.2 Muon Tagging of Heavy Flavor Jets

A muon identified within the jet cone signifies the presence of the c or b quark that initiated the jet. A b quark either decays directly into a muon with branching fraction of $BF(b \to \mu) = 10\%$ or via a cascade decay with $BF(b \to c \to \mu) = 10\%$. Hence total probability for a b quark to decay into a muon is about 20%. The c quark on the other hand decays only directly with the $BF(c \to \mu) = 10\%$. Higher probability of b quarks to decay into muon leads to higher efficiency to tag a b-jet than a c-jet. Therefore, it is difficult to directly tell about a heavy flavor jet containing a muon denoted as "μ-tagged jet" whether the jet was originiated via a b quark or a c quark. To perform the extraction of the number of W+c-jet events, one must develop a method to discriminate a c-jet from b-jet. Section 7.3 discusses the feature of W+c-jet used in this analysis to discriminate c-jet final state in conjunction with W.

There are other sources of μ-tagged jets from the $\pi^{\pm}$ or $K^{\pm}$ decays in the jet. The charged pions and kaons have lifetimes of 2.6×10^{-8} s and 1.2×10^{-8} s, respectively, which are longer than the lifetimes of the b or c quarks by about four orders of magnitude. These particles decays into muon via the processes: $\pi^+ \to \mu^+\nu$ ($\pi^- \to \mu^-\bar{\nu}$) and $K^+ \to \mu^+\nu$ ($K^- \to \mu^-\bar{\nu}$). In their rest frame the mean distance traveled by these particles before they decay is 7.8 m for $\pi^{\pm}$ and 3.7 m for $K^{\pm}$. Hence, in the detector frame of reference these relativistic particles have very small probability to decay within the finite radius of 53 cm covered by the tracking detector. However, this probability enhances with the increase in the detector radius, and becomes larger if full finite size of the detector before arriving at the muon detecting system is considered for the possibility of muons from the decays of

these particles. At the same time, it is worth noticing that the production probabilities of light flavored quarks (and hence the light hadrons $\pi^{\pm}$ and $K^{\pm}$) is two to three orders of magnitude larger than the heavy flavored quarks. The net contribution to the μ-tagged jets from the light-jets is therefore appreciable and must be correctly estimated. Section 7.4.1 describes the efficiency of the μ-tagged jets in light-jet, c-jet and b-jet.

7.3 Discrimination of W+c-jet Process

As the kinematics of a heavy flavor jet recoiling against a W boson are identical in general to that of a light flavored jet, one has to look at the decay properties of heavy flavor to distinguish a c- or b-jet from light- ($udsg$) jets. In the presented analysis a μ-tagged jet is used as an indicator of heavy flavor jets. This information alone is not sufficient to distinguish a c-jet from a light flavored jet where pions and kaons decay into the muon, or from a b-jet where $b \rightarrow \mu$ probability is double that of $c \rightarrow \mu$. The necessary information that will allow to extract the number of W+c-jet candidates from an inclusive sample of W + μ-tagged jet is the correlation between the muon charge from jet compared to the isolated lepton from W boson. A key characteristics of W+c-jet process is that the charm quark decays into a muon carrying an opposite-sign charge compared to that carried by the W boson, and the number of OS and SS events, N_{OS} and N_{SS}, respectively, satisfy $N_{OS} \gg N_{SS}$. There are physics and experimental sources of background contributing to the charge correlated final state as discussed in Secs. 7.3.1 and 7.3.2, respectively.

The following set of selection criteria is imposed to the inclusive sample of W + jets to select a μ-tagged jet in association with the reconstructed W boson. The μ-tagged jet must have a minimum JES calibrated p_T of 20 GeV before any correction due to the missing energy of muon and neutrino is imposed on the jet. A muon in the jet denoted as "jet-muon" is identified if it satisfies the requirements as itemized below.

- Muon must have at least two wire hits in the BC-layer and at least one scintillator hit in the BC-layer, except in the region not covered by these layers at the bottom

$(4.25 < |\phi| < 5.15)$ of the detector due to the support structure.

- Muon must pass cosmic veto based on the timing requirements on the A, B or C-layers. To further suppress the cosmics, the muons must satisfy that the distance of closest approach in the transverse plane is less than 0.16 cm.

- The transverse momentum of the muon must satisfy $p_T > 4$ GeV.

- The $|\eta|$ of the muon must be less than 2.0, according to the outermost muon system coverage.

- A central track is spatially matched with the BC track segment in the local muon system, and the p_T of the track measured in the central tracking system should be within 15 GeV of that determined from the global fit of the p_T measured by the central tracking and local muon system.

- The region ($4.25 < \phi < 5.15$ with $|\eta| < 1.1$) not covered by the local muon systems is inefficient, therefore muons produced in this region are simply removed.

- In the $W \rightarrow \mu\nu +$ jet sample, an additional cut is imposed to veto the $Z \rightarrow \mu^+\mu^-$ background by requiring the invariant mass, $M_{\mu\mu}$, of two final state muons (one is isolated and the other is "jet-muon") to be less than 70 GeV. Figure 7.1 illustrates the contribution to the OS events from $Z \rightarrow \mu^+\mu^-$ events in the high $M_{\mu\mu}$ region. The production cross section of the low mass Drell-Yan background decreases with the increase in the p_T of leptons and is predicted to not to contribute to the signal from the ALPGEN and PYTHIA. With this veto, the Z background could still have residual contribution to the $W+c$-jet signal due to the resolution effects of the Z mass. However, these events have no physical $\not\!\!E_T$, therefore such contribution is suppressed by $\not\!\!E_T$ restriction of at least 20 GeV. Further suppression is made by restricting the azimuthal angular separation, $\Delta\phi$, between the isolated muon from W boson and the $\not\!\!E_T$ in event to be greater than 0.4, as mentioned earlier in previous chapter in Sec. 6.1.

As an illustration, Fig. 7.2 shows the distribution of $\Delta\phi(\mu, \not\!\!E_T)$ peaking around zero specifically in the case where the charges of two muons are opposite (OS events), after imposing all cuts as mentioned so far except that the restriction on $\Delta\phi(\mu, \not\!\!E_T)$ is removed. The excess in data in the peak region may also reflect a small presence of the low invariant mass Drell-Yan background contribution. The MC simulation, however, shows the contribution from Drell-Yan to be negligibly small. Beyond the region $|\Delta\phi(\mu, \not\!\!E_T)| > 0.4$, the data has good agreement with the total MC expectations indicating that the Drell-Yan background is indeed negligibly small.

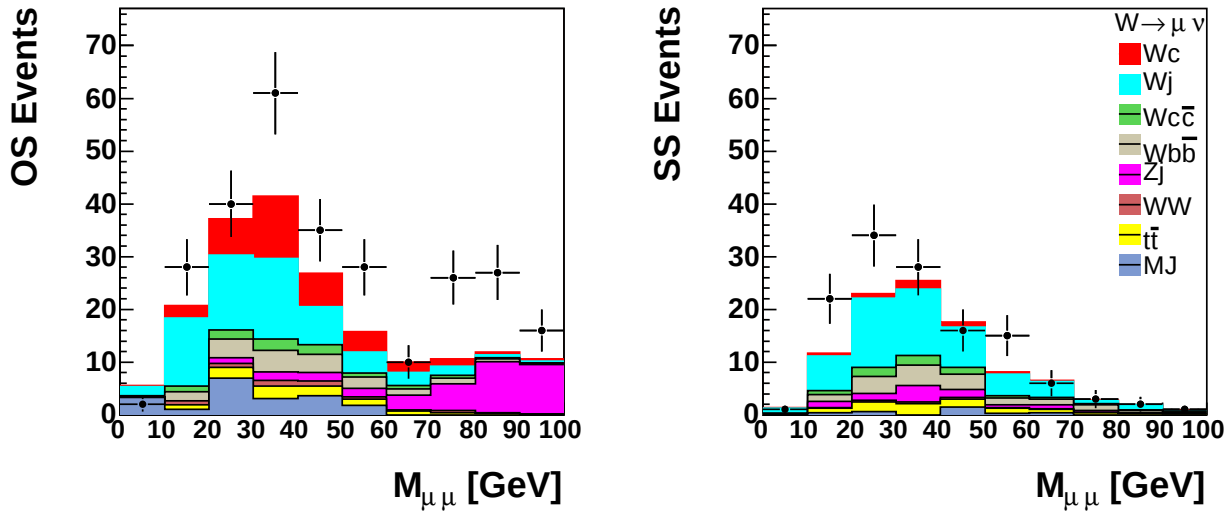

Figure 7.1: The distribution of invariant mass, $M_{\mu\mu}$, of two final state muons in the $W(\rightarrow \mu\nu)$+μ-tagged jet sample before the cut $M_{\mu\mu} < 70$ GeV cut. The restriction on high invariant mass of two muons suppresses the Z background. Events with the isolated muon charge opposite (equal) to that the muon present in the jet, OS events (SS events), are shown on the left (right) side. The total MC prediction is the sum of the expectations from the $W + c$-jet, $W +$ light-jet, $W + c\bar{c}$, $W + b\bar{b}$, $Z +$ jets, WW, $t\bar{t}$ productions processes estimated from ALPGEN-PYTHIA and the QCD jet productions estimated from the data sample as described in Sec. 7.3.2.

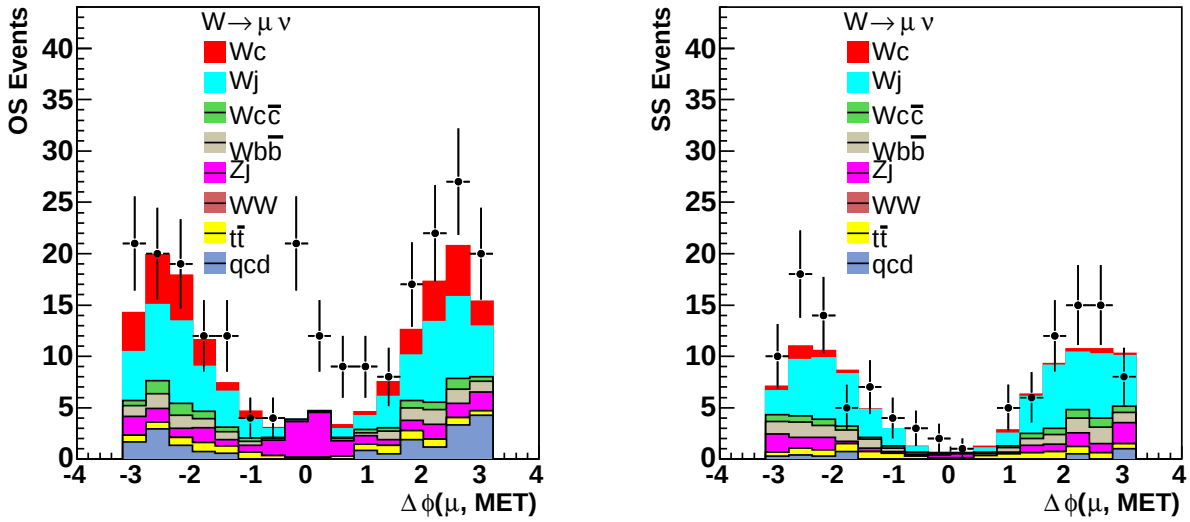

Figure 7.2: The $\Delta\phi(\mu, \not\!\!E_T)$ distribution in the $W(\rightarrow \mu\nu)$+μ-tagged jet sample before $\Delta\phi(\mu, \not\!\!E_T) > 0.4$ cut. The restriction on $\Delta\phi(\mu, \not\!\!E_T) > 0.4$ suppresses the experimental background and the physics Drell-Yan background. Events with the isolated muon charge opposite (equal) to that the muon present in the jet, OS events (SS events), are shown on the left (right) side. The total MC prediction is the sum of the expectations from the $W+c$-jet, $W+$light-jet, $W+c\bar{c}$, $W+b\bar{b}$, $Z+$jets, WW, $t\bar{t}$ productions processes estimated from ALPGEN-PYTHIA and the QCD jet productions estimated from the data sample as described in Sec. 7.3.2.

7.3.1 Physics background sources to W+c-jet

In the vector boson+jets physics processes (W+g, W+$c\bar{c}$, W+$b\bar{b}$, Z+jets) not involving a single charm recoiling against W boson, the charge of the jet-muon is uncorrelated with the charge of W boson. However, processes with light quark (u, d or s) initiated jets recoiling against the W boson can produce a small fraction of charge-correlated μ-tagged jets owing to leading particle effects [87]. There are other physics processes such as WW, $t\bar{t}$, $t\bar{b}$, W+$b\bar{c}$ and W+b that contribute to the charge correlated final state. The WW process has the highest cross section among these background processes, and amounts to about 5% level contribution. Other processes contributions are supressed by small production cross sections or tiny CKM matrix elements as given in Sec. 2.2. The MC simulation of

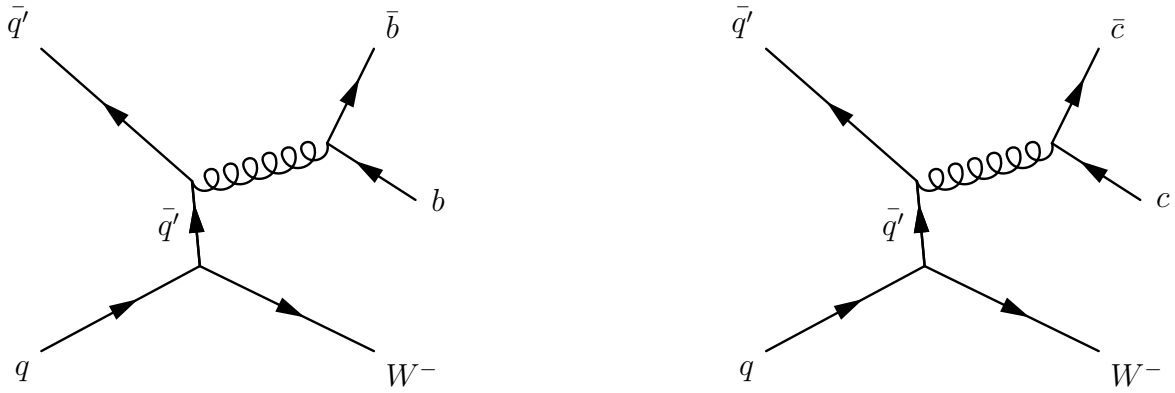

Figure 7.3: $q\bar{q}' \to Wb\bar{b}$ and $q\bar{q}' \to Wc\bar{c}$ Feynman diagrams.

Figure 7.4: A few possible Feynam diagrams contributing to the $Z+$jets final state.

ALPGEN and PYTHIA is used to estimate the size of WW, $t\bar{t}$ in OS and SS case. Tables 7.1 and 7.2 list the estimated contributions in the electron and muon channels, respectively. An estimation of single top background production in the OS and SS sample is made from the events generated by COMPHEP [34] followed by full detector simulation and reconstruction. The uncertainties in the prediction of WW, $t\bar{t}$ and the single top production is dominated by the uncertainties on the measured cross sections [88–90]. The contributions from $W+b\bar{c}$ and $W+b$ are expected to be negligibly small and simply ignored. The distribution of the μ-tagged jet is shown in Figs. 7.8 and 7.9 for the electron and muon channels, respectively, for a comparison of the observed events with the expectations in OS and SS cases. The data is in reasonable agreement with the theoretical expectation. A small deviation in data

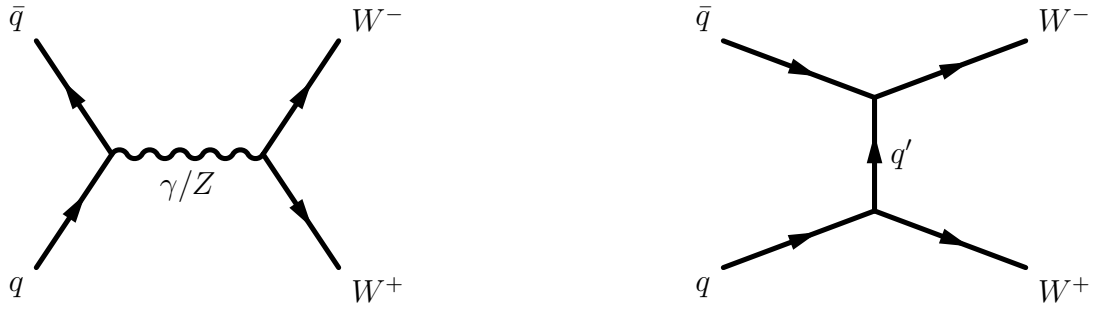

Figure 7.5: Possible Feynman diagrams at LO for W^+W^- production. The intermiate propagator is a boson on the left hand side and a quark fermion on the right hand side.

Figure 7.6: $t\bar{t}$ pair production and single top production subprocesses.

from the theoretical expectations in the first p_T bin is due to the p_T resolution effect of the μ-tagged jet.

Residual charge-correlated background from W+light-jet processes:

In the W + light-jet sample, the light quark-jets initiated by the u, d, s partons recoiling against the W boson have charge correlated particles ($\pi^{\pm}$ and $K^{\pm}$) with the W boson charge in case of no fragmentation effect. Hence a light-jet consisting of the shower of collinear pions and kaons being tagged as a μ-tagged jet, if π/K decay into the muon within the radial distance up to the calorimeter (90 cm), could contribute to the signal W + c-jet. It is worth noticing that in the calorimeter region the particles lose their energy rather quickly, and hence their momenta is not enough to allow them to decay into the muon

Selected $W(\rightarrow e\nu)$+μ-tagged jet events in data and MC		
Process	OS events	SS events
$W+c$-jet	58.7 ± 3.2	5.6 ± 0.9
$W+c\bar{c}$	15.8 ± 1.1	14.6 ± 1.1
$W+b\bar{b}$	24.5 ± 0.8	23.6 ± 0.8
$W+$light-jet	97.4 ± 3.8	84.4 ± 3.4
$Z+$jets	0.9 ± 0.3	1.6 ± 0.5
WW	6.2 ± 0.4	1.9 ± 0.2
$t\bar{t}$	18.3 ± 0.3	15.9 ± 0.3
single-top	6.3 ± 0.1	4.6 ± 0.1
MJ	13.3 ± 2.3	19.3 ± 2.9
Background-only prediction	176.3 ± 5.2	161.4 ± 4.7
Total prediction	235.0 ± 6.1	167.0 ± 4.8
Data	245	154

Table 7.1: Event yields in MC and data sample after the muon-tagged jet requirement in the $W(\rightarrow e\nu)+$jets sample.

Selected $W(\rightarrow \mu\nu)$+μ-tagged jet events in data and MC		
Process	OS events	SS events
$W+c$-jet	33.2 ± 2.2	4.6 ± 0.8
$W+c\bar{c}$	8.2 ± 0.7	6.2 ± 0.6
$W+b\bar{b}$	12.3 ± 0.5	12.6 ± 0.5
$W+$light-jet	60.8 ± 2.7	51.2 ± 2.5
$Z+$jets	12.2 ± 1.4	9.3 ± 1.2
WW	4.1 ± 0.3	1.2 ± 0.2
$t\bar{t}$	9.2 ± 0.2	8.1 ± 0.2
single-top	4.2 ± 0.1	3.0 ± 0.1
MJ	12.2 ± 4.6	8.8 ± 5.4
Background-only prediction	118.9 ± 5.6	97.4 ± 6.1
Total prediction	198.5 ± 6.0	102.0 ± 6.2
Data	203	122

Table 7.2: Event yields in MC and data sample after the muon-tagged jet requirement in the $W(\rightarrow \mu\nu)+$jets sample.

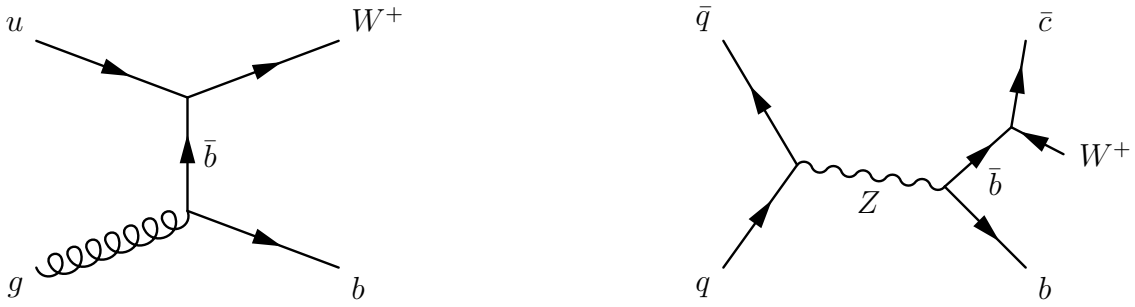

Figure 7.7: Possible diagrams for $W + b$ and $W + b\bar{c}$ processes. Contribution to these background processes is suppressed by small cross sections.

with $p_T > 4$ GeV. Therefore, contributions from decay are important only for tracks that decay before reaching the calorimeter. The fragmentation of the light flavored jets produces large number of pions and kaons and brings their momenta into an equilibrium as the total transverse momentum of the final state parton is distributed among all particles within the jet cone. This makes the average p_T of an individual particle to be small, and consequently reducing the probability of the particle to decay into the muon with a minimum p_T to be negligibly small. However, there is a leading particle effect that has been observed [87] by many experiments, which counteracts the fragmentation effect of light flavored jets to some extent, and enhances the probability of the highest p_T pion and kaon in the jet to decay into the muon with a minimum threshold. The highest p_T pion or kaon reflect the charge state of the leading order parton. Combining the fragmentation effect and the leading particle effect, the residual correlation between the leading π/K charges and the W boson charge is approximately 15%. The MC simulation allows to estimate the fractional size f_c^ℓ of the charge correlated events in the $W +$ light-jet sample. At DØ, only daughter particles produced from the decays within the tracking volume are stored into the truth particles bank, hence the information of the muon produced from the decay of π/K outside the tracking region can not be restored at the truth level. This issue is resolved by considering all π/K with minimum $p_T > 4$ GeV produced in the light quark initiated jets in the $W +$ light-jet sample and assigning weights equal to their decay and interaction

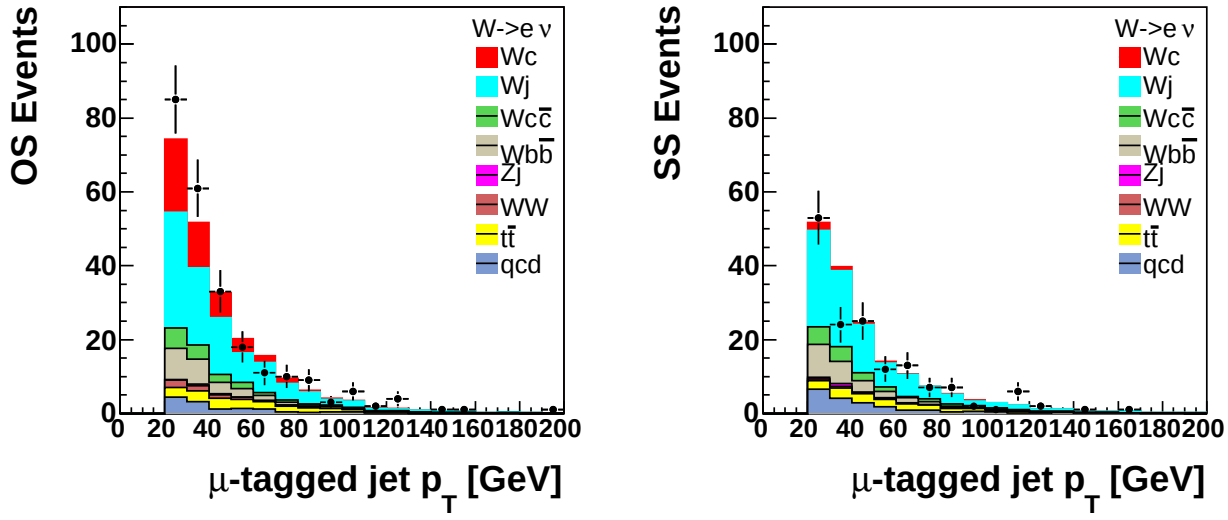

Figure 7.8: The jet p_T distribution of the μ-tagged jet in the $W(\rightarrow e\nu)$+μ-tagged jet sample after the final selection. Events with the isolated muon charge opposite (equal) to that the muon present in the jet, OS events (SS events), are shown on the left (right) side. The total MC prediction is the sum of the expectations from the $W+c$-jet, $W+$light-jet, $W+c\bar{c}$, $W+b\bar{b}$, $Z+$jets, WW, $t\bar{t}$ productions processes estimated from ALPGEN-PYTHIA and the QCD jet productions estimated from the data sample as described in Sec. 7.3.2.

probabilities before entering into the calorimeter. The f_c^ℓ is defined as

$$f_c^\ell = \frac{\int w_\pi(p_T) N_\pi^{\rm OS}(p_T) dp_T + \int w_K(p_T) N_K^{\rm OS}(p_T) dp_T}{\int w_\pi(p_T) N_\pi^{\rm SS}(p_T) dp_T + \int w_K(p_T) N_K^{\rm SS}(p_T) dp_T}, \tag{7.2}$$

where $w_\pi(p_T)$ and $w_K(p_T)$ denotes the p_T dependent weights for the pion and kaon respectively, and $N_\pi^{\rm OS}(p_T)$ $\left(N_\pi^{\rm SS}(p_T)\right)$ and $N_K^{\rm OS}(p_T)$ $\left(N_K^{\rm SS}(p_T)\right)$ represent the number of OS (SS) pions and kaons, respectively. A minimum energy of a π/K to reach the detector at a certain distance from the primary vertex is

$$p_{T;\pi/K}^{min} = reB, \tag{7.3}$$

where r is the cylindrical radius, e is the charge and B is magnetic field at DØ. The product of e and B is determined to be 0.003 GeV/cm at DØ. Thus for the π or K to reach a radial distance of 75 cm is required to be 0.225 GeV. There are some assumptions

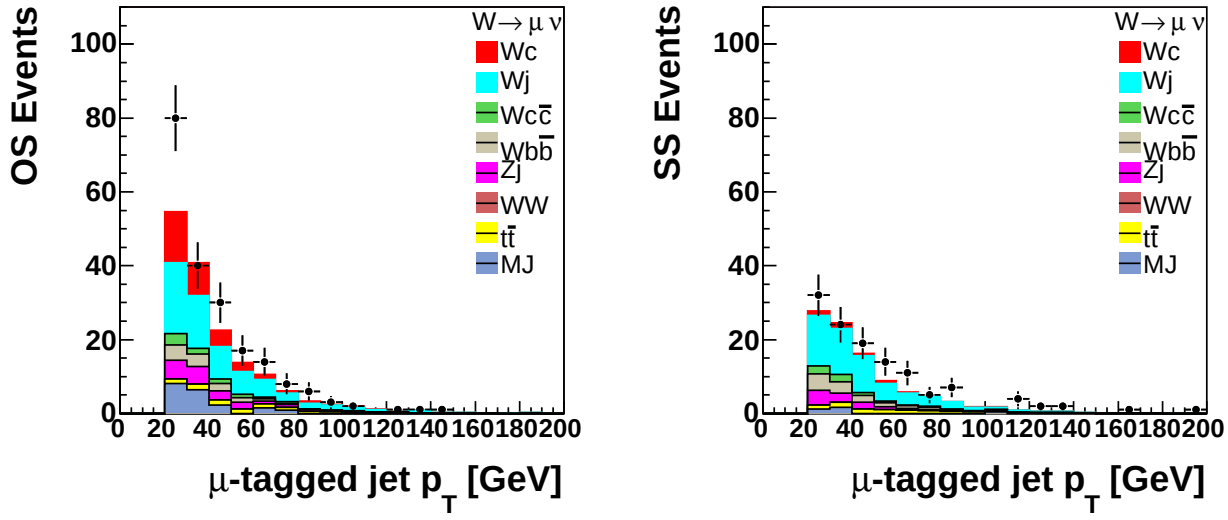

Figure 7.9: The jet p_T distribution of the μ-tagged jet in the $W(\rightarrow \mu\nu)$+μ-tagged jet sample after the final selection. Events with the isolated muon charge opposite (equal) to that the muon present in the jet, OS events (SS events), are shown on the left (right) side. The total MC prediction is the sum of the expectations from the $W + c$-jet, $W +$ light-jet, $W + c\bar{c}$, $W + b\bar{b}$, $Z +$ jets, WW, $t\bar{t}$ productions processes estimated from ALPGEN-PYTHIA and the QCD jet productions estimated from the data sample as described in Sec. 7.3.2.

made to the calculations of these weights, $w_\pi(p_T)$ and $w_K(p_T)$. These have only a small and conservative effect on the background estimate.

- The curvature of the high p_T pion and kaon tracks is assumed to be zero.
- These particles are assumed to transfer all of their energy to the muon after they decay.
- The maximum distance traveled by these particles in the transverse plane before they decay is considered to be 75 cm, out of which 53 cm distance is covered by the SMT and CFT tracker, and remaining by the solenoid and CPS detector.

Since the DØ detector is not homogeneous, the weights are derived separately for the pion and kaon produced and decayed in the regions upto the solenoid magnet. The weights for the π and K traversing some distances in the x-y plane with their final positions x_π and x_K,

respectively, within tracker region (where the probability of nuclear interaction negligibly is small) before they decayed are derived to be

$$w_\pi(p_T) = \left(1 - e^{\frac{-(x_\pi - x_\pi^o)}{c\tau_\pi \gamma_\pi}}\right), \tag{7.4}$$

$$w_K(p_T) = \left(1 - e^{\frac{-(x_K - x_K^o)}{c\tau_K \gamma_K}}\right) \times BF(K^+ \to \mu^+ \nu_\mu), \tag{7.5}$$

where x_π^o and x_K^o are the initial positions of these particles. The γ factors in the exponentials are the Lorentz factor $\left(1/\sqrt{1 - \frac{v^2}{c^2}}\right)$ which in the relativistic limit are equivalent to $\gamma_\pi = p_{T;\pi}/m_\pi$ and $\gamma_K = p_{T;K}/m_K$ for the pions and kaons moving in the transverse plane, respectively, where m_π, m_K, $p_{T;\pi}$ and $p_{T;K}$ are the masses and transverse momenta of the pions and kaons. More detailed description of the derivation of these weights is given in Appendix A. The branching fraction $BF(K^+ \to \mu^+ \nu_\mu)$ is 67%, compared to that of the $\pi^+ \to \mu^+ \nu_\mu$ decay [6]. Mean values of $c\tau$ have been measured to be $c\tau_\pi = 7.8$ m and $c\tau_K = 3.7$ m for the pion and kaons, respectively [6]. If these particles has traversed the distance beyond the tracking region but within the magnet region before they decay, the weights given by Eqs. 7.4 and 7.5 become

$$\begin{aligned} w_\pi(p_T) &= \left(1 - e^{\frac{-(53 - x_\pi^o)}{c\tau_\pi \gamma_\pi}}\right) \\ &\quad + \frac{\lambda_{sol}}{c\tau_\pi \gamma_\pi + \lambda_{sol}} \left(1 - e^{\frac{-(x_\pi - 53)}{c\tau_\pi \gamma}} e^{\frac{-(x_\pi - 53)}{\lambda_{sol}}}\right) e^{\frac{-(53 - x_\pi^o)}{c\tau_\pi \gamma_\pi}}, \end{aligned} \tag{7.6}$$

$$\begin{aligned} w_K(p_T) &= \left(1 - e^{\frac{-(53 - x_K^o)}{c\tau_K \gamma_K}}\right) \\ &\quad + \frac{\lambda_{sol}}{c\tau_K \gamma_K + \lambda_{sol}} \left(1 - e^{\frac{-(x_K - 53)}{c\tau_K \gamma}} e^{\frac{-(x_K - 53)}{\lambda_{sol}}}\right) e^{\frac{-(53 - x_K^o)}{c\tau_K \gamma_K}}. \end{aligned} \tag{7.7}$$

where λ_{sol} denotes the interaction length within the solenoid magnet material [91], which has 0.18 interaction lengths. These weights are applied to the pions and kaons carrying at least 4 GeV transverse momentum which are present in the light-jets within 0.5 cone radius around the jet axis. The factor f_c^ℓ is evaluated for both $W \to \mu\nu$ and $W \to e\nu$ decay modes. Figure 7.10 shows f_c^e and f_c^μ as a function of the jet p_T. As the sub-process $q\bar{q}' \to Wg$ dominates $qg \to Wq'$ at larger transverse momentum of the final state quark,

the deviation of the f_c^ℓ from unity reduces. The Wg final state essentially produces charge uncorrelated leptons.

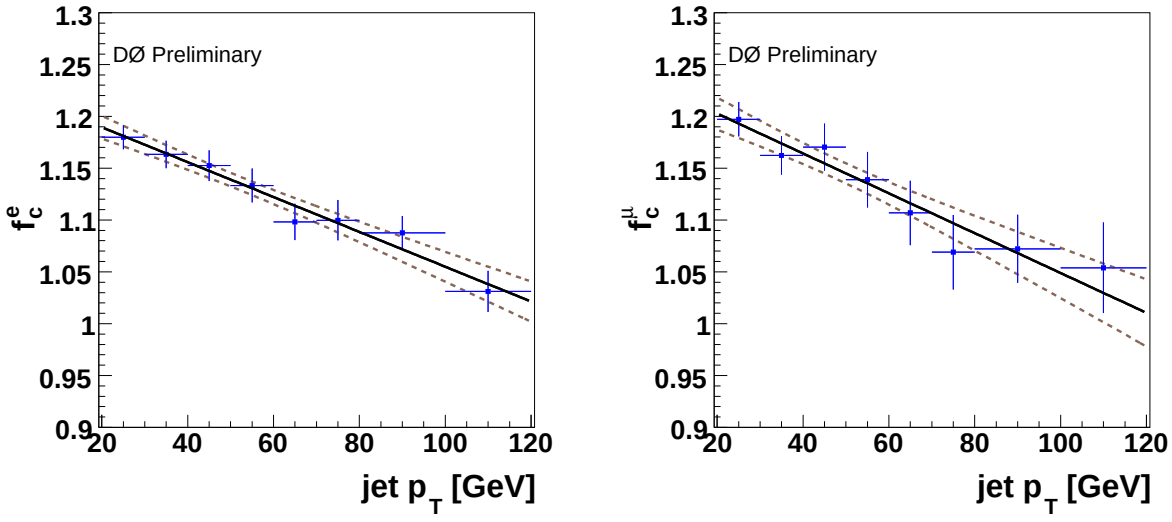

(a) (b)

Figure 7.10: The correction factor for the background contributed from the light quark-jet in the W+jets sample is shown as a function of fully corrected jet p_T at the particle level [92], (a) estimated from the $W(\rightarrow e\nu)$ + light quark-jets sample, $f_c^e = a_e + b_e \times p_T$, where $a_e = 1.223 \pm 0.016$ and $b_e = -0.0017 \pm 0.0003$, (b) estimated from the $W(\rightarrow \mu\nu)$+light quark-jets sample, where $a_\mu = 1.241 \pm 0.023$ and $b_\mu = -0.0019 \pm 0.0004$.

There are some systematic uncertainties associated with the estimation of f_c^ℓ, those are mainly due to the jet fragmentations, the relative fraction of the charged kaons to the pions, the relative cross section of the processes $W + c$-jet $W + b\bar{b}$, $W + c\bar{c}$, relative to the W+light-jets, and the PDFs. To estimate the sensitivity of the jet fragmentation, the data and MC predictions are compared for the ratio of the weighted number of reconstructed tracks, present in the jet cone, with charge opposite to that of the W boson to the weighted number of tracks, present in the jet cone, carrying charge equal to that of the W boson. Due to high p_T of selected tracks ($p_T > 4$ GeV), it is difficult to distinguish between pion and kaon tracks at DØ as can be seen from the energy loss distributions for $\pi^\pm$, $K^\pm$ and proton in Fig. 7.11. However, it is found that all tracks collectively show decent agreement

between data and MC for the ratio, f_c^ℓ, as shown in Figs. 7.12 and 7.13 for the tracks in the leading jet and in the next to leading jet, respectively. This implies that the jet fragmentation modeled in the MC well describes the data. A difference in the tracking efficiency can contribute to the uncertainty on the central value of f_c^ℓ estimated from MC.

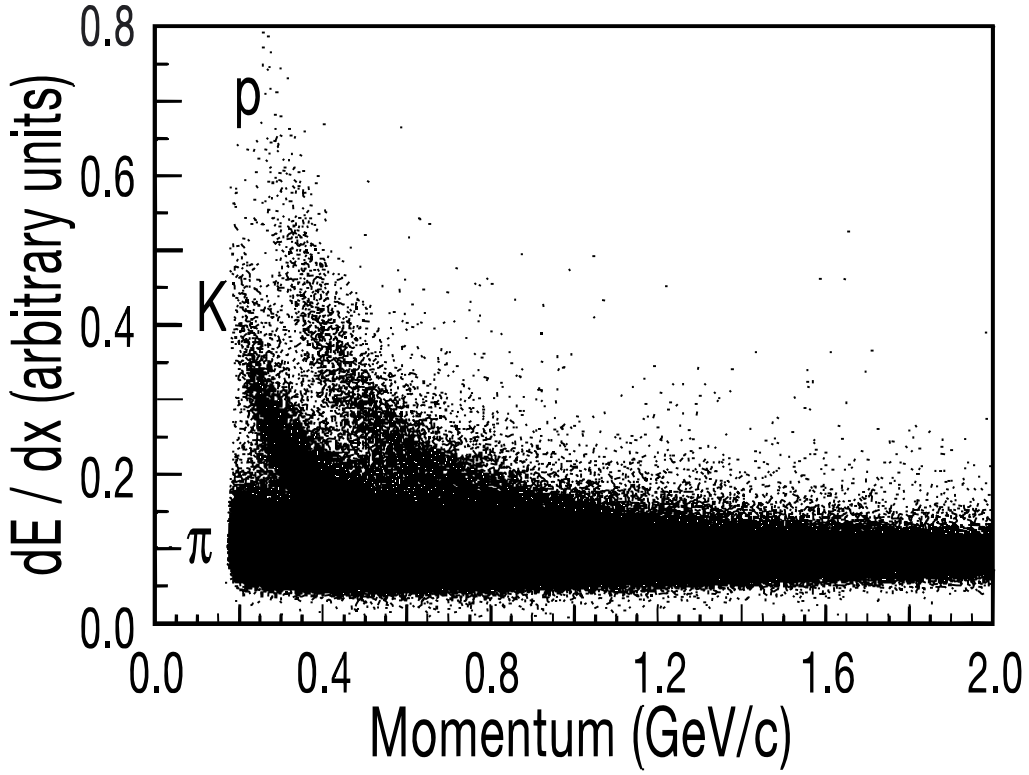

Figure 7.11: Energy loss (dE/dx) distribution of the pions, kaons and proton as a function of the tracks p_T [51]. At high p_T the discrimination between proton, kaon and pion goes to zero.

It is also worth noticing that the pions in jets are more correlated with the W boson charge than kaons in jets with the W boson charge. This is because leading $\pi^\pm$ can be created in $W+u$ or $W+d$ final states, whereas leading $K^\pm$ can only be created in $W+u$ final states. Furthermore, we expect $\sigma(W^-+u) < \sigma(W^-+\bar{d})$ or $\sigma(W^++\bar{u}) < \sigma(W^++d)$ because of the higher parton density of u quark than d quark in the proton. Figure 7.14 compares the ratio of the OS to SS ratio for the pions and for the kaons as a function of the transverse momentum. This variable shows no dependence for the kaons p_T implying less correlation

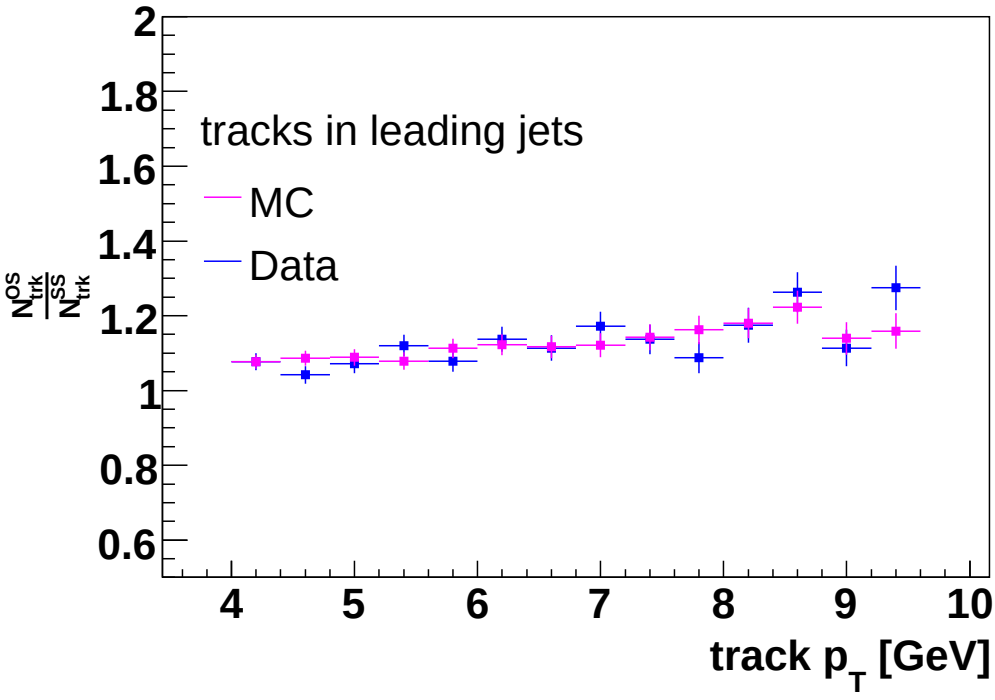

Figure 7.12: A comparison of data for the ratio of the OS weighted tracks to SS weighted present in the leading jet with the ratio of the OS pions to SS pions present in the jet is shown as a function of track transverse momentum p_T.

of the $K^{\pm}$ with the W boson charge. On the other hand the $\pi^{\pm}$ have relatively higher correlation and has stronger p_T dependence due to the leading particle effect. Therefore, the estimation of f_c^{ℓ} is directly sensitive to the relative contribution of the charged kaons with respect to the pions within the jet. The $K^{\pm}/\pi^{\pm}$ has been measured by several experiments at low energy scale, e.g $K^{+}/\pi^{+} = 0.146 \pm 0.005$ by CDHS collaboration in the neutrino-nucleon interaction experiment [93] and $K^{-}/\pi^{-} = 0.146 \pm 0.022$ in Au-Au collisions by STAR collaboration [94]. These measured ratios are expected to be lowered in the pp or $p\bar{p}$ collisions. In the presented analysis this ratio is not directly estimated because of the difficulty in distinguishing kaons from pions through the difference in energy loss by these particles while traversing through the material. It is relatively straight forward to construct the neutral kaon K^{o}_{S}, that has the shorter lifetime [6] 0.9×10^{-10} s, from two oppositely

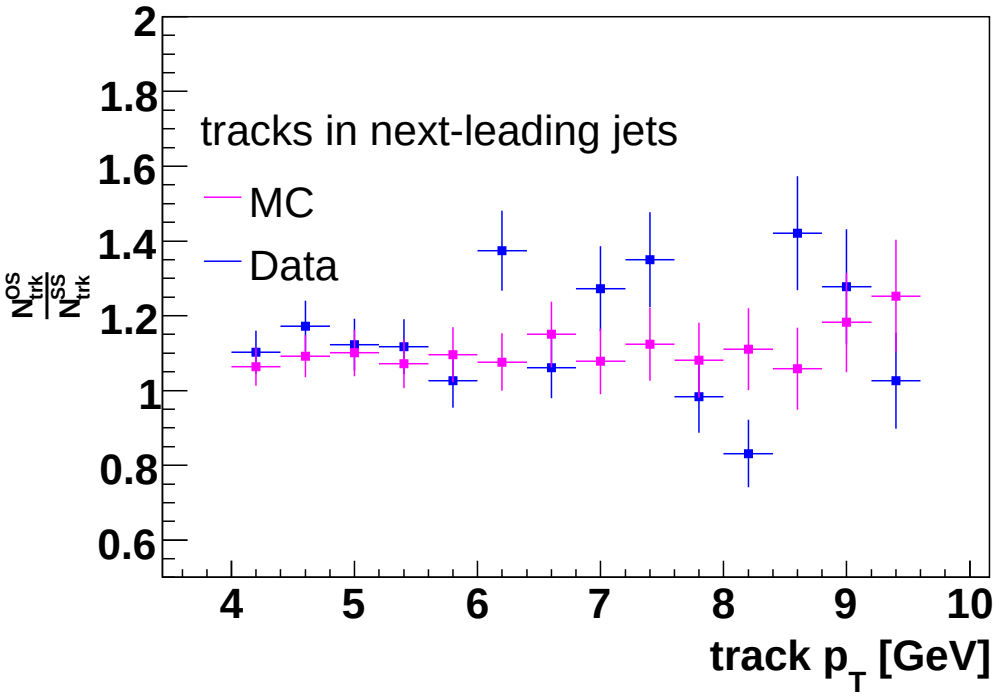

Figure 7.13: A comparison of data for the ratio of the OS weighted tracks to SS weighted present in the leading jet with the ratio of the OS pions to SS pions present in the jet is shown as a function of track transverse momentum p_T.

charged pions. An assumption is then made that an agreement in K^o_S production model with the data would imply that the charged kaons production model is also well described by the data. This would further indicate how well the jet fragmentation models describe the data. Measurements using e^+e^- data at LEP show that the jet fragmentation models (Lund's and Peterson's) describe the data well for the light flavored jets [95]. To test the consistency of the K^o_S production between data and MC, K^o_S are reconstructed from two oppositely charged tracks with $p_T > 0.1$ GeV lying within the jet cone. The invariant mass of these tracks is employed as an observable to count the number of reconstructed K^o_S with $p_T > 4$ GeV in the inclusive W+jets sample. To ensure good resolution of the reconstructed K^o_S mass, the level of the background is kept small by selecting good quality tracks that have produced at least 3 hits in the SMT tracking system and 9 hits in the CFT detector,

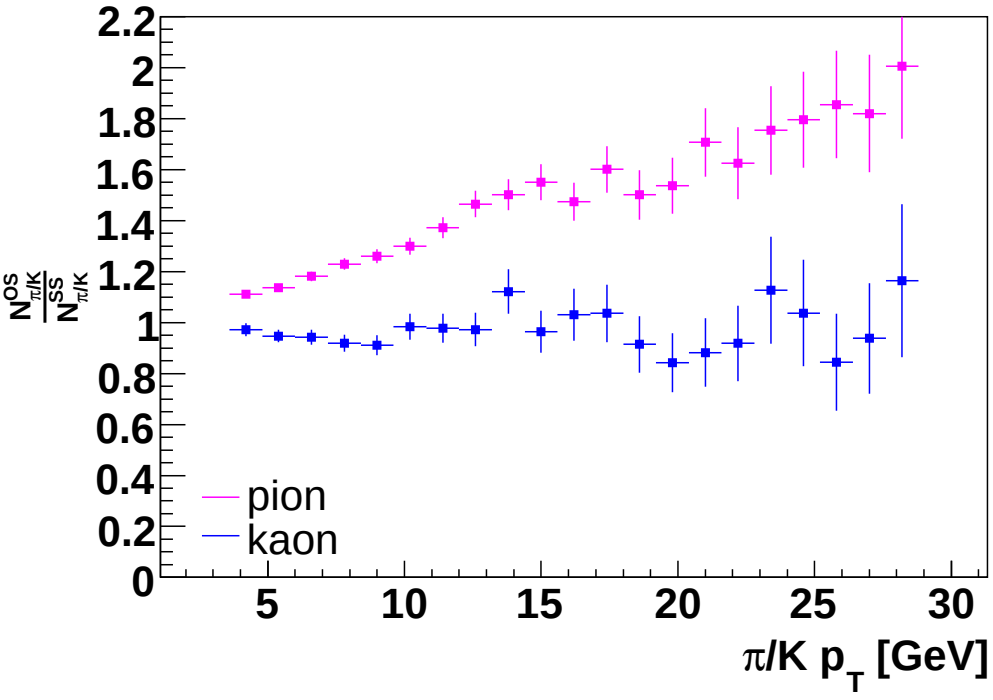

Figure 7.14: A comparison of the ratio of the OS kaons to SS kaons present in the jet with the ratio of the OS pions to SS pions present in the jet is shown as a function of their transverse momenta.

and have $\chi^2/\text{ndof} < 10$. Each track must have a point of closest approach in z within 1 cm from the primary interaction vertex, and a minimum significance of the distance of closest approach in the x-y plane with respect to the primary vertex should be above 3. The point of closest approach of the resulting vector constructed from two tracks must be within 0.02 cm of the primary vertex in the transverse plane. This selection strategy has been employed to enhance the b-jet tagging efficiency in $t\bar{t}$ production cross section analysis [96]. The rate of the reconstructed K^0_S in the jet is estimated to be 0.0028 ± 0.0002 in data and 0.0040 ± 0.0002 in MC. Because of larger inefficiencies due to tracking and vertexing, the data is observed to have 30% less reconstructed K^0_S rate than that in the MC. The tracking inefficiency is responsible for $10 - 12\%$ difference in the rate, while the rest is due to the vertex reconstruction inefficiency.

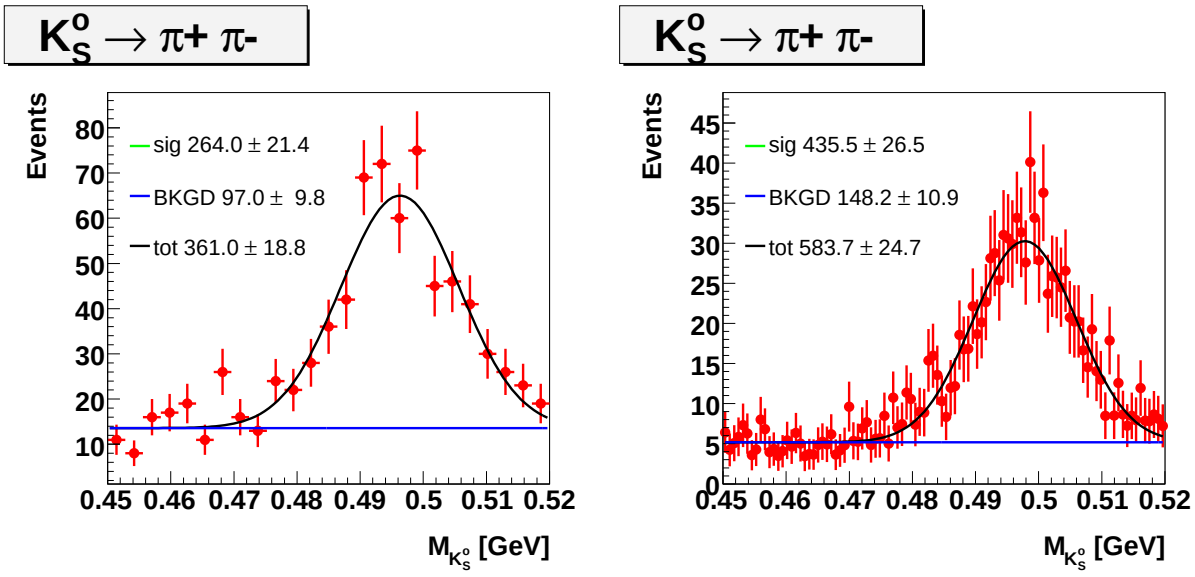

(a) (b)

Figure 7.15: Distribution of the invariant mass of K^o_S reconstructed from two oppositely charged tracks present in the jet in the data (a) and MC (b) samples of W + jets. Low statistics is due to high p_T restriction on the reconstructed K^o_S in the W + jets sample. After fitting the distribution with a Gaussian for the signal and a straight line for the background, a good agreement is found in the mean value of the mass of reconstructed K^o_S; for data $M_{K^o_S} = 0.4963 \pm 0.0007$ and for MC $M_{K^o_S} = 0.4978 \pm 0.0004$.

The vertex reconstruction efficiency decreases with increasing the decay length of K^o_S with respect to the primary vertex and drops to nearly zero at 20 cm. This significant lose of vertex efficiency is due to the deficiency of the silicon tracker in this region. The vertex reconstruction efficiency is not well modeled in the simulation, therefore the rate of reconstructed K^o_S per jet falls with respect to the proper decay length more steeply in the data than in the MC. Figure 7.16 shows a comparison of the K^o_S reconstruction rate per jet, $\frac{N_{K^o_S}}{N_{\text{jet}}}$, as a function of proper decay length in centimeters. For this purpose a large sample of di-jet QCD process in the data and MC. In this context the proper decay length is defined as $d_{PDL} = \frac{d_{DL} m_{K^o_S}}{p_T^{K^o_S}}$ which is closer to the physical observable $c\tau$ in the particle's rest frame, where d_{DL} is the distance of the secondary vertex of the K^o_S from the primary vertex in the x-y plane, $m_{K^o_S}$ is the mass of the K^o_S vertex, and $p_T^{K^o_S}$ is the transverse momentum of the

K^o_S. By fitting the measured rates in data and MC with exponential $p_0 e^{\frac{-d_{PDL}}{p_1}}$, where p_0 and p_1 are fit parameters, it is found that the mean value of the proper decay lengths are $p_1 = 0.56 \pm 0.02$ cm and $p_1 = 0.68 \pm 0.02$ cm, respectively. A discrepancy of a factor of 4 between these values and the measured value $c\tau = 2.68$ cm [6] is caused by the presence of tracking and vertexing inefficiencies in this data. The difference in the p_1 values in the data and MC is assigned as the systematic uncertainty associated with the vertexing efficiency, which is 20%. As the processes from the $W + c\bar{c}$, $W + b\bar{b}$ and $W + c$-jet are combined with

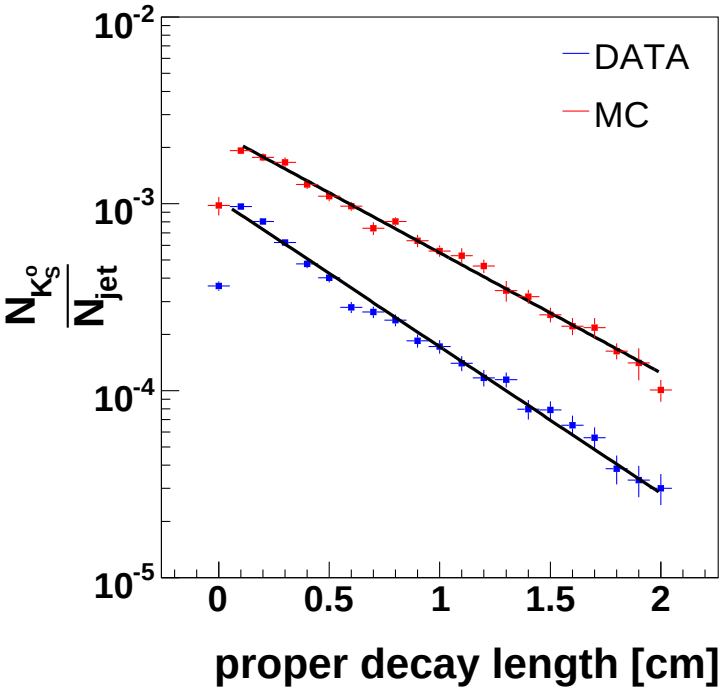

Figure 7.16: A comparison of the rate of reconstructed K^o_S in jet in data and simulation is shown here as a function of proper decay length, PDL, as defined in the text. The black line is an exponential fit, $p_0 e^{\frac{-d_{PDL}}{p_1}}$, where p_0 and p_1 are fit parameters representing the normalization constant and mean value of proper decay length, respectively. Fits to data and MC give $p_1 = 0.56 \pm 0.02$ cm and $p_1 = 0.68 \pm 0.02$ cm. These fit values differ by a factor of 4 compared to the measured value of $c\tau = 2.68$ cm [6] due to inefficiencies in the vertex reconstruction.

the inclusive W + light-jet sample to evaluate the factor f^{ℓ}_c, this factor gains sensitivity to

these cross sections relative to the W + light-jet cross section. The $W + c\bar{c}$ and $W + b\bar{b}$ do not contribute to this factor away from unity, as these produce uncorrelated final state leptons. The $W + c$-jet contribution is included for the case where the muon is produced from pion or kaon and not from the charm quark. The W + jets provided the largest contribution among all processes. An uncertainty of 50% is associated with the theoretical cross sections of $W + b\bar{b}$, $W + c\bar{c}$ processes, which amounts to less than 1% to the absolute uncertainty to the factor f_c^ℓ. The $W + c$-jet cross section is let to be varied by 100% to estimate the variation in the f_c^ℓ factor. Table 7.3 summarizes all systematics associated with f_c^ℓ estimation. Since the minimum value of the factor f_c^ℓ is known to be unity with no uncertainty, the total uncertainty on the deviation from unity is 12%.

The charges of the tracks are well measured at DØ. Isolated electrons have 1% charge mis-id rate for electrons in the central region of the calorimeter (CC) and 7-10% in the end cap region (EC). Isolated muons charges are very well measured with less than 0.1% systematic uncertainty. In rare cases, the jet-muon can be mis-identified due to wrong matching to the track in the central region because of larger track multiplicity within the jet cone. Using the MC simulation, this mis-identification rate has been measured to be less than 5% in most of the samples.

The uncertainties associated due to the CTEQ6 used for the parton distribution function for the generation of the processes involved in f_c^ℓ calculation is estimated by varying the central values of the PDFs set by its 40 error sets. The upward and downward uncertainties are $\sqrt{\Sigma_{i=1}^{20}(f_c^{\ell;\pm} - f_c^\ell)}$, where $f_c^{\ell;+}(f_c^{\ell;-})$ is the value of f_c^ℓ greater(less) than central f_c^ℓ that is estimated from central values of CTEQ6L fit. These upward and downward uncertainties are computed to be $^{+0.97\%}_{-0.64\%}$.

7.3.2 Multijet background to W+c-jet

The $b\bar{b}$ or $c\bar{c}$ production is a charge correlated final state. Due to small branching fractions ($BF(b \to \mu) \approx 20\%$ and $BF(c \to \mu) \approx 10\%$), these processes contribute to the background

Systematic uncertainty on the background fraction f_c^ℓ		
Sources	% δf_c^e	% δf_c^μ
$\sigma(W + c\text{-jet})$	$^{+0.25}_{-0.23}$	$^{+0.28}_{-0.26}$
$\sigma(W + c\bar{c})$	$^{+0.17}_{-0.30}$	$^{+0.22}_{-0.23}$
$\sigma(W + b\bar{b})$	$^{+0.13}_{-0.25}$	$^{+0.12}_{-0.23}$
pion multiplicity	$^{+0.15}_{-0.16}$	$^{+0.13}_{-0.15}$
$K^\pm/\pi^\pm$ ratio	$^{+0.45}_{-0.43}$	$^{+0.42}_{-0.40}$
PDF	$^{+0.97}_{-0.64}$	$^{+0.97}_{-0.64}$
charge mis-id	± 1	-
total	$^{+1.51}_{-1.35}$	$^{+1.13}_{-0.87}$

Table 7.3: Absolute systematic uncertainties associated with the background correction factor f_c^ℓ. To evaluate these uncertainties, $\sigma(W + c\text{-jet})$ is varied by 100%, $\sigma(W + b\bar{b})$ and $\sigma(W + c\bar{c})$ by 50%, pion multiplicity by 6%, $K^\pm/\pi^\pm$ by 20%.

Figure 7.17: $q\bar{q} \to c\bar{c}$ and $q\bar{q} \to b\bar{b}$ subprocesses.

in three ways:

1. Events with only one b/c quark decaying semileptonically can contribute to both OS and SS samples, if the final state lepton leaves the jet and is identified as an isolated lepton, and a μ-tagged jet is identified from fake muon or from uncorrelated pion or kaon decays.

2. Events with only one b/c quark decaying semileptonically into muon can contribute to both OS and SS samples, if the muon satisfies the conditions of a μ-tagged jet and another isolated lepton is misidentified from the sources such as jet-to-electron probability, or cosmics and punch through muons. These events are enriched in mostly uncorrelated final state leptons.

3. Events with both b/c quarks decaying semileptonically can contribute to the OS $W+$ c-jet signal events, if one lepton leaves the jet and is identified as an isolated lepton and the other muon satisfies the conditions of a μ-tagged jet.

Since the probability of the background from third kind is small, the net contribution from these processes have only weakly correlated final state leptons.

In the $W \to e\nu$ decay mode, the second source (as mentioned above) of background processes is due to the misidentified isolated electrons from the jets or photon in multijet or $\gamma +$ jet processes. In the $W \to \mu\nu$ decay mode the probability from the second source is small due to very small rate for punch through or cosmic muons that pass tight selection criteria. The contributions from all these sources are collectively regarded as the multijet background. In the electron channel the net multijet background produces more charge symmetric final states compared to that in the muon channel.

The estimation of multijet background in both channels is carried out using the matrix method described in previous chapter (Sec. 6.3.1). Both OS and SS samples are separately considered to get an individual estimate of the multijet backgrounds, $N_{\rm MJ}^{\ell,{\rm OS}}$ and $N_{\rm MJ}^{\ell,{\rm SS}}$, contributing to OS and SS events.

$$N_{\rm MJ}^{\ell,{\rm OS}} = \epsilon_{\rm MJ}^{\ell} \frac{N_T^{\ell,{\rm OS}} - \epsilon_W^{\ell} N_L^{\ell,{\rm OS}}}{\epsilon_{\rm MJ}^{\ell} - \epsilon_W^{\ell}}, \tag{7.8}$$

$$N_{\rm MJ}^{\ell,{\rm SS}} = \epsilon_{\rm MJ}^{\ell} \frac{N_T^{\ell,{\rm SS}} - \epsilon_W^{\ell} N_L^{\ell,{\rm SS}}}{\epsilon_{\rm MJ}^{\ell} - \epsilon_W^{\ell}}, \tag{7.9}$$

where $N_T^{\ell,{\rm OS}}$ and $N_T^{\ell,{\rm SS}}$ denote the samples of OS and SS events where the isolated lepton ($\ell = e, \mu$) satisfies the tight selection criteria, and $N_T^{\ell,{\rm OS}}$ and $N_T^{\ell,{\rm SS}}$ denote the samples of

OS and SS events where the isolated lepton ($\ell = e, \mu$) satisfies the loose selection criteria. The efficiencies, ϵ^{ℓ}_{W}, and the fake rate $\epsilon^{\ell}_{\rm MJ}$ are described in Sec. 6.3.1. The estimated sizes of this background are listed in Tables 7.1 and 7.2.

7.4 Efficiency of W+c-jet Selection

The reconstruction of W boson from an isolated lepton and $\not\!\!E_T$ is a common step in the event selection of an inclusive sample of the W+jets and the $W+\mu$-tagged jet. As the data sample containing $W+\mu$-tagged jet is a subset of an inclusive sample of W+jets, therefore the efficiency of the identification and reconstruction of W boson and at least one jet is expected to cancel in the ratio measurement. The relative efficiency of $W+c$-jet selection via muon tagging is a product of the muon tagging efficiency $\epsilon^{\mu\text{-tag}}_{c\text{-jet}}$ of a reconstructed c-jet, the correction A^{μ}_{c} to the signal events that contribute to the background, the correction $K^{\mu\rm JES}_{c}$ due to the muon and neutrino energies in the jet p_T, and the correction K^{μ}_{T} for the possible muon trigger biases in the $W(\rightarrow \mu\nu)+\mu$-tagged jet sample compared to the inclusive $W(\rightarrow \mu\nu)+$jets sample. Total efficiency of a c-jet originating from the c quark is defined as

$$\epsilon^{\mu}_{c} = \epsilon^{\mu\text{-tag}}_{c\text{-jet}} \times K^{\mu\rm JES}_{c} \times A^{\mu}_{c} \times \epsilon_{\rm SF}, \tag{7.10}$$

where $\epsilon_{\rm SF}$ represents the data-to-MC scale factor to correct for the detector inefficiencies that are not modeled in the MC samples, and A^{μ}_{c} corrects for the effect that a small fraction of SS events are produced in the $W+c$-jet sample that dilute the correlation between the final state lepton charges. This dilution arises from the fact that the c quark has only 10% probability to decay into muon and neutrino. Therefore, in the $W+c$-jet sample the presence of π and K in the c-jet decaying into the muon with small probability allows a reconstructed μ-tagged jet initiated by a c quark. Muon produced from the π and K are not correlated with the isolated muon or electron produced from the W boson decay. An additional source of the production of uncorrelated muons is the presence of the fake muons

that simply are punch-through particles from the calorimeter in reality and mis-identified as muons by the outermost muon system. The factor A_c^μ is defined as

$$A_c^\mu = \frac{N_{c\text{-jet}}^{\text{reco}\mu}|_{c\to\mu}}{N_{c\text{-jet}}^{\text{reco}\mu}}, \tag{7.11}$$

where $N_{c\text{-jet}}^{\text{reco}\mu}$ is the total number of μ-tagged c-jets in the OS and SS cases, i.e $N_{c\text{-jet}}^{OS} + N_{c\text{-jet}}^{SS}$. Assuming the contribution from uncorrelated μ-tagged jets to be the same in the OS and SS would give the total size of charge-symmetric events equivalent to $2N_{c\text{-jet}}^{SS}$. This would leave us with the total number of μ-tagged jets where muon is produced from the c quark, $N_{c\text{-jet}}^{\text{reco}\mu}|_{c\to\mu}$, equal to $N_{c\text{-jet}}^{\text{reco}\mu} - 2N_{c\text{-jet}}^{SS} = N_{c\text{-jet}}^{OS} - N_{c\text{-jet}}^{SS}$. Therefore A_c^μ is given as

$$A_c^\mu = \frac{N_{c\text{-jet}}^{OS} - N_{c\text{-jet}}^{SS}}{N_{c\text{-jet}}^{OS} + N_{c\text{-jet}}^{SS}}, \tag{7.12}$$

known as the asymmetry variable, and is estimated from the simulation of $W + c$-jet to be 0.81 ± 0.02((stat.)). It has approximately no dependence on the jet p_T as shown in Fig. 7.18 meaning that the kinematics of the fake or uncorrelated muons in the $W + c$-jet sample are not constrained by the jet p_T. Remaining factors $\epsilon_{c\text{-jet}}^{\mu\text{-tag}}$ and $K_c^{\mu\text{JES}}$ in the definition of ϵ_c^μ are determined as a combined product denoted as $\epsilon_{c\text{-jet}}^{\text{reco-}\mu}$.

$$\epsilon_{c\text{-jet}}^{\text{reco-}\mu} = \epsilon_{c\text{-jet}}^{\mu\text{-tag}} \times K_c^{\mu\text{JES}}. \tag{7.13}$$

The factor $\epsilon_{c\text{-jet}}^{\text{reco-}\mu}$ on the left hand side of this equation is simply the fraction of the number of c-jets that are μ-tagged, where the p_T of the tagged jet remains uncorrected for the unaccounted muon and neutrino energies in the jet. This factor is extracted from the MC simulation for b-jet, c-jet and light-jet, as described in Sec. 7.4.1. On the right hand side of the expression 7.13, this is factorized into two parts. The first factor represents the muon tagging efficiency of a fully corrected μ-tagged c-jet, and the second factor determines the fraction of the uncorrected number of μ-tagged jets that enter into its corrected jet p_T bin. The factor $K_c^{\mu\text{JES}}$ is about 0.5 on average, and have small p_T dependence.

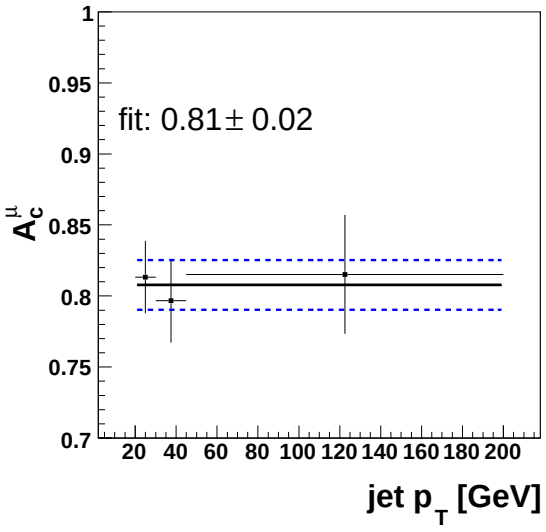

Figure 7.18: The dependence of asymmetry variable, A_c^μ, on the c-jet p_T estimated from the simulation of $W + c$-jet sample.

7.4.1 Muon tagging efficiency

The efficiency of a μ-tagged jet convolved with the jet p_T correction for the semileptonic decays is estimated from the MC simulation of $W + c$-jet, $W + b\bar{b}$ and $W +$ light-jet samples, for a c-jet, b-jet and light-jet. It is defined by Eq. 7.13, where the label c can be replaced by the b or light to refer to the b-jet or light-jet efficiency.

$$\epsilon_{b\text{-jet}}^{\text{reco-}\mu} = \epsilon_{b\text{-jet}}^{\mu\text{-tag}} \times K_b^{\mu\text{JES}}, \tag{7.14}$$

$$\epsilon_{\text{light-jet}}^{\text{reco-}\mu} = \epsilon_{\text{light-jet}}^{\mu\text{-tag}} \times K_{\text{light-jet}}^{\mu\text{JES}}. \tag{7.15}$$

Jets containing b, c or light jet flavors are selected from the $W+b\bar{b}$, $W+$c-jet and $W+$light-jet samples, respectively. To evaluate this convolved efficiency a subset of these flavored jets sample is selected that satisfies the presence of the muon within the jet with the criteria described in Sec. 7.3. The convolved efficiency defined as the ratio of the number of jets in two sets as shown in Fig. 7.19 is determined as a function of the jet p_T.

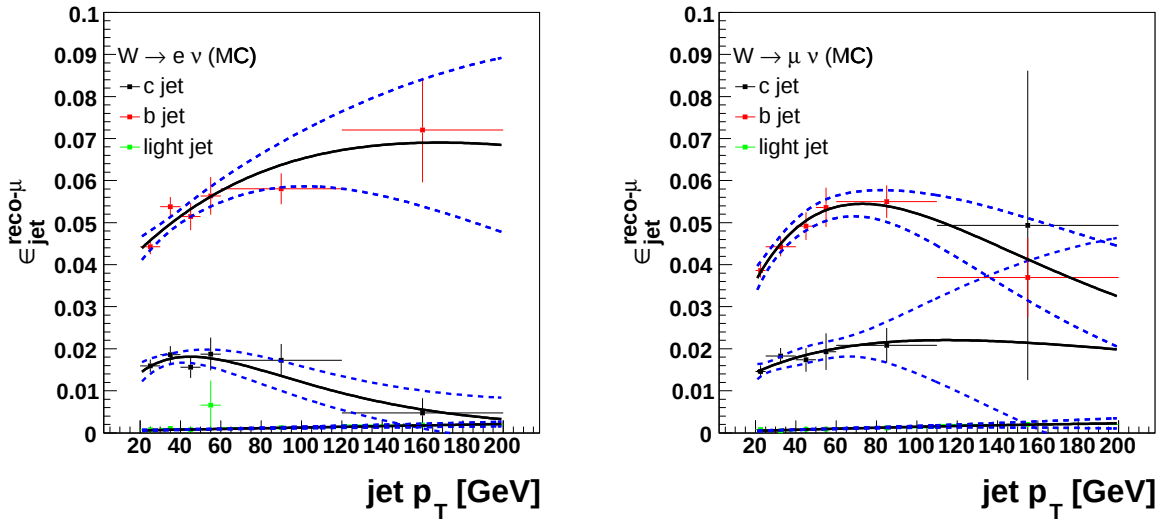

(a) (b)

Figure 7.19: The efficiency of the μ-tagged jet convoluted with the correction factor needed to apply to selected events to adjust the shift in the jet p_T spectrum caused by the missing energy due to the semileptonic decays, which is estimated from the W + jets sample for c-jet, b-jet and light-jet.

7.4.2 Data-to-MC scale factor for the muon tagging efficiency

Due to the degrading effects present in detector, the efficiency of reconstructed muon can be lower than what is estimated from the simulation, if these effects are not properly modeled in the MC simulation. To take into account this discrepancy between data and simulation, a large sample of $J/\psi \to \mu^+\mu^-$ events are employed. The "tag and probe" procedure that has been described previously is used to estimate the reconstruction and identification efficiency of the soft muon. According to this procedure, one of muon known as the "tag" muon reconstructing the J/ψ is restricted to pass the good muon selection requirements and the other muon known as the "probe" muon is tested for the efficiency. Both muon reconstructing the J/ψ must be non-isolated muons and must have $p_T > 4$ GeV. The efficiencies of the cut selections are estimated both in the data and MC samples, and the ratio of the efficiency estimated from the data sample to the efficiency estimated from the MC sample

is considered as the scale factor, $\epsilon_{\rm SF}$.

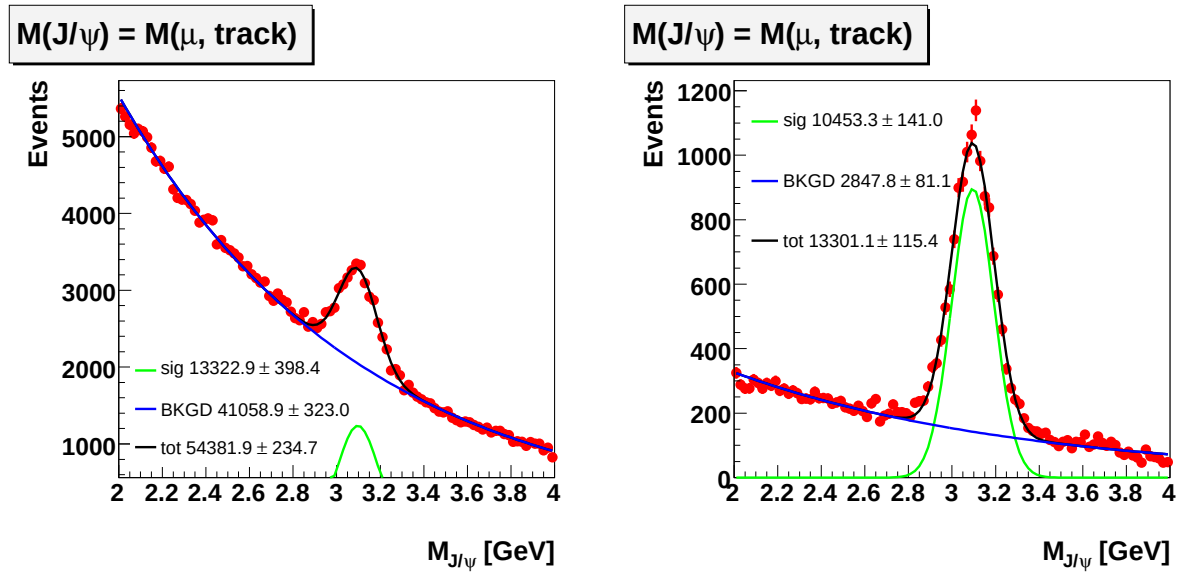

(a) (b)

Figure 7.20: The invariant mass distribution reconstructed from a muon and a track with opposite charges present in the jet cone. The distribution peaks around the J/ψ mass of 3.1 GeV, and fitted with the Gaussian for the J/ψ signal and an exponential for the background. (a) "tag" muon passes all quality cuts and have a reconstructed track, and "probe" track may or may not have matching with a good muon reconstructed in the muon systems, (b) both "tag" and "probe" muons satisfy the good quality.

7.4.3 Correction for the muon trigger biases

In the muon decay mode, the presence of two muons in the final state after applying muon tagging to the jet makes the single muon trigger selection more efficient relative to the single muon trigger selection for inclusive $W+$jets data sample. While this would bias the overall number of μ-tagged jets, it will also bias the excess of OS events in the μ-tagged jets sample. Such a bias is accounted for by applying a correction factor, K_T^{ℓ}, to the events with tagged jets. The same data sample is used to estimate the size of this correction, which is defined as the number of μ-tagged events where the muon contained in the jet is matched to the objects that fire the trigger at L1, L2 and L3 and the isolated muon is not

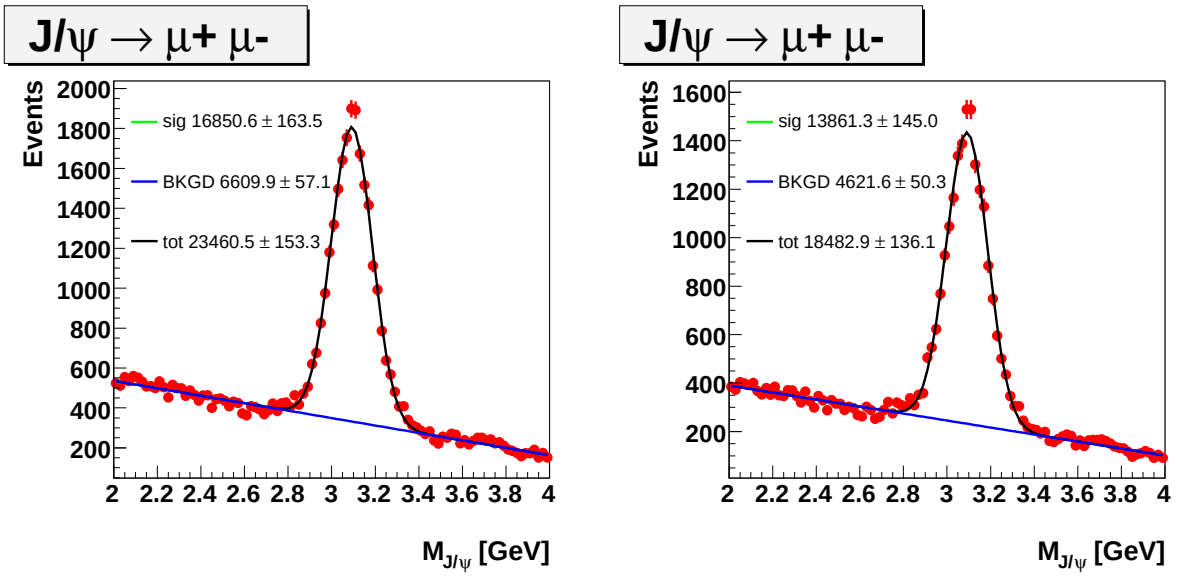

(a) (b)

Figure 7.21: The invariant mass distribution reconstructed from a muon and a track with opposite charges present in the jet cone. The distribution peaks around the J/ψ mass of 3.1 GeV, and fitted with the Gaussian for the J/ψ signal and a straight line for the background. (a) "tag" muon passes all quality cuts and have a reconstructed track, and "probe" muon passes all cuts except that it is not required to produce hits in the BC layers of the muon system, (b) both "tag" and "probe" muons must produce the BC hits in the muon system.

matched to the trigger objects. This factor is estimated to be $K_T^{\mu} = 1.18 \pm 0.12$, where the assigned systematic uncertainties to this estimation comes from the variations in the matching criteria applied to the offline reconstructed muon with the trigger objects. It is unity for the electron channel because of the single electron trigger requirement for the $W + c$-jet selection or an inclusive $W +$ jets selection by restricting the presence of only one isolated electron from the W boson decay.

7.5 Consistency for $W + c$-jet

As described in earlier sections, a sample consisting of a muon within the jet cone is enriched in semileptonic decays from the b or c mesons as well as from the pions and kaons. This section describes some checks on the selected signal events to show the consistency for the

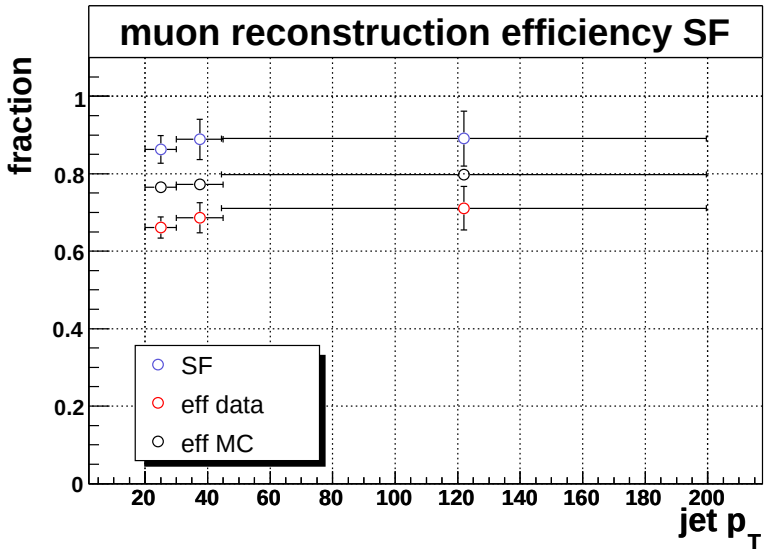

Figure 7.22: The figure provides the efficiencies of the muon reconstruction estimated using the $J/\psi \rightarrow \mu^+\mu^-$ data and MC sample corresponding to three jet p_T bins. Blue points show the data-to-MC scale factor in the muon reconstruction efficiency.

Muon identification and reconstruction efficiency scale factors			
CUT	Data	MC	ϵ_{SF}
Muon track match	0.865 ± 0.012	0.890 ± 0.003	0.972 ± 0.014
BC scintillator hit	0.823 ± 0.012	0.892 ± 0.003	0.922 ± 0.014
Cosmic muon rejection	0.940 ± 0.013	0.984 ± 0.001	0.955 ± 0.013
Muon ID	0.785 ± 0.026	0.753 ± 0.004	1.042 ± 0.035
Total	0.525 ± 0.021	0.587 ± 0.004	0.894 ± 0.040

Table 7.4: Efficiencies for muon identification and reconstruction determined from the data and MC using the "tag and probe" method applied to the reconstructed $J/\psi \rightarrow \mu^+\mu^-$.

presence of a c-jet exhibiting the relatively long lifetime properties as compared to that of the light-jet.

Ideally, the relative transverse momentum of the muon with respect to the parent hadron would be the best probe of the mass of the heavy quark. The higher transverse momentum of the muon reflects the jets initiated by massive quarks such as c or b. However, it is difficult to efficiently reconstruct the short lived heavy hadrons due to limited tracking efficiencies. Hence, the relative momentum of the muon transverse to the hadron momentum would not

provide an efficient observable for distinguishing the massive jets from light jets. To do this rather efficiently, this observable is modified by replacing the hadron momentum by the final state quark momentum, subsequently approximating the direction of the axis formed by the resulting momentum vector of the jet and muon as the quark axis. Figure 7.23(a) shows a schematic diagram of this observable denoted as $p_T^{\rm rel}$. While this observable is powerful for discrimination of b-jet from light-jets as can be seen from Fig. 7.24 (a), the discrimination between the c-jet and the light-jet is somewhat destroyed due to increasing mass of the jet with the gluons radiations. However, after subtracting off the background estimated using SS events from the OS data sample, the contributions from b or light jet sources can be minimized to zero and the $p_T^{\rm rel}$ distribution can be compared with that expected from ALPGEN+PYTHIA model for $W + c$-jet as shown in Fig. 7.24 (b) for a consistency check.

For further check the distribution of signed significance in impact parameter, $\frac{a}{\sigma_a}$, of the muon track with respect to the primary vertex is compared in the data and simulation after subtracting the background, where a is the projected distance of closest approach (dca) of the displaced muon track to the primary vertex in the transverse plane as shown in Fig. 7.23 (b). To ensure that displaced track is produced from the decays of heavy flavor mesons, the angular separation between the track and jet axis must be less than 180 degrees so that the *sign* of the impact parameter is assigned to be positive, i.e. the $sign(\sin\Delta\phi(\mu\text{track}, \text{jet}))$ should be positive. The distribution of signed $\frac{a}{\sigma_a}$ is expected to be enhanced on the positive side for heavy flavor jets, but it should be symmetric for the light-jets as illustrated in Fig. 7.25 (a). After subtracting the background, the distribution as shown in Fig. 7.25 (b) is found to be consistent with that expected from the c-jet in the $W + c$-jet sample.

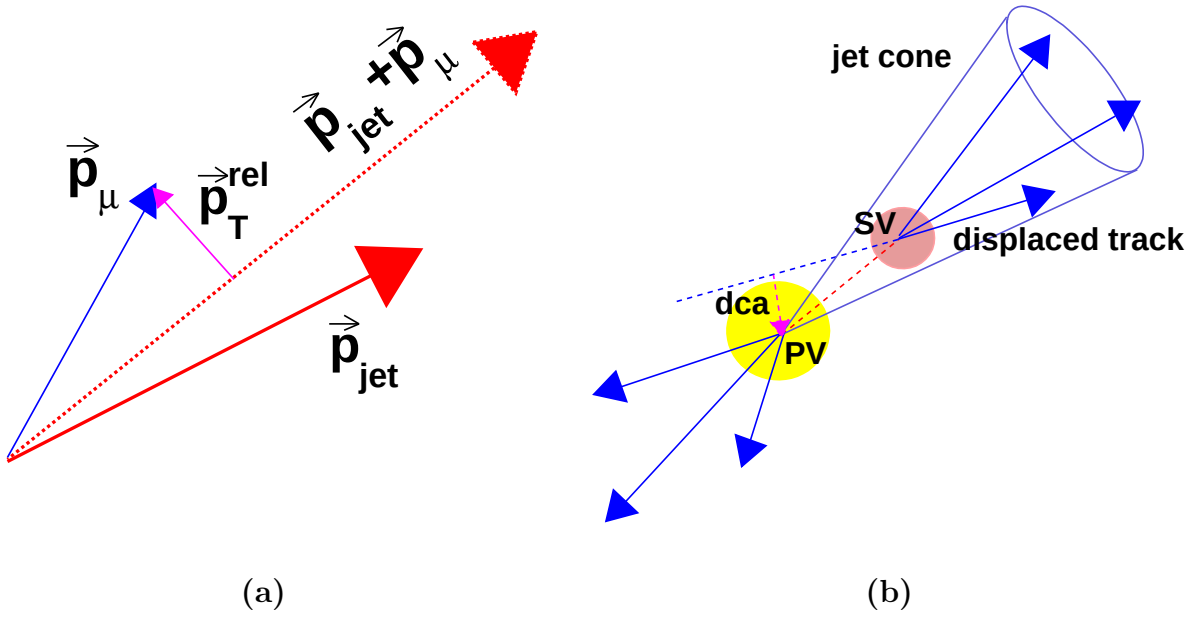

Figure 7.23: (a) The relative transverse momenta of the muon with the axis formed by the jet momentum direction and the muon momentum direction, p_T^{rel}, (b) Schematic diagram for the distance of closest approach (also called impact parameter) of the displaced track with respect to the primary vertex.

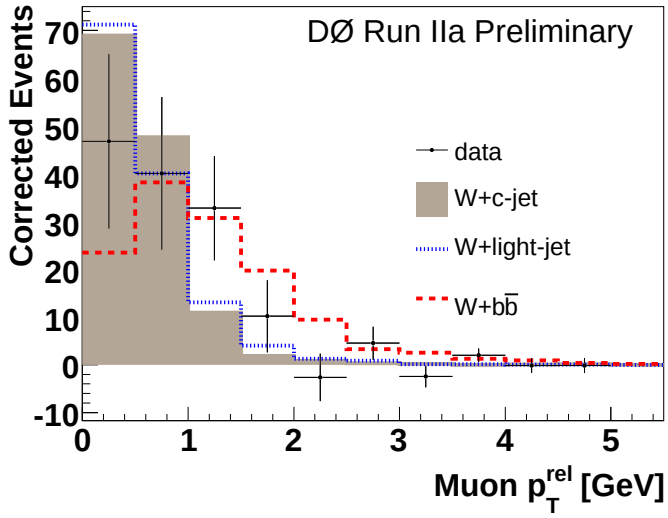

(a)

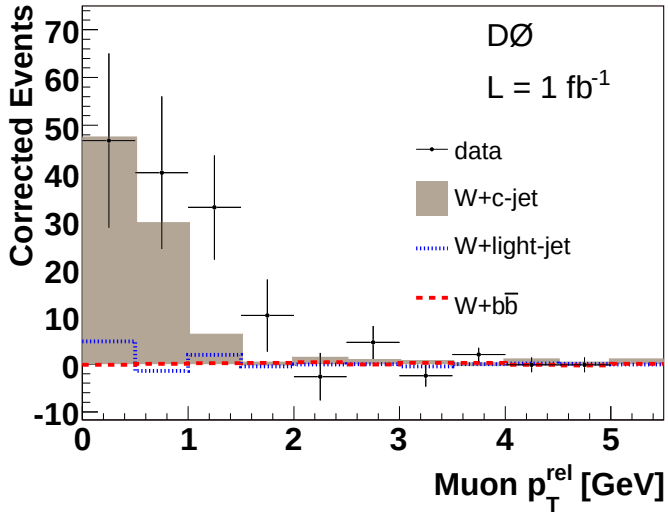

(b)

Figure 7.24: (a) Comparison of the shape of the muon $p_T^{\rm rel}$ for the b, c and light jet with the background subtracted data, $(N_{OS}^{\ell} - f_c^{\ell} N_{SS}^{\ell})$, distribution in the combined channels, the MC distributions are normalized to the data entries, (b) Comparison of $p_T^{\rm rel}$ distribution for the background-subtracted $(N_{OS}^{\ell} - f_c^{\ell} N_{SS}^{\ell})$ data in the combined electron and muon channels with the expectations from the MC simulation.

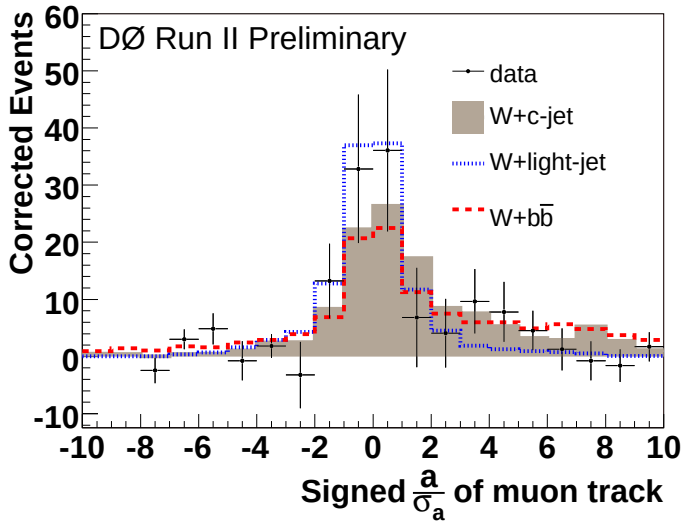

(a)

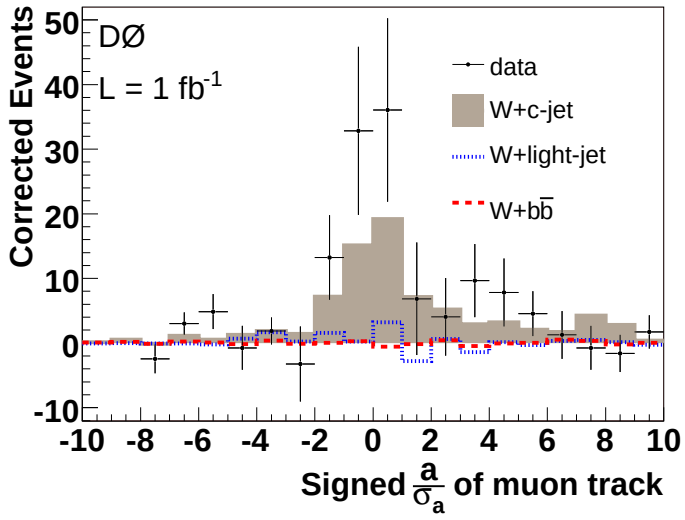

(b)

Figure 7.25: (a) Comparison of the shapes of the muon $\frac{a}{\sigma_a}$ for the b, c and light jet with the background subtracted data, $(N^{\ell}_{OS} - f^{\ell}_{c} N^{\ell}_{SS})$, distribution in the combined channels, the MC distributions are normalized to the data entries, (b) Comparison of $\frac{a}{\sigma_a}$ distribution for the background-subtracted $(N^{\ell}_{OS} - f^{\ell}_{c} N^{\ell}_{SS})$ data in the combined electron and muon channels with the expectations from the MC simulation.

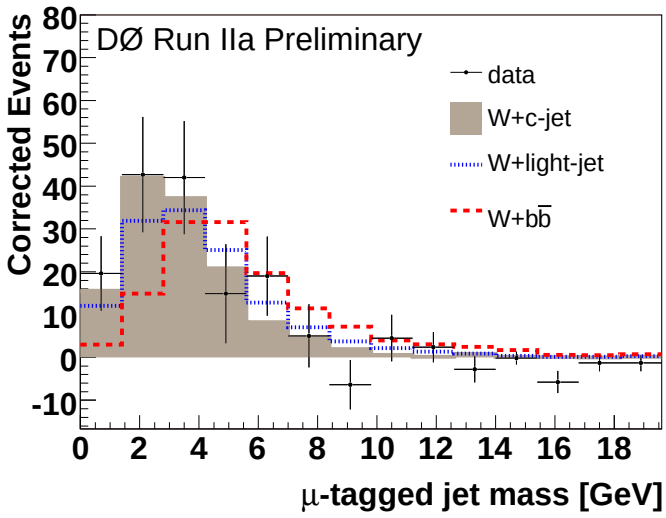

(a)

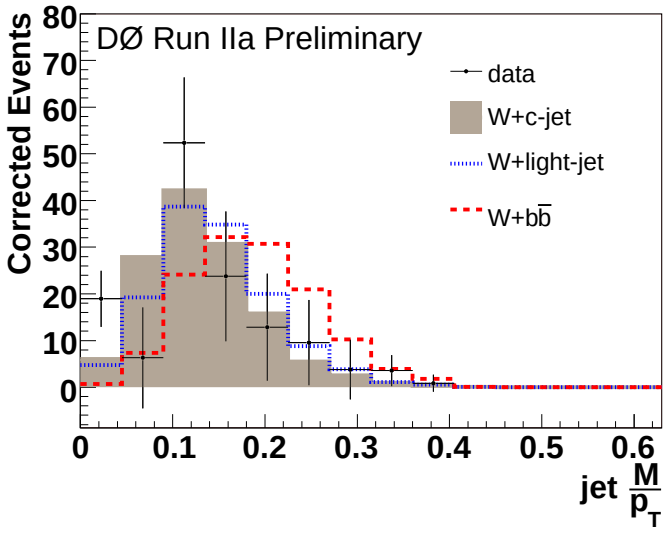

(b)

Figure 7.26: (a) Comparison of the shapes of the jet mass of μ-tagged jet for the b, c and light jet with the background subtracted data, $(N^{\ell}_{OS} - f^{\ell}_{c} N^{\ell}_{SS})$, distribution in the combined channels, the MC distributions are normalized to the data entries, (b) Comparison of the shapes of the ratio of the jet mass to the jet p_T of μ-tagged jet for the b, c and light jet with the background subtracted data, $(N^{\ell}_{OS} - f^{\ell}_{c} N^{\ell}_{SS})$, distribution in the combined channels, the MC distributions are normalized to the data entries.

Chapter 8

Measurement of Cross section Ratio of $p\bar{p} \rightarrow W$+c-jet to $p\bar{p} \rightarrow W$+jets Processes

This chapter describes the measurement of the ratio of the $W + c$-jet cross section to the inclusive $W +$ jets cross section which is unfolded to the particle level and is compared with the theoretical predictions. The information on the events yields for the signal and background processes described in previous two chapters is used here. The systematic uncertainties associated with the measurement is also reported in this chapter.

8.1 Cross Section Ratio $\frac{\sigma(p\bar{p} \rightarrow W+c\text{-jet})}{\sigma(p\bar{p} \rightarrow W+\text{jets})}$

Number of events observed in collisions are directly proportional to the cross section σ of the interaction

$$\begin{aligned} N &= \mathcal{L}\sigma\epsilon, \\ \sigma &= \frac{N}{\mathcal{L}, \epsilon} \end{aligned} \tag{8.1}$$

where $\mathcal{L}$ denotes the integrated luminosity and ϵ is the total acceptance times efficiency of the process within the detector geometries. The ratio of the cross section of the $W + c$-jet and the inclusive $W +$ jets process can be expressed as

$$\frac{\sigma(p\bar{p} \rightarrow W + c\text{-jet})}{\sigma(p\bar{p} \rightarrow W + \text{jets})} = \frac{N^{\ell}_{W+c\text{-jet}} \times \epsilon^{\ell}_{W+c\text{-jet}}}{N^{\ell}_{W+\text{jets}} \times \epsilon^{\ell}_{W+\text{jets}}}, \tag{8.2}$$

where the luminosity factor is cancelled out in the ratio. Here $N_{W+c\text{-jet}}$ and $N_{W+\text{jets}}$ denote the number of $W + c$-jet and $W +$ jets events, respectively, observed in the data sample, and $\epsilon_{W+c\text{-jet}}$ and $\epsilon_{W+\text{jets}}$, denote their respective acceptance times efficiencies. It is worth mentioning that the ratio measurement benefits from large cancellations of the efficiencies of objects selection, such as W boson and jet selections, and hence it is insensitive to the uncertainties associated with many efficiency factors and luminosity at the first order. Further, there is almost no dependence on the uncertainties associated with the theoretical models, such as factorization and normalization scales and the PDF at the first order. Effects from the jet energy scale and the jet energy resolution are also partially cancelled. Ratio measurement, once unfolded to the truth level, itself allows a direct comparison with the theoretical prediction because of the cancellations in uncertainties related to the cross sections.

As described in the previous chapter, the number of events $W + c$-jet observed in the data are determined by subtracting the background events N^{ℓ}_{bkd} from the OS events, N^{ℓ}_{OS}. The background is estimated from the SS data sample

$$N^{\ell}_{W+c\text{-jet}} = N^{\ell}_{\text{OS}} - N^{\ell}_{\text{bkd}}, \tag{8.3}$$

where

$$N^{\ell}_{\text{bkd}} = f^{\ell}_{c}\left(N^{\ell}_{\text{SS}} - N^{\ell,\text{non-}W+\text{jets}}_{\text{SS}}\right) + N^{\ell,\text{non-}W+\text{jets}}_{\text{OS}}, \tag{8.4}$$

where $N^{\ell,\text{non-}W+\text{jets}}_{\text{SS}}$ and $N^{\ell,\text{non-}W+\text{jets}}_{\text{OS}}$ denote the background contribution to the SS and OS samples from the processes such as W^+W^-, $t\bar{t}$, single top quark production and the multijet background processes.

$$N^{\ell,\text{non-}W+\text{jets}}_{\text{SS}} = N^{\ell,\text{MJ}}_{\text{SS}} + N^{\ell,WW}_{\text{SS}} + N^{\ell,t\bar{t}}_{\text{SS}} + N^{\ell,t\bar{b}}_{\text{SS}}, \tag{8.5}$$

$$N^{\ell,\text{non-}W+\text{jets}}_{\text{OS}} = N^{\ell,\text{MJ}}_{\text{OS}} + N^{\ell,WW}_{\text{OS}} + N^{\ell,t\bar{t}}_{\text{OS}} + N^{\ell,t\bar{b}}_{\text{OS}}, \tag{8.6}$$

While the SS events determine the size of the background from the data sample, it is difficult to directly measure the relative compositions of the background from the sources

other than the $W+$ jets. The background contributions from such sources is estimated from the simulation, and the uncertianties dominated by the measured cross sections of these background processes has been assigned. Therefore, total background contribution is given as,

$$N^{\ell}_{\rm bkd} = f^{\ell}_{c}\left(N^{\ell}_{\rm SS} - N^{\ell,{\rm MJ}}_{\rm SS} - N^{\ell,WW}_{\rm SS} - N^{\ell,t\bar{t}}_{\rm SS} - N^{\ell,t\bar{b}}_{\rm SS}\right) + N^{\ell,{\rm MJ}}_{\rm OS} + N^{\ell,WW}_{\rm OS} + N^{\ell,t\bar{t}}_{\rm OS} + N^{\ell,t\bar{b}}_{\rm OS}. \quad (8.7)$$

The $W+$ jets sample is a composition of the $W+$ light-jet, $W+c\bar{c}$ and $W+b\bar{b}$, $W+c$-jet with some contamination mainly from $Z+$ jets and multijet background. The number of $W+$ jets after the background subtraction are given by

$$N^{\ell}_{W+{\rm jets}} = (1 - f^{\ell}_{Z} - f^{\ell}_{\rm MJ})N^{\ell}_{Wj}, \quad (8.8)$$

where N^{ℓ}_{Wj} denotes the number of observed events in an inclusive $W+$ jets data sample, and f^{ℓ}_{Z} is the estimated fraction from the $Z+$ jets events and $f^{\ell}_{\rm MJ}$ represents the fraction of the multijet background events estimated from the data sample as described in Sec. 6.3.1. Inserting the expressions for $N_{W+c\text{-jet}}$ and $N_{W+{\rm jets}}$ in Eq. 8.2, we get

$$\begin{aligned} & \frac{\sigma(p\bar{p}\rightarrow W+c\text{-jet})}{\sigma(p\bar{p}\rightarrow W+{\rm jets})}, \\ = \; & \frac{N^{\ell}_{\rm OS} - f^{\ell}_{c}\left(N^{\ell}_{\rm SS} - N^{\ell,{\rm MJ}}_{\rm SS} - N^{\ell,WW}_{\rm SS} - N^{\ell,t\bar{t}}_{\rm SS} - N^{\ell,t\bar{b}}_{\rm SS}\right) - N^{\ell,{\rm MJ}}_{\rm OS} - N^{\ell,WW}_{\rm OS} - N^{\ell,t\bar{t}}_{\rm OS} - N^{\ell,t\bar{b}}_{\rm OS}}{(1 - f^{\ell}_{Z} - f^{\ell}_{\rm MJ})N^{\ell}_{Wj}} \\ & \times \frac{\epsilon^{\ell}_{W+{\rm jets}}}{\epsilon^{\ell}_{W+c\text{-jet}}}. \end{aligned} \quad (8.9)$$

Since most of the efficiencies such as the jet reconstruction and W boson reconstruction, are common in $\epsilon^{\ell}_{W+{\rm jets}}$ and $\epsilon^{\ell}_{W+c\text{-jet}}$, the relative efficiency is considered as the product of the μ tagging efficiency, ϵ^{ℓ}_{c}, of the c-jet and the relative trigger correction factor, K^{ℓ}_{T}, to account for the bias in the $W+c$-jet selection compared to the inclusive $W+$ jets selection. The ϵ^{ℓ}_{c} as defined in Sec. 7.4 by Eq. 7.10 includes

- the branching fraction from the c quark to the μ decay,
- the efficiency of the muon reconstruction and identification,

- the efficiency of the muon kinematical selection in the jet,
- the jet energy correction,
- the efficiency of the charge correlation between the final state leptons in the W + μ-tagged c-jet sample,
- a scale factor for the correction of the detector effects.

Thus,

$$\frac{\epsilon^{\ell}_{W+\text{jets}}}{\epsilon^{\ell}_{W+c\text{-jet}}} = \frac{1}{\epsilon^{\ell}_{c} K^{\ell}_{T}}. \tag{8.10}$$

By substituting the expression for the relative acceptance times efficiency in Eq. 8.9, we get the final expression for the cross section ratio of the $W + c$-jet to the $W +$ jets processes.

$$\begin{aligned} &\frac{\sigma(p\bar{p} \to W + c\text{-jet})}{\sigma(p\bar{p} \to W + \text{jets})} \\ = \; &\frac{N^{\ell}_{\text{OS}} - f^{\ell}_{c}\left(N^{\ell}_{\text{SS}} - N^{\ell,\text{MJ}}_{\text{SS}} - N^{\ell,WW}_{\text{SS}} - N^{\ell,t\bar{t}}_{\text{SS}} - N^{\ell,t\bar{b}}_{\text{SS}}\right) - N^{\ell,\text{MJ}}_{\text{OS}} - N^{\ell,WW}_{\text{OS}} - N^{\ell,t\bar{t}}_{\text{OS}} - N^{\ell,t\bar{b}}_{\text{OS}}}{(1 - f^{\ell}_{Z} - f^{\ell}_{\text{MJ}}) N^{\ell}_{Wj}} \\ &\times \frac{1}{\epsilon^{\ell}_{c} K^{\ell}_{T}}. \end{aligned} \tag{8.11}$$

Table 8.1 summarizes the quantities used in this expression.

8.2 Systematic Uncertainties

The dominant sources of systematic uncertainties in this measurement are associated with the c-jet tagging efficiency ϵ_c, the jet energy scale, the jet momentum resolution, the background correction factor f^{ℓ}_{c} and the relative efficiency of the trigger selection. The systematic uncertainties associated with the measurement are obtained by varying all these sources one at a time by ± 1 standard deviations (σ) and repeating the analysis.

jet p_T [GeV]	(20–30)	(30–45)	(45–200)
$W \to e\nu$ decay channel			
N^e_{Wj}	35695	24412	22640
$N^e_{\rm OS}$	83	77	85
$N^e_{\rm SS}$	45	41	68
$N^{e,\rm MJ}_{\rm OS}$	4.5±1.0±1.2	4.2±0.9±1.1	4.6±1.0±1.2
$N^{e,\rm MJ}_{\rm SS}$	5.6±1.1±1.4	5.1±1.0±1.3	8.5±1.5±2.2
$N^{e,WW}_{\rm OS}$	1.8±0.6	2.1±0.7	2.3±0.8
$N^{e,WW}_{\rm SS}$	0.4±0.1	0.6±0.2	0.9±0.3
$N^{e,t\bar{t}}_{\rm OS}$	2.4±0.6	4.6±1.1	11.8±2.8
$N^{e,t\bar{t}}_{\rm SS}$	2.1±0.5	4.1±1.0	10.0±2.4
$N^{e,t\bar{b}}_{\rm OS}$	1.1±0.3	2.1±0.6	3.1±0.9
$N^{e,t\bar{b}}_{\rm SS}$	0.8±0.2	1.4±0.4	2.5±0.7
f^e_c	1.183±0.017±0.018	1.164±0.019±0.017	1.118±0.024±0.017
ϵ^e_c	$0.0113\pm0.0015^{+0.0017}_{-0.0017}$	$0.0125\pm0.0011^{+0.0019}_{-0.0019}$	$0.0125\pm0.0020^{+0.0019}_{-0.0019}$
$\frac{\sigma[W(\to e\nu)+c\text{-jet}]}{\sigma[W(\to e\nu)+\text{jets}]}$	$0.079\pm0.031^{+0.013}_{-0.022}$	$0.100\pm0.038^{+0.017}_{-0.016}$	$0.043\pm0.049^{+0.007}_{-0.007}$
$W \to \mu\nu$ decay channel			
N^μ_{Wj}	27378	17325	13241
$N^\mu_{\rm OS}$	76	64	63
$N^\mu_{\rm SS}$	28	38	56
$N^{\mu,\rm MJ}_{\rm OS}$	4.6±1.8±3.3	3.8±1.5±2.7	3.8±1.5±2.7
$N^{\mu,\rm MJ}_{\rm SS}$	2.0±1.3±1.4	2.8±1.7±2.0	4.1±2.5±2.9
$N^{\mu,WW}_{\rm OS}$	0.8±0.3	1.6±0.5	1.8±0.6
$N^{\mu,WW}_{\rm SS}$	0.3±0.1	0.3±0.1	0.6±0.2
$N^{\mu,t\bar{t}}_{\rm OS}$	1.2±0.3	2.3±0.6	5.8±1.4
$N^{\mu,t\bar{t}}_{\rm SS}$	1.0±0.2	2.0±0.5	5.1±1.2
$N^{\mu,t\bar{b}}_{\rm OS}$	0.7±0.2	1.4±0.4	2.1±0.6
$N^{\mu,t\bar{b}}_{\rm SS}$	0.5±0.1	0.8±0.1	1.8±0.5
f^μ_c	1.195±0.025±0.014	1.174±0.027±0.013	1.121±0.035±0.013
ϵ^μ_c	$0.0110\pm0.0011^{+0.0016}_{-0.0017}$	$0.0122\pm0.0013^{+0.0018}_{-0.0019}$	$0.0148\pm0.0018^{+0.0022}_{-0.0023}$
K^μ_T	1.18±0.02±0.12	1.18±0.02±0.12	1.18±0.02±0.12
$\frac{\sigma[W(\to \mu\nu)+c\text{-jet}]}{\sigma[W(\to \mu\nu)+\text{jets}]}$	$0.123\pm0.037^{+0.024}_{-0.033}$	$0.076\pm0.050^{+0.016}_{-0.013}$	$0.000\pm0.058^{+0.014}_{-0.008}$

Table 8.1: Summary of quantities used in W+c-jet cross section ratio; the first uncertainties quoted are statistical and the second systematic.

	$W \to e\nu$ decay channel	$W \to \mu\nu$ decay channel
N^{ℓ}_{Wj}	82747	57944
$N^{\ell}_{\rm OS}$	245	203
$N^{\ell}_{\rm SS}$	154	122
$N^{\ell,\rm MJ}_{\rm OS}$	13.3±2.6±3.4	12.2±4.6±8.7
$N^{\ell,\rm MJ}_{\rm SS}$	19.3±2.9±4.9	8.8±5.4±6.3
$N^{\ell,WW}_{\rm OS}$	6.2±2.1	4.2±1.6
$N^{\ell,WW}_{\rm SS}$	1.9±0.5	1.2±0.4
$N^{\ell,t\bar{t}}_{\rm OS}$	18.8±4.5	9.3±2.2
$N^{\ell,t\bar{t}}_{\rm SS}$	16.1±3.9	8.1±1.9
$N^{\ell,t\bar{b}}_{\rm OS}$	6.3±1.8	4.2±1.2
$N^{\ell,t\bar{b}}_{\rm SS}$	4.6±1.3	3.1±0.9
f^{ℓ}_{c}	1.149±0.007±0.017	1.148±0.007±0.013
ϵ^{ℓ}_{c}	$0.0124\pm0.0012^{+0.0019}_{-0.0019}$	$0.0122\pm0.0012^{+0.0018}_{-0.0019}$
K^{μ}_{T}	-	1.18±0.02±0.12
$\frac{\sigma[W(\to\ell\nu)+c\text{-jet}]}{\sigma[W(\to\ell\nu)+\text{jets}]}$	$0.073\pm0.023^{+0.012}_{-0.014}$	$0.075\pm0.031^{+0.015}_{-0.017}$

Table 8.2: Summary of quantities used in W+c-jet cross section ratio for the jet $p_T > 20$ and $|\eta| < 2.5$; the first uncertainties quoted are statistical and the second systematic.

jet p_T [GeV]	$\frac{\sigma[W(\to\ell\nu)+c\text{-jet}]}{\sigma[W(\to\ell\nu)+\text{jets}]}$
(20–30)	$0.097\pm0.024^{+0.016}_{-0.026}$
(30–45)	$0.091\pm0.031^{+0.016}_{-0.015}$
(45–200)	$0.025\pm0.038^{+0.005}_{-0.004}$
(20–200)	$0.074\pm0.019^{+0.012}_{-0.014}$

Table 8.3: Cross section ratio measurement combined in the electron and muon decay channels; the first uncertainties quoted are statistical and the second systematic. The systematic uncertainties are considered to be fully correlated between the electron and muon channels.

8.2.1 Jet energy scale uncertainty

The systematic uncertainty due to the jet energy scale is estimated by varying the jet p_T by ± 1 $\sigma_{\rm jes}$ in the simulation samples and repeating the MC analysis [66]. The $\sigma_{\rm jes}$ represents the total uncertainty in data and MC jet energy scales, i.e $\sqrt{\left(\sigma_{\rm jes}^{\rm data}\right)^2 + \left(\sigma_{\rm jes}^{\rm MC}\right)^2}$, where $\sigma_{\rm jes}^{\rm data} = \sqrt{\left(\sigma_{\rm jes}^{\rm data,stat}\right)^2 + \left(\sigma_{\rm jes}^{\rm data,syst}\right)^2}$ and $\sigma_{\rm jes}^{\rm MC} = \sqrt{\left(\sigma_{\rm jes}^{\rm MC,stat})^2 + (\sigma_{\rm jes}^{\rm MC,syst}\right)^2}$. The difference in the resulting cross section ratios from the central value is considered as a systematic uncertainty. Table 8.5 lists the uncertainty associated with the measurement due to the jet energy scale in three p_T bins, as well as for the full region with $p_T > 20$ GeV.

8.2.2 Relative p_T resolution of jet in data and MC

In order to bring the MC jet p_T resolution in agreement with the jet p_T resolution in the data sample, the jet p_T in the MC samples is smeared by the relative p_T resolution in the data and MC samples. The relative p_T resolution is given by $\sigma_{\rm jpr}^{\rm rel} = \sqrt{\left(\sigma_{\rm jpr}^{\rm data}\right)^2 - \left(\sigma_{\rm jpr}^{\rm MC}\right)^2}$, where $\sigma_{\rm jpr}^{\rm data}$ ($\sigma_{\rm jpr}^{\rm MC}$) represents the jet p_T resolution in the data (MC) sample [82]. The smearing to the jet p_T is performed using Gaussian distributed random number with the width of the Gaussian equal to $\sigma_{\rm jpr}^{\rm rel}$. The uncertainty associated with the jet p_T smearing (JPR) is obtained by varying the smearing factor by ± 1 $\sigma_{\rm jpr}^{\rm rel}$ and repeating the MC analysis. The deviation in the result from the central value is attributed as the systematic uncertainty on the measurement. Table 8.5 lists the estimated systematic uncertainty associated with the measurement in each bin.

8.2.3 ϵ_c^ℓ systematic uncertainty

The factor ϵ_c^ℓ as defined by Eq. 7.10 absorbes several efficiency factors, and uncertainties associated with these factors are estimated to get the total uncertainty. The sources of uncertainties on ϵ_c^ℓ are mainly due to the branching fraction $BF(c \to \mu)$, c-jet fragmentation, A_c^ℓ factor, muon p_T resolution, the correction factor for muon and missing energy in the jet p_T, the data-to-MC scale factor. Table 8.4 summarizes the size of these invidual

uncertainties. Table 8.5 gives total uncertainty on ϵ_c^ℓ for all p_T regions of jet.

sources	fractional systematic uncertainty
$BF(c \to \mu)$	9.5%
c-jet fragmentation	4.5%
A_c^μ	6.0%
muon p_T resolution	$^{+4.1\%}_{-4.4\%}$
$K_{c\text{-jet}}^{\mu\text{JES}}$	4.3%
ϵ_{SF}	7.0%

Table 8.4: Average uncertainties associated with ϵ_c^ℓ. The uncertainty due to $K_{c\text{-jet}}^{\mu\text{JES}}$ varies with the jet p_T bin, larger for low p_T bin and smaller for high p_T bin.

8.2.4 f_c^ℓ systematic uncertainty

The systematic uncertainty on the cross section ratio due to the background correction factor f_c^ℓ is assigned to be the variation in the observed ratio by varying f_c^ℓ by 1 standard deviation, which is $^{+1.13\%}_{-1.17\%}$ for the $W \to e\nu$ channel and $^{+0.60\%}_{-0.58\%}$ for the $W \to \mu\nu$ channel. Total uncertainty due to f_c^ℓ is given in Table 8.5 for all p_T regions of the jet.

8.2.5 PDF uncertainty

The measurement presented in this dissertation is insensitive to the uncertainties associated with the parton distribution functions at the first order. The PDFs provided by the CTEQ project on QCD are used in the theoretical prediction of the cross section ratio calculation. To estimate the uncertainty due to CTEQ6.5M PDFs on the cross section ratio, the MCFM package [97] v5.2 is used as a MC tool. The CTEQ6.5M has 40 error sets. The MCFM package provides the calculations of the cross section for the W+jets and $W+c$-jet processes corresponding to every eigen vector upto the next-to-leading order in α_s. The upward and downward uncertainties are defined to be $\delta\sigma_{pdf}^{\pm} = \sqrt{\sum_{i=1}^{20}(\sigma_{pdf,i}^{\pm} - \sigma_{pdf,0})^2}$, where $\sigma_{pdf,i}^{+}$ ($\sigma_{pdf,i}^{-}$) denotes the cross section ratio observable having value greater (less) than the value of the observable, $\sigma_{pdf,0}$, corresponding to the central values of the CTEQ6.5 fit parameters. A 1.9% (2.2%) upward (downward) is found for the W+jets sample, 5.5% (5.1%) for $W+c$-jet

	e channel					μ channel					
p_T	JES	JPR	f_c^e	ϵ_c^e	total	JES	JPR	f_c^μ	ϵ_c^μ	K_T^μ	total
GeV	%	%	%	%	%	%	%	%	%	%	%
20–30	$^{+0}_{-21.6}$	$^{+2.4}_{-4.8}$	$^{+3.8}_{-4.1}$	$^{+15.7}_{-15.6}$	$^{+16.3}_{-27.4}$	$^{+0}_{-17.6}$	$^{+5.0}_{-7.5}$	$^{+2.5}_{-3.3}$	$^{+15.3}_{-16.2}$	± 10	$^{+19.2}_{-27.2}$
30–45	$^{+6.4}_{-4.3}$	$^{+2.1}_{-4.3}$	$^{+4.3}_{-4.7}$	$^{+14.5}_{-14.4}$	$^{+16.5}_{-16.3}$	$^{+9.8}_{-0.7}$	$^{+4.5}_{-6.7}$	$^{+3.1}_{-4.3}$	$^{+14.1}_{-14.9}$	± 10	$^{+20.6}_{-16.9}$
45–200	$^{+2.2}_{-2.2}$	$^{+2.2}_{-4.5}$	$^{+6.9}_{-7.6}$	$^{+14.7}_{-14.6}$	$^{+16.5}_{-17.2}$	$^{+27.7}_{-0}$	$^{+4.7}_{-7.0}$	$^{+4.0}_{-5.2}$	$^{+15.0}_{-15.8}$	± 10	$^{+33.6}_{-24.5}$
20–200	$^{+0}_{-9.0}$	$^{+2.3}_{-4.5}$	$^{+4.5}_{-5.2}$	$^{+15.1}_{-15.0}$	$^{+18.8}_{-15.9}$	$^{+5.9}_{-2.4}$	$^{+4.7}_{-7.1}$	$^{+3.1}_{-4.3}$	$^{+14.9}_{-15.7}$	± 10	$^{+19.7}_{-22.2}$

Table 8.5: Fractional systematic uncertainties on the measurement in the $W \to e\nu$ and the $W \to \mu\nu$ channels.

p_T	JES	JPR	f_c^ℓ	ϵ_c^ℓ	K_T^ℓ	total
GeV	%	%	%	%	%	%
20–30	$^{+0}_{-20.0}$	$^{+3.4}_{-5.9}$	$^{+3.3}_{-3.8}$	$^{+15.6}_{-15.9}$	± 3.9	$^{+16.7}_{-26.8}$
30–45	$^{+7.7}_{-2.9}$	$^{+3.0}_{-5.2}$	$^{+3.8}_{-4.5}$	$^{+14.3}_{-14.6}$	± 3.9	$^{+17.4}_{-16.9}$
45–200	$^{+12.1}_{-1.4}$	$^{+3.2}_{-5.5}$	$^{+5.8}_{-6.6}$	$^{+14.8}_{-15.1}$	± 3.9	$^{+20.5}_{-17.8}$
20–200	$^{+2.3}_{-6.5}$	$^{+3.2}_{-5.5}$	$^{+4.0}_{-4.8}$	$^{+15.0}_{-15.3}$	± 3.9	$^{+16.5}_{-18.6}$

Table 8.6: Combined fractional systematic uncertainties on the measurement in the $W \to e\nu$ and the $W \to \mu\nu$ channels.

and 6.1% (5.1%) on the cross section ratio $\sigma(W+c\text{-jet})/\sigma(W+\text{jets})$. It is important to note that this uncertainty does not reflect a true uncertainty due to the strange quark PDF fit, because the CTEQ6.5M does not include the uncertainty due to the magnitude and shape of the s quark distribution function relative to the non-strange sea quarks ($\bar{u}$ and $\bar{d}$).

8.3 Results

The measured cross section ratio integrated over jet $p_T > 20$ GeV and $|\eta| < 2.5$ in two channels are

$$\frac{\sigma(p\bar{p} \to W(\to e\nu) + c\text{-jet})}{\sigma(p\bar{p} \to W(\to e\nu) + \text{jets})} = 0.073 \pm 0.023(\text{stat.})^{+0.012}_{-0.014}(\text{syst.}),$$
$$\frac{\sigma(p\bar{p} \to W(\to \mu\nu) + c\text{-jet})}{\sigma(p\bar{p} \to W(\to \mu\nu) + \text{jets})} = 0.075 \pm 0.031(\text{stat.})^{+0.015}_{-0.017}(\text{syst.}).$$

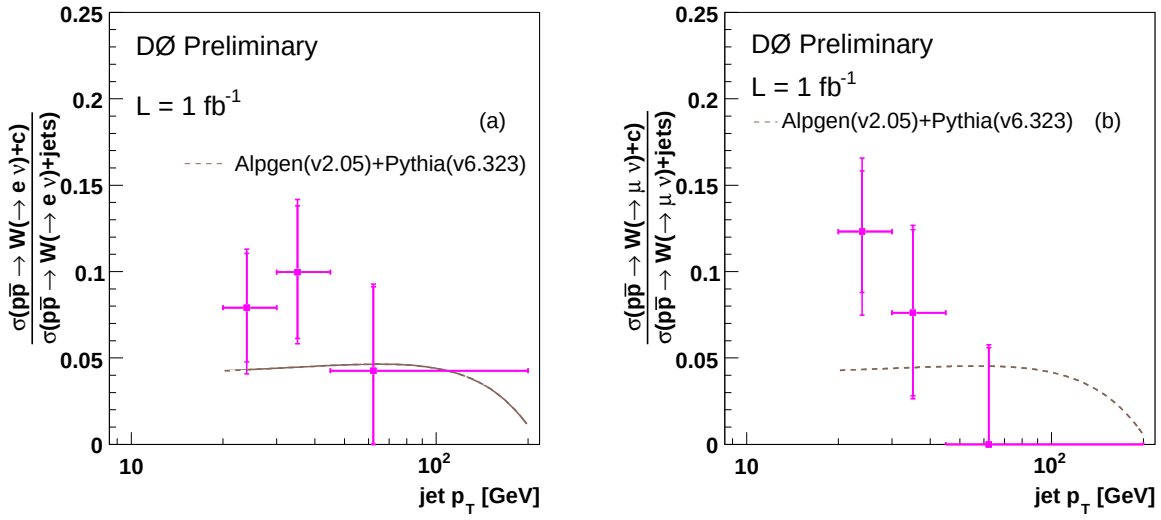

(a) **(b)**

Figure 8.1: Measured ratio $\frac{\sigma(p\bar{p}\to W+c\text{-jet})}{\sigma(p\bar{p}\to W+\text{jets})}$ as a function of jet p_T which is corrected to the particle level. (a) $W \to e\nu$ mode, (b) $W \to \mu\nu$ mode. Minimum threshold for the jet p_T is required to be 20 GeV and the pseudorapidity $|\eta| < 2.0$ in each p_T bin. The data points are shown with the theoretical expectation of ALPGEN+PYTHIA, where ALPGEN is for tree level matrix element calculation and PYTHIA is for the parton shower. Inner error bars represent the statistical only uncertainty on the measurement and the outer error bars corresponds to the total uncertainty where statistical and systematic uncertainties are added in quadrature.

The measurements in two channels are combined to achieve better statistical precision

$$R = \frac{\sum_i \frac{R_i}{\sigma_i^2}}{\sum_i \frac{1}{\sigma_i^2}}. \tag{8.12}$$

Combination of two channels yields

$$\frac{\sigma(p\bar{p} \to W + c\text{-jet})}{\sigma(p\bar{p} \to W + \text{jets})} = 0.074 \pm 0.019(\text{stat.})^{+0.012}_{-0.014}(\text{syst.}).$$

In the combination, the systematic uncertainties are considered to be fully correlated between electron and muon channels.

The theoretical prediction of the W+c-jet production rate using the ALPGEN and PYTHIA

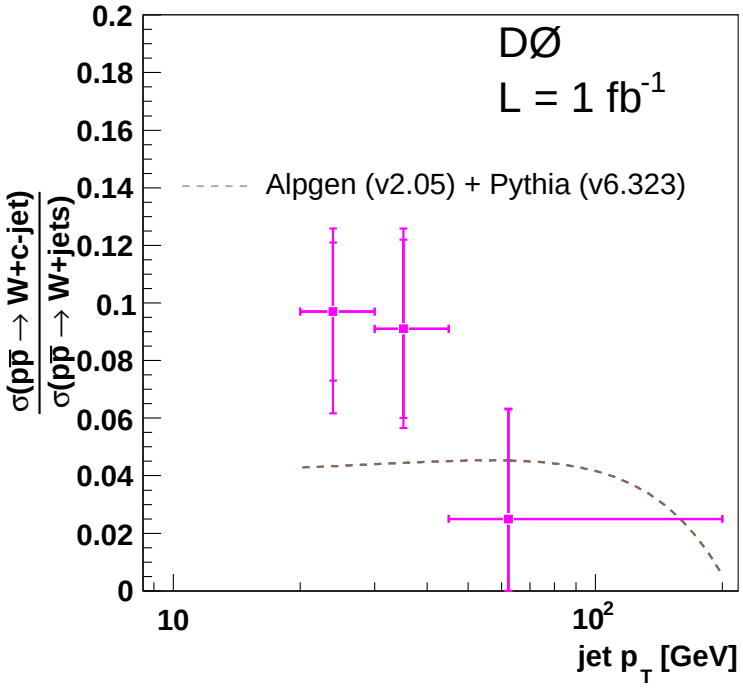

Figure 8.2: Combined measurement of the ratio $\frac{\sigma(p\bar{p}\to W+c\text{-jet})}{\sigma(p\bar{p}\to W+\text{jets})}$ in the electron channel and the muon channel, for the particle level corrected p_T with a minimum threshold of 20 GeV and the pseudorapidity $|\eta| < 2.0$ in each p_T bin. The data points are shown with the theoretical expectation of ALPGEN+PYTHIA. Inner error bars represent the statistical only uncertainty on the measurement and the outer error bars corresponds to the total uncertainty where statistical and systematic uncertainties are added in quadrature.

is 0.044 ± 0.003, where the quoted theoretical uncertainty is due to CTEQ6.5M PDFs. An additional small source of uncertainty on the theoretical prediction arises from relatively small contributions of $W + b\bar{b}$ and $W + c\bar{c}$ in the inclusive $W +$ jets sample. By doubling or halving their cross sections would change the theoretical predictions of $W + c$-jet rate by less than 5%.

The measurement is distributed into three p_T bins of leading jet, (20-30), (30-45) and (45-200) such that total entries in bin are same in c-jet p_T spectrum obtained from the $W + c$-jet simulation sample. Figure 8.1 (a) and (b) show the measured cross section ratio in the electron and muon channels, respectively, where the dots represent the measurement

and the inner error bar show the statistical uncertainty and the full bar show the statistical and systematic uncertainties on the measurements added in quadrature. The dashed line represents the ALPGEN and PYTHIA theoretical predictions at the leading order in perturbative QCD. The combined differential $W + c$-jet fraction is shown in Fig. 8.2 comparing the data with the theoretical prediction.

8.4 Statistical Significance of the $\frac{\sigma(p\bar{p}\rightarrow W+c\textbf{-jet})}{\sigma(p\bar{p}\rightarrow W+\textbf{jets})}$ Measurement

The statistical significance is a measure of the total probability that the observed signal is not due to the upward fluctuations of the background events. The size of the $W + c$-jet signal is estimated from the excess of OS events in the data sample after subtracting the background which is largely determined from SS events. In order to quantify the fact that the excess of OS events is not due to an upward fluctuation of the background events in the data sample, sets of pseudo experiments are generated based on the Poisson distributed random trial statistics.

The Poisson probability to observe N events given that the expected number of events are n is given by

$$p(N|n) = \frac{e^{-n}n^N}{N!}. \tag{8.13}$$

The generation of pseudo experiments is based on the random Poisson trials seeded by the sampled mean values of background event predictions from the ALPGEN. These Poisson mean values are obtained after fluctuating the nominal ALPGEN predictions according to the Gaussian distributed systematic uncertainties associated with each parameter. The systematic uncertainties include the uncertainties associated with the normalization (cross sections and luminosity), isolated lepton reconstruction efficiency, jet reconstruction efficiency, the energy scale and resolution of jets, the background correction factors $f^{\ell}_{\rm MJ}$, f^{ℓ}_{Z} and f^{ℓ}_{c}, the relative efficiency of c-jet tagging, and finally the relative efficiency of the trigger selections K^{ℓ}_{T}. These uncertainties are further classified into three different types:

- Type 1: correlated parameters among the OS and SS events predictions such as production cross section of various processes involved in the background sample composition, luminosity, isolated lepton reconstruction efficiency, jet reconstruction efficiency, jet energy scale and resolutions, the branching fractions into the muon and the muon reconstruction efficiency.

- Type 2: correlated parameters among the OS, SS and inclusive $W+$jets events predictions such as luminosity, isolated lepton reconstruction efficiency, and jet reconstruction efficiency and relative jet energy scale and resolution.

- Type 3: uncorrelated parameters such as f_c^ℓ, f_Z^ℓ, $f_{\rm MJ}^\ell$, charge correlations in the W^+W^-, $t\bar{t}$ and multijet background processes, and the relative trigger efficiency factor K_T^ℓ. The uncertainty on ϵ_c^ℓ is also partially included in this category, as this is the factor that need to be divided to calculate the cross section ratio. The uncertainty associated with jet-muon reconstruction is taken to be common with the ϵ_c^ℓ and the ones classified as Type 1.

The correlation among the parameters is considered to be zero. The uncertainties associated with the DØ luminosity is 6.1%, and the cross sections uncertainties for various processes varies from 15% (such as $W+$ light-jet) to 30% (such as $W+b\bar{b}$ or $W+c\bar{c}$).

To test the null hypothesis the number of OS and SS events in both decay channels, $N_{\rm OS}^{\ell,i}$ and $N_{\rm SS}^{\ell,i}$ respectively, in each pseudo experiment are defined in the absence of the signal as

$$\begin{aligned} N_{\rm OS}^{\ell,i} &= f_c^{\ell,i} N_{{\rm SS},W+\text{light-jet}}^{\ell,i} + N_{{\rm SS},Wb\bar{b}}^{\ell,i} + N_{{\rm SS},Wc\bar{c}}^{\ell,i} + N_{{\rm OS},Z+\text{jets}}^{\ell,i} + N_{{\rm OS},WW}^{\ell,i} + N_{{\rm OS},t\bar{t}}^{\ell,i} + N_{\rm OS,MJ}^{\ell,i}, \\ N_{\rm SS}^{\ell,i} &= N_{{\rm SS},W+\text{light-jet}}^{\ell,i} + N_{{\rm SS},Wb\bar{b}}^{\ell,i} + N_{{\rm SS},Wc\bar{c}}^{\ell,i} + N_{{\rm SS},WW}^{\ell,i} + N_{{\rm SS},Z+\text{jets}}^{\ell,i} + N_{{\rm SS},t\bar{t}}^{\ell,i} + N_{\rm SS,MJ}^{\ell,i}. \end{aligned} \tag{8.14}$$

where the factor $f_c^{\ell,i}$ denotes the background factor in the i^{th} experiment, and $N_{{\rm SS},W+\text{light-jets}}^{\ell,i}$, $N_{{\rm SS},Wb\bar{b}}^{\ell,i}$, $N_{{\rm SS},Wc\bar{c}}^{\ell,i}$, $N_{{\rm SS},Z+\text{jets}}^{\ell,i}$, $N_{{\rm SS},WW}^{\ell,i}$, $N_{{\rm SS},t\bar{t}}^{\ell,i}$ and $N_{\rm SS,MJ}^{\ell,i}$ denote the number of SS events contributed from $W+$light-jets, $W+b\bar{b}$, $W+c\bar{c}$, $Z+$jets, W^+W^-, $t\bar{t}$ and multijet background,

respectively, in the i^{th} pseudo experiment. Similarly $N^{\ell,i}_{\mathrm{OS},Z+\mathrm{jets}}$, $N^{\ell,i}_{\mathrm{OS},WW}$, $N^{\ell,i}_{\mathrm{OS},t\bar{t}}$ and $N^{\ell,i}_{\mathrm{OS,MJ}}$ denote the number of OS events contributed from $Z+\mathrm{jets}$, W^+W^-, $t\bar{t}$ and multijet background, respectively, in the i^{th} pseudo experiment. The number of inclusive $W+\mathrm{jets}$ events in each pseudo experiment is modelled as

$$N^{\ell,i}_{W+\mathrm{jets}} = (1 - f^{\ell,i}_{Z} - f^{\ell,i}_{\mathrm{MJ}})N^{\ell,i}_{Wj}. \tag{8.15}$$

The cross section ratio is evaluated for every pseudo experiment using the formula

$$R^{\ell,i}_{\mathrm{null}} = \frac{N^{\ell,i}_{\mathrm{OS}} - N^{\ell,i}_{\mathrm{SS}}}{K^{\ell,i}_{T}\epsilon^{\ell,i}_{c}N^{\ell,i}_{W+\mathrm{jets}}}, \tag{8.16}$$

where $\epsilon^{\ell,i}_{c}$ and $K^{\ell,i}_{T}$ deonte the c-jet tagging efficiency and the trigger bias correction factor in the i^{th} experiment. The null hypothesis is tested by computing the fraction of pseudo experiments in which the value of $R^{\ell,i}_{\mathrm{null}}$ is greater than or equal to the observed cross section ratio in both the electron and muon channels. Figure 8.3 shows the distribution of $R^{\ell,i}_{\mathrm{null}}$ in the pseudo experiments. The intergal of the shaded distribution in this figure equal to or above the observed value of the cross section ratio in both electron and muon channels represents the events emerging from the upward fluctuation of background. The ratio of these events with respect to the total generated events gives the p-Value, as commonly known in the statistical analyses. Thus using the ensemble test the probablity of the upward fluctuation of the background to produce the signal is evaluated to be 2.5×10^{-4}, which corresponds to 3.5 one sided Gaussian sigma. The Gaussian significance level (SL) that corresponds to this probability is defined as

$$\int_{SL}^{\infty} \frac{1}{\sqrt{2\pi\sigma}} e^{\frac{(x-x_o)^2}{2\sigma^2}} = p\text{-Value}, \tag{8.17}$$

where the mean $x_o = 0$ and the Gaussian error $\sigma = 1$.

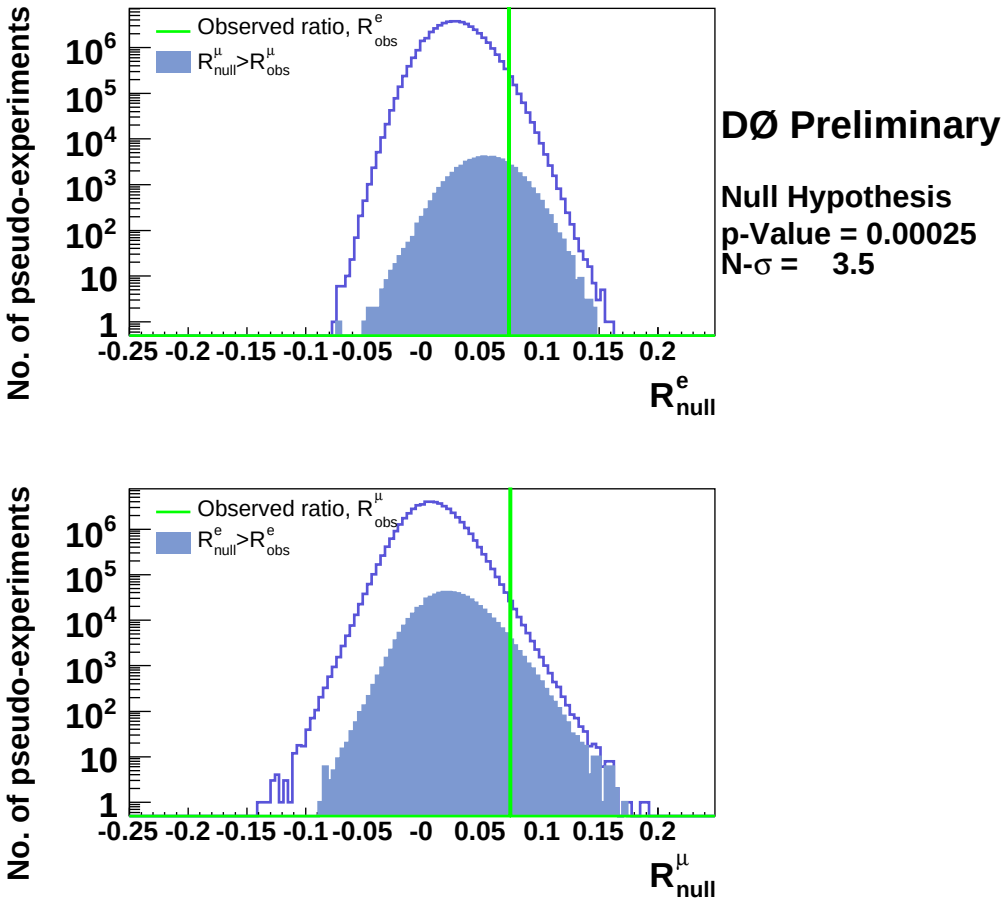

Figure 8.3: The probability distribution of the expectations of the cross section ratio R_{bkd} in the null hypothesis. In the ensemble test, all possible configurations of the OS and SS events and the inclusive W + jets events are obtained by allowing variations according to the systematics uncertainties associated with the parameters.

Chapter 9

Conclusion

A measurement of the cross section ratio of the $W + c$-jet process to the inclusive $W +$jets is performed using the DØ detector at the Fermilab Tevatron Collider. The DØ data utilized for this measurement amount to about 1 fb^{-1} of luminosity. The identification of the W boson is carried out using its leptonic decays $W \to e\nu$, $W \to \mu\nu$. The taus from the W bosons are included if they subsequently decay leptonically, $\tau \to e\bar{\nu}_e\nu_\tau$ or $\tau \to \mu\bar{\nu}_\mu\nu_\tau$. The c-jet is identified from the presence of muon in the jet together with the correlation between the charge of this muon with that of the associated W boson. The measured rate of $W + c$-jet production is 0.074 ± 0.023, which is consistent with the LO perturbative QCD predictions determined from ALPGEN+PYTHIA packages. This also allows us to conclude that the data agrees with the s quark PDF evolved from low momentum Q^2 scale which is at least two orders of magnitude below that of this measurement at the Tevatron. The statistical tests show that the probability that the background fluctuations could produce equal to or greater than the observed rate of $W + c$-jet production is 2.5×10^{-4}, which corresponds to a 3.5 σ one-sided Gaussian significance.

9.1 Future Prospects

The data collected by the DØ detector is increasing with time, so far approximately 3 fb^{-1} integrated luminosity of data has been recorded on tapes. The Tevatron is scheduled to run until the year 2009 at least. By that time the integrated luminosity is expected to increase

up to 6 fb^{-1}. The current measurement of $W + c$-jet is statistics limited, and the precision of the measurement can be improved to 13% with 6 times more data. Due to additional silicon layer closest to the beam pipe, there will be further improvement in the significance of the $W + c$-jet observation.

The future machine for the hadron physics experiments is the Large Hadron Collider (LHC) at CERN, that will collide the proton beam with another proton beam at the center-of-mass energy of 14 TeV. The cross section of quark-gluon interaction at LHC will be significantly larger than that of the quark-antiquark interactions. The $W + c$-jet measurements at both the CDF and DØ experiments provide a direct evidence of the quark-gluon interactions. At LHC, the production cross section of $W + c$-jet will be about 30 times higher than that at the Tevatron.

Bibliography

[1] V. M. Abazov and et al., Phys. Rev. Lett. **94**, 161801 (2005).

[2] A. Abulencia and et al., Phys. Rev. Lett. **74**, 032008 (2006).

[3] T. Aaltonen and et al., Phys. Rev. Lett. **100**, 091803 (2008).

[4] H. L. Lai and et al., arXiv:hep-ph/0702268 **v2** (2007).

[5] F. Halzen and A. D. Martin, *Quarks and Leptons: An Introductory Course in Modern Particle Physics*, volume 1st Ed., John Wiley and Sons, 1984.

[6] W.-M. Yao and et al., J. Phys. G **33**, 1 (2006).

[7] E. A. Paschos, *Electroweak Theory*, volume 1st Ed., Cambridge University Press, 2007.

[8] R. K. Ellis, W. J. Stirling, and B. R. Webber, *QCD and Collider Physics*, volume 1st Ed., Cambridge University Press, 1996.

[9] H. D. Politzer, Phys. Rev. Lett. **30**, 1346 (1973).

[10] D. J. Gross and F. Wilczek, Phys. Rev. Lett. **30**, 1343 (1973).

[11] T. L. E. W. Group, 2008, http://lepewwg.web.cern.ch/LEPEWWG/.

[12] S. Weinberg, Phys. Rev. Lett. **36**, 294 (1976).

[13] B. L. Lee, C. Quigg, and H. Thacker, Phys. Rev. Lett. **38**, 883 (1977).

[14] the TEVNPH Working group, hep-ex/0804.3423v1 (April 2008).

[15] E. Ma, hep-ph/0306218 **v1** (June 2003).

[16] the LEP collaborations, the LEP Electroweak Working Group, and the SLD Heavy Flavour Group, hep-ph/0212036 **v3** (April 2003).

[17] S. P. Martin, hep-ph/0709356 **v3** (June 2006).

[18] T. E. W. G. for the CDF and D. Collaborations, arXiv:hep-ex/0803.1683 **v1** (2008).

[19] S. L. Alder, Phys. Rev. **143**, 1144 (1963).

[20] D. J. Gross and C. H. L. Smith, Nucl. Phys. B **14**, 337 (1969).

[21] V. Gribov, Sov. J. Nucl. Phys. **15**, 438 (1972).

[22] L. Lipatov, Sov. J. Nucl. Phys. **15**, 675 (1972).

[23] L. Lipatov, Sov. J. Nucl. Phys. **20**, 94 (1975).

[24] G. Altarelli and G. Parisi, Nucl. Phys. B **126**, 298 (1977).

[25] Y. Dokshitzer, Sov. Phys. JETP **46**, 641 (1977).

[26] F. Halzen and D. Scott, Phys. Rev. D **18**, 3378 (1978).

[27] R. D. Field and R. P. Feynman, Phys. Rev. D **15**, 2590 (1977).

[28] X. Artru and G. Mennessier, Nucl. Phys. B **70**, 93 (1974).

[29] M. G. Bowler, Zeit. Phys. C **11**, 169 (1981).

[30] B. Andersson, G. Gustafson, and B. Soderberg, Nucl. Phys. B **264**, 29 (1986).

[31] R. D. Field and S. Wolfram, Nucl. Phys. B **213**, 65 (1983).

[32] B. R. Webber, Nucl. Phys. B **238**, 492 (1984).

[33] V. Barger and R. Phillips, *Collider Physics, Frontier in Physics Lecture Note Series*, volume 1st Ed., Addison-Wesley Publishing Company, 1987.

[34] E. Boos and et al., Nucl. Instrm. Methods Phys. Res. A **534**, 250 (2004).

[35] D. Mason, et al., and (the NuTeV collaboration), Phys. Rev. Lett. **99**, 192001 (2007).

[36] M. Goncharov, et al., and (the NuTeV collaboration), Phys. Rev. D **64**, 112006 (2001).

[37] P. Vilain, et al., and (the Charm II collaboration), Eur. Phys. J. C **11**, 19 (1999).

[38] A. O. Bazarko, et al., and (the CCFR collaboration), Z. Phys. C **65**, 189 (1995).

[39] S. A. Rabinowitz, et al., and (the CCFR collaboration), Phys. Rev. Lett. **70**, 134 (1993).

[40] R. Turlay, et al., and (the CDHS collaboration), Z. Phys. C **15**, 19 (1982).

[41] M. Holder, et al., and (the CDHS collaboration), **69**, 377 (1977).

[42] H. L. Lai, et al., and (the CTEQ collaboration), Eur. Phys. J. C **12**, 375 (2000).

[43] H. L. Lai, et al., and (the CTEQ collaboration), Phys. Rev. D **51**, 4763 (1995).

[44] W. C. Leung, et al., and (the CCFR collaboration), **317**, 655 (1993).

[45] J. Pumplin and et al., arXiv:hep-ph/0201195 (2002).

[46] M. L. Mangano, JHEP **0307**, 001 (2003).

[47] W. K. Tung and et al., arXiv:hep-ph/0611254 (2006).

[48] A. D. Martin and et al., **604**, 61 (2004).

[49] V. M. Abazov and et al., **to be published** (2008).

[50] On-line plotting and calculation, http://durpdg.dur.ac.uk/hepdata/pdf3.html.

[51] V. Abazov, et al., and (the DØ collaboration), Nucl. Instrm. Methods Phys. Res. A **565**, 463 (2006).

[52] B. Casey et al., Determination of the effective inelastic p pbar cross-section for the do luminosity measurement using upgraded readout electronics, DØ Note 4958, 2005.

[53] G. Borissov, Technical details of aa tracking, All DØmeeting, 2005.

[54] A. Khanov, Htf: histograming method for finding tracks. the algorithm description., DØ Note 3778, 2000.

[55] P. Hough, Machine analysis of bubble chamber pictures, International Conference on high energy Accelerators and Instrumentation, CERN, 1959.

[56] R. Fruhwirth, Nucl. Instrm. Methods Phys. Res. A **262**, 444 (1987).

[57] A. Schwartzman and C. Tully, Primary vertex reconstruction by means of adaptive vertex fitting, DØ Note 4918, 2005.

[58] A. Schwartzman and M. Narian, Vertex fitting by means of the kalman filter techinque, DØ Note 3907, 2001.

[59] A. Schwartzman and M. Narian, Probabilistic primary vertex selection, DØ Note 4042, 2002.

[60] http://www-d0.fnal.gov/phys_id/emid/d0_private/emid_intro.html.

[61] G. Steinbruck, Measurement of the angular distribution of electron from w boson decays, PHD thesis, 1999.

[62] S. Jung, Electron likelihood in p14, DØ note 4449, 2004.

[63] B. Andrieu, Jet finding algorithms at the tevatron, DØ note 5168, 2006.

[64] A. Harel, Jet id optimization, DØ note 4919, 2005.

[65] A. Harel and R. Wagner, Improved l1 confirmation, DØ note 4932, 2005.

[66] http://www-d0.fnal.gov/phys_id/jes/d0_private/certified/v07-01-02/links.html.

[67] P. Calfyan and et al., Muon identification certification for p17 data, DØ note 5157, 2007.

[68] http://www-d0.fnal.gov/computing/algorithms/calgo/met/metdoc.html.

[69] T. Sjöstrand and et al., Comput. Phys. Commun. **135**, 238 (2001).

[70] S. Hoche et al., arXiv:hep-ph/0602031 **v1** (2006).

[71] J. C. Collins, arXiv:hep-ph/0312336 **v1** (2003).

[72] http://www-d0.fnal.gov/computing/MonteCarlo/MonteCarlo.html.

[73] R. Brun and F. Carminati, Geant package, CERN Program Library Long Write up W5013, 1993.

[74] D. J. Lange, Nucl. Instrm. Methods Phys. Res. A **462**, 152 (2001).

[75] http://root.cern.ch.

[76] http://www-d0.fnal.gov/Run2Physics/cs/caf/.

[77] http://www-d0.fnal.gov/Run2Physics/cs/index.html.

[78] http://www-d0.fnal.gov/phys_id/emid/d0_private/emid.html.

[79] J. Hays, J. Mitrevski, C. Schwanenberger, and T. Toole, Single electron efficiencies in p17 data and monte carlo, DØ note 5025, 2006.

[80] J. Collin, D. Soper, and G. Sterman, **250**, 199 (1985).

[81] G. A. Ladinsky and C. P. Yuan, Phys. Rev. D **50**, 4239 (1994).

[82] N. Makovec and J. F. Grivaz, Shifting, smearing and removing simulated jets, DØ Note 4914, 2005.

[83] M. Voutilainen and C. Royon, Jet p_t resolution using jetcorr v7.1, DØ Note 5381, 2006.

[84] M. Voutilainen, Jet p_t resolution for run iia final jes v7.2 with dijet j4s jet corrections, DØ Note 5499, 2008.

[85] V. Abazov, et al., and (the DØ collaboration), Phys. Rev. Lett. **94**, 152002 (2005).

[86] V. Abazov, et al., and (the DØ collaboration), Phys. Rev. Lett. **98**, 181802 (2007).

[87] K. Abe and et al. (the SLD collaboration), Phys. Rev. Lett. **78**, 3442 (1997).

[88] V. M. Abazov and et al (the DØ collaboration), Phys. Rev. Lett. **94**, 151801 (2005).

[89] V. M. Abazov and et al (the DØ collaboration), Phys. Rev. D **76**, 092007 (2007).

[90] V. M. Abazov and et al (the DØ collaboration), Phys. Rev. Lett. **98**, 181802 (2007).

[91] R. P. Smith, Describing the dø solenoid in dø geant, DØ Note 4803, 2005.

[92] C. Butter and et al., arXiv:hep-ph/0803.0678v1 **v2** (2008).

[93] H. A. et al. and (the CDHS collaboration), Z. Phys. C **17**, 283 (1983).

[94] C. A. et al. and (the STAR collaboration), **21**, 143 (2004).

[95] G. Abbiendi, et al., and (the OPAL collaboration), Eur. Phys. J. C **37**, 25 (2004).

[96] A. Khanov, Measurement of the $t\bar{t}$ production cross section at $\sqrt{s} = 1.96$ tev using lifetie tagging, PHD thesis, 2004.

[97] J. Campbell and K. Ellis, MCFM package, http://mcfm.fnal.gov/.

Appendix A

Probabolity of muons from π and K decays in jets

Let N_o represents a number of relativistic particles (π or K) after the $p\bar{p}$ interaction happens. In a medium with infinite interaction length, the decay rate of particles is

$$\begin{aligned} \frac{dN}{dx} &= \frac{-N}{c\tau\gamma} \\ N(x) &= N_o e^{\frac{-x}{c\tau\gamma}} \end{aligned} \tag{A.1}$$

where τ is the average life time of the particle, and γ is the Lorentz's factor. Here $N(x)$ represents the survival probability of the particles as they travel distance x. So the decay probability of the particle after it traveled distance x would be

$$\begin{aligned} N_D(x) &= N_o - N(x) \\ &= N_o \left(1 - e^{\frac{-x}{c\tau\gamma}}\right) \end{aligned} \tag{A.2}$$

For a dense material (e.g steel) with some interaction length λ there is an additional mechanism for particle loss due to nuclear interactions. The rate of change of the number of particle after traversing a distance x would become

$$\begin{aligned} \frac{dN^m}{dx} &= \frac{dN}{dx}|_D + \frac{dN}{dx}|_I \\ &= -\frac{N}{c\tau\gamma} - \frac{N}{\lambda} \\ N^m(x) &= N_o e^{\frac{-x}{c\tau\gamma}} e^{\frac{-x}{\lambda}}. \end{aligned} \tag{A.3}$$

The number of particles that interacted with or decayed in the material would be

$$\begin{aligned} N^m_{ID}(x) &= N_o - N^m(x), \\ &= N_o \left(1 - e^{\frac{-x}{c\tau\gamma}} e^{\frac{-x}{\lambda}}\right). \end{aligned} \tag{A.4}$$

The probability of particles that decayed in the material, N^m_{ID}, after these particles traveled distance x can be re-expressed as

$$N^m_{ID}(x) = N^m_I(x) + N^m_D(x), \tag{A.5}$$

where

$$\begin{aligned} N^m_I(x) &= \int \frac{dN}{dx}|_I dx = \int -\frac{N}{\lambda} dx \\ &= -\frac{N}{\lambda} x \end{aligned} \tag{A.6}$$

and

$$\begin{aligned} N^m_D(x) &= \int \frac{dN}{dx}|_D dx = \int -\frac{N}{c\tau\gamma} dx \\ &= -\frac{N}{c\tau\gamma} x \end{aligned} \tag{A.7}$$

This implies

$$\begin{aligned} N^m_{ID}(x) &= N^m_D(x) \left(\frac{N^m_I(x)}{N^m_D(x)} + 1\right) \\ &= N^m_D(x) \left(\frac{c\tau\gamma}{\lambda} + 1\right) \\ &= \frac{c\tau\gamma + \lambda}{\lambda} N^m_D(x) \end{aligned} \tag{A.8}$$

Using this in Eq.(A.4) we get

$$N^m_D(x) = \frac{\lambda}{c\tau\gamma + \lambda} N_o \left(1 - e^{\frac{-x}{c\tau\gamma}} e^{\frac{-x}{\lambda}}\right) \tag{A.9}$$

The DØ detector is inhomogeneous with various type of detecting material over the radial distances from the beam interaction center. There is a negligible probability for the particles

to interact in the CFT region which is surrounded by a magnet with a particle interaction length of 0.18λ [91]. The calorimeter is situated after the solenoid magnet, where particles are very unlikely to decay into high p_T muons due to their rapid energy loss in showering process. Therefore, the radius of the detector where π/K decays become more important is upto 75 cm. Inside the tracker region (53 cm), particles will only decay, while in the magnet region ($53 < r < 75$ cm) particles will shower as well as decay. Thus, inside the CFT tracker region the decay probability would be

$$N_{CFT}(x, x_o) = N_o \left(1 - e^{\frac{-(x-x_o)}{c\tau\gamma}}\right) \tag{A.10}$$

and inside the magnet region

$$\begin{aligned} N_{sol}(x, x_o) &= N_{CFT}(53, x_o) \\ &\quad + N_o \frac{\lambda_{sol}}{c\tau\gamma + \lambda_{sol}} \left(1 - e^{\frac{-(x-53)}{c\tau\gamma}} e^{\frac{-(x-53)}{\lambda_{sol}}}\right) e^{\frac{-(53-x_o)}{c\tau\gamma}} \end{aligned} \tag{A.11}$$

where x_o is the position of the particle in x-y plane of the detector where it originated. The total probability for a particle to decay would be the sum of equations (A.10 and A.11). The interaction length, λ_{sol}, within the solenoid magnet is given by

$$\lambda_{sol} = \frac{A}{N_A \rho \sigma_N} \tag{A.12}$$

where $N_A = 6.022 \times 10^{23}$ is the Avagadro's number, ρ is the density of the magnet material, A is the atomic weight, and $\sigma_N = \pi^2 r_N$ is the cross sectional area of the atomic nucleus with radius $r_N \approx 1$ fm. Assuming the whole solenoid to be a copper material with density $\rho = 8.96$ g/cm^3, the nuclear interaction of particles inside the copper is $\lambda_{sol} = 118.6$ cm. In terms of the λ_{sol}, the cylindrical radius covered by the region between tracking detector and calorimeter is $0.14\ \lambda_{sol}$.